High Yield Production and Biofunctionalization of Plasma Polymerized Nanoparticles for Applications in Biomedicine

Laura Libnan Haidar

Supervisors: Professor Marcela Bilek, Dr Behnam Akhavan

A thesis submitted in fulfilment of the requirements for the degree of Doctor of Philosophy

This research reported in this thesis was supported by the award of a Research Training Program scholarship to the PhD Candidate.

School of Physics
Faculty of Science
The University of Sydney

March 2024

Statement of Originality

This is to certify that to the best of my knowledge the content of this thesis is my own work. This thesis has not been submitted for any degree or other purposes.

I certify that the intellectual content of this thesis is the product of my own work and that all the assistance received in preparing this thesis and sources have been acknowledged.

X

Laura Libnan Haidar

Date: 05/03/2024

Abstract

The advent of nanoparticle technology in the medical and pharmaceutical sectors offers significant potential in the quest for more effective healthcare solutions. Surface biofunctionalization, the engineering of nanoparticle surfaces for targeted biomedical applications, is critical for the development of personalized medicine in the delivery of diagnostic and therapeutic agents. However, the transition from laboratory research to commercial scale production faces substantial challenges in ensuring scalability of synthesis methods, consistent nanoparticle quality and addressing safety concerns related to toxicity. The commercial viability of nanoparticle-based medical products requires the precedence of translation into clinical settings warranting their integration into cellular environments while maintaining bioactivity. Traditional methods for nanoparticle synthesis and functionalization often fall short from achieving this aim due to inconsistencies in particle sizes, high production costs, reagent toxicity and subsequent complex wet-chemical processing.

This thesis introduces plasma polymerization as a high-throughput method for producing surface-active polymeric nanoparticles, through a more environmentally friendly, dry synthesis process. Chapter 1 introduces the foundational role of polymer nanoparticles in nanomedicine, emphasizing their surface functionalization mechanisms for improved diagnostics and therapeutics, and identifies challenges in overcoming biological barriers for targeted cellular delivery. Chapter 2 presents the general methodologies used throughout the thesis. In Chapter 3, an enhancement of the collection yield was achieved while maintaining the physicochemical properties required for subsequent surface treatment. This was demonstrated through the biofunctionalization of the resulting plasma polymerized nanoparticles (PPNs), achieved through a single-step, reagent-free immobilization of various diagnostic molecules. This process led to the formation of strong, non-cytotoxic covalent bonds, as confirmed by *in vitro* cellular studies and imaging in Chapter 4. The long-term stability and integrity of the nanoparticles was studied under various storage conditions in Chapter 5, providing evidence for their bioactivity after one year of storage. Finally, the last chapter presented detailed characterization and diagnostics in the plasma reactor used for PPN synthesis, validating a continuum fluid model against experimental data to refine the model's predictive accuracy and enhance our understanding of parameters that affect plasma-assisted nanoparticle synthesis.

This thesis has established the capability of PPNs in bridging the gap between laboratory innovation and clinical utility. By demonstrating a scalable approach to nanoparticle production and biofunctionalization, PPNs can pave the way for the development of next-generation nanomedicines for disease diagnostics and treatments.

Acknowledgements

I stand at the culmination of an incredible journey that has been my PhD, a journey that was as much personal as it was academic. This pivotal chapter, filled with challenges and triumphs, would not have been possible without a constellation of remarkable individuals and institutions, to whom I extend my heartfelt thanks.

First and foremost, I bow my head in deep gratitude to Allah, the Most Gracious and Most Merciful, for bestowing upon me the strength, patience and endurance required to navigate the challenges of this PhD journey. It is through His Divine grace and endless blessings that I have been able to reach this significant milestone and for this, I am eternally thankful.

I express my profound appreciation to my supervisors, Professor Marcela Bilek and Dr. Behnam Akhavan, whose expertise, attention to detail and rigorous standards pushed me to refine my work to its best version. Your guidance was not just academic but also a moral compass during those moments of doubt and uncertainty. I am immensely thankful for your unwavering support.

I extend my gratitude to the unforgettable members of my research group, Kosta, Thao, Khadijeh, Aaron, Ian, Phil, Oliver, Mark, Julian and Alex for their time and insightful comments, which widened my research perspectives. And to members of neighbouring research groups, Professor Joe Khachan, Richard, Nico, and many more, your input was crucial in shaping the direction of my research. A special thank you to Caleb and staff from the Physics workshop for their expertise in design and engineering when needed in the laboratory.

To my peers and fellow researchers, Luke, Elmer, Alice, Bingyan, Jiayan, Ghazal, Massoud, Jerry, Lucy, thank you for the stimulating discussions and endless rants. It was a pleasure to walk through this journey with you and a joy to help supervise the brief research projects of Emma, Angelina, Himeth, Yu, Tom and Caitlin.

My deepest gratitude goes to my family, especially my parents and siblings for their love, sacrifices, and unwavering belief in my capabilities. You were my rock in times of hardship and the first to celebrate every small victory. And to my brave little brother, Ali, your resilience in facing life's challenges has inspired me every day. Your journey, filled with silent battles, taught me the true meaning of perseverance and strength. Thank you for being my silent motivator.

To my dear husband, thank you for believing in me even when I didn't. You have supported me with my research and work through the ups and downs. Your presence, love, and endless patience was a blessing that made all the difference. This achievement is as much yours as it is mine.

The completion of this thesis was shadowed by the indescribable struggles of the Palestinian people, whose indomitable faith amidst egregious suffering and injustice has deeply impacted me. Their extraordinary resilience in the face of genocide has starkly put into perspective the relative insignificance of the obstacles I encountered in my academic journey, imbuing me with a profound sense of humility and perspective. May Allah have mercy on the souls lost. Leve Palestina.

Academic outputs

Patents

International PCT patent application PCT/AU2022/051135.
'High Yield Plasma Polymerization of Nanoparticles'.

Journal publications

Baldry, M., Haidar, L. L., Akhavan, B., & Bilek, M. M. (2021). Continuum modelling of an asymmetric CCRF argon plasma reactor: Influence of higher excited states and sensitivity to model parameters. Plasma Processes and Polymers, 18(6), 2000243.

Haidar, L. L., Baldry, M., Fraser, S. T., Boumelhem, B. B., Gilmour, A. D., Liu, Z., Bilek, M.M. & Akhavan, B. (2022). Surface-active plasma-polymerized nanoparticles for multifunctional diagnostic, targeting, and therapeutic probes. ACS Applied Nano Materials, 5(12), 17576-17591.

Haidar, L. L., Bilek, M., & Akhavan, B. (2024). Surface Bio-engineered Polymeric Nanoparticles. Small, 2310876.

(Submitted for publication) Haidar, L.L., Wang, Y., Gilmour, A. D., Boumelhem, B. B., Austria Jr., E., Khan, N. A., Fadzil, A.A., Fraser, S. T., Bilek, M.M. and Akhavan, B. (2024). Direct covalent attachment of fluorescent molecules on plasma polymerized nanoparticles: a simplified approach for biomedical applications.

Conference Presentations

"Plasma Polymerized Nano particles: Synthesis, Diagnostics, and Bio-functionalization."
Oral presentation at *SICT 2023 / PlasmaTech 2023/ Tribology 2023 Joint Conferences. Lisbon, Portugal.*

"RF Plasma Protocol for the Facile Fabrication and High-Yield Collection of Bio-Functional Polymeric Nanoparticles." *Oral presentation at the Gaseous Electronic Meeting 2022. Sydney, Australia.*

"A Simple Polymeric Nanoparticle Synthesis Approach for the Facile Surface Conjugation of Functional Molecules." *Oral presentation at the Materials Oceania 2021 conference. Brisbane, Australia (Virtual).*

"CCRF Plasma for the Facile Fabrication of Bio-Functional Polymeric Nanoparticles." *Oral presentation at the 10th International Workshop on Functional Nanocomposites 2021. Varese, Villa Cagnola, Italy (Virtual).*

"RF Plasma for the Facile Synthesis of Bio Functional Polymeric Nanoparticles." *Poster presentation at the 8th International Conference on Plasma Medicine 2021. Seoul, Republic of*

Korea (Virtual).

"RF Plasma for the Facile Fabrication of Bio-Functional Polymeric Nanoparticles." *Poster presentation at the American Vacuum Society AVS 67 Virtual Symposium 2021.*

Awards and Scholarships

.

- Research Training Program stipend scholarship.
- "Best Student Talk" award at the GEM conference 2022.
- Postgraduate Research Support Scheme x2
- The University of Sydney Nano Institute Student Ambassador Scholarship
- Faculty of Science Completion Scholarship

Authorship attribution statement

Chapter 1 has been published as a review article in Small as: 'Surface Bio-engineered Polymeric Nanoparticles' by Haidar, L. L., Bilek, M. M., & Akhavan, B. (2024).
I performed the literature research, critically analysed the field, wrote the review, developed the conclusions, and suggested future directions. I received feedback from my supervisors, Marcela and Behnam.

Chapter 3 is adapted from a manuscript which has been published in ACS Applied Nano Materials as: 'Surface-active plasma- polymerized nanoparticles for multifunctional diagnostic, targeting, and therapeutic probes.' by Haidar, L.L., Baldry, M., Fraser, S.T., Boumelhem, B.B., Gilmour, A.D., Liu, Z., Zheng, Z., Bilek, M.M. and Akhavan, B. (2022).
I designed the study, developed the high yield collection strategy, performed surface conjugation and characterization experiments, analysed the data, and wrote the drafts of the manuscript with guidance from my supervisors. Dr. Aaron Gilmour performed the cytotoxicity assay, Drs. Bob Boumelhem and Stuart Fraser executed the flow cytometry/nanometry, Dr. Behnam Akhavan conducted the XPS measurement, Mr. Zhong Zheng carried out TEM at my direction, and Dr. Mark Baldry performed the modelling, guided by my input on the plasma system.

Chapter 4 is adapted from a manuscript submitted for publication in Nanoscale as: 'Direct covalent attachment of fluorescent molecules on plasma polymerized nanoparticles: a simplified approach for biomedical applications.' by Haidar, L.L., Wang, Y., Gilmour, A.D., Boumelhem, B. B., Austria Jr., E., Khan, N.A., Fadzil, A.A., Fraser, S.T., Bilek, M.M. and Akhavan, B. (2024).
I contributed to the design of the study, produced the particles, conducted surface conjugations, performed particle characterizations, conducted the cell imaging, analysed the data and wrote the drafts of the manuscript with guidance from my supervisors. Mr. Elmer Austria Jr. contributed to the Nile Blue study at my direction, and adsorption and FITC studies were conducted by Dr. Yuheng Wang with Drs. Bob Boumelhem and Stuart Fraser. Guidance on cell studies was provided by Dr. Aaron Gilmour, with EPR results assisted by Dr. Thao (Clara) Tran and performed at UNSW. Surface and molecular analyses involved Ms. Arifah Anwar Fadzil's water contact angle measurements, Dr. Naveed Aziz Khan's SEM work, and XPS by Dr. Behnam Akhavan, including Tof-SIMS measurements at UniSA (Adelaide).

Chapter 5 is currently being drafted for publication. I designed the study, conducted the particle production and storage, carried out the characterization experiments, analyzed the data, and wrote the drafts of the manuscript with guidance from my supervisors. Mr. Elmer Austria Jr. aided with the Nile Blue study and the TEM measurements were carried out by Dr. Zhong Zheng and Dr. Hong Zhao at my direction.

In **Chapter 6,** the modeling results are adapted from a manuscript published in Plasma Processes and Polymers as: 'Continuum modelling of an asymmetric CCRF argon plasma reactor: Influence of higher excited states and sensitivity to model parameters.' by Baldry, M., Haidar, L. L., Akhavan, B., & Bilek, M. M. (2021)
I performed experiments for data validation for the model built by Dr Mark Baldry, assisted in developing the theory behind the model, contributed to the discussions, and provided feedback on

the draft of the manuscript. I also designed the plasma characterization study, set up and performed the plasma diagnostics, analyzed the data and wrote the chapter with guidance from my supervisors. Langmuir probe measurements and discussions were carried out with the aid of Dr Seyaedeh Khadijeh Alavi and Mr Jerry Zhao.

My supervisors have provided feedback on all aspects of these projects. All measurements were performed at my direction, observation, and/or involvement in the experimental design. All other planning, treatments, measurements, analyses and writing were conducted by me.

The above represents an accurate summary of my contributions to this thesis, and I give my consent for this thesis to be added to the University of Sydney Library's digital repository and made available for public use.

X

Laura Libnan Haidar

Date: 5/3/2024

As supervisors for the candidature upon which this thesis is based, we can confirm that the authorship attribution statement above is correct.

X

Marcela M. M. M. Bilek

Date: 4/3/2024

Behnam Akhavan

Date: 5/03/2024

Contents

List of Figures

List of Tables

In His name, the Most Gracious, the Most Merciful…

Chapter 1. Introduction & Literature Review

This chapter reviews and discusses the advances in surface functionalization of polymeric nanoparticles (PNPs) for biomedical applications, emphasizing biosensing, bioimaging, targeted drug delivery, and cancer therapy. It highlights the significance of polymeric nanoparticles in achieving sustainable healthcare solutions, evaluates the benefits of employing various biofunctionalization techniques, including plasma polymerization, and identifies the existing gaps in the research landscape.

Chapter 1 has been partially published as a review article in Small entitled: "Surface Bio-engineered Polymeric Nanoparticles". DOI: https://doi.org/10.1002/smll.202310876.

1.1. Introduction

In the face of global grand challenges, the field of nanotechnology is finding itself at the forefront of international endeavours for sustainability. Upon the United Nation's call for the Decade of Action, the world's research has been redirected to achieve a list of Sustainable Development Goals (SDGs) by 2030 to "end poverty, protect the planet and improve the lives and prospects of everyone, everywhere" [1]. As a result, many efforts have been made to employ nanotechnology in progressing toward these goals, including promoting sustainable agriculture [2-4], improving water security [5-7], advancing electronics [8-10], and combating the latest Covid-19 pandemic disease [11-14]. In the pursuit of the "*Good health and well-being*" SDG, nanoparticles are proving to be the leading candidates for the design and fabrication of new medicinal products. Nanoparticles can also be engineered to exhibit a variety of opto-magnetic [15, 16], pharmacokinetic [17, 18] or catalytic [19, 20] properties. For biomedical applications, spanning from on-demand drug delivery in precision medicine to disease diagnostics, nanoparticles have gained tremendous scientific and commercial interest over the past few decades [21-25].

Polymeric nanoparticles (PNPs) present significant advantages in these emerging biomedical applications that inorganic materials do not possess. The flexible long-chain structure of polymers enables stable colloidal dispersions with minimal aggregation due to steric hindrance and electrostatic repulsion [26]. PNPs have shown great promise as attractive platforms for disease diagnostics, such as bioimaging, owing to their stability and dispersibility [27, 28]. They can also be successfully employed for cancer treatment because of their high loading capacity of active ingredients [29-31]. Their compatibility with biomolecular and cellular systems and modulated degradability facilitate their circulation in the blood and the removal of the load after its release. For all these intriguing applications, the meticulous selection of nanoparticle composition and surface properties is fundamental to their end-application success. As surface properties are correlated with bulk properties, the choice of the polymer depends on the desired surface characteristics of the particle and the nature of its load, both of which are governed by its intended biological role [32].

Surface functionalization of PNPs using bioactive tethering moieties, referred to as 'biofunctional molecules' in this review, is an established route to inducing specific cellular responses. The biofunctional molecules in this context can be categorized as molecules designed to have specific functions within biological systems and can be attached to the surface atoms of nanoparticles via their functional head groups [33]. They can range from small organic compounds (e.g., alkanethiols, amines, and carboxylic acids) to polymers like polyethylene glycols, surfactants, and functional biomolecules such as proteins, DNA, and peptides.

Successfully grafting biofunctional molecules onto nanoparticles modulates their surface characteristics and achieves desired biological activity such as biosensing [34-36], bioimaging [37, 38], and targeted therapy [39, 40] (**Figure 1**. For instance, nanoparticle structures specifically modified with ions, fluorophores, or antibodies can behave as nanoprobes for surface chemical fluctuations such as pH as well as sensors for reactive oxygen species (ROS) and biologically threatening agents [41, 42]. Further, surface functionality attained with metallic and non-metallic ionic groups as well as selectively-binding peptides can facilitate the recognition and imaging of tumours or cancerous cells [43-45]. Surface functionalization using polymer coatings can also

control the duration of circulation in the blood, or half-life, and prevent nanoparticle uptake by the immune system, thus significantly impacting its in vivo fate [46, 47]. Using hydrophilic polymers such as polyethylene glycol (PEG) or polysaccharide heparosan (HEP) grafted on the surface of the nanoparticle can provide "stealth" properties and increase their residence time in the blood [48-50]. On the other hand, surface treatment via the immobilization of a specific tumour-homing ligand, such as an antibody, antibody fragment, folic acid, peptide, aptamer, or polysaccharide, can facilitate specificity towards a diseased location, increase load-binding capacity and enhance cellular internalization necessary for effective targeted therapy [51-53]. Thus, the surface decoration with biofunctional molecules determines not only the surface nature of the particles but also the physico-chemical properties fundamental to realizing their application potential [54].

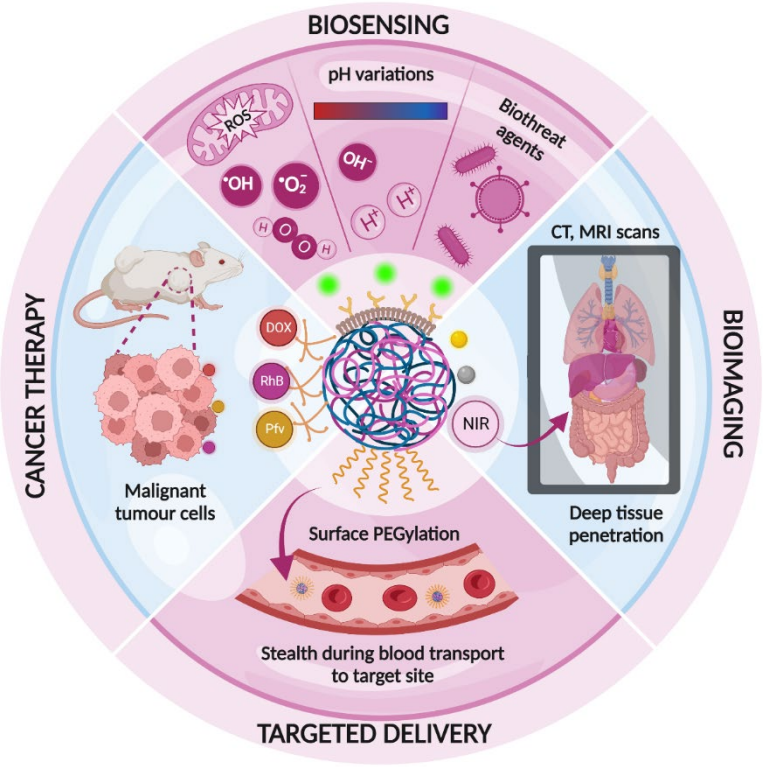

*Figure 1. Schematic illustration of surface-bioengineered polymeric nanoparticles (PNPs) for biomedical applications, including biosensing, bioimaging, stealthy delivery and targeted therapy. PNPs surface-functionalized by carbohydrates, antibodies, or acids can be utilized for biosensing through the fluorescence of fluorophores that detach upon interactions with reactive oxygen species (ROS), pH fluctuations, or markers of biothreat agents such as bacteria or viruses. For bioimaging using computed topography (CT), magnetic resonance imaging (MRI), or optical imaging requiring deep tissue penetration, Gold and other metallic particles can be conjugated to the surface of PNPs to track organs through mechanisms such as Near Infra-Red (NIR) Fluorescence. The delivery of any of these particles requires the extension of their duration in the blood stream for as long as possible. This can be achieved by modifying the nanoparticle surface with a polymer such as Polyethylene glycol (PEG), known as PEGylation. Conjugating models of drugs such as Doxorubicin (Dox), Rhodamine B (RhB) and Proflavine (Pfv) onto nanoparticle surfaces can be facilitated by a linker molecule such as Tannic Acid (TA) that have proven to increase the efficiency of the targeted delivery and therapy of diseased cellular sites, especially in malignant tumour cells.*This article critically reviews the recent advances made in developing PNPs

with biochemically modified surfaces for an array of biomedical implementations, including biosensing, bioimaging, and the targeted delivery of therapeutics. Although several review articles have served as an excellent resource for understanding the existing nanoparticle surface modification methods, they have often stemmed from an isolated perspective of a specific type of PNP [55-57] or a single biomedical application [58-60]. Here, we shed light on the mechanisms of biomolecule interactions with PNP surfaces, underpinning their function for a range of biomedical applications. This review seeks to consolidate and critically discuss recent progress made in tailoring PNP interfaces for biological activity.

A key emphasis of this review is to distinguish between the covalent and noncovalent nature of the bonds responsible for anchoring biomolecules to the surfaces of PNPs. We discuss how this distinction impacts the selection of functional molecules used to effectively tackle specific biological barriers. The stability and biological efficacy of the surface-functionalized PNPs are evaluated in the detection, diagnostics and treatment of diseases, including cancerous tumours, *in vitro* and *in vivo*. Finally, the review concludes with an overview of the challenges hindering further development, together with a perspective on the future of the field, before concluding with recommendations for the areas of focus that may be carried out to expedite the clinical translation of surface-functionalized PNPs.

1.2. Biofunctional molecules attached to polymeric nanoparticles: Mechanisms of surface attachment

Nanoparticles integrated within cellular environments induce a biological response that either recognizes them as compatible entities or attempts to eliminate them. Surface functionalization can tune the nanoparticle interactions with the physiological medium to prevent their extraction by the immune system. The type of surface functionalization processes can generally be classified as non-covalent [61, 62] or covalent [63, 64], with a difference in the nature and strength of the bonds. In this section, we provide an overview of noncovalent and covalent approaches to couple biofunctional molecules to PNPs, describe the mechanisms of attachment and evaluate their advantages and disadvantages (**Figure 2a**).

Noncovalent coupling of functional molecules to nanoparticles, also referred to as physisorption or physical adsorption, is achieved via physical interactions of the molecules in their internal cavities or on their surfaces. The underlying mechanism for such attachment includes van der Walls interactions, hydrogen bonding, and electrostatic interactions (also known as ionic bonding) [65]. Using oppositely charged surfaces or the polarity of the materials for the surface decoration of nanoparticles is a relatively simple modification strategy to immobilize molecules on surfaces since there is no linker chemistry involved, and often requires no or minimum preparation [66]. One example, among many, is the positively-charged functional groups of chitosan ($-NH_3^+$) that can electrostatically attach anti-HER2 antibodies on the surface of polymeric poly(lactic-co-glycolic acid) (PLGA) nanoparticles loaded with Doxorubicin [67]. Despite the simplicity of the process, the non-covalent nature of adsorption renders the functional molecule susceptible to exchange in the presence of other biomolecules with greater affinity to the surface. Also known as the Vroman effect, this competitive exchange needs to be investigated pre- attachment to assess the likelihood of instability of the conjugate [68-70].

Covalent coupling addresses the need to surface functionalize PNPs with more durable bonds. Covalent reactions between the surface of nanoparticles and the desired molecules can permanently alter the surface chemistry, achieved by binding the molecules via stronger chemical bonds. Covalent attachment via wet-chemical methods, as commonly used for bioreceptor immobilization, is either mediated by a precisely chosen linker added onto the particle surface or by the addition of suitable functional groups to anchor the biomolecules (**Figure 2b**).
Introducing an additional linker or spacer molecule is an established approach to facilitate the binding of a molecule with certain functional groups. As one recent example, this linker-mediated approach has been used to design DNA probes for the detection of peptides and proteins. The covalent attachment of amine-polyethylene glycol (PEG)-azide to carboxylated polystyrene particles aided the subsequent DNA aptamer probe attachment to the azide-PEG nanoparticle surface [71]. The targeting of histidine tags and VEGF protein was achieved at greater stability than conventional labels with high affinity and specificity. Although PEG and silane are generally employed as carbon-chain linker molecules, the existence of natural derivatives such as dopamine and chitosan offers a competitive variety of surface chemistries to be utilized for covalent functionalization.

Another method for covalent conjugation of functional molecules, as illustrated in **Figure 2b**, relies solely on reactive groups present on the surface of the nanoparticles. It entails the direct attachment of the molecules to the surface of nanoparticles without the need for separate linker molecules. The addition of organic functional groups, such as $R-NH_2$ and R-COOH, is widely applied in the field to directly bind biomolecules to nanoparticles [72]. Silica nanoparticles, for example, can be functionalized by aminosilanes, which introduce an amino group on the surface [73], whereas noble metals such as gold are often modified using crosslinkers with -SH or $-NH_2$ groups [74]. Through the oxidation of carbon-based nanomaterials, carboxyl (-COOH), hydroxyl (-OH), and carbonyl (-C = O) functional groups can be generated on the nanoparticle surface [75]. One of the most commonly used covalent conjugation chemistries is the carbodiimide-based coupling that facilitates the binding between the surface of PNPs and a variety of desired conjugates, including proteins, gold nanoclusters, fluorescent compounds and antibodies [76-79]. Further advances in conjugation chemistries have enabled more precise control over surface

modifications by using site-selective methods to conjugate ligands or functional groups to nanoparticles [80-82]. These approaches control the arrangement of chemically distinct and active sites, presenting prospects for additional modifications through the selective masking or exposure of reactive groups [83]. For instance, harnessing site-selective chemistries such as vinyl sulfone conjugation [84], maleimide functionality [85] and azidation [86] to conjugate antibody fragments to PLGA–based NPs has been shown to enhance antigen binding compared to conventional methods. By refining the reaction domains, formulations with increased binding affinities can be produced, optimizing ligand orientation for maximal interaction and enhancing the effectiveness of the covalent conjugation [87, 88]. Nonetheless, strong covalent binding faces limitations arising from the control of environmental conditions during functionalization, such as pH [89] as well as non-specific interactions between living systems and the nanoparticles [90].

The complex nature of wet-chemical covalent conjugation approaches remains their major drawback. Current protocols necessitate multiple steps, encompassing polymer or conjugate preparation, chemical intervention during or after particle polymerization, and are often followed by subsequent purification procedures [45, 91-94]. For example, the covalent PEGylation of polystyrene nanoparticles requires aminated PEG, carboxyl-modified nanoparticles, cross-linking agents like 1-ethyl-3-(3-dimethylaminopropyl)-carbodiimide, and quenching agents such as glycine, often entailing over three incubations, prior to any biofunctional molecule conjugation [91, 95]. Intermediate wet chemical coupling steps can be complicated, time-consuming, and necessitate high costs. PNPs covalently linked with imaging agents also exemplify the challenges associated with dissolving and labelling polymers, often requiring elevated temperatures (60 °C - 130 °C), overnight incubations, and multiple purification cycles [45, 93]. In addition, the choice of nanoparticle fabrication material and the reaction conditions (pH, temperature, duration, etc.) can be detrimental to the conjugation if the resultant product lacks the appropriate and sufficient reactive functional groups [89, 96]. Due to the toxic or volatile nature of some common solvents used in the synthesis of nanoparticles and their modifications, such as Ethylene Glycol, glutaraldehydes, amines and pungent acids [97, 98], wet-chemical protocols can also require high standards of safety procedures. The need for reagent-free covalent attachment strategies to PNPs devoid of these fabrication complications is hence evident.

Dry plasma-based techniques for nanoparticle synthesis and surface modification, facilitating covalent attachment, have arisen as a more sustainable alternative to conventional wet-chemistry methodologies [99, 100]. Plasma, commonly referred to as the fourth state of matter, is a partially ionized gas consisting of charged and neutral species, including gas molecules, electrons and radicals (**Figure 2c**). These dry plasma-based techniques operate without the use of any reagents, other than vapours from which the nanoparticles are comprised or cargo molecules to be conjugated to them, significantly reducing cost, environmental impact and safety risks. Key factors for comparing plasma-based and wet-chemical processes include costs (initial setup, materials, energy, maintenance), resource utilization (labour, space, waste disposal), operational efficiency, environmental impact, and scalability. In biological research, plasma polymerization presents a cost-effective alternative to expensive and inconsistently available coated cultureware, with systems achieving return on investment within a year in high-throughput labs and further enhancing outputs with automated control systems and process data logging[101]. As one example, in the treatment of contact lenses, despite plasma polymerization being initially 12 times more expensive than Layer-by-Layer (LBL) coating, it becomes more cost-effective annually due

to significantly lower material usage and minimal effluent production [102]. LBL methods necessitate extensive wastewater treatment, a factor which is often overlooked in preliminary economic analyses that significantly increases operational costs. Thus, while the choice between plasma and wet-chemical processes depends on specific needs, scalability, and long-term considerations, balancing initial capital investment against operational costs and environmental impacts favours plasma-based technologies due to their inherent single-step efficiency [102, 103].

Plasma-based technologies can be categorized into non-depositing and depositing processes. Non-depositing plasma processes, such as plasma immersion ion implantation (PIII) and atmospheric pressure plasma treatment, modify the surfaces via physical and/or chemical changes without depositing an additional layer [66, 104-108]. Depositing plasmas, on the other hand, coat the surfaces of substrates with either an additional layer like plasma polymer films [109-114] and magnetron-sputtered coatings [115-120] or synthesize new material such as nanoparticles [121-124].

The plasma processes share a common underlying concept: The electrons in the plasma are accelerated by electric fields, and they excite the reactant gases, resulting in ionization, radical fragmentation, and enhanced plasma phase chemistry [110]. With an organic gas such as acetylene [125] or monomer vapours such as allylamine [126, 127], acrylic acid [128], octadiene [129, 130], or thiophene [131, 132], plasma polymerization can be used not only for the coating of particulate surfaces but also for the production of organic nanoparticles [123, 124, 133]. Originally known as plasma dust or powder, plasma polymerized nanoparticles (PPNs) were explored as by-products in space or contaminants in semi-conductor industry plasma processes [134]. More recently, their potential as nanocarriers in the biomedical field has been realized and is being explored for multi-functional therapeutics [135]. Plasma polymerization of nanoparticles results in radical-rich surfaces allowing the immobilization of multifunctional biomolecules in a single incubation step [124, 136]. Thus, plasma polymerization presents an appealing alternative to wet chemical surface functionalization for applications in biomedicine.

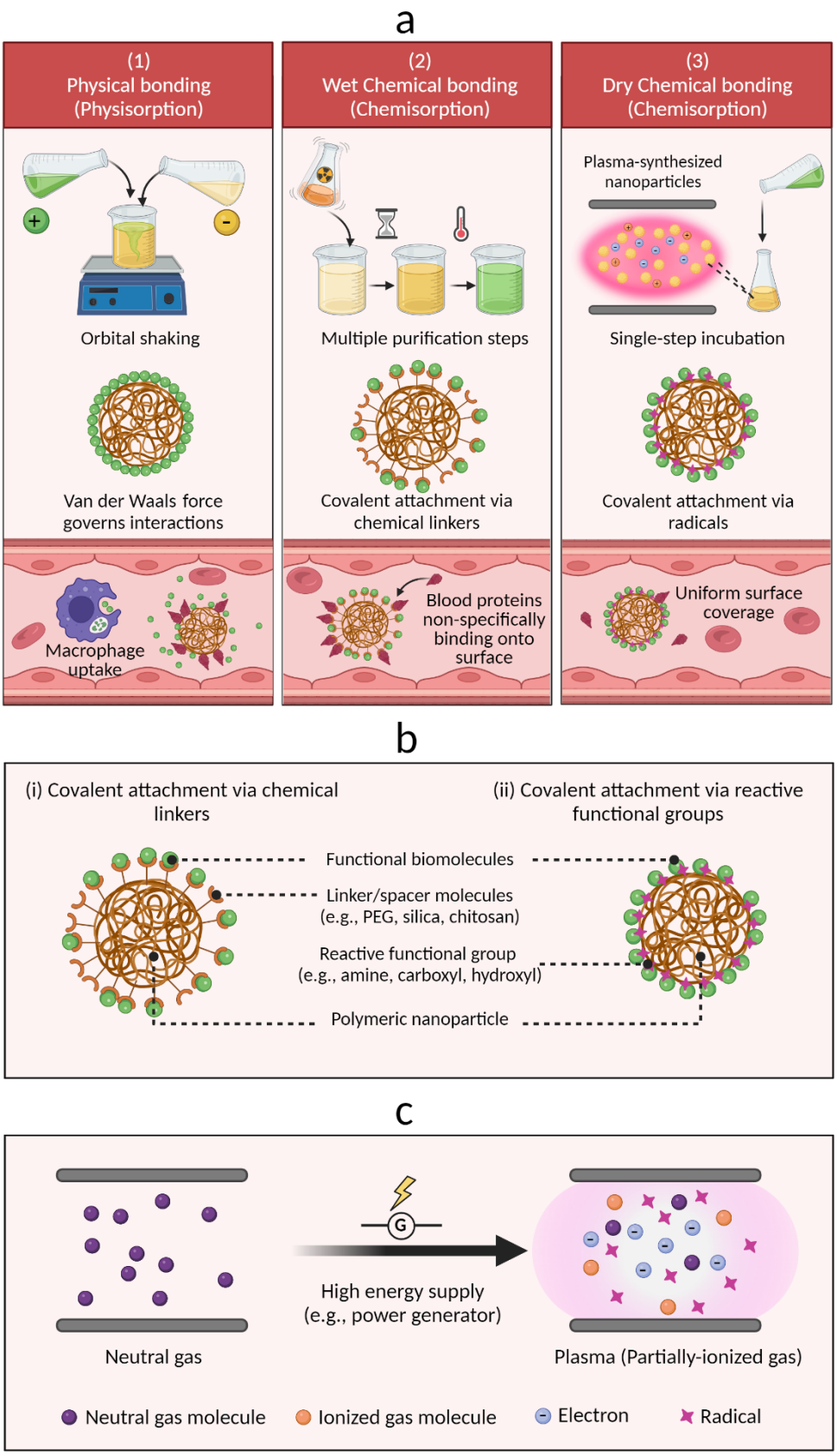
a
(1)
Physical bonding
(Physisorption)
(2)
Wet Chemical bonding
(Chemisorption)
(3)
Dry Chemical bonding
(Chemisorption)
Orbital shaking
Multiple purification steps
Plasma-synthesized
nanoparticles
Single-step incubation
Van der Waals force
governs interactions
Covalent attachment via
chemical linkers
Covalent attachment via
radicals
Macrophage
uptake
Blood proteins
non-specifically
binding onto
surface
Uniform surface
coverage
b
(i) Covalent attachment via chemical
linkers
(ii) Covalent attachment via reactive
functional groups
Functional biomolecules
Linker/spacer molecules
(e.g., PEG, silica, chitosan)
Reactive functional group
(e.g., amine, carboxyl, hydroxyl)
Polymeric nanoparticle
c
High energy supply
(e.g., power generator)
Neutral gas
Plasma (Partially-ionized gas)
Neutral gas molecule
Ionized gas molecule
Electron
Radical

Figure 2. (a) Surface functionalization of nanoparticles using physical and chemical methods. Physisorption results in interactions governed by Van der Waals forces, hydrogen bonds or hydrophobic forces and can be easily achieved with prolonged mixing or orbital shaking of the nanoparticle solution and the immobilization solution. Despite their abundance, the immobilized agents are typically weakly bound and can detach in the blood, inducing macrophage uptake and an immune response. Wet and dry chemisorption achieve stronger bonds due to the nature of the covalent surface attachment. However, dry synthesis of PNPs has the advantage of fewer, faster, and more environmentally-friendly conjugation steps that achieve more uniform surface modification. (b) Two methods for covalent coupling between functional molecules and the surface of PNPs: (i)using a linker/spacer molecule such as PEG, silica, chitosan, dopamine, etc. or (ii) reactive functional groups (amine, carboxyl, sulfhydryl, hydroxyl groups) embedded in the surface of the nanoparticle. (c) Schematic representation of a plasma, the fourth state of matter. Subjecting a neutral gas to a high-energy source creates a plasma discharge comprising neutral and ionized molecules, radicals and electrons.

1.3. Surface biofunctionalized PNPs: Biomedical applications

1.3.1. Biosensing systems

The advancement of highly sensitive small-scale sensors that detect biological agents is of integral importance for many biomedical and environmental sciences. These biosensors are typically designed with a recognition element to identify and specifically bind with target analytes and a transducer component whose primary role is to report the binding event in the form of an electrochemical, colourimetric, or fluorescent signal [137] (**Figure 3**).

PNPs offer an appealing platform for surface functionalization in biosensing, particularly in the fields of disease theranostics and prevention (**Table 1**). PNPs possess versatile physicochemical properties that can be fine-tuned, and their surface can be equipped with specific functional groups, enabling them to serve as both receptor and signalling components within the biosensor systems [138]. The ability of these systems to accurately detect various physiological conditions and species is critical for ensuring cellular stability, preventing organ system deterioration and combating global biological threats. These factors are expressed by pH value [139-148], reactive oxygen species (ROS) [149-151], and small biological agents [42, 152-154], discussed in detail in the following sections.

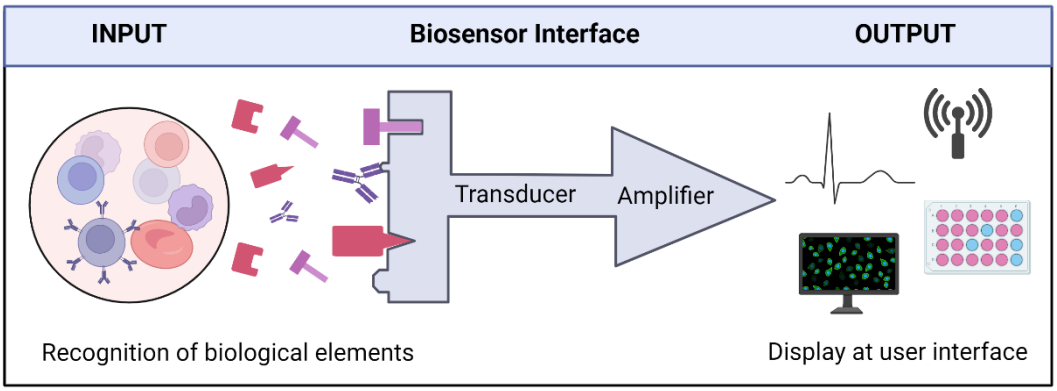

Figure 3. The core components of a biosensor operate to recognize biological elements (such as antibodies, amino acids, enzymes, etc.) at the interface. They subsequently transduce and amplify this recognition into a measurable signal, which is then presented on the output user interface, typically in the form of electrochemical, electrical, or optical measurements.

Table 1. *Examples of polymeric nanoparticles and their chemical surface modification with functionalizing agents employed for biosensing pH, reactive oxygen species, and biothreat agents.*

Material of Nanoparticle	***Functionalizing agent(s)***	***Mechanism(s) of functionalization***	***Biomedical application***	***In vitro cell studies***	***In vivo studies***	***Ref***
Polyacrylonitrile (PAN)	Lanthanide metal Terbium (Tb) and Europium (Eu)	Schiff base reaction	Biosensors to Bacillus anthracis bacteria in aqueous solution	N/A	N/A	[42]
Polyacrylamide	Oregon green OG fluorophore, fluorescein FS, Rhodamine B RhB	Isothiocyanate of each dye solution reacting with NH_2-Nanoparticles	pH biosensing and measurement intracellularly in endosome-lysosome pathway	Fluorescent signal calibration in a cytoplasm-mimicking buffer and successful internalization via HepG2 cells	N/A	[141]
Poly(phenylacetylene) (PPA) and poly(phenylacetylene-co-acrylic acid) (P(PA-co-AA))	Dexamethasone (DXM) *(encapsulated)*	*Modified surfactant free emulsion	pH biosensing, tissue engineering and cancer treatment	Hydrophilic groups in the copolymers P(PA-co-AA) induced a higher loading efficiency and an enhanced surface charge ideal for the controlled release of the drug upon pH fluctuations.	N/A	[155]
Polyacrilonitrile (PAN)	Boronate/ FITC	Schiff base reaction	Fluorescence based sensing of intracellular hydrogen peroxide	The cellular uptake, viability, and microscopic imaging of BPAN nanoparticles were evaluated in RAW264.7 cells.	N/A	[151]
Lanthanide Coordination Polymer Nanoparticles (Phe/Tb CPNPs)	Phenylalanine (Phe) as bridging ligands, terbium ions (Tb^{3+}) as metal nodes, carboxyphenylbor	Chemical coordination of 4-carboxyphenylboronic acid (CPBA) with Phe/Tb CPNPs	Fluorescence based H_2O_2 sensing	H_2O_2 selectivity was demonstrated in aqueous solutions and urine samples		[156]

	onic acid (CPBA) Carboxyphenylboronic acids (CPBAs) as guest ligands					
Lipopolymer 1,2-distearoyl-sn-glycero-3-phosphoethanolamine-N-[amino(polyethylene glycol)-2000] (DSPE-PEG-NH_2)	4-carboxy-3-fluorophenylboronic acid (FPBA), 7-hydroxycoumarin (HC), and Alizarin red S (ARS)	HC and FPBA were each conjugated with DSPE-PEG-NH_2 through a condensation reaction between amino and carboxyl groups while the nanoparticle was achieved by combining the three polymer grafts via film hydration. ARS forms adducts with boronic/boric acid of the FPBA.	Ratiometric biosensing of hydrogen peroxide	N/A	N/A	[150]
Polystyrene	Nile Red *(encapsulated)* and FITC fluorescein dye (surface)	Covalent coupling to the particle surface via amine groups.	Ratiometric measurements of pH in biofilms	Fluorometric monitoring of the time-dependent changes in pH in E. coli biofilms	N/A	[157]
Self-immolative polymer mix	chlorin e6 (Ce6) dye *(encapsulated)*, poly(ethylene glycol) PEG (surface)	Ce6 was loaded via both hydrophobic interactions and π–π stacking, while Poly(ethylene glycol) methyl ether (mPEG-OH) was conjugated to the particle surface by	Chemiluminescent imaging of Reactive Oxygen Species for disease diagnostics	N/A	Sustainable signals were generated at the target site of four disease bearing mice models	[158]

		an ester bond				
Chitosan (CHIT) nanocomposite and graphene nanoribbons (GNRs)	Sarcosine oxidase (SOx)	Covalent immobilization via glutaraldehyde coupling	Prostate cancer diagnostics via sensing of blood sarcosine	Study performed on blood samples from apparently healthy persons vs. prostate cancer patients	N/A	[159]
Polymer/Gold hybrid	Heparin	Covalent linkage via maleimide-thiol bonding.	Colorimetric sensing for diagnostics	N/A	N/A	[160]
Lignin	Chitosan	Layer-by-layer assembly	Electrochemical sensor	N/A	N/A	[161]
3-Polythiophene Acetic Acid (3-PTAA)	Alpha-fetoprotein antibody (anti-AFP)	Covalent bond between the amine group of anti-AFP and the carboxylic group of 3-PTAA via ethyl-3-(3-dimethyl aminopropyl) carbodiimide	Electrochemical Immunosensing of Liver Cancer	Detected AFP in human blood samples	N/A	[162]

		(EDC)/N-hydroxysuccinimide (NHS) linkage.				
Porphyrin-Based Porous Organic Polymer FePor-TPA	Gold nanoparticles (AuNPs), the rabbit anti-Staphylococcus aureus Rosenbach tropina antibody (Ab2), and Glucose oxidase (GOx)	*In situ growth method	Dual-mode bacterial biosensing platform	N/A	N/A	[163]

*The nature of the surface interaction was not assessed

1.3.1.1. pH sensors

Intracellular pH plays various pivotal roles in cellular metabolic pathways, including endocytic processes, enzyme activity, and protein misfolding [164, 165]. Abnormal values of pH are thus associated with cellular dysfunctions, which can lead to an increased risk of various diseases, such as cancer and Alzheimer's disease [166-169]. Over the past few years, pH nanosensors have emerged as valuable tools to quantify intracellular pH values. Their ability to offer high signal intensities, rapid response times, ease of modification, and efficient intracellular loading makes them particularly promising in this domain [170-174].

The most frequently used fluorescent nanosensors for pH measurement operate as "turn-on" or "turn-off" systems, relying on changes in fluorescence intensity at a specific excitation wavelength to function. Depending on the specific chemical properties of the nanosensors, the signal can either become brighter (turn-on) or dimmer (turn-off) in response to variations in pH levels at that particular wavelength. However, due to having only one emission signal for detection, the signal results are adversely influenced by variations in the environmental conditions, photobleaching, leakage from the cells, excitation intensity and sensor concentration [175, 176].

Ratiometric fluorescent sensing, in contrast, relies on multiple wavelengths of an excitation or emission spectrum to detect local environmental changes. Based on two emission signals at two distinct wavelengths, dual ratiometric fluorescent sensors have emerged to eliminate the effects of the limitations associated with those based on single intensity change [177-179]. Among these ratiometric nanosensors, polymer assemblies have the superior benefit of allowing non-invasive and in-situ tracking of cellular dynamics and processes [180]. One example in this area is a tuneable ratiometric fluorescent pH nanosensor developed by conjugating aggregation-induced emission (AIE)-based fluorescent dyes to the surface of hyperbranched PNPs [139]. In this system, two different dyes based on 1,8-naphthalimide are incorporated, with one functioning as pH-sensitive and the other serving as a reference. The pH-sensitive (green) dye, which undergoes protonation of the amino group in acidic conditions, and the pH-insensitive fluorophore (blue) are attached to the surface of the nanoparticles via 1-Ethyl-3-(3-dimethylaminopropyl) carbodiimide EDC HCl as a coupling reagent. Intracellular pH sensing using such biofunctionalized PNPs was successfully conducted in HeLa cells, as evidenced by distinct fluorescence emissions in each channel. These ratiometric fluorescent nanosensors exhibited strong emissions, good biocompatibility, and selective accumulation in acidic organelles (**Figure 4A**). Notably, this study generated a calibration curve covering the pH range of 5.6 to 8.0 through additional intracellular calibration experiments, using a pH-dependent signal derived from the combination of both channels (**Figure 4B**).

Another example of ratiometric fluorescent sensing is the development of a polymer nanosensor that relies on the fluorescence resonance energy transfer (FRET) between a pair of dyes covalently coupled to the nanoparticles [140]. A covalent bond is formed in the polymer particle matrix due to the presence of an unsaturated polymerizable double bond in the donor dye, 4-ethoxy-9-allyl-1,8-naphthalimide (EANI). The acceptor, fluorescein isothiocyanate (FIT-C), is conjugated onto the surface of the nanoparticles through a reaction between its isothiocyanate groups and the amino groups on the surfaces of nanoparticles. The response characteristics of these nanosensors have been shown to alter from emitting intense blue fluorescence at low pH, to turning

into luminous green at high pH values, effectively visualizing the intracellular pH changes at the lysosomal pathways (**Figure 4C**).

Triple-labelled pH nanosensors expanded the field of ratiometric measurements and introduced a novel strategy for multi-functionalization [141, 146]. In the work of Rikke V. Benjaminsen et al., for example, an additional pH-sensitive fluorophore, Oregon Green (OG), was covalently conjugated to the nanoparticles coupled with a pH-probing and pH-inert reference dye fluorescein (FS) and rhodamine B (Rh-B), respectively **(Figure 4D(i))** [141]. This combination was synthesized on an acrylamide crosslinked matrix and effectively performed pH detection at the endosome-lysosome system (**Figure 4D(ii)**). The enhanced nanosensor offers the advantage of a larger, well-defined sensing measurable range than the dual-labelled sensor. In this work, often-neglected aspects of calibration **(Figure 4D(iii))**, background subtraction, and localization in cells, are addressed, paving the way for subsequent research to further tune pH sensing measurements. Ratiometric pH measurements can also be performed using self-organization principles where the desired functionalities are introduced throughout the design of the nanoparticle pH sensors [142, 143]. Notably, a mixed micelle approach based on triblock copolymers allows for controlling the spectroscopic properties and surface density of the surface targeting molecules by adjusting the amount of peptide-bearing polymers in the nanosensor composition [142].

The pH range that a pH nanosensor covers is another important element that influences its performance, particularly in live cell measurements. The development of design strategies for the preparation of pH-sensitive systems from individual nanoprobes to dual-/triple-system surface-modified nanoparticles has further extended pH range measurements [144, 145, 147]. In a work by Sun et al., for example, it is shown that different combinations of fluorophores (FITC /BCECF, Rhodamine B /Alexa 633) extend the pH sensitivity range and thus the potential for measuring the physiologically relevant pH interval to 4 units in almost all mammalian cellular environments using conjugated PNPs (**Figure 4E**) [144]. Although in this work, a robust binding of the fluorescence dyes to the nanoparticles was achieved by the reaction of isothiocyanates (ITC) with the free primary amine groups of the nanoparticles, complications with FRET and sufficient linearity of the ratiometric curve had to be carefully considered for the efficient choice of fluorophore combinations.

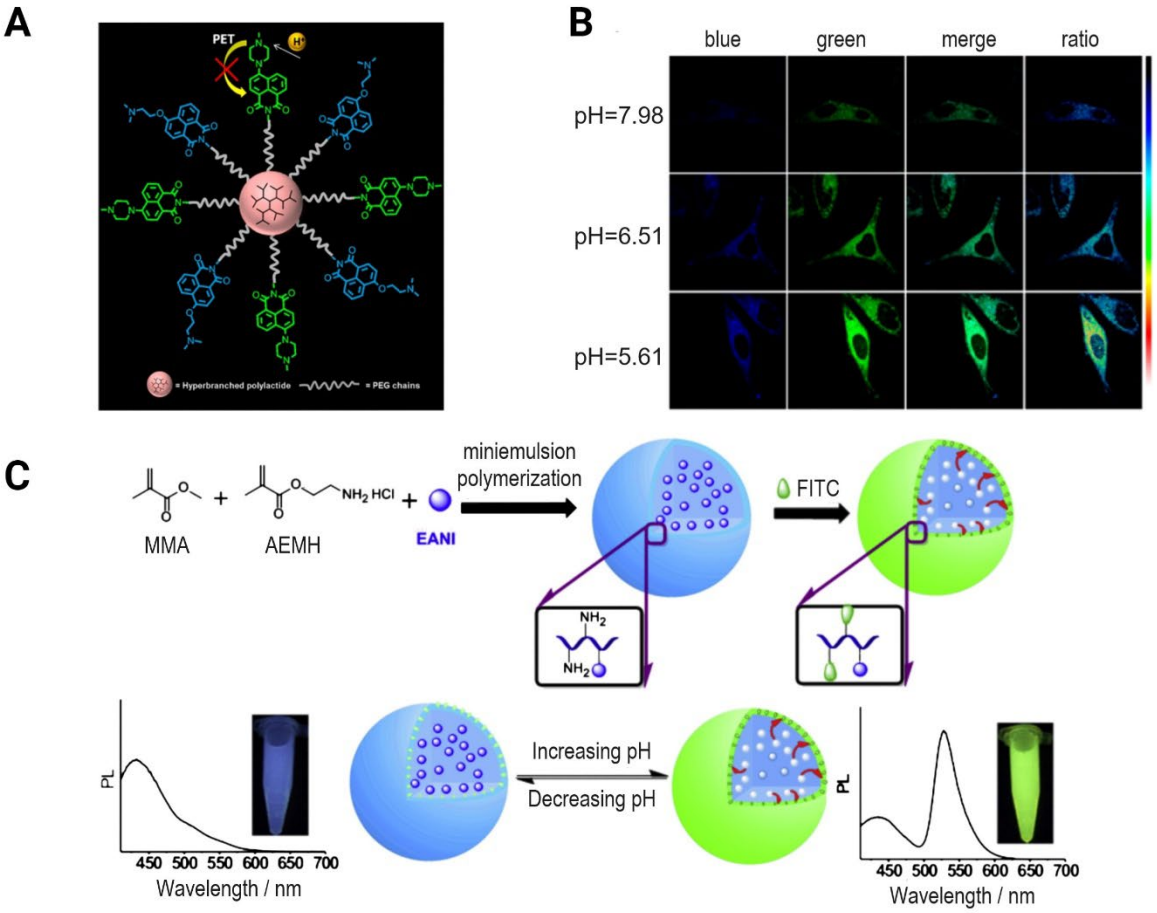
A
PET
= Hyperbranched polylactide
= PEG chains
B
blue
green
merge
ratio
pH=7.98
pH=6.51
pH=5.61
C
MMA
AEMH
NH2 HCl
EANI
miniemulsion polymerization
FITC
NH2
NH2
PL
450 500 550 600 650 700
Wavelength / nm
Increasing pH
Decreasing pH
PL
450 500 550 600 650 700
Wavelength / nm
D
(i)
(ii)
pH
3.5
4.5
5.5
(iii)
Normalized intensity ratio (488/561)
1.0
0.8
0.6
0.4
0.2
0
2
3
4
5
6
7
8
pH
OG
OG-FS
FS
E
BCECF
succinimidyl ester
Alexa 633
succinimidyl ester
Oregon
Green ITC
BCECF
Oregon green
Alexa 633
NP-Oregon-BCECF-Alexa 633
FITC
Oregon Green ITC
Fluorescein
Oregon Green
Rhb
NP-Oregon-Fluorescein-RhB
RhB-ITC

Figure 4. (A) Hyperbranched Polylactide Nanoparticles Functionalized as ratiometric pH nanosensors with a green fluorophore as the pH-sensitive probe and a blue one as the reference. (B) The hyperbranched polymer nanoparticles were used as an efficient sensing platform for intracellular pH in living HeLa cells clamped at pH 5.61, pH 6.51, and pH 7.98. (A) and (B) Reprinted (adapted) with permission from [139]. Copyright 2015 American Chemical Society. (C) A schematic representation of the preparation of pH-sensitive ratiometric fluorescent polymer nanosensors and their application in water. Reprinted from [140], Copyright (2016), with permission from Elsevier. (D) Triple-labeled polyacrylamide nanoparticle nanosensor (i) schematic, (ii) a combined confocal microscopy image showing its uptake by a HepG2 cell and a linear scale for the pH measurements and (iii)in vitro calibration curves with Oregon Green, Fluorescein, and their combination. Reprinted (adapted) with permission from [141]. Copyright 2014 American Chemical Society. (E) Schematic illustration of the preparation route for pH nanosensors: NP–Oregon–fluorescein–RhB and NP–Oregon–BCECF–Alexa 633 through surface functionalization Reproduced from Ref [144] with permission from the Royal Society of Chemistry.

1.3.1.2. ROS Sensors

Reactive oxygen species (ROS) naturally form because of oxygen metabolism and are crucial in cell signalling pathways for the growth of living organisms [181-183]. However, substantial increases in reactive oxygen species, such as hydrogen peroxide (H_2O_2) levels, can cause oxidative stress, potentially altering protein stability and causing (sub)cellular damage. As a result, functional deterioration of organ systems, such as neurodegenerative disorders, cardiovascular diseases, and cancers, might ensue [184-186]. Therefore, studies surrounding the detection, quantification and tracking of ROS in complex live cellular systems have surged [187-189].

Electron spin resonance (ESR) is one traditional method for ROS detection that relies on the presence of magnetic moments associated with at least one unpaired electron in the molecular structure. However, unlike other reactive oxygen species such as superoxide radicals ($O_2^{\bullet-}$) and hydroxyl radicals (•OH), H_2O_2 lacks an unpaired electron spin. Thus, spin-trapping probes would require the formation of intermediate detectable radicals via cascades of redox reactions [190]. The potential of this approach for H_2O_2 *in vivo* imaging is limited by the degree of spin trapping specificity, instability of the probes, the high cost of ESR spectrometers, and the potential influence of redox mediators on cell metabolism [191].

PNPs have drawn increasing interest as fluorescent sensing probes for retaining solubility and prolonged blood circulation, favourable for H_2O_2 detection in almost any biological environment [149, 192-194]. Surface modification of PNPs adds the benefit of high versatility to their composition and functionalization to exhibit high-contrast images specific to H_2O_2. Boronate-based fluorescent probes, in particular, offer high specificity among contrast agents employed for hydrogen peroxide sensing at physiologic concentrations [195-199].

One widely used sensing mechanism in this field relies on conjugating chemical compounds onto the PNP that can achieve fluorescence resonance energy transfer (FRET) via single-wavelength excitation [200-203]. For example, the fluorescence emission spectrum of 7-hydroxycoumarin (HC) at 450 nm overlaps with the absorbance spectrum of 4-carboxy-3-fluorophenylboronic acid (FPBA) when it is bound with Alizarin red S (ARS) dye, achieving FRET and a new fluorescence emission peak at 600 nm (**Figure 5A**) [150]. In the presence of H_2O_2, ARS dissociates from the surface of the nanoprobe, decreasing the intensity at 600 nm as the fluorescence intensity at 450

nm increases which allows for a sensitive and selective ratiometric fluorescence response for H_2O_2 detection.

Alternatively, PNPs can be customized to produce a photoinduced electron transfer (PET) effect specific to H_2O_2. The Pinner method, for instance, can be used to achieve a Schiff base on polyacrylonitrile (PAN) nanoparticles, causing a PET reaction upon the treatment with boronate esters [151]. When the boronate-modified polyacrylonitrile (BPAN) nanoparticle interacts with H_2O_2, the fluorescence intensity changes, and the emission peak shifts distinctively (**Figure 5B**). This method was successfully demonstrated *in vitro* using BPAN nanoparticles inserted into RAW264.7 living cells, modelling macrophages in which endogenous H_2O_2 was produced. The lack of nanoparticle penetration into the mitochondria and the nucleus was a clear indication that the BPAN nanoparticles were taken up by the cells and are nontoxic, offering an attractive method for detecting elevation in H_2O_2 levels under conditions of oxidative stress using polymeric nanoprobes.

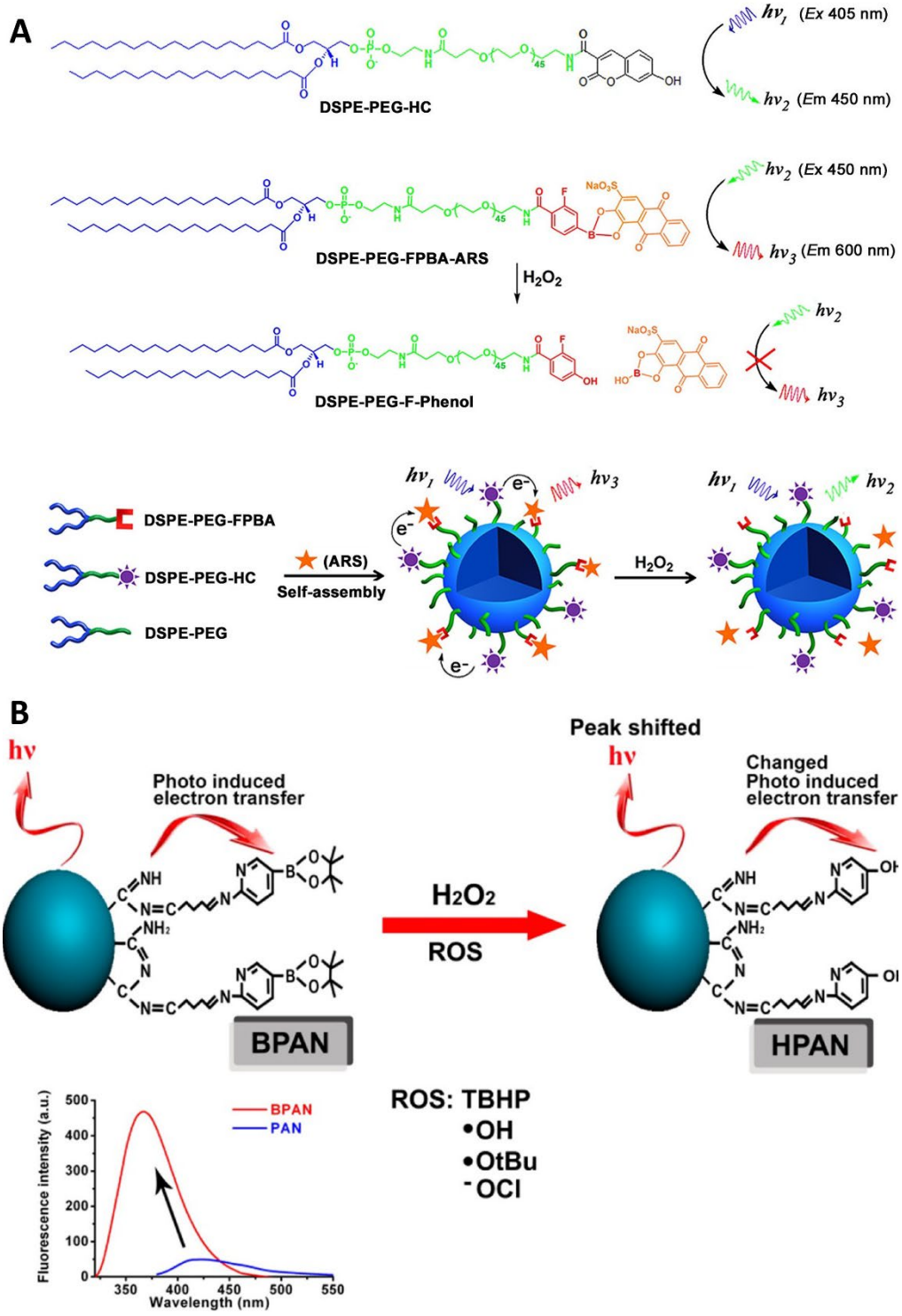

Figure 5. (A) Schematic diagram of the polymeric nanoprobe self-assembly using ARS-FPBA fluorescence resonance energy transfer (FRET) ratiometric fluorescence for the detection of H_2O_2 Reprinted (adapted) with permission from [150]. Copyright 2017 American Chemical Society. (B) Schematic diagram of the photo-induced electron transfer mechanism for H_2O_2 detection using boronate-surface-functionalized polyacrylonitrile (BPAN) nanoparticles. Below is a graph showing the visible increase in fluorescence

spectra of BPAN (red) compared to PAN (blue) nanoparticles. Reprinted (adapted) with permission from [151]. Copyright 2012 American Chemical Society.

1.3.1.3. Biothreat agent sensors

The rise of globally threatening biological agents, including viruses, bacteria, and toxins, each with varying degrees of transmissibility and infectivity, underscores the critical demand for effective sensors. As an exemplar, the recent COVID-19 outbreak has accentuated the necessity for swift biothreat agent identification. The diversity of such threatening agents and their varying degrees of infectivity and transmissibility rendered their detection highly challenging [204]. Established detection methods such as genome sequencing [205], enzyme-linked immunosorbent assay (ELISA) [206], and polymerase chain reaction (PCR) [207] are being continuously developed to overcome these challenges. However, these methods are typically used only after a diagnosis of the pathogen is suspected by a clinician. These assays are also often not suitable for use in the field, are time-consuming (hours to days) and can be limited in their sensitivities [208-210]. The creation of a rapid, cost-effective, yet autonomous pathogen detection system that can be easily applied in the field necessitates the reduction of sample preparation steps [211]. By capitalizing on large surface/volume ratios, dispersibility, and unique nanoscale interactions, nanoparticle-based biosensors are being developed with sensitivity and accuracy that surpass traditional biothreat detection methods [212].

PNPs with engineered surfaces have also emerged as a promising frontier in the field of virus detection [11, 213]. These nanoparticles can be designed to mimic the properties of host cells, i.e., cells that provide a conducive environment for viral reproduction, to make them particularly effective in detecting viruses [214]. This approach involves coating the PNPs with human-cell-derived membranes sourced from specific cells that viruses naturally interact with, such as immune CD4 T cells, the target of the recent severe acute respiratory syndrome coronavirus 2 (SARS-CoV-2) [215]. The cell-mimicking nanoparticles present molecular structures on their surfaces that mimic the receptor sites on the host cells that the virus normally binds to, such as human immunodeficiency virus type 1 (HIV-1) gp120 receptors and sialic acid for avian influenza virus (AIV) [216, 217].

Nanoparticles conjugated with antibodies can detect viruses by attaching virus-specific antibodies to their surfaces. When exposed to a virus, the antibodies bind to viral antigens, triggering a detectable signal and allowing for highly specific and sensitive virus detection [218]. For instance, PNP-laden nanocarriers (PNLNs) loaded with chromogens (phenolphthalein and thymolphthalein) have been conjugated with antibodies specific to target viruses influenza virus A (IVA) subtypes H1N1 and H3N2 [219]. When these PNLNs, along with anti-virus antibody-conjugated magnetic nanoparticles (MNPs), interact with the target viruses and undergo magnetic separation, a colourimetric reaction occurs due to pH changes, enabling the detection of the viruses with high specificity and low limits of detection in human serum samples. Similarly, conjugating influenza virus A (IVA)-antibodies to conductive 3,3',5,5'-tetramethylbenzidine (TMB) polymer-based nanoparticles formed an immunocomplex sandwich structure with the virus [220]. Interaction with the virus produced an optical signal response due to the catalytic oxidation of released TMB molecules, which resulted in a highly sensitive colorimetric sensor for the detection of airborne respiratory viruses. Another recognition mechanism includes conductive polymer-based

nanoparticles (CPVs) with a peptide with affinity for hemagglutinin, a protein found on the surface of the influenza virus [221]. The peptide-conjugated CPVs (PCPVs) exhibit an optical response mechanism through altered π–π interactions upon binding to the virus. The multifunctionalization of such nanoparticles with targeting biomolecules and antiviral drugs not only imparts specificity to these nanosensors but also incorporates antiviral therapeutics that inhibit and protect against viruses [222, 223].

Dipicolinic acid (DPA), one of the bacterial biomarkers, is a major component of the Bacillus anthracis spore, which is considered a high risk for biological warfare. Luminescence of Lanthanide ion metals, i.e., rare-earth metals, has emerged as one of the most promising methods for the detection of DPA due to its long fluorescence lifetime and large Stokes shift [152, 224, 225]. Polymer nanoparticles can be functionalized into photoluminescent bioagent sensors by their surface modification with a specific lanthanide ion. For example, anchoring the Lanthanide metal europium (Eu) onto Schiff-base modified polyacrylonitrile (S-PAN) nanoparticles as a sensing moiety has been successful in detecting B. anthracis spores with high selectivity over aromatic molecules in aqueous solution [42]. For grafting the europium onto the nanoparticles, in the first step, ethylenediamine (EDA) is covalently grafted onto S-PAN nanoparticles. Ethylenediamine tetraacetic acid dianhydride (EDTAD) is introduced onto the nanoparticles, leading to the reaction between the amino groups and the anhydride groups. The resulting EDTAD molecule on the nanoparticles is then converted into [Eu(EDTA)–$(H_2O)_3$] complex by reaction with $EuCl_3$ (**Figure 6A**). These abundant functional groups on the surface of the PAN nanoparticles provide facile surface modification via covalent bonding. The photoluminescence spectra of SPAN nanoparticles increase the quantum yield of PAN nanoparticles, providing reference fluorescence and functional groups for the covalent attachment of lanthanide metals.

Antibody conjugation to the surface of nanoparticles is also used to recognize bacterial antigens, generally with the assistance of a fluorescent dye either anchored on or encapsulated in the probe. Synthesizing nanoparticles with acetoacetoxyethyl methacrylate AAEM, for example, endows diketone group functionalities that facilitate the covalent surface linking of S Salmonella typhi (S. typhi) antibodies (Ab) without any crosslinker or activator [153]. The covalent bond between the two moieties is facilitated when the amino groups of the S. typhi antibody (Ab) interact with the keto-enolic functional group found in the AAEM component of the fluorescent polymeric nanoparticles (FPNPs). This interaction results in the formation of antibody-nanoparticle conjugates (Ab-FPNP), as illustrated in **Figure 6B**.). In this work, a sandwich format was utilized for the capture and tracking of the bacteria: antibody-modified polycarbonate membranes (mPC-S. typhi Ab) were used for the selective capturing of S. typhi, while the pyrene-loaded antibody-nanoparticle probes (Ab-FPNP) generated a fluorescent signal upon antigen recognition. The immune-complex (mPC-S. typhi Ab-Ag-Ab-FPNP) was tracked with the bright fluorescence of polycyclic aromatic hydrocarbon pyrene dye encapsulated inside the polymeric nanoparticle.

Aside from acids and antibodies, carbohydrates have also been increasingly considered in crucial recognition events as alternative bioreceptors. Carbohydrates are particularly attractive due to their higher resistant to denaturation and higher binding affinity [154, 226]. Mannose is a carbohydrate molecule that can function as a receptor for Escherichia coli as it binds with the lectin proteins on the bacterial surface [227, 228]. Decorating amphiphilic conjugated PNPs with mannose has recently led to a solution-processable electrochemical sensing layer nanoparticle biosensor that

demonstrated targeting ability toward E. coli pili protein [154]. The mannose-functionalized PNPs resulted in the fabrication of an innovative biointerface with dispersibility and a high surface ratio, which could facilitate the development of strategies for the design of new imaging probes and biosensors. However, it is worth noting that mannose was physically adsorbed onto the outer surface of the PNPs. This coating relied on hydrophilic−hydrophilic interactions between the triethylene-glycol-thiophene TEG segments on the outer surface of the nanoparticles and the hydroxyl groups of the mannose. This noncovalent method remains susceptible to potential detachment or instability in biological environments that require further assessment in cellular environments.

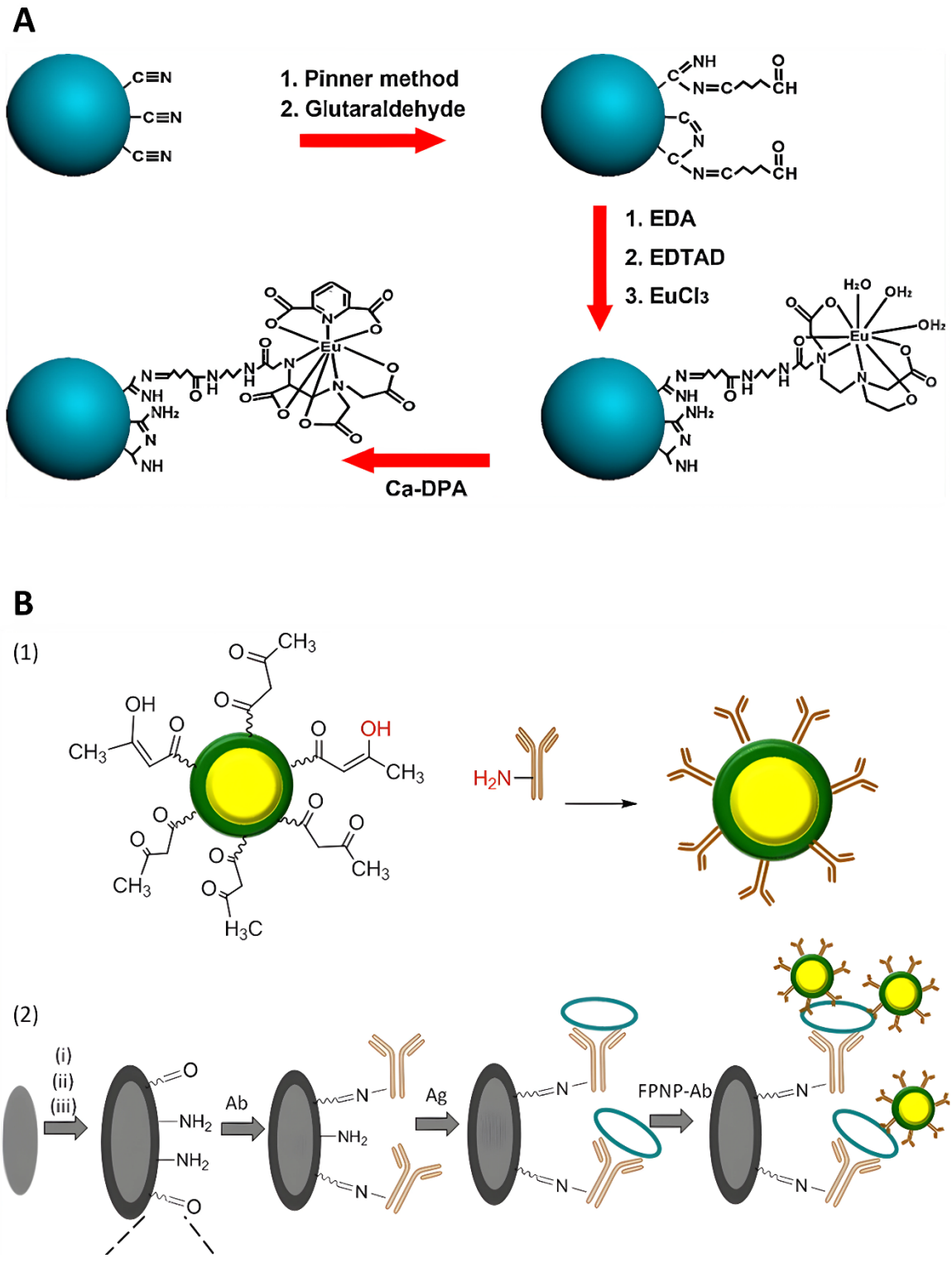

Figure 6. (A) Schematic illustration of the fabrication procedure of europium (Eu)- polyacrylonitrile (PAN) nanoparticles and the following surface functionalization steps to achieve sensing of Bacillus anthracis bacterial spore with Ca-DPA. Reprinted from [42], Copyright (2011), with permission from Elsevier. (B) (1) Bioconjugate probe synthesis via the surface functionalization of polymeric fluorescent nanoparticles with covalently bound Salmonella typhi anti body. (2) Schematic representation of the formation of mPC

fluoroimmunoassay utilizing (i) nitric acid (ii) sodium borohydride (iii) glutaraldehyde, antibody (Ab), antigen (Ag), and the bioconjugate probe (FPNP-Ab) for the detection of Salmonella bacterial antigen. Reprinted with permission from [153].

1.3.2. Bioimaging systems

Molecular imaging is a diagnostics technique for the visualization and quantification of physiological changes using imaging probes or agents. Advanced molecular imaging techniques have enabled the *in-situ* monitoring of variations at the cellular level for the early detection of diseases [229-231]. Over the last decade, there has been increasing interest in using PNPs as imaging agents for the spatiotemporal evaluation of cellular functions and tracking the expression of disease biomarkers [59, 232, 233]. The advantage of nanoparticles functioning as molecular imaging agents is that their size facilitates their passage through cellular barriers without inducing foreign body immune reactions. Furthermore, their large area-to-volume ratio enables high loading capacity, allowing them to deliver concentrated imaging agents at target areas. The surface functionalization of PNPs enhances their functional performance in imaging in several ways, such as (i) enhanced biocompatibility with existing biochemical processes, (ii) multimodal imaging capability, and (iii) their multiplexing ability to attach signalling or receptor targeting moieties in a single nanocomposite. Surface-modified PNPs have been successfully employed as contrast agents for a number of imaging modalities such as Xray [44, 45, 234-237], optical imaging [238-243], and magnetic resonance imaging (MRI) [244-247], as discussed in the following sections.

1.3.2.1. X-ray contrast agents

Computed tomography (CT) is a well-established imaging modality that is extensively used in hospitals and clinical investigations of a wide range of diseases [248-250]. CT utilizes X-rays as a source of ionizing radiation to non-invasively produce high-resolution 3D images of organs and reconstruct them using computer algorithms [251]. Contrast agents with high molecular weight can passively accumulate in tissues with increased vascular permeability, such as cancerous sites, via the enhanced permeability and retention (EPR) effect [252]. Although the most frequently used contrast-generating elements are iodine [253], gold [254], and bismuth [255], lanthanides have also been explored due to their high atomic number -critical for X-ray attenuation [256-258]. However, small contrast molecules based on these elements are not ideal for most clinical applications due to the associated toxicity at the concentrations required for imaging and their short circulation half-lives [259, 260].

These drawbacks are commonly countered by incorporating contrast agents (CA) into nanoparticles with a surface layer of a hydrophilic polymer, lipid, silica, or other compounds that yield biocompatibility in biological media (**Table 2**). For instance, a biodegradable polymer poly-ε-caprolactone (PCL) layer stabilizes metallic nano-contrast agents in aqueous media in comparison with conventional free-standing iodinated contrast agents [234]. Similarly, bismuth and lanthanides nanoparticles with a polyvinylpyrrolidone (PVP) coating exhibit a superior in vitro X-ray attenuation than free iohexol commercial contrast agents [44]. The use of non-ionic surfactants, such as PEGylated surfactants, during the synthesis method of lipid nanoparticles, has also been explored as a modifying factor for increased stability after intravenous (IV)

administration [235]. In addition, gold is known to exhibit a superior CT imaging efficiency than other elements due to its high atomic number of 79. The linkage of solubilized, meso-tetrakis(4-carboxyl)-21H,23H-porphine (TCPP) functional gold nanoparticles (CD-AuNPs@TCPP) onto the surface of a covalent organic polymer nanoparticle (COP-8) has been designed to form COP@Au@TCPP nanocomposites for CT tumour imaging and photodynamic cancer therapy [236]. After the COP@Au@TCPP nanocomposites aggregate in the tumour site through EPR, imaging information can be obtained to characterize the tumour through the CT imaging capacity of CD-AuNPs. Meanwhile, the CD-AuNPs act as catalyzers that decompose H_2O_2 into O_2, preceding its sensitization by the TCPPs to achieve effective photodynamic therapy (PDT). The tandem catalysis PDT efficiency of the COP@Au@TCPP can then be tracked and visualized in this CT-imaging-guided PDT system demonstrated in **Figure 7A**.

However, hydrophobic interactions govern the linkage of the CD-AuNPs to the n-octyl groups on the surface of COP-8. The hydrophilic coating of contrast agents combined with hydrophobic surface attachments presents a risk of the untimely release of encapsulated or weakly tethered compounds during imaging procedures. This may be attributed to the hydrolysis of the polymeric shell, the leakage of the confined agents, or the breakage of surface bonds via reactions with the surrounding physiological environment.

Consequently, modifying the PNPs by covalent bonds offers an optimized polymeric nanoconstruct for CT applications. In a study by Joëlle Balegamire et al., it has been demonstrated that potential iodine leakages can be prevented by covalently grafting the iodine moiety onto the polymeric backbone, such as triiodobenzoyl moiety onto poly(vinyl alcohol) for imaging the liver, the spleen and the cardiovascular system [45]. In this work, the PEGylated functionalized polymeric nanoparticles were radiopaque for several hours well within the radiology working attenuation window and presented an enhanced biocompatibility over nanoemulsions with an iodinated oil core and polymeric shell. Another example is using an amide bond to covalently link thirty-seven (37) 3-N-[(N′,N′-dimethylaminoacetyl)amino]-R-ethyl-2,4,6-triiodobenzenepropanoic acid (DMAA-IPA) molecules to the surface of a starburst PAMAM Generation 4 (G-4) dendrimer (**Figure 7B**) [237]. The outcome was iodine-labelled nanoparticles with biocompatible and stable features for CT imaging despite the need for further biological evaluation. Further research investigating *in vitro* and *in vivo* CT imaging of iodinated polymeric nanoparticles has since propelled massive development into CT imaging-guided cancer treatment. Not only can PNPs functionalized with contrast agents improve the visibility of inflammation and tumours, but they can also accurately identify the size and location of tumours [261], track the distribution of photothermal agents [27], and reflect therapeutic results when conjugated with targeting agents too [27].

Table 2. *Examples of polymeric nanoparticles and their chemical surface modification with functionalizing agents specifically for bioimaging applications.*

Material of Nanoparticle	***Functionalizing agent(s)***	***Mechanism(s) of functionalization***	***Biomedical application***	***In vitro cell studies***	***In vivo studies***	***Ref***
Magnetic ferric oxide core	Chitosan coating and Fluorescein isothiocyanate (FITC)	Covalent reaction between the isothiocyanate group of FITC and the primary amino group of chitosan	Magnetic resonance contrast agents for MR imaging and optical probes for cancer detection	Efficiently internalized into SMMC-7721 cancer cells easily visualized using clinical MRI imager in vitro	N/A	[262]
Poly(lactic-co-glycolic acid) (PLGA) + Fe_3O_4 + QD	Fe_3O_4 NPs surface attachment through amine-terminals	Fe_3O_4 NPs surface attachment through amine-terminals	Optical and MR imaging-guided	MR T2-weighted images of Au NR/QD/Fe_3O_4/Taxol-loaded PLGA NPs were measured using a 3T MR system	Imaging signal evaluated after administration to A549 (lung cancer cells)-induced SCID mice the tumour area	[263]
Poly (l-glutamic acid) (PLGA)	Polyfluorene containing oxadiazole moieties (PFO) assembly	Electrostatic complex of positively charged PFO with negatively charged PG-drug conjugate	Turn on/ turn off Fluorescence imaging	PFO/PG-Dox complex up taken into A549 cells and the PFO displayed bright blue fluorescence upon Dox release in lysosome, showing the "turn-on" state of PFO/PG-Dox complex.	N/A	[264]
Polyacrylonitrile (PAN)	Anti-ErbB2 antibody	Pristine PAN NPs acquired amine functional groups after treatment with ethylenediamine (EDA). Antibodies were then anchored via N-ethyl-N′-(3-dimethylaminopropyl) carbodiimide hydrochloride (EDC)/N-	Label-free imaging of breast cancer cells	Imaging of human breast cancer SK-BR-3 cells, exhibiting a fluorescence quantum yield higher than that of DAPI by 2.6-fold and lasting for 11 hours.	N/A	[265]

		hydroxysuccinimide (NHS) activation				
Poly(ethylene glycol) (PEG) + methyl methacrylate backbone	1,4,7,10-tetraazacyclododecane-N,N′,N″,N‴-tetraacetic acid (DOTA) as a chelator + the positron emitter ^{64}Cu + GRGDS peptide	Radical Addition-Fragmentation Transfer (RAFT)	Radioactive and confocal imaging potent for tumour angiogenesis, metastasis, inflammation, certain cardiovascular abnormalities, and bone resorption	High cellular internalization in U87MG human glioblastoma cells was imaged with the ^{64}Cu-labeled multivalent CNPs .	Study on blood retention, liver, and spleen accumulation of ^{64}Cu-labeled CNPs in Sprague-Dawley rats	[266]
Tetraphenylmethane-based (TPM) microporous polymer network	Rhodamine 6G	Mixing dye solution with surfactant-stabilized nanoparticles followed by dialysis	Energy transfer, Catalysis, optoelectronic applications, imaging	N/A	N/A	[238]
Hyperbranched polyprodrug amphiphiles (hPAs)	Gd Guanidine residues	Click reaction of alkynyl functionalized DOTA(Gd) complex with the azidation product of h-P(CPTM-co-GMA)-bP(OEGMA-co-GPMA) making the covalently tethered Gd complex.	Tumour imaging	Imaging of HepG2 cells	In vivo blood circulation of hPA-2 and guanidine-free hPA-3 was examined in healthy rats, exhibiting comparable half-lives and potent uptake.	[267]
Methacrylic acid monomer (MMA) + Azobisisobutyronitrile initiator + 2-aminoethyl methacrylate hydrochloride (AEMH)	Reference fluorescent dye (4-ethoxy-9-allyl-1,8-naphthalimide: EANI) in the core of nanoparticle, and	FITC was covalently linked onto the particle surface via amino groups that resulted from the one-pot miniemulsion polymerization of EANI into the nanoparticles	Photoinduced electron transfer (PET) and intracellular fluorescence imaging of Hg^{2+} for bioremediation such as mercury detection	Cell viability and selectivity towards Hg^{2+} were demonstrated in HeLa cells incubated in Hg^{2+}	By encapsulating another dye, ratiometric fluorescence and selective recognition of Hg^{2+} in totally aqueous solution were achieved in	[243]

	Hydrophilic dye fluorescein derivative (AEMH-FITC)				live cells as well as tap and drinking water, showing excellent water dispersibility.	
PLA-PEG with oily core	IR780 molecules fluore scent dye	Covalent attachment via one-pot copper-free strain-promoted alkyne-azide cycloaddition (SPAAC) reaction with IR-PLA conjugates Physical non-covalent attachment was achieved by mixing with water to obtain a suspension of the dye during the NP synthesis	Image-guided diagnosis.	Using J774A.1 macrophage-like cell line, covalently and noncovalently attached molecules were compared for fluorescence imaging efficacy.	N/A	[268]
Zirconium dioxide (ZrO_2) with Polydopamine (PDA)	Doping Mn^{2+} ions, Functionalizing with Tween 20,	Mn^{2+} directly chelated by the coordination effect of catechol or carboxyl groups in PDA π-π stacking and hydrogen bonding interaction of PDA with nanocomposites surface	Computed tomography (CT) imaging, magnetic resonance (MR) imaging	CT and MR imaging effects were demonstrated with high resolution.	Infra-Red thermal images of BALB/c nude mice bearing SMMC-7721 cells mice injected intratumorally	[269]
Poly (lactic-co-glycolic acid) (PLGA)-polyethylene glycol (PEG) (PLGA–PEG)	Fluorescent probe, coumarin-6 Near-infrared fluorescent dye (DiR)	A modified nanoprecipitation technique that exposes the positively charged polymer on the surface allowing free carboxylic groups of PLGA-PEG NP react with multiple exposed amine groups on PAMAM and PEI.	Fluorescence imaging in major organs (brain, heart, lung, liver, kidney, spleen, and pancreas) for Blood Brain Barrier (BBB) studies	Tracking of NPs in BBB cell culture model (monoculture of human brain microvascular endothelial cells, hCMEC/D3)	IVIS-200 visualization of the fluorescence intensity in brains of mice bearing GBM orthotopic xenografts with PTX-loaded PGM NPs.	[270]

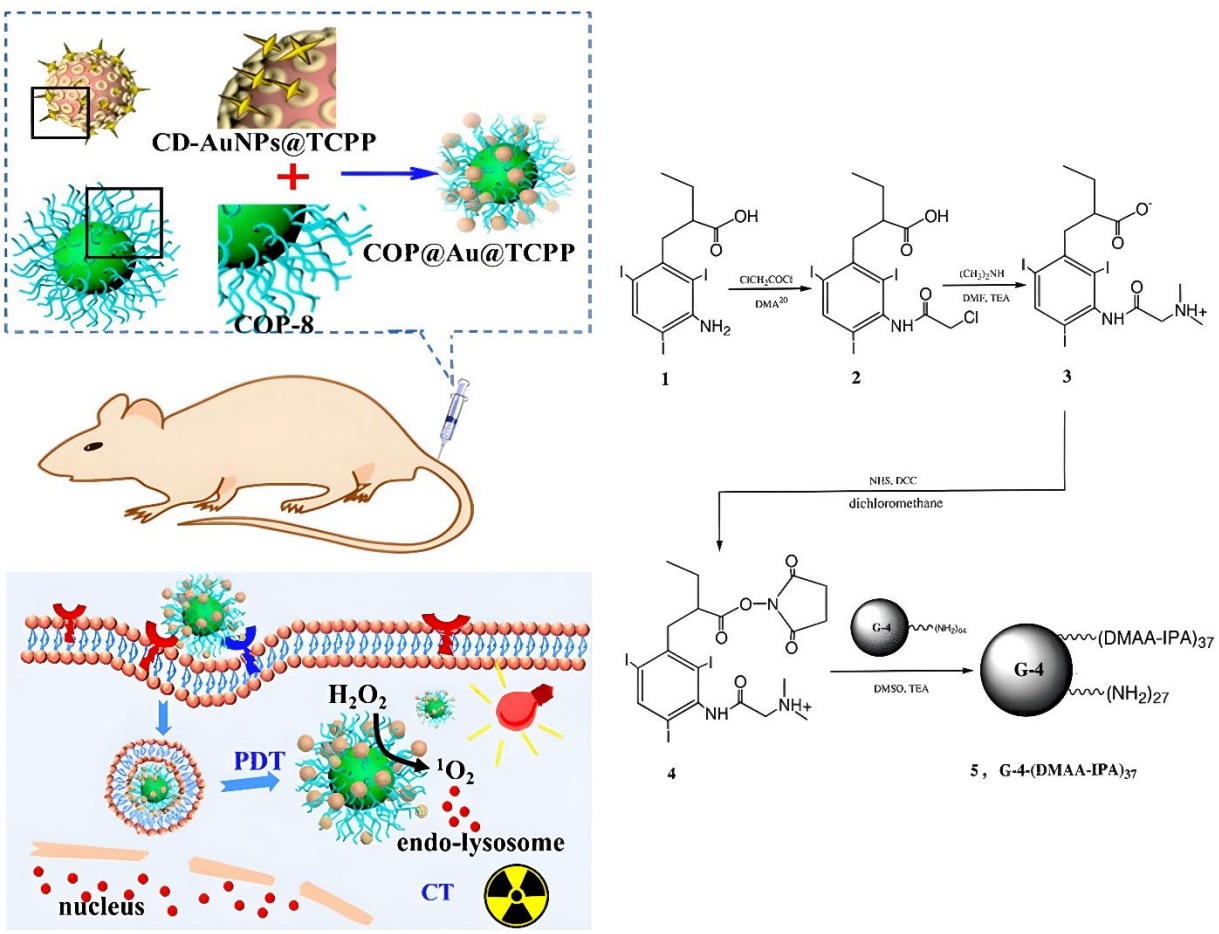

Figure 7. (A) Schematic diagram showing the binding of meso-tetrakis(4-carboxyl)-21H,23H-porphine (TCPP) functional gold nanoparticles (CD-AuNPs@TCPP) onto the surface of a covalent organic polymer nanoparticle (COP-8) (COP@Au@TCPP) via hydrophobic interaction. In addition to their CT imaging capacity, CD-AuNPs act as catalyzers that decompose H_2O_2 into O_2. TCPPs then sensitize O_2 into $^1O_2$ to achieve effective photodynamic therapy. Reprinted (adapted) with permission from [236]. Copyright 2020 American Chemical Society. (B) Scheme showing the surface functionalization of an iodinated polymeric particle with covalently linked thirty-seven (37) 3-N-[(N',N'-dimethylaminoacetyl) amino]-R-ethyl-2,4,6-triiodobenzenepropanoic acid (DMAA-IPA) molecules for Computed tomography (CT) imaging with high contrast and long-lived vascular concentrations. Reprinted (adapted) with permission from [237]. Copyright 2002 American Chemical Society.

1.3.2.2. Optical contrast agents

Optical imaging, such as fluorescence and bioluminescence imaging, has enabled researchers to enhance the field of disease diagnostics through the optical visualization of complex subcellular biological events in living systems [271]. Recent developments in optical imaging instruments using PNPs have accrued exponential growth in molecular imaging due to their non-invasive advantage combined with the high photostability of the carrier particle [28, 272, 273].

Fluorescence imaging, in particular, can employ optical probes with unique features, such as multi-colouring or signal activation control, to increase the signal-to-background ratio [274, 275].
The fluorescence signal of PNPs and its duration is governed by the chemical reactions that result from coupling selective fluorescent agents to the particle surfaces. For example, energy transfer from microporous organic tetraphenylmethane nanoparticles to surface-bound Rhodamine 6G dye molecules can induce a detectable green emission (**Figure 8**) [238]. However, in this work, the coated Rhodamine 6G nanoparticles were prepared by mixing the dye solution with a dilute dispersion of surfactant-stabilized nanoparticles. Such methods of physical adsorption by mixing jeopardize the intrinsic fluorescent properties of the fluorescent label after exposure to physiological environments. Covalent binding of the conjugated moiety circumvents the deterioration of the fluorescent agent, as is the case for near-infrared dyes (NIRFs). NIRFs are a specific class of dyes with the fluorescence capability of deep tissue penetration [239]. The cyanine (Cy) NIRF dye family covalently links to polymeric matrices of the nanoparticles due to their amine-reactive properties. For example, Cy5-conjugated polylactide (Cy5-PLA) [276], Cy5.5–conjugated glycol chitosan (Cy5.5-GC) [240], Cy7- poly (ether amine) (Cy7-PEA) [241], and Cy7.5- polyethylene glycol-poly(lactic-co-glycolic acid) (Cy7.5- PEG-PLGA) [242] nanoparticles have been employed as robust dyes with fluorescent stability lasting up to days. Similarly, hydrophilic dye fluorescein derivative AEMH-FITC covalently binds to PNPs with abundant amino groups on their surfaces for imaging in HeLa living cells, as was demonstrated by the work of Hong Wang et al [243]. In this work, the surface-bound dye functioned as a mercury recognition group, while a reference hydrophobic dye, 4-ethoxy-9-allyl-1,8-naphthalimide (EANI), was encapsulated into the nanoparticle core. As a result, this ratiometric fluorescence method, primarily found in biosensors, can be adapted to complement bioimaging in selective areas of the human body with high detection limits.

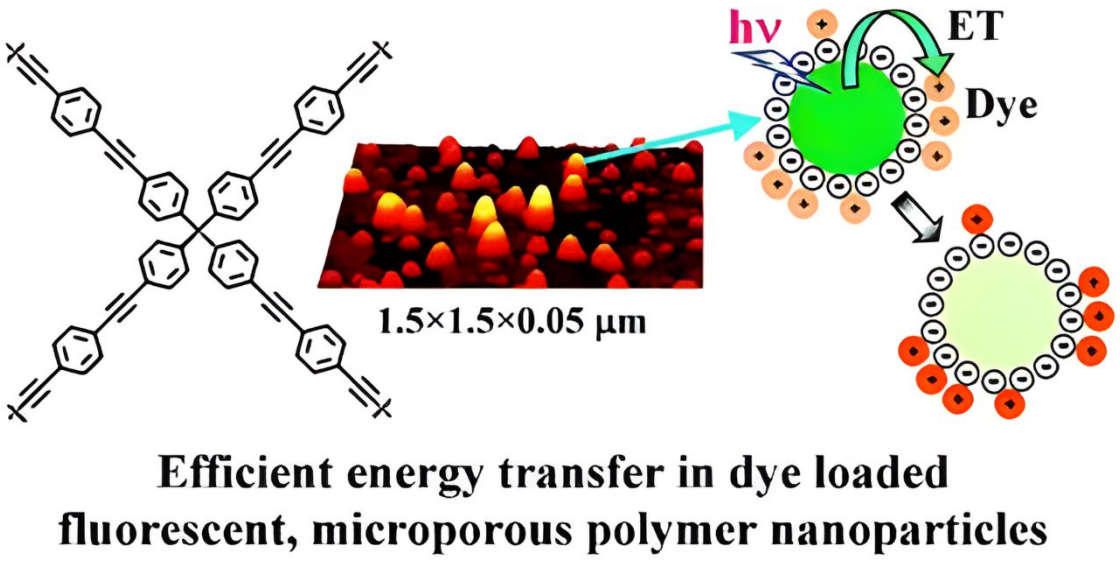

Figure 8. [Left to right] A diagram of the tetraphenylmethane-based microporous organic polymer (TPM-MOP) nanoparticles, AFM topography image of TPM-MOP nanoparticles deposited on a quartz plate, and a schematic illustration of the strong green emission observed via excitation energy transfer from the TPM-

MOP nanoparticles to the surface-bound Rhodamine 6G acceptor dye molecules. Reproduced from Ref [238] with permission from the Royal Society of Chemistry.

1.3.2.3. Magnetic resonance (MR) contrast agents

Magnetic resonance imaging (MRI) is a prevalent imaging technique in the clinical field used for disease diagnostics. The abundance of practitioners offering non-invasive MRI imaging is directly related to its safety for the brain and central nervous system as it does not involve the use of ionizing radiations [277]. MRI produces high-resolution three-dimensional maps of sections in soft tissue samples, highlighting the differences in local proton density and delineating interior anatomical features of the specimen [278]. Contrast agents are used to overcome the inherent sensitivity problems that hamper the differentiation between pathological and normal tissues at cellular and molecular levels. The contrast in MR images is determined based on the longitudinal (T1) or transverse (T2) relaxation time of the surrounding water protons within the tissue environment under a strong external magnetic field [279]. Contrast agents are characterized by their relaxivity, a measure of the sensitivity of the contrast agent, referring to the degree to which they can improve the longitudinal or transverse water relaxation rate constants (R1 = 1/T1 or R2 = 1/T2, respectively) [280]. When injected, contrast agents induce water proton density changes that shorten (T1) or (T2) and subsequently increase relaxivity while altering the brightness or darkness of the resultant image, respectively.

A variety of paramagnetic compounds have been evaluated as MR contrast agents, but gadolinium-based small molecules are currently preferred as T1 contrast agents due to their favourable electronic and magnetic structures [281-283]. However, if free Gd ions are released, Gd agents may exceed recommended dosage limits and cause nephrotoxicity [284]. Using Gd-chelates (e.g., 1,4,7,10-tetraazacyclododecane-1,4,7,10-tetraacetic acid (DOTA) -Gd, diethylenetriaminepentaacetic acid (DTPA) -Gd) can bind the Gd ions and prevent them from leaching out in vivo, but they would still lack in vivo stability as the smaller size results in rapid renal clearance. On the other hand, Gd-chelate conjugated PNPs can concentrate Gd^{3+} ions on the nanoparticles, and increase the T1 signal intensity ratio [244]. To enhance the stability of the immobilization, spacer-aided covalent grafts are used to introduce necessary functional groups to the nanoparticle surface. For instance, different spacers were covalently coupled to the carboxylate groups at the PLGA nanoparticle surface to introduce primary amines necessary for the conjugation of chelating molecules DTPA or DOTA- Gd [245]. The stability of the surface grafts using branched Polyethyleneimine PEI as a spacer was superior to linear spacers due to its higher thermodynamic and kinetic stability (**Figure 9A**). The covalent surface-grafting of the chelating molecules reduces the toxicity risk of free Gd^{3+} and enhances the cellular uptake of Gd^{3+} ions through the size-tuneable, biocompatible nanoparticle favourable for blood pool imaging or the recognition of capillary lesions. High relaxivities of up to 14.381 m M^{-1} s^{-1} have been achieved using DTPA-Gd chelated to a nanoparticle with PLGA core and a paramagnetic-folate-coated PEGylated lipid shell layer [246]. The paramagnetic (DTPA-Gd) chelated nanoparticle PLGA/PFPL exhibited an approximately three-fold enhancement in the longitudinal relaxivity compared to the commercial small-molecular-weight MRI contrast agent, Magnevist®, as shown in **Figure 9B**. MR images of the nanoparticle system (PLGA/PFPL) also showed that T 1 -

weighted bright contrast imaging was achieved at lower concentrations of Gd compared to Magnevist ® **(Figure 9C)**. In addition, in vivo experiments have been performed with Gd- DTPA surface-modified polyethylenimine-grafted poly(L-lysine) (PEI–PLL) nanoparticles as novel polymeric micellar MR imaging contrast agents [247]. The DTPA conjugated polymers, followed by complexation with $Gd^{3}+$ yielded an MR imaging contrast agent with high Gd^{3+} loading density. As a result, an improvement in contrast enhancement and significantly prolonged circulation time with high T1 relaxivity in blood vessels has been confirmed relative to that of conventional contrast agent Gd–DTPA (**Figure 9D**). One possible reason given was the large molecular weight of PEI–PLL–DTPA (>30 kDa), which could hinder its excretion from the kidney [285].

Surface-functionalized PNPs, hence hold a great promise for an optimal contrast media design as they possess the attributes of biocompatibility, strong signal generation, and high CA load rates with long periods of stealth.

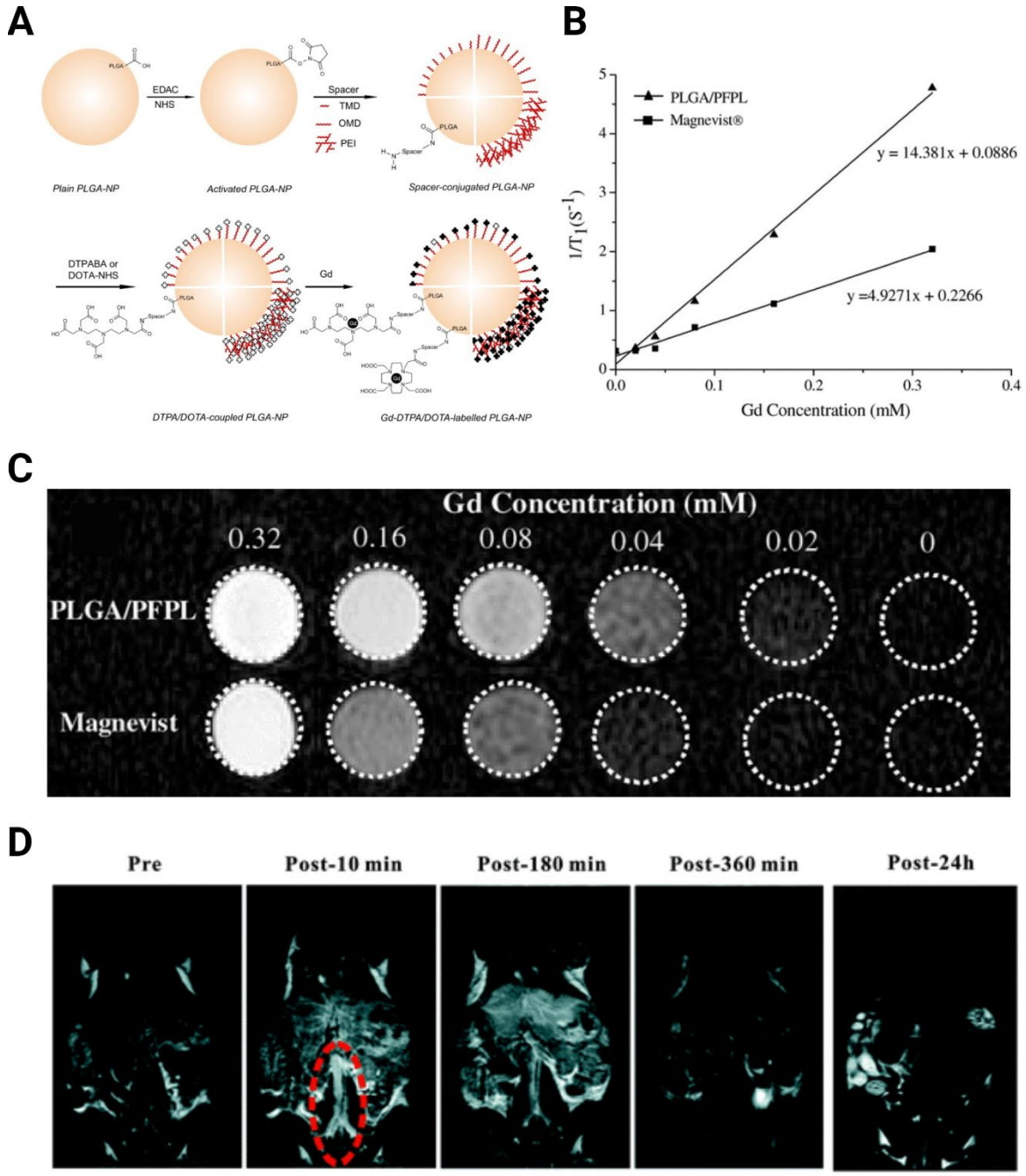

Figure 9. (A) Schematic diagram showing the step-by-step surface functionalization of PLGA nanoparticles with gadolinium Gd. The addition of a spaced/linker layer supports the covalent grafting of the Gd reduces the toxicity risk of free Gd^{3+} and enhances the cellular uptake of Gd^{3+} ions through the size-tuneable, biocompatible nanoparticle. This combination is favourable for blood pool imaging, the recognition of capillary lesions and the enhancement of imaging stability. Reprinted from [245], Copyright (2010), with permission from Elsevier. (B) Relaxivity plot showing the distinct enhancement in PLGA/PFPL over Magnevist ® with values 14.381 mM-1.s-1 compared to 4.927 mM-1.s-1 respectively and (C) MR images of nanoparticle system (PLGA/PFPL) showing T 1 -weighted bright contrast imaging at lower concentrations of Gd compared to Magnevist ® [246]. (B) and (C) Copyright © 2011 WILEY-VCH Verlag GmbH & Co. KGaA, Weinheim. (D) The T1-weighted MR images of a Kunming mouse injected with PEI–PLL–DTPA–Gd showing the in vivo blood pool contrast enhancement (CE) for the liver, vessels, heart and

abdominal aorta (marked in red) up to 24 h post-injection. Reproduced from [247] with permission from the Royal Society of Chemistry.

1.3.3. Targeted delivery and cancer therapy

Nanoparticles have been extensively explored as platforms for the transport of therapeutic drugs to diseased cellular sites [67, 286]. However, targeted drug delivery via nanoparticles is confronted with the challenge of nonspecific physiological interactions between the nanocarriers and biological fluid in which they must travel [287]. For instance, nonspecific adhesion to blood components could disrupt the morphology of normal blood cells, result in aggregation or precipitation, and cause changes in cellular and intravascular functions [288, 289]. An additional challenge during the nanoparticle circulation in the bloodstream is their exposure, detection and subsequent sequestration by the body's mononuclear phagocyte system (MPS), such as scavenger endothelial cells in the liver [290]. Therefore, the engineering of nanoparticles for drug transportation needs to prevent the detrimental effects of the adverse interactions at these sites. As the first direct contact with bio-organic fluid is through the surface, the successful intravenous distribution of nanocarriers mainly relies on their surface characteristics. Surface-modified nanoparticles are, hence, designed to overcome the obstacles of the nonspecific interactions with blood components and rectoendothelial systems in order to specifically target pathogenic sites [291]. **Table 3** summarizes a collection of surface-functionalized PNPs applied in targeted drug delivery and therapeutic applications over the past two decades.

Table 3. *Examples of polymeric nanoparticles and their chemical surface modification with functionalizing agents for applications in targeted drug delivery and cancer therapy.*

Nanoparticle	***Functionalizing agent(s)***	***Mechanism(s) of functionalization***	***Biomedical application***	***In vitro cell studies***	***In vivo studies***	***Ref***
α-acetoxy-poly(ethylene glycol)-poly(d,l-lactide) block copolymer (acetal-PEG–PDLLA)	Peptidyl ligands (phenylalanine (Phe) and tyrosyl–glutamic acid (Tyr–Glu)	Transformation of the acetal groups into aldehyde groups followed by Schiff base and reductive amination	Potential drug carriers with modulated surface charge	N/A	N/A	[292]
Poly(lactide-co-glycolide) PLGA, Poly-ethylene glycol (PEG) spacer	Biotin and folic acid Paclitaxel cancer drug (encapsulated)	Interfacial Activity Assisted Surface Functionalization (IAASF)	Tumour-targeted drug delivery	Molecule-conjugated nanoparticles were extensively taken up relative to free nanoparticles by different cancer cell lines with overexpressed receptors.	Enhanced accumulation and improved efficacy in mouse MCF-7 xenograft tumour model.	[293]
Poly(lactic-co-glycolic acid) (PLGA) + Fe_3O_4 + QD	Taxol (paclitaxel)-(encapsulated), Fe_3O_4 NPs and quantum dots (QDs), and Anti-Her2 monoclonal antibodies	Fe3O4 NPs and quantum dots (QDs) surface attachment through amine-terminals, Anti-Her2 monoclonal antibodies were immobilized on the surface of Au NR/QD/Fe3O4/Taxol-loaded PLGA NPs	Tumour-targeted chemotherapy via photothermal-control drug release with chemotherapy and photothermal destruction	Distributed HeLa cells (cervix cancer cells) in an MTT assay effectively killed due to Taxol release.	Strong anticancer performance demonstrated in vivo on a subcutaneous dorsal flank injection of tumour cells (MBT-2 bladder cancer cells) with laser irradiation. The treated mice were still alive after two months, with 100% tumour decrease or no regrowth	[263]

					after therapy.	
Poly (l-glutamic acid) (PLGA)	The model anticancer drug doxorubicin Dox	Electrostatic assembly of cationic conjugated polymer PFO and anionic PLGA covalently- -conjugated with anticancer drug doxorubicin (PFO/PG-Dox).	Cancer therapy	Controlled Dox release upon uptake of PFO/PG-Dox complex into lung cancer A549 cells	N/A	[264]
Anticancer drug camptothecin (CPT) molecules + oligomer chain of ethylene glycol (OEG)	CPT conjugated inherently, Water-soluble drug—doxorubicin salt (DOX·HCl), calcein, cisplatin or phosphotungstic acid (PTA) as dyes (encapsulated)	The carboxylic acid of the OEG lead to a direct ester formation of CPT	Dual-drug chemotherapy	The nanocapsules delivered anticancer drugs revealing in a synergetic cytotoxicity to cancer cells, assessed in SKOV-3 ovarian cancer cells and MCF-7 breast cancer cells MTT assay.	The in vivo antitumor activity of OEG-DiCPT was preliminarily assessed using athymic mice bearing intraperitoneal (ip) tumors showing fast and significant tumor suppression with DiCPT drug	[294]
polyacrylonitrile (PAN)	Anti-ErbB2 antibody	Pristine PAN NPs acquired amine functional groups after treatment with ethylenediamine (EDA). Antibodies were then anchored via N-ethyl-N′-(3-dimethylaminopropyl) carbodiimide hydrochloride (EDC)/N-hydroxysuccinimide (NHS) activation	Active targeting of breast cancer cells	Low cytotoxicity and good uptake into human breast cancer SK-BR-3 cells were demonstrated by antibody-conjugated surface-treated PAN nanoparticles (anti-ErbB2 tPAN)	N/A	[265]

Poly(ethylene glycol) (PEG) + methyl methacrylate backbone	1,4,7,10-tetraazacyclododecane-N,N′,N″,N‴-tetraacetic acid (DOTA) as a chelator + the positron emitter ^{64}Cu + GRGDS peptide	*Radical Addition-Fragmentation Transfer (RAFT)	Targeted therapeutics	High cellular internalization in U87MG human glioblastoma cells was achieved and assessed at increasing ratios of conjugated RGD. Specificity towards the tumour integrin $\alpha_v\beta_3$, was confirmed in comparison to integrins of macrophages and blood platelets.	In vivo study on blood retention, liver, and spleen accumulation of 64Cu-labeled nanoparticles in normal rats showed proportionality between loadings and effect on blood retention	[266]
Hydrophobic drugs (doxorubicin (DOX) and camptothecin (CPT)) + (poly-L-lactide) polymer conjugate	Lipid-polymer coating (Egg PC and 1,2-distearoyl-sn-glycero-3-phosphoethanolamine-N-carboxy-(polyethyleneglycol)-2000 (DSPE-PEG-COOH))	*Nanoprecipitation	Dual-drug delivery for chemotherapeutics	Dual-drug loaded nanoparticles showed an enhanced cytotoxicity against MDA-MB-435 breast cancer cells compared to mixtures of the drug-polymer conjugates.	N/A	[295]
Poly(phenylacetylene) (PPA) and poly(phenylacetylene-co-acrylic acid) (P(PA-co-AA))	Dexamethasone (DXM) (encapsulated)	*Modified surfactant free emulsion	Tissue engineering and cancer treatment	Introduced DXM loaded nanoparticles to be used in the apoptosis inhibition of human tumour cells (HeLa)	N/A	[155]
PEGylated Poly[9,9-bis(N-but-3'-ynylN,N-dimethylaminohexyl)-fluorenyldivinylene-alt-4,7-(2',1',3',-benzothiadiazole) dibromide] (PFVBT) with derivatives	Doxorubicin (DOX)	DOX covalently conjugated to PFVBT by a thioketal linker.	On-demand photodynamic therapy and chemotherapy	Invitro cytotoxicity of TCP-DOX NPs was assessed in MDA-MB-231 cells and indicated negligible toxicity.	N/A	[296]

Hyperbranched polyprodrug amphiphiles (hPAs)	Gd Guanidine residues (encapsulated) Oligo(ethylene glycol) monomethyl ether methacrylate (OEGMA) and guanidinopropyl methacrylamide (GPMA) (OEGMA-co-GPMA) (hPA-2)	Click reaction of alkynyl functionalized DOTA(Gd) complex with the azidation product of h-P(CPTM-co-GMA)-bP(OEGMA-co-GPMA) making the covalently tethered Gd complex. RAFT copolymerization governed the synthesis of hPA-2	Drug delivery, release, and tumour imaging	In-vitro cytotoxicity of guanidine-decorated hPA-2 was evaluated using MTT assay and showed an activated drug release.	In vivo blood circulation of hPA-2 and guanidine-free hPA-3 was examined in healthy rats, exhibiting comparable half-lives and potent uptake.	[267]
Poly(lactic-co-glycolic acid) PLGA NPs	Albumin (Al) Rhodamine B label Paclitaxel (encapsulated)	Three methods of Al attachment: physisorption, interfacial embedding, and dopamine (pD) polymerization compared	Drug delivery into tumours with controlled surface interactions	Improved transport, less inflammation, greater biodistribution and higher tumour accumulation (B16F10 tumor-bearing mice) were achieved with pD-mediated functional Al-NPs	An in vivo study using C57BL/6 mice bearing B16F10 melanoma revealed a greater accumulation of pD-Al-functionalized NPs in tumours with lesser phagocytotic interactions compared to NPxAl.	[297]
PEG-ylated poly[hexadecyl cyanoacrylate-co-methoxypoly(ethylene glycol) cyanoacrylate] (P(HDCA-co-MePEGCA))	Biotin treatment Streptavidin FITC-anti-$A\beta_{1-42}$ monoclonal antibody,	Biotin/streptavidin (Sav) ligation strategy yielding extraordinarily high non-covalent affinity, as verified in [298]	Alzheimer's disease therapy	N/A	Significant reduction in soluble forms of Aβ and memory recovery in transgenic mice with Alzheimer's-like disease	[299]

Upconversion nano-onions (UCNOs) with stacked polymer coating layers (UCNPs-PEIRB-PEISeSe)	siRNA, R8 peptide, and hyaluronic acid (HA)	Residual $-NH_2$ group on UCNPs-PEIRB-PEISeSe surface and carboxyl groups on peptide R8 covalently modified the nanoparticle surface, Negatively charged HA linked to positively charged siRNA-R8-modified NPs via electrostatic interaction.	Precise drug delivery and tumour therapy.	R8- and HA-mediated recognition and delivery specificity, effectively improved the gene silencing efficiency in vitro	Suppressed tumour growth in vivo using HepG2 cell tumour-bearing nude mice by revealing massive cell shrinkage and nuclei absence with NIR irradiation.	[300]
PLA-PEG with oily core	IR780 molecules fluorescent dye	Covalent attachment via one-pot copper-free strain-promoted alkyne-azide cycloaddition (SPAAC) reaction with IR-PLA conjugates Physical non-covalent attachment was achieved by mixing with water to obtain a suspension of the dye during the NP synthesis	Photosensitizers for photodynamic therapy.	In vitro release studies and cell viability studies with the J774A.1 macrophage-like cell line showed that covalently-linked IR NPs were less cytotoxic, better maintained their dye in biological environments, and resulted in less uptake than physically attached IR NP.	N/A	[268]
Upconversion nanoparticle (UCNP) core NaYF4:Yb/Ho/Nd@NaYF4:Nd core	A middle silica shell with the first photosensitizer (PS) methylene blue (MB) encapsulated, an outside mesoporous silica shell (MS) with the second PS rose 39engal (RB), anticancer drug	Surface treated with boronic acid (BA) molecules, Modified NH_2 groups for positively charged outmost MS shells, Negatively charged RB were attached onto channel walls through electrostatic attractions,	Synergistic chemotherapy (Chemo) and photodynamic therapy (PDT)	Antitumour efficiency tests in HeLa model cell confirmed biological safety of the nanoparticles and their synergistic chemo/PDT ability killed almost all the cancer cells.	In vivo antitumor efficiency tested on mice bearing HeLa tumours indicated that although the PDT is more efficient than Chemo, when Chemo and PDT were combined, tumour	[301]

	doxorubicin hydrochloride (DOX) uploaded into channel pores, and Cyclodextrine (CD) conjugated on the nanoparticle surface	DOX was loaded into the pores through physical diffusions. CD molecules were conjugated onto the nanoparticle surface via acid-labile linker associating with pre-anchored BA molecules.			growth massively dropped (0.8-fold), revealing a "super additive antitumor efficacy".	
Zirconium dioxide (ZrO_2) with Polydopamine (PDA)	Doping Mn^{2+} ions, Tween 20, Drug doxorubicin hydrochloride (DOX)	Mn^{2+} directly chelated by the coordination effect of catechol or carboxyl groups in PDA π-π stacking and hydrogen bonding interaction of PDA with nanocomposites surface	Chemotherapeutic drug loading and release	Free nanocomposites were biocompatible against SMMC-7721 carcinoma and glioma cells until loading with DOX induced highest killing rate relative to photothermal and chemo- therapy. In vitro CT and MR imaging effects were also demonstrated with high resolution.	Controllable DOX release revealed as in vivo tumour growth was efficiently suppressed with the antitumor rate up to 87.92% upon triggering by the near-infrared (NIR) irradiation and acidic pH	[269]
Conjugated polymer nanoparticles (CPNs)	Therapeutic pDNA (HSP70-pTRAIL-EGFP), W-7 molecule (encapsulated)	Electrostatic interactions	NIR photothermal conversion and cancer theranostics	The CPNs locally released W-7, which enhanced cancer cell apoptosis	Conjugated CPNs showed strong antitumor efficacy and high biosafety upon accumulation at tumor sites.	[302]
Poly(lactic-co-glycolic acid) PLGA	EL4 T-cell plasma membrane	Asymmetric repulsion driving right-side-out cell membrane coating	Cancer treatment	T-PLGA inhibited phagocytosis and achieved targeted delivery to bone marrow-derived	In vivo cancer growth inhibited in C57BL/6 mice injected with B16-F10 cells	[303]

				macrophages and B16-F10 cells respectively.		
Poly(D,L-lactide-co-glycolide)–poly(ethylene glycol) PLGA-PEG	Small cancer cell targeting peptide WQP	Maleimide–thiol chemistry	Prostate cancer targeting	Selective targeting achieved in a variety of cell lines	N/A	[304]
Poly(ethylene glycol)–poly(glycerol) (PEG–PG) block copolymers	Phenylalanine (Phe) moieties	Hydrolyzable ester bonds.	mRNA-based cancer treatment	PEG–PG(Phe) demonstrated significant potential for facilitating endosomal escape in a variety of cell lines	Conjugate ensured prolonged protein expression in BALB/c mice	[305]

*The nature of the surface interaction was not assessed.

1.3.3.1. Targeted drug delivery

The engineering of effective surface-functionalized PNPs for targeted drug delivery thus takes into consideration three key factors: the surface modification method, the compatibility of the surface with the circulation environment, and the targeting ability of the functionalized particle. Different surface modification methods have varying effects on the conformation of the surface functionalizing agent and its interactions with diseased microenvironments. Hyun et al. compared physisorption, interfacial embedding, and a novel method based on dopamine polymerization to functionalize the surface of PLGA nanoparticles with albumin (Al) (**Figure 10A**) [297]. The oxidative polymerization of dopamine into polydopamine (pD) binds the latter with amine- or thiol-surface groups to form functional coatings [306]. Dopamine polymerization-mediated albumin conjugation, pD-Al, results in the preservation of the protein conformation as opposed to interfacial embedding, which changes the folded structure of the albumin during surface modification. Moreover, the pD-Al surface layer facilitated nanoparticle transport and interaction with cancer cells via albumin-binding proteins gp60 and SPARC. On the other hand, denatured albumin promoted MPS uptake due to direct and indirect interactions with "J774A.1" macrophages assessed as a phagocytic cell model [297]. In addition to contributing a thin biocompatible layer, the dopamine self-polymerization method introduces a high ligand anchoring ability on the particle membrane [307]. Folate, chitosan and peptides are examples of molecules that have been immobilized onto the membranes of PNPs using polydopamine-based conjugation for the development of targeting nano drug carriers [308-310]. However, several risks emerged from pD-based surface functionalization, including shifting the optical properties of the carrier nanoparticles and jeopardizing the stability of the polymer or drug due to the alkaline condition essential for polymerization [311]. As a result, tannic acid (TA) has been identified as an alternate surface modifier composed of plant-derived polyphenolic compounds [312, 313]. These polyphenols deposit reactive layers on surfaces of polymeric particles in the form of oligomers and accommodate thiol- or amine-terminal groups. The interactions of TA- surface functionalized PLGA NPs with target cells have been characterized after different molecules, such as fluoresceinamine (fla), folate-conjugated and amine-terminated PEG (pFol), albumin, or low molecular weight chitosan (LMWC) were bound to the TA coating [314]. Moreover, (hetero) aromatic drugs doxorubicin (Dox), proflavine (Pfv), and rhodamine B (RhoB) were loaded to the surface of PLGA-TA and displayed a high affinity to the surface modifier. The drug loading efficiency registered a linear increase with Dox and Pfv but saturated at an upper limit with RhoB (**Figure 10B**). This difference was attributed to the primary amine groups found in Dox and Pfv that can be covalently conjugated to the TA coating but are missing from RhoB linkages. Upon the successful loading of drugs onto the surface of the PNPs, an important step remains to ensure the biocompatibility of the functional particle within its circulating medium.

The hydrophilicity of surface-modified particles is critically important because it complements their targeting ability and site specificity, defining their performance as targeting agents. During their circulation in the body, PNPs modified with hydrophilic surfaces can evade uptake by the rectoendothelial system [315], prolong blood circulation half-life [316], and reach the target organs or cells [49, 317]. Adding hydrophilic spacers to a surface introduces steric effects of surface shielding and prevents biomolecular compounds from distorting the surface and degrading its performance, which is particularly important in *in-vivo* targeting applications [192, 318]. For colorectal cancer therapy, as an example, a biodegradable chitosan layer is engineered to enhance the biodegradability and biocompatibility of polymeric drug-loaded nanoparticles [92, 319, 320].

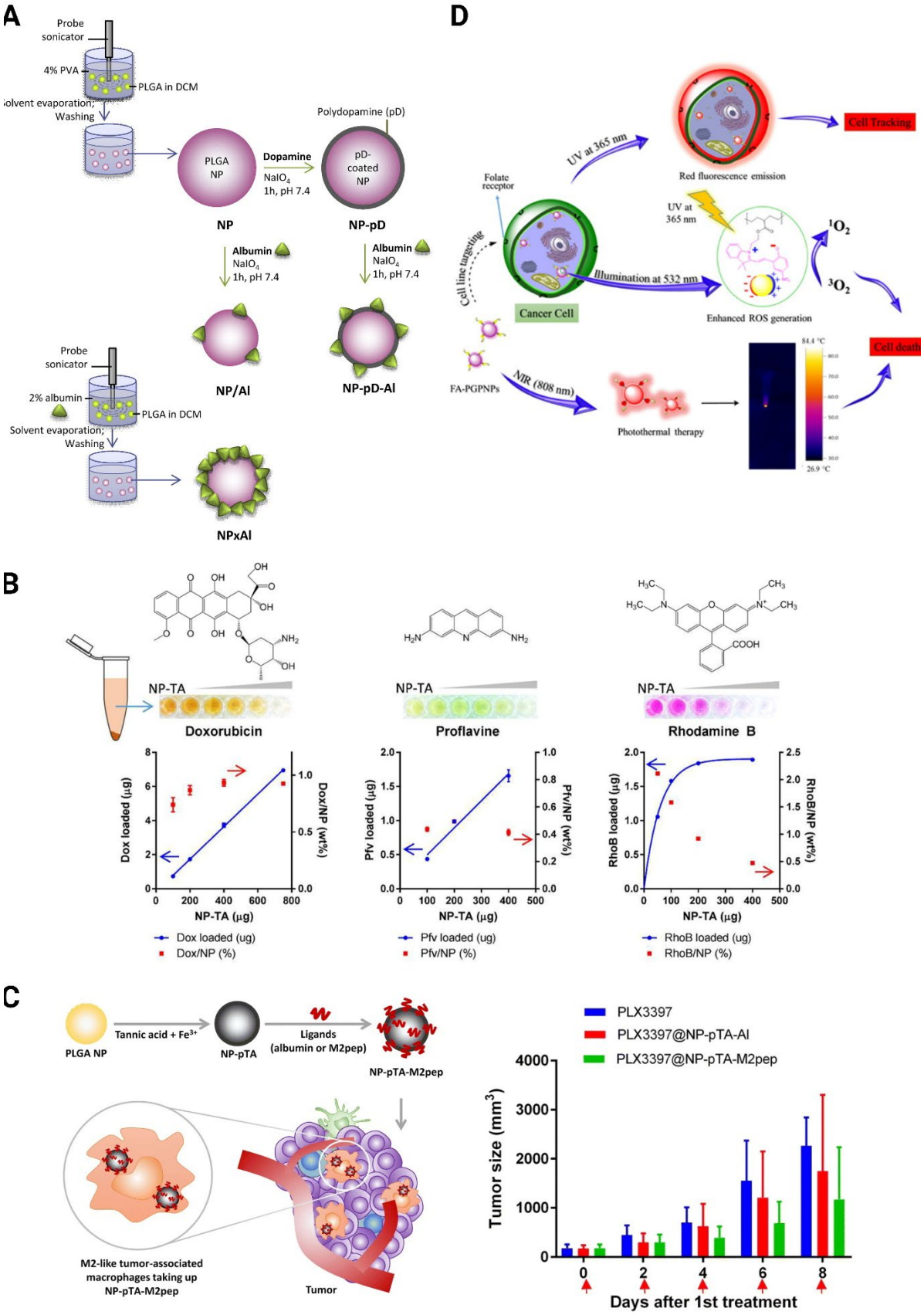

Figure 10. (A) A schematic drawing of the three methods used to conjugate albumin (Al) to PLGA nanoparticles with and without polydopamine pD. Reprinted from [297], Copyright (2018), with permission from Elsevier. (B) Functionalization of NP-TA with Dox, Pfv, and RhoB and calculations of

the amount of each compound using their supernatants. Reprinted (adapted) with permission from [314] Copyright 2016 American Chemical Society. (C) (Left) Diagram illustrating the process of nanoparticle functionalization using M2pep to enhance uptake by tumour-associated macrophages. (Right) In vivo evaluation of free PLX3397 drug, PLX3397-loaded nanoparticles coated with M2pep (PLX3397@NP-pTA-M2pep), and PLX3397-loaded nanoparticles coated with a different material (PLX3397@NP-pTA-Al) in C57BL/6 mice with subcutaneous B16F10 tumours, demonstrated by monitoring changes in tumour volume recorded every other day. Reprinted with permission from [43]. (D) Schematic drawing of the process of synthesis and application of folate-conjugated gold–photoactive polymer nanoparticles. Upon surface functionalization with folic acid, the particles demonstrate strong capabilities in the photogeneration of reactive oxygen species and targeted photothermal therapy of C6 glioma brain cancer cells. Reprinted (adapted) with permission from [321]. Copyright 2018 American Chemical Society.

Electrostatic adsorption on the surface of negatively charged particles allows for the development of a coating chitosan layer due to its cationic charge [322]. For example, the in vitro anticancer activity of Imatinib (IMT)-loaded PNPs was sustained due to the presence of a chitosan corona on the nanoparticle surface [319]. The chitosan protected red blood cells from destruction expected by the IMT, caused higher and controlled cytotoxicity against CT26 colon carcinoma cell lines, and maintained physical stability with minor variations after six months. In addition, significant inhibition of colon cancer cells (HT-29) has been demonstrated for chitosan-coated DTX and 5-FU drug-loaded PLGA nanoparticles compared to uncoated nanoparticles in [320] and [92], respectively.

1.3.3.2. Cancer therapy

For site-specific or targeted delivery to malignant tumour cells, surface-modifying molecules are elected to guide the nanoparticles to the desired site. Ligands with a high affinity for elements within the tumour microenvironment, such as pH fluctuations and overexpressed proteins, enhance binding efficiency to target receptors and amplify drug activity at the tumour site. Tumour-associated macrophages (TAMs), for example, play a pivotal role by activating signalling pathways that promote the proliferation of cancer stem cells. Consequently, TAMs have emerged as attractive targets for potential cancer therapies [323]. As such, PLGA nanoparticles were surface-modified with a tannic acid-iron complex before coating with M2pep, a peptide ligand that selectively binds to M2-polarized macrophages [43]. M2pep-coated nanoparticles showed high localization of $CD206^+$ macrophages in mice B16F10 melanoma models, compared to uncoated nanoparticles. PLX3397, a colony-stimulating factor inhibitor [324], was then encapsulated in M2pep-coated nanoparticles and attenuated tumour growth better than the free drug counterpart and Albumin-coated nanoparticles (**Figure 10C**).

Another promising targeting agent applied in this domain is folic acid (FA) due to the overexpression of folate-receptor binding sites on the surface of cancerous cell line tissues [325]. Photo-responsive gold-immobilized acrylic polymer nanoparticles (PGPNPs) were surface-modified with folic acid through L-cysteine linkages to function as site-specific tumour-targeting agents that enhance intracellular uptake via endocytosis (**Figure 10D**) [321]. The FA-conjugated PGPNPs improved targeting efficiency in rat brain C6 glioma cancer cell line by a factor of ~2.5 compared to the nonconjugated nanoparticles. This assembly consisting of a functional molecule as a targeting element, a PNP as a stealthy carrier, and a drug as a therapeutic element has been explored for treating respiratory infections, ovarian cancer, Alzheimer's disease and more [326-331]. This progress has paved the way for combining further diagnostic moieties to achieve dual targeting, image-guided therapy, and a diversity of novel multifunctional disease theranostic agents [27, 332-334].

In conclusion, developing surface-functionalized PNPs for targeted drug delivery represents a promising avenue in nanomedicine. Overcoming challenges related to nonspecific interactions in biological fluids and evasion of the mononuclear phagocyte system (MPS) is crucial for effective drug transport. Surface modification methods, such as dopamine polymerization and tannic acid-based coating, offer diverse approaches to functionalize nanoparticles while preserving their biocompatibility. Hydrophilic surface modifications enhance nanoparticle circulation, prolonging their half-life and improving targeting specificity. The choice of targeting ligands, like M2pep and folic acid, enables precise delivery to tumour sites, enhancing drug efficacy. The ongoing exploration of multifunctional nanoparticles holds excellent potential for future theranostic applications in various disease treatments, further advancing the field of nanomedicine.

1.4. Future directions

Although there has been significant progress in surface biofunctionalized PNPs for diagnostics and therapeutic applications, progress toward their clinical translation remains limited.

Among all the nanomedicines accessible in the market or in various stages of clinical translations in June 2021, only %10 were polymer-based [335]. Reasons for this shortage of translation into biomedical modalities likely stem from the complexities of entities beyond cells. A considerable portion of the PNPs for diagnostics and drug delivery applications have been largely evaluated *in vitro* and have yet to simulate the physiological surroundings where the nanoparticles are to be tested. Despite our evolving understanding of *in vivo* environments, precise interactions between nanoparticle surfaces and biological media are yet to be investigated. Moreover, subsequent immune responses vary across species, adding to the challenge of establishing replicable in vivo assays for clinical translation.

Although the tunability of surface functionalization techniques has presented a notable step towards solving some of these challenges, there exists a deficit in scaling-up technologies for the fabrication of functionalized PNPs in large quantities. Factors such as scale-up strategies, reproducible manufacturing, and the progression towards industrial partnerships and commercialization are also in shortage.

Fortunately, promising medical procedures are currently being explored as alternatives to animal models, including stem cell research, microfluidics, and organ-on-a-chip technologies. As of January 2023, the U.S. Food and Drug Administration FDA no longer requires animal testing for new drugs, paving the road to accelerated advancements in these technologies, which are still in their early stages.

Further prospects for innovation exist in developing new technologies for the biofunctionalization of nanoparticles as diagnostics and drug delivery systems with greater precision. Such advances can bring the field closer to a multifunctional platform that will compete with the implementation of individual counterparts. Two notable examples of such technologies gaining significant attention are plasma polymerization and the plasma treatment of nanoparticles. These methods are receiving considerable interest for multifaceted biomaterial applications due to their scalability and versatility [100, 110, 123, 124, 336, 337]. The growing research in plasma polymerized nanoparticles is projected to have pivotal implications in diagnostic and therapeutic applications. Their solvent-free fabrication using small amounts of gases and rapid polymerization rates as well as their biofunctionalization via reagent-free single-step incubations, promise large-scale industrial production, a feature critical for their efficient clinical translation. In addition,

improvements in the synthesis and control techniques of biomolecules present new pathways for the customization and optimization of multifunctional biomolecules that can mimic natural tissue and cellular mechanisms [338]. One new avenue to improve biofunctionalization methods is controlling the orientation of the biomolecule to achieve the precise arrangement for it to interact with desired entities [339].

1.5. Conclusions

As the field of nanotechnology develops in the face of grand challenges, nanoparticles continue to present tremendous potential for achieving the global goal of "good health and well-being" by 2030. Their design as conjugated carrier systems can fundamentally change how medical diagnostics are achieved, treatments processed, and therapeutics delivered compared to their free counterparts. Polymer nanoparticles, in particular, offer the advantages of circumnavigating biological barriers due to their biocompatibility and biodegradability.

The surface bio-engineering of PNPs via integrating bioactive elements allows for a higher degree of control over their interactions at diseased cellular sites, an aspect critical for clinical translation. The recent advances in the surface functionalization of PNPs for biosensing, bioimaging, drug delivery and targeted therapeutics applications were discussed. The physical, wet chemical, or dry chemical surface functionalization mechanisms were evaluated relative to each application, where demonstrated in the literature, and remarked where further assessment was necessary.

An array of hydrophilic polymer coatings, biosensing agents, bioimaging probes, targeting therapeutic molecules, and combinations of these were demonstrated, elaborating on the electrostatic, physisorbed, ionic, or chemical interactions governing their immobilization to PNPs. Covalent and non-covalent bonds responsible for their functionalities were compared, with a focus on both direct and linker-mediated immobilization and highlighting the advantages and disadvantages of these approaches. The significance of covalent bonds in increasing the specificity of the functionalized PNP was emphasized in sensing pH variations, reactive oxygen species (ROS), and biothreat agents (viruses, bacteria, toxins, etc.).

Similarly, the review of the immobilization methods in computed tomography, magnetic resonance, and optical imaging showed that covalent linkages circumvent the deterioration of fluorescent and contrast agents upon incorporation with cellular environments. Nonetheless, the importance of physisorption for surface attachments became evident in the delivery and therapeutical role of bioconjugates that necessitate their controlled release upon contact with targeted cells. In vitro and in vivo applications were summarized, and their innovative contributions to advancing the field of biomedicine were highlighted over the past two decades. Although there remain numerous unexplored avenues for further growth of the existing approaches, surface functionalization of PNPs has demonstrated promising potential in improving the field of nanomedicine. Compared to the conventional free agents, tuneable PNP-based imaging, targeted drug delivery, and therapeutics can, therefore, become an excellent multifunctional tool for designing diagnostics and treatment strategies against diseases.

Chapter 2. General Methodology

This chapter provides an overview of the materials and methods used in different sections of the thesis. The specific methodologies relevant to each chapter are described within their own sections.

2.1. Materials

High purity argon (99.99%), nitrogen (99.99%), and acetylene (98%) gases used in the plasma process were supplied from BOC Australia. Fluorescein isothiocyanate (FITC), Nile Blue A (NB), and all other buffer reagents such as Sodium Dodecyl Sulfate (SDS) and Phosphate-Buffered Saline (PBS) were purchased from Sigma Aldrich and used without further processing, unless stated otherwise. Costar or Falcon (Sigma Aldrich) 24-well cell culture collector plates were used in the particle collection and suspension process.

2.2. Plasma polymerization of nanoparticles

Plasma polymerization of nanoparticles was conducted inside a custom-built cylindrical stainless-steel chamber that was previously designed and used for deposition of plasma-activated coatings [113, 340, 341]. The top electrode was powered at 100 W by an RF (13.56 MHz) ENI generator (OEM-6AM-1) and a matching network (RFPP AM-5) (**Figure 11**). A commercial polystyrene 24 well cell culture plate was placed on a substrate holder located 8 cm below the RF electrode to collect PPNs. For every experiment, the chamber was first pumped down to a base pressure of below 5×10^{-5} Torr using a dual dry vacuum pumping system. A combination of argon, nitrogen and acetylene gases (BOC Australia) was introduced at constant mass flow rates of 3, 10 and 6 standard cubic centimetres per minute (sccm), respectively, through a perforated ring to provide an axisymmetric gas distribution from the top of the chamber. The pressure, temperature, mass and volumetric flow rate of each gas were monitored and injected by a mass flow controller (Allicat Scientific) controlled by Flow Vision software. A starting pressure of 150 mTorr was achieved by fine-tuning an inline valve placed in between the vacuum system and the chamber, modulating the pumping speed and hence the pressure and residence time of the species within the chamber. A plasma discharge was then generated by coupling the RF power generator to the top electrode using an automated impedance matching box to minimize reflected power.

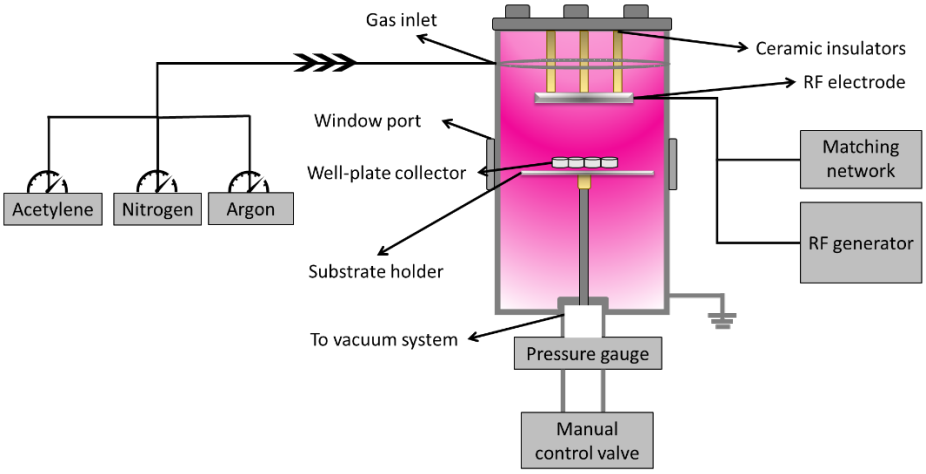

Figure 11. Schematic drawing of the plasma reactor connected to an RF generator and matching network with a well plate placed on the substrate holder for the collection of plasma polymerized nanoparticles.

2.3. Optical Emission Spectroscopy (OES)

During the nanoparticle synthesis process, non-invasive, in situ Optical Emission Spectroscopy (OES) was employed to monitor the polymerization and the excited species within the plasma phase. An optical fiber, positioned perpendicularly to one of the chamber windows, captured the emitted radiation from excited atoms and molecules. This was achieved using an Acton SpectraPro 2750 spectrometer from Princeton Instruments, equipped with a grating of 1,200 grooves per mm, and connected to an intensified charge-coupled device (Princeton PI-MAX ICCD) for spectral acquisition. The spectrometer, set with an exposure time of 100 μs and an intensifier gain of 250 in Shutter Mode, allowed for the capturing of emission spectra with a resolution of 0.03 nm. To enhance the signal-to-noise ratio, 2000 consecutive acquisitions were averaged, and the temporal evolution of the excited species was tracked. The emission intensities across specific wavelengths were recorded and displayed on a computer screen using Winspec-32 software, facilitating the analysis of well-defined central wavelengths and their corresponding emission intensities throughout the polymerization process.

2.4. Hydrodynamic size and zeta potential measurements

The zeta potential and hydrodynamic size of the nanoparticles were measured using a Malvern Analytical NanoZS zetasizer. The temperature was set to 25 °C with 60 seconds cell equilibration time. After collection, the nanoparticles were suspended into polystyrene vials and resuspended into disposable folded capillary cells (Malvern, DTS1070) under sterile conditions using 1 mL syringes. Unless otherwise specified, all measurements were performed in de-ionized MilliQ® water, with a pH value of approximately 5.5, as confirmed by a pH meter.

2.5. Attenuated Total Reflection – Fourier Transform Infrared Spectroscopy (ATR-FTIR)

The study of functional groups was conducted using a Bruker ALPHA portable FTIR system (Bruker Optik GmbH, Germany) equipped with a platinum attenuated total reflection (ATR) single reflection diamond attachment. Background scans were performed before each sample scan. All background and sample spectra were collected with a resolution of 4 cm^{-1}, spanning the spectral range from 400 to 4000 cm^{-1} with an average of 128 scans. Subsequently, all FTIR spectra were subjected to processing and baseline correction using OPUS 8.7 software (Bruker Optik GmbH, Germany).

Chapter 3. Optimized yield of surface-active plasma-polymerized nanoparticles for multifunctional diagnostic, targeting, and therapeutic probes

This chapter aimed to present a novel strategy to enhance particle collection yields for the synthesis and functionalization of polymeric nanoparticles using plasma polymerization. It highlights the significance of this advancement as a simplified, dry process over conventional wet-chemical methods, and identifies areas for future research in optimizing and applying these biofunctional nanoparticles for diagnostics and therapeutics.

Chapter 3 is adapted from a manuscript which has been published in ACS Applied Nano Materials entitled: "Surface-active plasma-polymerized nanoparticles for multifunctional diagnostic, targeting, and therapeutic probes". DOI: https://doi.org/10.1021/acsanm.2c03213.

3.1. Introduction

Polymeric nanoparticles have become increasingly popular for a broad range of modern and emerging applications from organic optoelectronics [342, 343] to environmental remediation [344, 345] and biomedicine [346]. For example, their adjustable electronic structures have made them suitable candidates for implementation in organic devices such as highly selective nano-sensors [347] and hybrid imaging scanners [348]. Polymeric particles can also be engineered to attain hydrophobic surfaces that achieve cross-linking in water and promote high affinity to contaminants in soil [129]. Biomedicine is another important growing area of application spanning theranostics [349], imaging [59], sensing [350] and degenerative disease amelioration such as retrieving vision impaired by retinal dystrophy [351]. Their high surface-area-to-volume ratio has also given rise to their role as particulate carriers for drug delivery [352] and cancer treatments [297, 353].

Polymeric nanoparticles can either be prepared from natural polymers such as albumin, chitosan and gelatin [354], or assembled from synthetic polymers such as polylactic acid (PLA) and poly(lactic-co-glycolic) acid (PLGA) [355]. Synthetic polymeric nanoparticles are typically prepared either by dispersion of preformed polymers into a specific shape using techniques such as nano-precipitation [356] and emulsification [357]; or by the direct polymerization of monomers into nanoparticles [358]. The physicochemical characteristics of the nanoparticles are influenced by the preparation method, leading to structures such as nanospheres, nanocapsules, or polymersomes [94]. Both dispersion-based and direct polymerisation processes rely on time-consuming chemical syntheses and multi-step protocols with complicated techniques common to all wet-chemistry approaches [94]. Dry, physical methods for material synthesis at the nanoscale are thus extensively sought to produce polymeric nanoparticles with tailored physical and chemical properties devoid of these fabrication complications.

Plasma polymerization has recently emerged as a novel, green alternative to traditional wet-chemistry methods to create nanoparticles [123, 359]. Plasma, commonly referred to as the fourth state of matter, is a gaseous mixture of charged particles, electrons and neutral atoms with an overall neutral charge. The plasma polymerization process takes place by generating a glow discharge using an organic precursor gas such as acetylene [125] or monomer vapours such as allylamine [126], acrylic acid [112], thiophene[132] or octadiene [130]. Plasma polymerization has conventionally been used for the deposition of thin films for applications ranging from bio-functional materials [113, 360] to water purifying agents [129, 131]. Plasma polymers (PP) in the form of nanoparticles, however, can also be produced by careful choice of the operational parameters, including the precursor gas pressure inside the reaction chamber and plasma input power [361]. For example, in a capacitively coupled radio frequency discharge of ethylene, low gas pressures and high power-to-gas flow rate ratios favour the formation of highly amorphous and relatively dense polymeric powders [362]. Whilst plasma polymerized nanoparticles (PPNs) were initially considered as undesirable by-products which reduce the quality of PP films, they hold an unprecedented potential to solve a wide range of challenges in the fields mentioned above.

We have recently shown that plasma polymerized nanoparticles synthesized from precursor gas mixtures of acetylene, argon and nitrogen are excellent platforms for simple, reagent-free, and one-step immobilisation of multifunctional cargo [123]. Argon's metastable excited states add crucial energy to the plasma discharge, aiding in breaking up monomers, generating radicals, and enhancing surface reactivity, while its inertness ensures stability and facilitates plasma discharge. The tunability of the plasma polymerization process enables precise modulation of the surface properties of the nanoparticles such as chemistry, charge, and hydrophobicity. The adjustable, pH-dependent surface charge of these nanoparticles permits control of the density and orientation of surface-attached

biomolecules by modifying the electrostatic interactions in the immobilization solution, as we have recently shown for radical-rich plasma polymers in the form of coatings [339].

The controlled synthesis of PPNs offers a technology platform that can provide fully organic nanoparticles with tuneable surface functional groups, suitable for a wide range of biomedical applications. One example is the work of Pleskunov et al. that showed the efficacy of the plasma polymerization process in the production of polymeric nanoparticles from acrylic acid precursor monomers[122]. The particles synthesized with functionalized coatings are particularly attractive for stable aqueous dispersions aimed at overcoming the major concern of acidification and its damaging effects on cells, as well as supporting biomolecular immobilization. Despite the versatility and potential applications of PPNs, a critical challenge that can limit their scaled-up application is to effectively collect them within low-pressure plasma polymerization chambers and minimize their loss into vacuum systems.

Plasma dust, or particles suspended in a plasma, have been typically collected in vacuum chambers either from the plasma volume [363] or after their deposition on a solid surface [364]. The collection relies on dragging the particles out of the plasma discharge towards the targeted boundaries of the deposition chamber by manipulating the forces acting on them [365]. During their growth process, nanoparticles in a plasma are generally subjected to an electrostatic force due to their negative charge as well as gravitational, thermophoretic, neutral drag, and ion drag forces [366]. When the dominant electrostatic force is overcome by oppositely directed forces, the equilibrium that suspends the particles in the discharge is broken and the particles drift out of the plasma allowing their collection. Hence, particle extraction and trapping strategies require external manipulation of electric fields [367, 368], temperature gradients [369], or neutral drag forces. For example, the sudden application of a pressure gradient to a dusty Ar/C_2H_2 plasma was used as a strategy to collect the nanoparticles formed [370]. However, such collection methods usually entail design complexity, require specific fittings such as high-cost vacuum feedthroughs, and result in the unsought modification of nanoparticles, making them unsuitable for the intended subsequent use, particularly for biomedical applications.

Here, we present a facile strategy to dramatically increase the collection of PPNs without the limitations of traditional collection methods and with minimal particle loss. We show that by simply delaying the inflow of the hydrocarbon gas (in this case acetylene) into an argon and nitrogen plasma discharge, the collection yield of PPNs arriving on a cell culture well plate increases dramatically compared to the usual protocol where all gasses are injected together before the application of the power that creates the plasma. We shed light on the mechanisms governing this discovery using a combination of plasma diagnostics and finite element simulations. We characterized the morphology and surface properties of the particles to ensure their desired physical and chemical properties remained unchanged. We also show the facile conjugation of fluorescent proteins in a single, reagent-free step that preserves their function upon attachment to the nanoparticles. Further, the potential cytocompatibility of the nanoparticles was evaluated *in vitro* via lactate dehydrogenase (LDH), cell proliferation and morphology. The non-invasive strategy, requiring no further equipment, introduced in this paper allows for an enhanced collection of PPNs with important implications for the high throughput commercial production of biofunctional nanoparticles.

3.2. Materials and methods

3.2.1. Plasma polymerization strategies

PPNs were synthesized in a stainless-steel chamber as explained in Section 2.2 and depicted in Figure 11. The production of the PPNs was carried out using one of two strategies: simultaneous or delayed inflow of acetylene. In the case of the simultaneous inflow protocol, argon, nitrogen and acetylene gases were pumped into the chamber and the starting pressure was achieved. A plasma discharge was then maintained after reaching an equilibrium state for a polymerization duration of 5 minutes. For the delayed inflow of acetylene, we initially introduced only argon and nitrogen gases into the chamber at the base pressure. After reaching the starting pressure, the discharge was ignited for 90 seconds before acetylene gas was introduced into the reactor. This delay ensured a sufficient time window for the argon/nitrogen plasma to reach an equilibrium state and the acetylene inflow to the chamber to be manually initiated. The plasma discharge of the three gases was then maintained for 5 more minutes. An RF input power of 100 W was used for the plasma polymerization of all samples. Compared to our previous works [123, 363], in this work, we introduced an oxygen cleaning protocol between runs to ensure the starting conditions were reproducible. The oxygen cleaning process carried out between polymerisation runs used a flow of 50 sccm oxygen, a starting pressure of 150 mTorr and an RF input power of 100 W for 30 minutes.

3.2.2. Hydrodynamic size and pH-dependent zeta potential measurements

The size and zeta potential measurements were taken by suspending PPNs in pH buffer solutions prepared using buffers of acids/bases at 5 mM with ionic strength IS = 10 mM and titrations to adjust to the required pH. The specifications of each buffer solution are documented below in Table . For each solution, the primary buffer mass was dissolved in approximately 900 ml of pure water. NaCl salt was added to the solution, followed by titration to the desired pH at 25 °C using a monovalent strong acid or base. The solution was then diluted to a final volume of 1000 ml with pure water. Absorbance at 405 nm excitation light was measured using a ELx800 Biotek plate reader, yielding a value of 0.5 ± 0.05 with Milli-Q water as the control. The nanoparticles were then transferred to disposable folded capillary cells under sterile conditions using 1 mL syringes.

Zeta potential values were obtained from at least three measurements with every pH solution, whereby the nanoparticles were collected from each of three independent runs following each protocol. The averaged values were reported as the zeta potential for a specific pH, with standard deviations on the zeta potential and pH values accounting for the error bars. The hydrodynamic size measurements were conducted on nanoparticles resuspended as above, except in Milli-Q water at pH 5 and the average of three measurements was obtained from at least three independent runs.

Table 4. Composition of pH buffers with corresponding buffer type, buffer mass, and salt mass. Mr: molecular weight.

pH	***Buffer***	***Buffer mass (g)***	***Salt mass (g)***
2	Phosphoric acid (Mr = 98)	0.49	0.456
3	Citric acid, monohydrate (Mr = 210.1)	1.05	0. 454
4	Acetic acid (Mr = 60.05)	0.3	0.538
5	Acetic acid (Mr = 60.05)	0.3	0.392
6	MES free acid (Mr = 195.2)	0.976	0.466
7	NaH_2PO_4 (Mr = 120)	0.6	0.021
9	Tris base (Mr = 121.14)	0.605	0.552
10	CAPS free acid (Mr = 221.3)	1.106	0.51
11	Methylamine (Mr = 31.1)	0.156	0.2

3.2.3. X-ray photoelectron spectroscopy (XPS)

The surface chemical composition of the PPNs was investigated by XPS using a SPECS FlexMod spectrometer. For these measurements, silicon wafers (8 x 8 mm) were washed with ethanol and acetone and placed in wells of the collector plate prior to the polymerization process. The nanoparticle samples collected on the wafers were then mounted on the XPS sample holder using conductive carbon tape. The instrument was equipped with a monochromatic X-ray source (Al Kα, hv = 1486.7 eV) operating at 10 kV, 20 mA. Survey spectra of the samples were acquired at a fixed take-off angle of 90°, and the measurements were conducted at base pressures below 5.0×10^{-8} mbar. Survey spectra were used for elemental composition calculations, which were conducted using *Avantage* software (version 5.9902). The emitted photoelectrons were detected by a multi-channel electron detector MCD9 at a pass energy of 30 eV and a resolution of 0.5 eV, while the high-resolution C 1s spectra were recorded at a pass energy of 50 eV and a resolution of 0.1 eV. The spectra were charge-corrected with reference to the binding energy of aliphatic carbon (284.6 eV). The electron energy was analysed using a hemispherical analyzer (PHOIBOS 150) and the C 1s higher resolution spectra were curve fitted using a Voigt function, a convolution of a Gaussian function (wG for FWHM) and a Lorentzian function using *OriginLab 2021.*

3.2.4. Transmission Electron Microscopy

The Transmission Electron Microscopy (TEM) of the PPNs was conducted with a 200 kV JEOL-2100 to investigate the size, morphology and structural evolution of the nanoparticles synthesized under different conditions. For the TEM specimen preparation, the PPNs were scraped off from the well wall with a tweezer onto a 3 × 3 mm copper grid (covered with a carbon lacy support film). The bright-field TEM images of the PPNs were taken from the film areas where the particles were loosely distributed.

3.2.5. Measurement of particle collection yield

To measure the yield, we suspended the nanoparticles into MilliQ water. The absorbance was measured in a Biotek ELx800 microplate reader with a wavelength of 450 nm. The samples were subject to laser light scattering (NanoSight NS300). For each measurement, samples were injected into the system at a constant flow rate and temperature (25 °C). The video tracking and analysis software (*NanoSight NTA 3.0*) was used to visualize the PPNs and obtain concentration distribution curves from the statistical analysis of three independent measurements. The average concentration was hence used to obtain a calibration curve of the absorbance as a function of the concentration of the PPNs. This curve was then referred to in subsequent experiments to convert a measurement of the particles' absorbance into the concentration (particles/mL) in the well. Normalizing the number of particles found by the total projected surface area gave the total yield per unit collection area of the well plates.

3.2.6. rGFP Conjugation and flow nanometry measurements

Various masses of recombinant Green Fluorescent Protein (rGFP, Roche, Truganina, Victoria) were resuspended in 100 μL MilliQ double distilled water and incubated at room temperature with 100,000 PPN in a 1.5 mL microcentrifuge tube for 30 minutes. PPNs were washed with 1 mL MilliQ double distilled water and centrifuged at 13,200 rpm in a benchtop centrifuge. The supernatant was removed and the pelleted PPNs were resuspended in 200 μL of buffer containing PBS and 0.1% (w/v) bovine serum albumin. Resuspended PPN were added to flow cytometry tubes and flow nanometry was

performed using a Beckman Coulter Gallios cytometer. Machine settings were altered to decrease the size threshold allowing for detection of the PPN. The fluorescent signal from rGFP immobilised on PPN was detected in fluorescent channel 1 (FL1). Data was analysed using the FlowJo software package (Treestar, Ashland, OR, USA).

3.2.7. Cytotoxicity assay

Human dermal fibroblasts (GM3348) were seeded at 2×10^2 cells per well of a 96 well plate (Greiner bio-one) 24 hours prior to nanoparticle exposure, in 100 μL DMEM with 10% fetal bovine serum (FBS). Nanoparticles fabricated using both the simultaneous and delayed strategies were suspended in sterile PBS and adjusted to a concentration of 4×10^{10} nanoparticles/mL. The nanoparticle suspensions were exposed to UV in a Class II biosafety cabinet for 30 minutes immediately prior to use. Nanoparticle solutions were serially diluted 1 in 100 to produce 5x stock concentrations ranging from 4×10^2 - 4×10^{10} nanoparticles/mL. Immediately prior to inoculation of the cells with nanoparticles, 50 μL of media was removed from each well and replaced with 50 μL of media with 15% FBS. Nanoparticles were added in triplicate for each concentration, 25 μL per well, with control wells receiving 25 μL of PBS or all media being replaced with 1% FBS in DMEM for proliferation negative controls only. The final concentrations were 1×10^9, 1×10^7, 1×10^5, 1×10^3 and 1×10^1 nanoparticles per well. All assays were run at 3 and 7 days post-inoculation with nanoparticles. Cytotoxicity was assessed using 50 μL of media from each well with the Cyquant LDH assay (ThermoFisher Scientific) as per kit instructions. Absorbance was measured on a UV/VIS/Fluorescence plate reader (Tecan, Infinite M1000) at 490 nm with background reference at 680 nm. In addition, the Cyquant proliferation assay (ThermoFisher Scientific) was used to determine if the nanoparticles inhibited proliferation as per the manufacturer's instructions for adherent cells and fluorescence intensity was measured with excitation at 485 nm and emission at 530 nm. Lastly, the cells used for the LDH assay were fixed with 4% neutral buffered formaldehyde for 10 minutes at room temperature. Fixed cells were rinsed twice with PBS and stained with ActinRed and NucBlue (Invitrogen) for 15 minutes at room temperature. Cell morphology was visually assessed at 3 and 7 days for any notable differences in cell morphology and nuclei size.

3.2.8. Statistical analysis

The data is expressed as mean ± standard deviation, unless otherwise specified, and analyzed with OriginLab software (version 2021b) or Excel. Differences between the particles produced by the Simultaneous and Delayed strategies were analyzed using a two-sample Student's t-test assuming equal variance to calculate statistical significance. Statistical analysis of the cell culture data was conducted in Prism (version 9.3, Graphpad) using 2-way ANOVA with a Dunnett *post-hoc* test, with all comparisons relative to either 3 or 7-day positive controls. Statistical significance is indicated in figures as $*P \leq 0.05$, $** P \leq 0.01$, $*** P \leq 0.001$, and highly significant if $**** P \leq 0.0001$.

3.2.9. Computational modelling procedures

3.2.9.1. Computational fluid dynamics modelling of reactor flow field

A numerical model of the fluid flow in the plasma reactor was built to better understand the hydrodynamic forces acting on the nanoparticles during their growth and deposition phases at different operating (particle formation) pressures. Given the low-pressure regime, the Knudsen number was calculated using Eq. 1 to assess the flow rarefaction regime [371]. Here λ is the mean free path of the gas molecules, k_B is Boltzmann's constant, T is the gas temperature (assumed to be 300 K in a non-thermal ccrf plasma), d is the kinetic diameter of the gas molecule (in this case 340

pm for argon [372]), p is the gas pressure (81 mTorr), and L is the characteristic length of the system (RF electrode-lid spacing, 89 mm). The mean free path and Knudsen number were found to be 601 μm and 0.007, respectively, confirming the continuum flow regime for the bulk fluid flow.

$$Kn = \frac{\lambda}{L} = \frac{k_B T}{\sqrt{2}\pi d^2 p L} \quad \text{(Eq.1)}$$

The $Ar/N_2/C_2H_2$ gas mixture was modelled as steady-state, laminar, fully compressible flow using the continuity and Navier-Stokes equations (Eq. 2 and Eq 3) [373]. Here p is the fluid pressure, ρ is the fluid density, $\boldsymbol{u}$ is the fluid velocity, μ is the dynamic viscosity, and $\boldsymbol{I}$ is the identitiy matrix. The simulations were carried out in *COMSOL Multiphysics 5.5* using a 2D axisymmetric computational domain. The reactor geometry consisted of a 105 mm chamber radius, 350 mm chamber height, 62.5 mm RF electrode radius, 15 mm RF electrode thickness, 80 mm substrate holder radius, and 3 mm substrate holder thickness. The RF electrode was located 89 mm below the lid of the reactor, and the substrate holder 97 mm below the RF electrode.

$$\nabla \cdot (\rho \boldsymbol{u}) = 0 \quad \text{(Eq.2)}$$

$$\rho(\boldsymbol{u} \cdot \nabla \boldsymbol{u}) = -\nabla p + \nabla \cdot (\mu(\nabla \boldsymbol{u} + (\nabla \boldsymbol{u})^T) - \frac{2}{3}\mu(\nabla \cdot \boldsymbol{u})\boldsymbol{I}) \quad \text{(Eq.3)}$$

The fourteen 1 mm diameter inlet orifices in the gas shower of the reactor were represented numerically as a single 1 mm slit annulus located 16 mm below the reactor lid adjacent to the wall. A normal mass flow boundary condition was applied here as per Eq. 4, where r is the radius at the inlet position and $\dot{m}$ is the prescribed mass flow rate calculated using a weighted average density and viscosity of each component gas.

$$-\int_{\partial\Omega} \rho(\boldsymbol{u} \cdot \mathbf{n}) 2\pi r \, dS = \dot{m} \quad \text{(Eq.4)}$$

The outlet boundary condition was set as a constant gauge pressure of 0 Pa and all remaining walls were set as no-slip boundaries ($\boldsymbol{u} = 0$). The model was run with a chamber operating pressure of 81 mTorr and 132 mTorr, the values to which the pressure equilibrates while the discharge is running in the simultaneous and delayed nanoparticle production strategies, respectively. The well-plate was not included in the modelling for simplicity. A sample modelling result overlayed onto the geometrical sketch of the chamber can be seen in Figure 12 below.

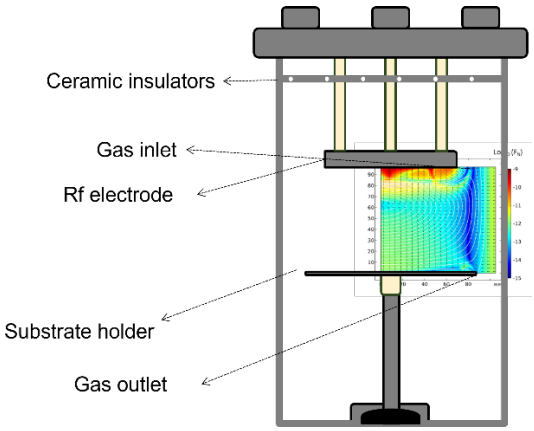

Figure 12. A sample modelling output overlayed onto the geometrical sketch of the chamber specifying the gas inlet, outlet, and electrodes.

3.2.9.2. Force balance on nanoparticles during growth and deposition

The gravitational ($\boldsymbol{F}_g$), electrostatic ($\boldsymbol{F}_e$), and ion drag ($\boldsymbol{F}_i$) forces acting on the nanoparticles throughout the reactor were estimated to understand the overall net force ($\boldsymbol{F}_N$) acting on them at any given point in the reactor ($\boldsymbol{F}_N = \boldsymbol{F}_g + \boldsymbol{F}_e + \boldsymbol{F}_i$). This was used to qualitatively inform the interpretation of observed particle deposition patterns in the reactor, assuming the thermophoretic force is similar in the delayed and simultaneous cases.

The gravitational force is given by Eq. 5, and is effectively invariant with pressure across the range investigated, considering the fluid density (ρ_f) is negligible compared to the particle bulk density (ρ_p).

$$\boldsymbol{F}_g = \frac{m_p \boldsymbol{g}(\rho_p - \rho_f)}{\rho_p} \quad \text{(Eq.5)}$$

The electrostatic force ($\boldsymbol{F}_e$) acting on a nanoparticle in the discharge was calculated using Equation 6, where q_p is the particle charge and $\boldsymbol{E}$ is the local electric field [374, 375]. The Debye radius (λ_D) was estimated using Eq. 7 [376], whilst the floating potential (ϕ_p) and particle charge were calculated using OML theory (Eq. 8 and 9)[377]. The ratio of ion density (n_i) to electron density (n_e) was assumed constant and used to estimate n_i, whilst the ion temperature was assumed to be 0.03 eV[378]. The electron density, electric field, electron temperature (T_e), and ion drift velocity values were estimated based on experimental data and results from a 2D axisymmetric, time-periodic steady state, capacitively coupled radiofrequency (CCRF) argon plasma model built in *COMSOL Multiphysics 5.5*. The continuum plasma model applies the drift-diffusion approximation along with Poisson's equation and a heavy species multicomponent diffusion model to self-consistently simulate a weakly-ionised plasma discharge [379-384]

$$\boldsymbol{F}_e = q_p \boldsymbol{E} \quad \text{(Eq.6)}$$

$$\lambda_D = \sqrt{\frac{k_B T_e}{4\pi n_e e^2}} \quad \text{(Eq.7)}$$

$$\phi_p = \frac{k_B T_e}{e} \ln\left(\frac{n_i}{n_e}\left(\frac{m_e T_e}{m_i T_i}\right)^{1/2}\right) \quad \text{(Eq.8)}$$

$$q_p = 4\pi\epsilon_0 r_p \phi_p \quad \text{(Eq.9)}$$

The ion drag force ($\boldsymbol{F}_i$) was estimated using Eq. 10 [377, 385] where v_s is the mean speed of the ions approaching the particle [374], b_c and $b_{\pi/2}$are impact parameters given by Eq. 11 and 12, Γ is the coulomb logarithm (Eq. 13), and $q_i = Z_i e$ is the ion charge [375, 377, 385]

$$\boldsymbol{F}_i = n_i m_i \boldsymbol{u}_i v_s \pi (b_c^2 + 4 b_{\pi/2} \Gamma) \quad \text{(Eq.10)}$$

$$b_c = r_p \sqrt{1 - \frac{2 q_i \phi_f}{m_i v_s^2}} \quad \text{(Eq.11)}$$

$$b_{\pi/2} = e q_p / m_i v_s^2 \quad \text{(Eq.12)}$$

$$\Gamma = \frac{1}{2}\ln\left(\frac{\lambda_D^2 + b_{\pi/2}^2}{b_c^2 + b_{\pi/2}^2}\right) \quad \text{(Eq.13)}$$

3.3. Results & Discussion

3.3.1. Collection of plasma polymerized nanoparticles in well-plates

We produced plasma polymerized nanoparticles from a mixture of argon, nitrogen and acetylene following one of two strategies: simultaneous or delayed insertion of the polymerizable gas, i.e., acetylene. The former entailed the introduction of all three gases together; whereas in the latter strategy, acetylene was delayed for 90 seconds allowing a nitrogen and argon discharge to reach a steady-state prior to its insertion. The nanoparticles were collected in a commercial polystyrene 24 well-plate placed on a substrate holder below the RF electrode. The strategy with simultaneous inflow of acetylene with the other gases into the vacuum chamber resulted in a pattern of brown dust-like powder deposited inside the wells, around the 24-well plate, on the substrate holder and the chamber walls. As observed in **Figure *13***a, the nanoparticles were collected predominantly in the centre of the well-plate with a lower concentration towards the edges, showing a minimal presence around the peripheral wells.

We explain this distribution pattern based on the effects of size-dependent forces on the nanoparticles as they grow in the plasma volume and move towards the substrate holder. The forces that drag the particles out of the plasma volume are the neutral drag force F_n (proportional to r^2), the ion drag force F_i (proportional to r^2), the thermophoretic force F_t (proportional to r^2) and the gravitational force F_g (proportional to r^3), where r is the particle radius [386]. The negative charging of the particles during their growth causes their confinement in the more positive plasma potential [366] until such time that the outward-directed forces overcome the inward-directed electrostatic force. The electrostatic force, F_e (proportional to r), dominates throughout the growth phase and levitates the particles in a ring or dust cloud that expands as the particle size increases. A sheath forming around the substrate holder [387], creates an electric field within it directed towards the well surfaces and intersecting them along the surface normal direction. The field strength is proportional to the inverse of the sheath thickness, which is reduced at the sharp edges of the wells, resulting in maximum local electric field strength in these locations. These enhanced fields around the edges of the wells create an "electrostatic lens effect" [363], causing the particles to be deflected into the wells by localized electrostatic forces schematically shown in **Figure 13**b. If the wells are sufficiently large and the sheath thin enough to allow the plasma to penetrate them, the particles will continue to grow inside the wells, moving downward as they do and approaching the bottom of the collector. In the case of the 24-well plate, the spacing between the edges of the well is greater than the thickness of the two sheaths at opposing walls. Hence, the plasma and the particles are able to penetrate the wells.

To direct the flow of the particles into the wells, we seek to reduce their drift into the neutral gas stream. We hypothesize that, for a constant power input and constant starting pressure, delaying the inflow of the hydrocarbon gas allows for an increase in the partial pressures of initially present argon and nitrogen and an enhanced density of their ions in the plasma formed, relative to a strategy where all three gases are inlet together. This would result in an increase in the fragmentation of subsequently injected acetylene that occurs as it is being introduced, resulting in a reduced overall pressure drop from acetylene consumption. To verify this hypothesis, we delayed the inflow of acetylene after maintaining a nitrogen and argon discharge for 90 seconds. **Figure *13***c shows images of the PPN distribution on the well-plates in the case of simultaneous $Ar/N_2/C_2H_2$ plasma discharge (left) and in

the Ar/N_2 plasma with delayed C_2H_2 inflow (right). This delay in acetylene inflow resulted in a significantly different spatial distribution of the nanoparticles as can be seen in **Figure *13***c. The pattern of collection was closer to a uniform deposition of thicker layers of the nanoparticles. The peripheral wells had a more darkened collection pattern than the central wells, while the substrate holder showed little, if any, particles accumulated. This indicated a higher particle concentration in peripheral wells and an overall bolstered process yield verified by the following yield measurements.

A confirmation of the higher number of particles gathered in the peripheral wells of the collector following the delayed C_2H_2 inflow was achieved by measuring the corresponding yields. Particles were collected from the well-plate by dispersing them into Milli-Q water and pipetting them to a sterile absorbance plate reader. The yield of the peripheral and central wells indicated in **Figure *13***a were measured from and represented by wells D3 and C3, respectively. As shown in **Figure *13***d, the yield in the peripheral wells (D3) was twice as high as that in the central region with the delayed acetylene inflow. In contrast, central wells (C3) had a yield of over three times that of the wells in the peripheral region, in the case of the simultaneous inflow of all three gases. The total yield from the 24 wells was greater by a factor of 2.5 in the case of delayed acetylene inflow compared to that with simultaneous inflow, as shown in **Figure *13***e.

The percentage of particles collected in the well plate can be estimated using the mass of collected particles and the mass of organic gas, i.e., acetylene, introduced into the chamber. The details of these calculations are given in the supplementary information (S1 in [124]), and the estimated collection efficiency percentages were in the range of 70-88% and 27-37% for the delayed and simultaneous strategies, respectively. Together, these results indicate that modulating the flow of the carbon-containing polymerizing gas is an effective strategy to significantly increase the nanoparticle collection yield and, importantly, reduce the loss of nanoparticles to the vacuum chamber peripheries.

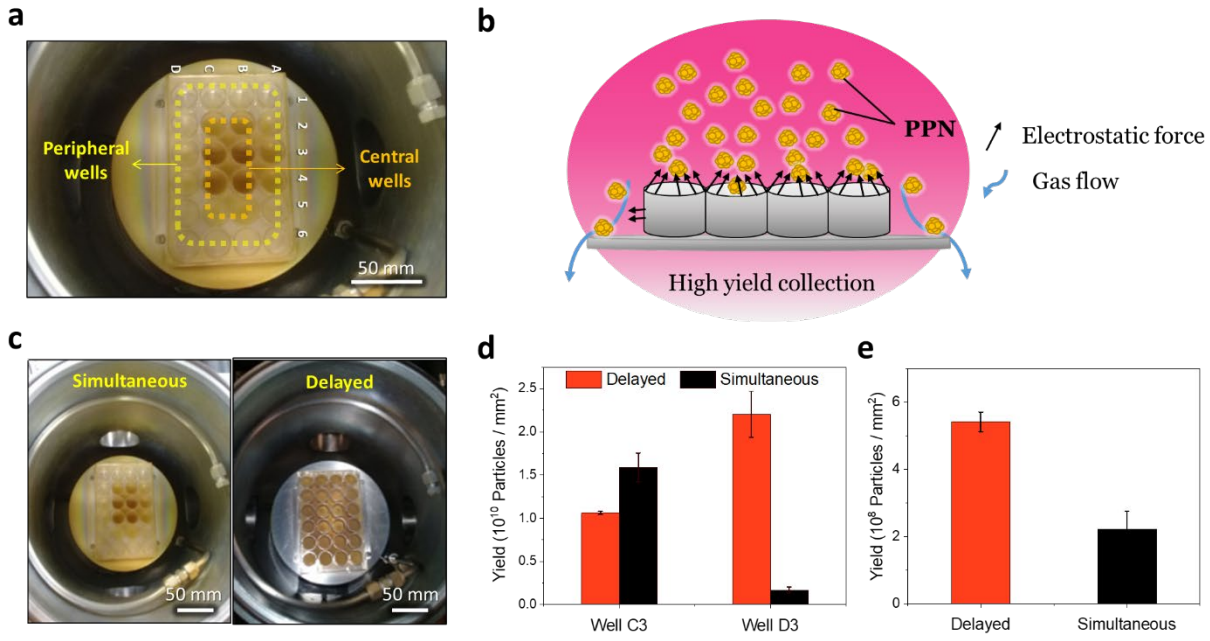

Figure 13. (a) Nanoparticle distribution pattern under plasma polymerization from a discharge in a mixture of argon, nitrogen and acetylene gases introduced to the vacuum chamber simultaneously. The dotted lines delineate the peripheral and central wells in a standard 24-well cell culture plate. (b) A sketch of the nanoparticle collection in a well plate geometry under the focusing effect of the electric field $\boldsymbol{F_e}$ arising from the reduced sheath thickness at the edges of the wells. The black arrows represent the electrostatic forces on the negatively charged plasma polymerized nanoparticles. (c) The nanoparticle distribution pattern in the

case of simultaneous Ar/N_2/C_2H_2 plasma (left) and the Ar/N_2 plasma with delayed C_2H_2 inflow (right). (d) The yield of plasma polymerized nanoparticles collected from central (C3) and peripheral (D3) wells as indicated in ***Figure 13****a. (e) The PPN yield collected from all the 24 wells in the case of simultaneous Ar/N_2/C_2H_2 plasma discharge and in the Ar/N_2 plasma with delayed C_2H_2 inflow.*

3.3.2. Monitoring nanoparticle growth mechanism

Information on the evolution of PPNs during their growth and collection provides useful knowledge underpinning their collection yield and pattern. To gather this information, we collected time-resolved optical emission spectra for PPNs fabricated using the delayed and simultaneous strategies. The relative intensities and shapes of the emission lines/bands depend on collisional and radiative mechanisms, which create a "spectral fingerprint" for each combination of plasma parameters. **Figure 14**a shows the optical emission spectra of excited species in the 385 - 395 nm wavelength range of the Ar/N_2 plasma prior to acetylene inflow and of the Ar/N_2/C_2H_2 plasma, 20 seconds after acetylene inflow. The zoomed-in spectral range was chosen to allow for the high resolution of the rotational-vibrational band-heads of nitrogen-based excited molecules and CN radicals. These radicals are significant in forming carbon-nitrogen hybrids in plasma-synthesized particles, making their detection during deposition essential for understanding various growth mechanisms. Before acetylene addition, bands attributable to N_2^+(0-0) and N_2(1-4) are present at 391.6 nm, and 394.4 nm, respectively. Upon the addition of acetylene gas into the plasma, bands corresponding to CN (2-2), CN (1-1), and CN (0-0) populations at 386.2 nm, 387.4 nm, and 388.5 nm, respectively, emerged. The primary molecular band originates from transitions within the CN violet system ($B^2\Sigma^+ \rightarrow X^2\Sigma^+$), spanning from 386 nm to 389 nm [388]. The most prominent band peak occurs precisely at 388.5 nm, resulting from transitions of electronically excited CN radicals in the υ=0 vibrational state (CN (0−0)). The second molecular band corresponds to rotational-vibrational transitions of N_2^+ molecular ions (0–0) from the first negative system ($B^2\Sigma^u \rightarrow X^2\Sigma^g$), ranging from 389 nm to 392 nm, with a peak centered at 391.6 nm. The third molecular band arises from transitions of excited neutral N_2 molecules (1–4) from the second positive system ($C^3\Pi^u \rightarrow B^3\Pi^g$), featuring a band peak centered at 394.4 nm. The identified plasma species displayed a dominant emission in the N_2 spectral window with a decrease in the intensity of N_2^+ after inflowing acetylene into the mixture. This significant decrease highlights the transition from ionized to non-ionized nitrogen as direct evidence of the input energy transfer to the fragmentation of acetylene molecules. This energy transfer is a key element for maintaining the fragmentation of C_2H_2. Throughout the N_2 plasma breakdown, the energy per species is accumulated before C_2H_2 is introduced, contributing to the formation of other species and their corresponding excited states. The CN radicals were only detected after acetylene inflow, revealing the role of carbon from the C_2H_2 monomer in initiating the growth of the particles. This growth process can be divided into three phases: Nucleation, Coagulation/Agglomeration, and Accretion [389]. During nucleation, successive chemical reactions occur in the gas phase fragmenting the background gas monomers into clusters of atomic or molecular species. The chemically bonded clusters grow by undergoing collisions and increasingly collect negative charges. This coagulation phase eventually terminates due to the mutual Coulomb repulsion of the charged clusters. Once each condensed particulate becomes electrostatically charged, a relatively slow collection of radicals and positive ions takes place, and the number density remains almost constant. Thus, monitoring the changes in the intensities of each species throughout the particle growth process is a viable approach to illuminate their mechanism of formation.

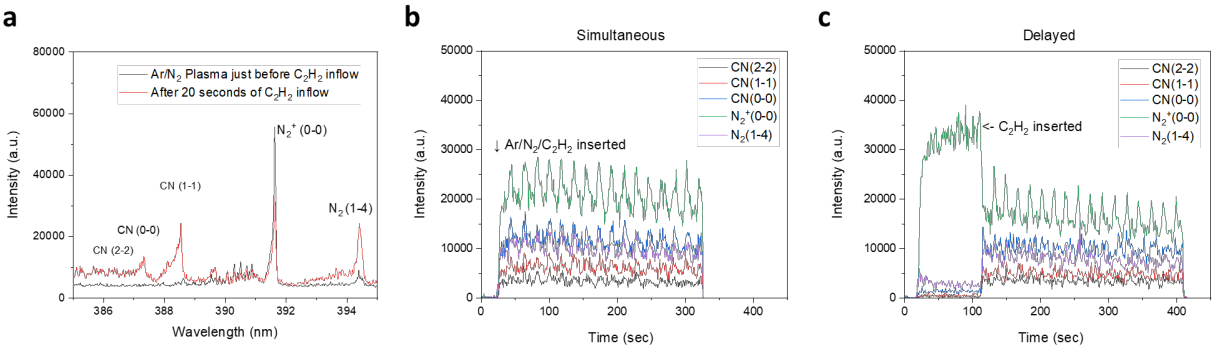

Figure 14. (a) Optical emission spectrum showing the 385-395nm wavelength range of excited species in the Ar/N_2 plasma compared with their intensities 20 seconds after acetylene inflow commenced. (b) The temporal evolution of the emission spectrum of nitrogenous species in an $Ar/N_2/C_2H_2$ plasma and (c) in an Ar/N_2 plasma with delayed C_2H_2 inflow. The instants of gas flows are indicated by arrows.

To illustrate the dynamics of the periodic particle growth cycles, we tracked the evolution of nitrogenous emission lines with time. **Figure 14**b and **Figure 14**c show the temporal evolution of the emission spectra of the chosen species in an $Ar/N_2/C_2H_2$ plasma and in an Ar/N_2 plasma with delayed C_2H_2 inflow. The delayed inflow of C_2H_2 induced a sharp decrease of N_2^+ ion emissions accompanied by an increase in N_2 emissions, suggesting a redistribution of energy. As energy is diverted to the decomposition of acetylene, the overall excitation level of the nitrogen gas is reduced, increasing the population of the lower energy N_2 excited state at the expense of the higher energy ionised state. The increase in the emission intensities of CN species indicates their production at the start of the nucleation phase of the particles. The periodic behaviour of the emission lines shows the correlation between the plasma species and the nanoparticle formation. These spectral oscillations can be attributed to the variation of electron temperature and density as electrons in the plasma are removed by the negative charging of the PPNs. These spectral oscillations correlate directly to the phases of the PPN growth cycle during polymerization in both strategies, i.e., in the presence of Ar, N_2 and C_2H_2, as the increase of the N_2^+ molecular ion intensity trends in phase with the increase of the other species at the beginning of each growth cycle. The radicals and N_2 molecules then decrease in emission intensity proportional to the decrease of N_2^+ ions in the second half-cycle. The spectral envelops of these species, measured at the same spectrometer settings, maintain their intensities and behaviour throughout the 5 minutes of polymerization in each case. Their period of oscillation is found to be about 16 seconds for both strategies, indicating that with the flow rate of the gases and the discharge conditions maintained constant, the growth process taking place in the two plasma strategies appears to be similar.

The relative intensities and shapes of the emission bands depend on collisional and radiative mechanisms, which create the "spectral fingerprint" for each combination of plasma parameters[390]. Before acetylene inflow, the dominant emission can be attributed to the band emission of the nitrogen ion from the first negative system $N_2 + (B^2\Sigma_u \rightarrow X^2\Sigma_g)$ (0–0). This result is in excellent agreement with the literature and suggests that the dominant direct excitation reaction for this plasma was produced through electron impact ionization [390]

$$e^- + N_2 \rightarrow (N_2^+)^* + 2e^- \qquad \text{(Eq.14).}$$

The subsequent radiative decay of excited nitrogen ions N_2^+ ($B^2\Sigma_u^+$, υ') → N_2^+ ($X^2\Sigma_g^+$, υ'') + hν releases the photon energy hν detected by our spectroscope [391]. Upon acetylene inflow, the intensity of nitrogen ion lines decreases as that of nitrogen molecule lines increases along with the emergence of CN lines. The radiative recombination reaction $e + N_2^+ \rightarrow N_2 + h\nu$ where hν is the is the energy of the released photon, indicates the energy transfer into the N_2 molecule. Due to the relatively high energy threshold for Eq.14 (E_{th} = 18.8 eV) high energy electrons become the main contributors to the production of molecular ions [392].

In plasma polymerization, pressure is a major discharge parameter that influences the clustering kinetics of the particle synthesis process [393, 394]. An increase in pressure reduces the mean free path of the species and induces an increase in the collision probability. To track the changes of pressure for the two strategies, we logged the change in pressure values with time inside the reactor. **Figure 15**a shows the evolution curve of the pressure inside the chamber throughout the plasma polymerization process resulting from the delayed and the simultaneous strategies. In the delayed strategy, the starting pressure of 150 mTorr increases for 30 seconds, in agreement with the fragmentation of only argon and nitrogen. Their energized plasma-generated products then allow the desorption of species sedimented inside the reactor into the gas phase. Initially, these reactions increase the pressure before it stabilizes with time. The subsequent introduction of acetylene induces a spike in pressure with the onset of acetylene fragmentation, followed by a sharp drop within 100 seconds, which shows that C_2H_2 is effectively consumed in plasma chemical reactions. The pressure reduction is followed by continuous fluctuations near the operating pressure of 132 mTorr until the polymerization process ends. In the case of simultaneous insertion of acetylene, however, an immediate drop in starting pressure takes place within 40 seconds of the plasma discharge and stable fluctuations are recorded around an operating pressure of 81 mTorr. When all the species were present, turning on the RF power led to their fragmentation and rapid consumption which was depicted by the instant pressure decrease. The pressure oscillations measured downstream are likely correlated to the periodic consumption of reactive acetylene fragments associated with the particle growth cycles in the OES spectra oscillations.

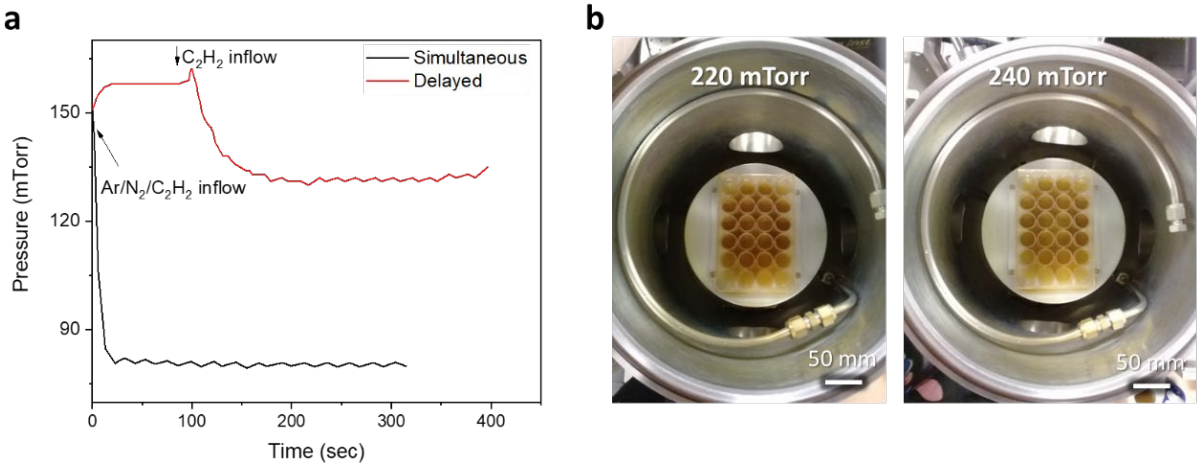

Figure 15. (a) The pressure variation in plasmas produced by both the Simultaneous and Delayed strategies over time. The delayed inflow of acetylene into the argon and nitrogen plasma is marked in the top curve at 90 seconds. The simultaneous flow of the three gases is also indicated at t=0 in the bottom curve. The drop in pressure can be noted with distinct fluctuations after reaching a stable value. (b) The PPN deposition patterns inside the collection cell culture plates after plasma polymerization with starting pressures of 220 mTorr and 240 mTorr.

In order to investigate the role of higher operating pressure in the delayed strategy, we attempted to

reach the same operating pressure by the simultaneous strategy initiated at higher starting pressures than 150 mTorr. **Figure 15**b shows two photos of the PPN deposition patterns after their formation in a plasma with starting pressures of 220 mTorr and 240 mTorr, respectively. The collection patterns in the well plates seem to be improved compared to the original simultaneous protocol starting at 150 mTorr and appear closer to that created by the delayed strategy. However, the starting pressure of 220 mTorr dropped immediately to an operating pressure of ~109 mTorr and 240 mTorr to ~118 mTorr. A starting pressure high enough to reach the operating pressure observed in the delayed strategy (132 mTorr) could not be achieved without manual adjustment of the pumping system valve after the acetylene inflow. In addition, the particle waste visible by their loss to the substrate holder, the walls and the base of the chamber was much higher for each of the higher pressures. Starting pressures of 260 mTorr and above in the simultaneous protocol produced aggregates which could not be dispersed. Hence, we limited our discussions to this maximum starting pressure. The operating pressure under these conditions (~119 mTorr) resulted in the creation of larger-sized aggregates having two size populations with an average hydrodynamic size of 1814.7 +/- 57 nm. Further details are shown in the supplementary information (Figures S1, S2, and S4 in [124]). Hence, increasing the pressure in the simultaneous protocol did not achieve the desired goals of increased well-plate collection yield of monodisperse nanoparticles with minimal losses to the chamber and pumping system.

3.3.3. Simulation of the flow field and estimation of the net forces

To further investigate the mechanism behind the observed particle deposition patterns, simulations within the reactor were carried out, along with estimations of the net forces experienced by the nanoparticles. The spatially varying net force acting on the PPNs, along with the electron density distribution in the reactor, was simulated at operating pressures of 81 mTorr (**Figure 16**a) and 132 mTorr (**Figure 16**b), representing the simultaneous and delayed gas inflow strategies, respectively. A similar trend was observed for the net force in both cases, starting from a region of high magnitude near the RF electrode and decreasing towards the reactor walls. The region of low net force can be seen closest to the reactor wall, between 80 and 100 mm from the origin of the axis. The steady-state fluid velocity throughout the discharge region at the operating pressures of 81 mTorr and 132 mTorr are plotted in **Figure 16**c and **Figure 16**d, respectively. The structure of the flow field is similar in both cases, with faster flow observed for the lower pressure case resulting in greater perturbation in the bulk plasma region. In both cases, the region of maximum electron density is located at the central axis of the reactor and 60 mm above the substrate holder (**Figure 16**a, **Figure 16**b). Due to the relatively high concentration of activated precursors, more nanoparticles are likely to be polymerized in the region of high electron density. In the simultaneous strategy, the forces on particles in this region are directed outwards from the central axis to the reactor wall, suggesting that large groups of PPNs will be driven into the fluid stagnation zones and entrained in the neutral gas flow towards the pump. However, in the delayed strategy, the net force on the PPNs formed below the RF electrode results in their downwards drift towards the collector plate within the first 40 mm from the central axis. This leads to the greater deposition of condensed particles in the collector plates, as observed for the delayed case.

As a result, the operating pressure of 132 mTorr becomes the key factor identified for achieving the improved collection yield of the PPNs, whilst maintaining minimal loss to the vacuum system. The delay of acetylene inflow has been demonstrated as an efficient strategy to achieve this operating pressure without risking damage to the vacuum system or increasing environmental waste. Regulation of this pressure could also be achieved by introducing a feedback control mechanism which implements valve adjustments to ensure the operating pressure stabilizes at 132 mTorr throughout the plasma polymerization process. However, the delayed inflow protocol is preferred

because it does not require additional feedback control instrumentation.

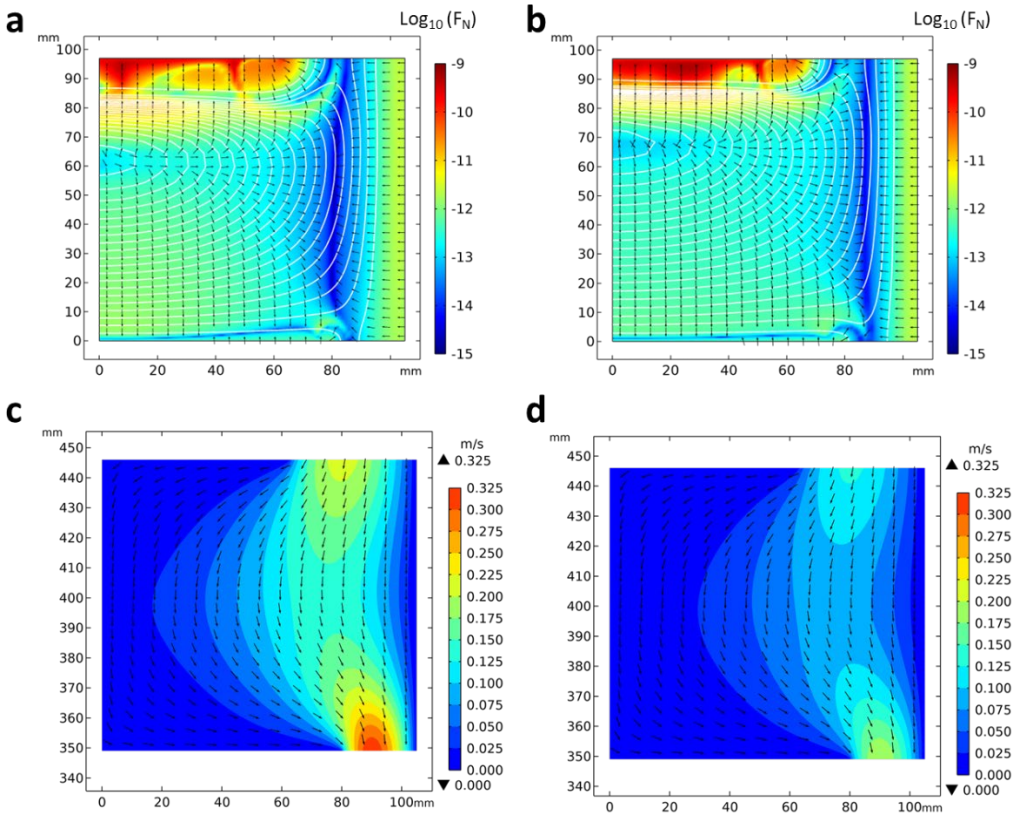

Figure 16. Calculated net force acting on the PPNs. Arrows represent normalised vectors indicating the direction of the net force, whilst the coloured surface represents the magnitude of the net force, FN, in Newtons (N), shown on a log10 scale. Electron density contours are overlaid in white for comparison. Results are shown for operating pressures of (a) 81 mTorr and (b) 132 mTorr, representing the simultaneous and delayed gas inflow strategies, respectively. (c) Steady state velocity contours for 81 mTorr and (d) 132 mTorr operating pressures respectively. Arrows represent normalised vectors indicating the direction of the particle velocity.

3.3.4. Physical and chemical properties of the plasma polymerized particles

We have shown that the delayed inflow of acetylene into an argon and nitrogen plasma has resulted in an increased yield of nanoparticle collection. However, the physical and chemical properties of the particles remain an integral factor that determines their utilization capabilities in various domains. In particular, the morphology, average size, size distribution, surface charge and surface chemistry are critical for applications in biomedicine as these properties can influence the function of particles.

3.3.5. Surface chemistry and zeta potential of PPNs

The surface chemistry of PPNs is an important characteristic playing a pivotal role in almost any surface interaction. To compare the surface chemistry of the particles generated using the two plasma strategies, we analysed the nanoparticles, collected on silicon wafer substrates, using XPS. **Figure 17**a shows the XPS survey spectra of nanoparticles synthesized in plasmas with and without the delayed inflow of acetylene. For both strategies, the spectra showed distinct signals of carbon, nitrogen, and oxygen with almost the same atomic concentrations of around 65%, 30% and 5%, respectively (**Figure 17**b). No silicon signal was detected, indicating that the silicon wafer

underneath the layer of nanoparticles was covered with layers of particles greater than the sensitivity depth of XPS, which is around 10 nm [104, 111, 395]. The origin of the oxygen content on the surface of the nanoparticles is suggested to be either from residual oxygen in the plasma chamber or from the exposure to atmosphere post plasma polymerization. Due to the relatively low base pressure (below $5x10^{-5}$ Torr), oxidation reactions that take place post-production are the more likely contributors to the presence of oxygen on the PPNs. Such oxidation of plasma polymers upon exposure to air is commonly referred to as autoxidation [341].

To further explore the effect of acetylene delay on the carbon composition of the particles, we curve-fitted the C 1s high-resolution spectra obtained for particles produced using simultaneous and delayed protocols as shown in **Figure 17**c. Three peaks associated with C–C/C–H at binding energy (BE) ≅ 284.6 eV and C–O/C–N at BE ≅ 286.5 eV, and C=O/N–C=O at BE ≅ 288.0 eV were fitted in the C 1s high-resolution spectra [340, 396]. In addition, we calculated the area percentage of the C 1s compounds plotted in **Figure 17**d. As observed, the C1s area percentage corresponding to each of the carbon bonds has not exhibited any shifts with the change in the PPN synthesis strategy. The N1s high resolution spectra can be found in the supplementary information (Figure S3). These results indicate that delaying the acetylene insertion had no significant effect on the nature and concentration of various elements and their bonding in the organic PPNs.

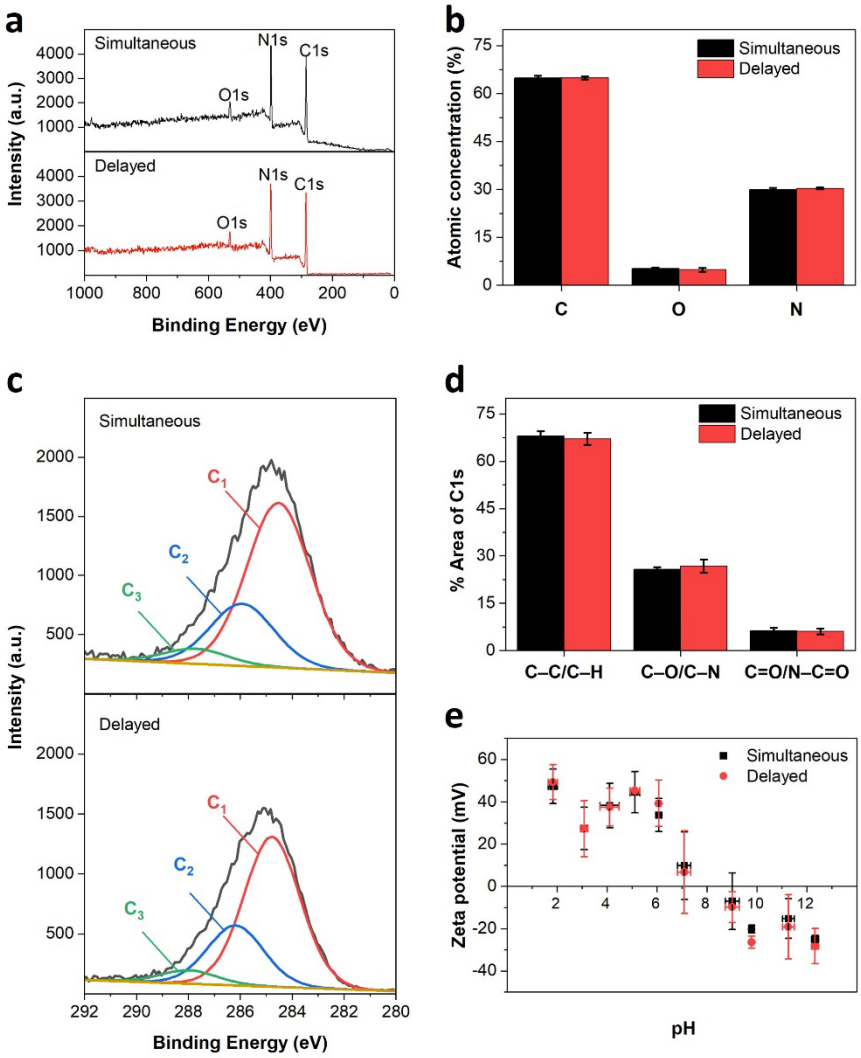

Figure 17. Characterization of the PPN surface chemistry. (a) X-ray photoelectron spectroscopy (XPS) survey spectrum showing the organic elemental composition of PPNs from the Simultaneous and Delayed strategies. (b) Curve-fitted C 1s high-resolution spectra of the PPNs with C_1: C–C/C–H, C_2: C–O/C–N, and C_3: C=O/N–C=O bonds identified. (c) XPS spectral analysis revealing the same elemental atomic concentration on the surfaces of nanoparticles synthesized in both plasmas. (d) The variation of zeta potential as a function of pH of the PPNs collected from both plasmas. The data indicates that both surfaces become negatively charged in solutions with pH above 8. Error bars are standard deviations of at least 3 measurements.

A known concern in small particles as nanocarriers is that they may aggregate in aqueous media, hampering their applications in biologically-relevant environments[397]. The surface charge is critical for dispersion in aqueous solutions as it can influence how particles are ingested into cells based on the charged groups present on the surface. Positively charged polymeric particles are up taken to a higher extent than the negatively charged anionic ones as cells are able to internalize and retain them for a longer time [398]. The colloidal stability of most nanoparticle suspensions is typically determined by their surface zeta potential (ζ). This stability is driven by electrostatic repulsion between charged particles. As the zeta potential depends on the interaction between the particle's surface and the dispersion medium, adjusting the solution pH varies the dissociation of the developed C, N, and O-containing charged moieties, and influences the zeta potential and isoelectric point (IEP). In **Figure 17**e, the zeta potential values are plotted against pH for PPNs obtained using

the delayed and simultaneous protocols. These data demonstrate that the zeta potentials decrease with pH from 49.3 ± 8 and 47.3 ± 8 mV at pH 1.8 to -28.3 ± 8 and -24.9± 2 mV at pH 12.3 for PPNs synthesized following a delayed and simultaneous protocol, respectively. To ensure a constant ionic strength in each measurement, each pH solution was prepared with a fixed buffer concentration of 5 mM and ionic strength of 10 mM. The PPN surface fluctuated between positive and negative surface charge around neutral pH, indicating that the isoelectric point (at which $\zeta = 0$ mV) is at pH $\simeq$ 7. The zeta potential becomes successively more positive below this pH value and successively more negative further above it. An increased rate of protonation reactions of nitrogen-containing groups at lower pH increases the zeta potential, while deprotonation of carboxyl and oxidized carbon groups at higher pH values lowers the zeta potential. As such, tuning the amounts of these surface functional groups by varying the parameters of particle production, such as the relative flow rates of acetylene and nitrogen, will shift the isoelectric point[123]. The high surface charges at either ends of the pH range depict suitable colloidal stability for nanoparticle suspensions from both synthesis protocols. Tuning pH of the solutions used to functionalise the nanoparticles can therefore be used to achieve stable dispersions as well as controlling the surface charge interactions with the functional moieties being immobilized. After functionalization, the zeta potential of the particles will vary according to the molecules immobilised.

3.3.6. Size distribution and surface morphology of PPNs

Particle size and morphology play an important role in cell-tracking, imaging, gene and drug-delivery system designs as they control the mechanism and rate of the cellular uptake of nanoparticles. Particle-cell adhesion and interaction, relevant to each particle size, influence the efficiency and pathway of cellular uptake and thus the particles' ability to permeate through tissue [399]**.** To study the morphological properties of PPNs after deposition, we used transmission electron microscopy (TEM). The TEM images taken allow visualisation of the morphology and dry size of a small sample of nanoparticles collected from D3 but cannot be considered as representative of the entire population. **Figure 18** shows TEM images of PPNs collected from well D3 of the collector plates generated using the (a) delayed and (b) simultaneous production strategies. The average size of the particles measured by TEM was 103 ± 18 nm and 91 ± 12.5 nm for the delayed and the simultaneous inflow of C_2H_2, respectively. Both images display solid, amorphous particles as expected from the similar growth cycles presented by the OES measurements (**Figure 14**). The PPNs attain their spherical structure and similar size during the agglomeration phase of their synthesis, in which cluster-cluster collisions and rapid growth take place, controlled by electrostatic interactions with surface-radicals.

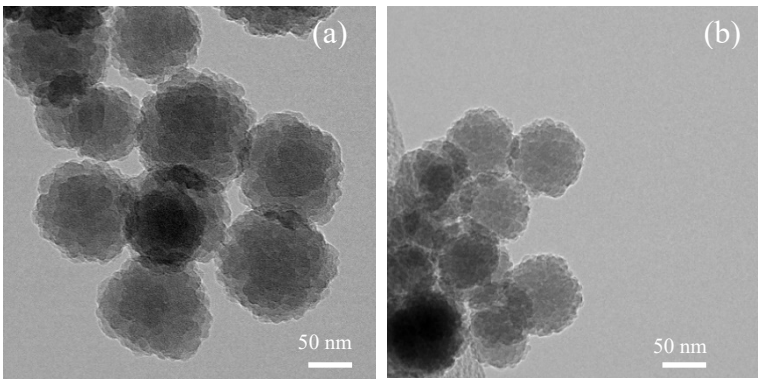

Figure 18. TEM images of the PPNs extracted from well D3 of the (a) delayed and (b) simultaneous acetylene inflow strategies. The images show the spherical morphology of the particles and their amorphous surfaces resulting from the aggregation of particles through their growth phase.

We next measured the hydrodynamic size of the particles collected from peripheral and central wells and produced in both plasma protocols using dynamic light scattering. **Figure 19**a compares the average hydrodynamic size of the particles collected in peripheral (D3) and central (C3) wells of the plates subjected to the two plasma protocols. The hydrodynamic size of PPNs following the delayed strategy was 155 ± 5 nm and 195 ± 2 nm in wells C3 and D3, respectively. Whereas in the simultaneous strategy, wells C3 and D3 collected particles of size 174 ± 1 nm and 178 ± 2 nm. As TEM measurements were conducted in a dry state, the increase in the diameter of particles can be attributed to the ionic double layer formed at the particle surface after resuspension in water. A t-test conducted for the hydrodynamic size measurements verified the statistical significance in particle size between particles collected in central and peripheral wells in the delayed acetylene plasma with a P value of 0.0081; whereas in the simultaneous protocol $Ar/N_2/C_2H_2$ plasma case, no statistical significance was found with a P value of 0.3639. These results suggest that the peripheral wells collected larger particles in the case of delayed acetylene inflow, whereas those of the simultaneous inflow collected similar sizes in both wells.

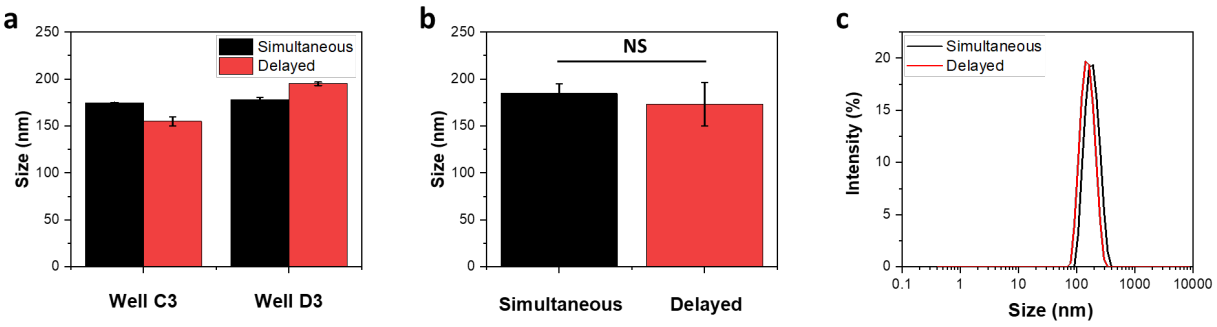

Figure 19. (a) The average hydrodynamic size of PPNs collected from peripheral and central wells taken from two Ar/N2/C2H2 plasmas with delayed and simultaneous acetylene inflow respectively. (b) The average hydrodynamic size of nanoparticles collected from all the wells taken from two Ar/N2/C2H2 plasmas with and without delay of C2H2 inflow. (c) Size distribution of the nanoparticles extracted from all the wells from both plasma synthesis strategies.

The variation in particle hydrodynamic size between wells C3 and D3 from the plasma with the delayed acetylene inflow could be related to nanoparticle segregation throughout their evolution. As

a result of the cyclic growth protocol, multiple generations of particles have been previously observed to grow in spatial succession [366]. The formation of new generations is induced inside the dust-free spaces in the core of the discharge volume, called the void [400]. This results in the simultaneous existence of different, each mono-sized, generations of particles inside the same discharge [401]. The dynamics behind this theory can be explained by the action of the global forces on the nanoparticles driving the larger particles toward the peripheral parts of the dust cloud. The smaller particles levitating in the inner part of the cloud and the larger ones in the outer parts, fall into the central and peripheral wells of the collector, respectively. However, a different situation is observed in the $Ar/N_2/C_2H_2$ plasma, which can be explained as originating from a strong electrostatic interaction between the different generations. Recalling that these particles are negatively charged (**Figure 13**b), new dust particles can be trapped in the plasma core as they become confined by a surrounding previous generation. Hence, the growth of the new generation into the same size as the older one takes place until equilibrium is broken near sheath regions and both generations fall into the well plates.

To obtain an average hydrodynamic size for the total number of particles collected, size measurements were conducted on an equivalent volume of particles taken from all the 24 wells. **Figure 19**b shows the average particle diameter from the well plates subjected to the two plasma strategies. The average hydrodynamic size of the particles collected from all the 24 wells as produced by the simultaneous and delayed strategies was 184.7 +/-10 nm and 173.3 +/- 23 nm, respectively. These values were obtained from at least 3 measurements of 3 independent samples. The two-tailed P value equals 0.4789 which, indicates that the difference is not statistically significant (NS). This lack of significant difference in nanoparticle size is further supported by the size distribution curves obtained for nanoparticles produced by both strategies, shown in **Figure 19**c. **Figure 19**c displays peaks of the hydrodynamic size distributions in both plasma synthesis strategies resulting in an average particle diameter of 170 – 200 nm. This range is particularly suitable for theragnostic applications in which nanoparticles with a hydrodynamic size of 10 – 200 nm can be deployed as drug carriers with tumour-targeting functionalities specific to cancerous sites [402, 403].

3.3.7. Biofunctionalization of PPNs and interactions with cells

3.3.7.1. rGFP conjugation and flow nanometry measurements

The advancement of nanoparticles in the biological field has often been hindered by the array of required wet-chemistry steps that significantly complicate immobilization processes [404]. In this work, the radical-rich PPNs facilitate the attachment of biomolecules and allow for their immobilization through a simple, single-step incubation at room temperature. The reagent-free conjugation in aqueous solution bypasses the intermediate chemical linkages and multiple purification approaches that often interfere with the efficiency of the functionalization. To demonstrate the efficacy of these PPNs in biomedical applications, we tested their ability to bind biomolecules onto their surfaces. We used recombinant Green Fluorescent Protein (rGFP), extracted from jellyfish *Aequorea victoria*, a biomolecule that exhibits bright green fluorescence when exposed to light in the blue to UV range. This all-round probe acts as a highly suitable model to validate reagent-free surface conjugation to the PPNs. GFP forms a beta barrel, cylinder-shaped tertiary structure which is essential for generating a fluorescent signal. Impairment of the beta-barrel tertiary structure can lead to reduced autofluorescence so GFP also serves to as a probe to determine whether conjugation to the PPN surface compromises native biomolecule conformation.

To validate the attachment of the protein on the PPN surfaces, we used flow nanometry as a novel nanoparticle fluorescence detection method. **Figure 20** shows the mean fluorescence intensity (MFI) of the PPNs obtained using the two plasma production strategies following the conjugation of 0, 5 and 10 picograms of rGFP per PPN. The MFI was calculated after 50,000 counts per condition. As expected, there was a proportional increase in mean fluorescence intensity with increasing r-GFP concentration, suggesting successful conjugation of the probe to the PPNs. A two-sample Student's T-test conducted on the MFIs of the PPN surfaces comparing values obtained for the two production strategies for each rGFP concentration revealed no significant difference, with *P* values greater than 0.1 (**Figure 20**). These results indicate that the PPN activated surfaces from both production strategies can attach a functional protein strongly whilst maintaining its native conformation. The delayed strategy maintained a highly activated surface suitable for conjugations of fluorescent agents. Additionally, the plasma polymerization technology introduced here provides a potential platform to create multifunctional nanoparticles decorated with combinations of various molecules, including therapeutic drugs, antibodies, imaging dyes, and diagnostic agents.

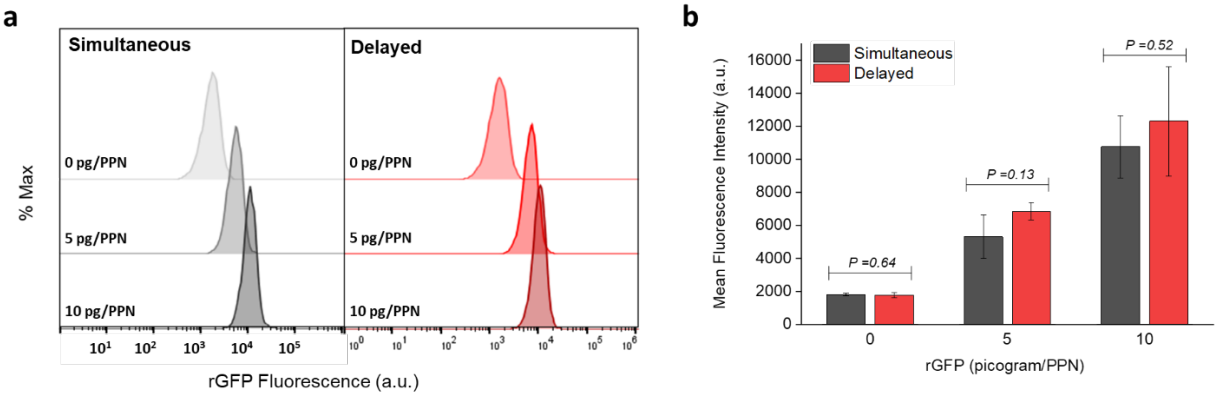

Figure 20. (a) Representative flow nanometric histogram plots of rGFP mean fluorescence intensity (MFI) in nanoparticles collected from the Simultaneous and Delayed strategies. (b) Column plot of the mean fluorescent intensities (MFIs) measured by the flow nanometer from the rGFP fluorescence. Two-sample Student's T test for each rGFP mass per PPN were conducted with P values indicating no statistical significance between Delayed and Simultaneous MFIs taken from three independent measurements on each PPN batch produced from Delayed and Simultaneous plasmas.

3.3.7.2. Cytotoxicity Assay

Cytotoxicity is a crucial factor to address when evaluating the potential of nanoparticles for medical purposes. We assessed the cytotoxicity of PPNs in Human dermal fibroblasts using Cyquant lactate dehydrogenase (LDH) proliferation assays. The assays were run at 3- and 7-days post-inoculation on concentrations of PPNs ranging between 1×10^1 and 1×10^9 nanoparticles per well to evaluate the % LDH release and fluorescence intensity, as shown in **Figure 21**. After 3 and 7 days of exposure to the PPNs obtained from either delayed or simultaneous protocol, the cells displayed a basal LDH release level which indicates that there was no evidence of plasma membrane damage in the cell population, as demonstrated in **Figure 21**A. This observation was supported by the absorbance measurements in **Figure 21**B which show that the cell proliferation after 7 days of exposure to increasing concentrations of PPNs was comparable to positive controls. The PPNs produced by both the simultaneous or delayed protocols were not cytotoxic nor did they affect the fibroblast proliferation after 7 days, as shown in **Figure 21**A and B, with nanoparticle to cell ratios of up to 5×10^5 nanoparticles per cell (at the time of cell seeding). There was a slight depression in cell proliferation at 3 days in response to the highest concentration tested; however, this was absent after 7 days (**Figure 21**B). We also evaluated the cell morphology and nuclei size for notable differences

after PPN exposure. Cell morphology was not affected by the presence of nanoparticles as evaluated by actin filament and nuclei staining shown in **Figure 22**. No cytotoxicity was observed for all nanoparticle concentrations. This is consistent with the results of previous cytotoxicity studies that showed that PPNs produced using the simultaneous protocol are cytocompatible and have no impact on cell proliferation [123, 135]. Our results show that the nanoparticles produced by the delayed strategy can not only be effectively collected and easily biofunctionalized but are also comparable in cytocompatibility to those produced with the simultaneous protocol. The facile collection, conjugation and safety of these particles uncover their excellent potential for an array of applications from imaging agents for disease diagnostics to cell-targeted drug delivery in therapeutic treatments.

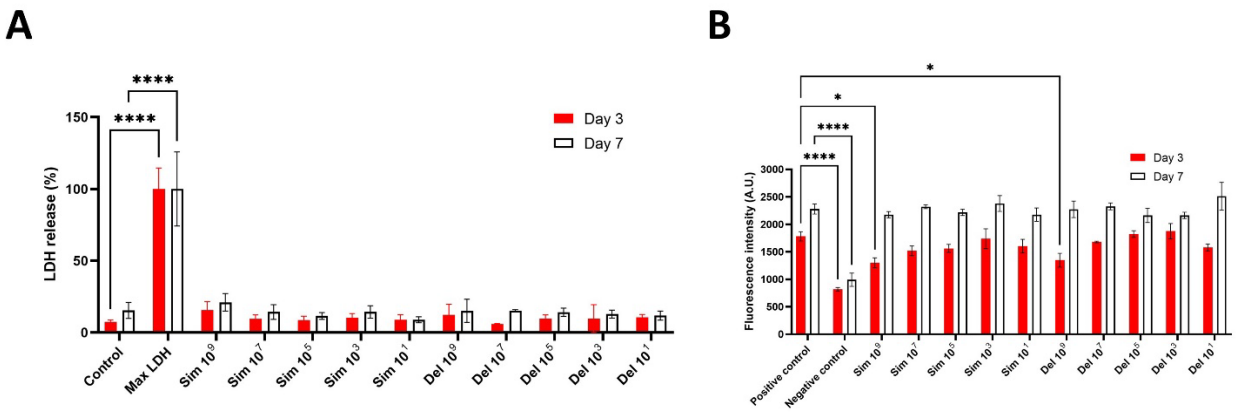

Figure 21. Nanoparticle cytotoxicity as measured by the (A) LDH release (B) proliferation after 3 and 7 days of exposure to increasing concentrations of PPNs. No cytotoxicity was observed for all nanoparticle concentrations and after 7 days cell proliferation was comparable to positive controls. The highest nanoparticle concentration for both simultaneous and delayed nanoparticles resulted in a non-significant depression of fibroblast proliferation at 3 days however this trend was not evident after 7 days.

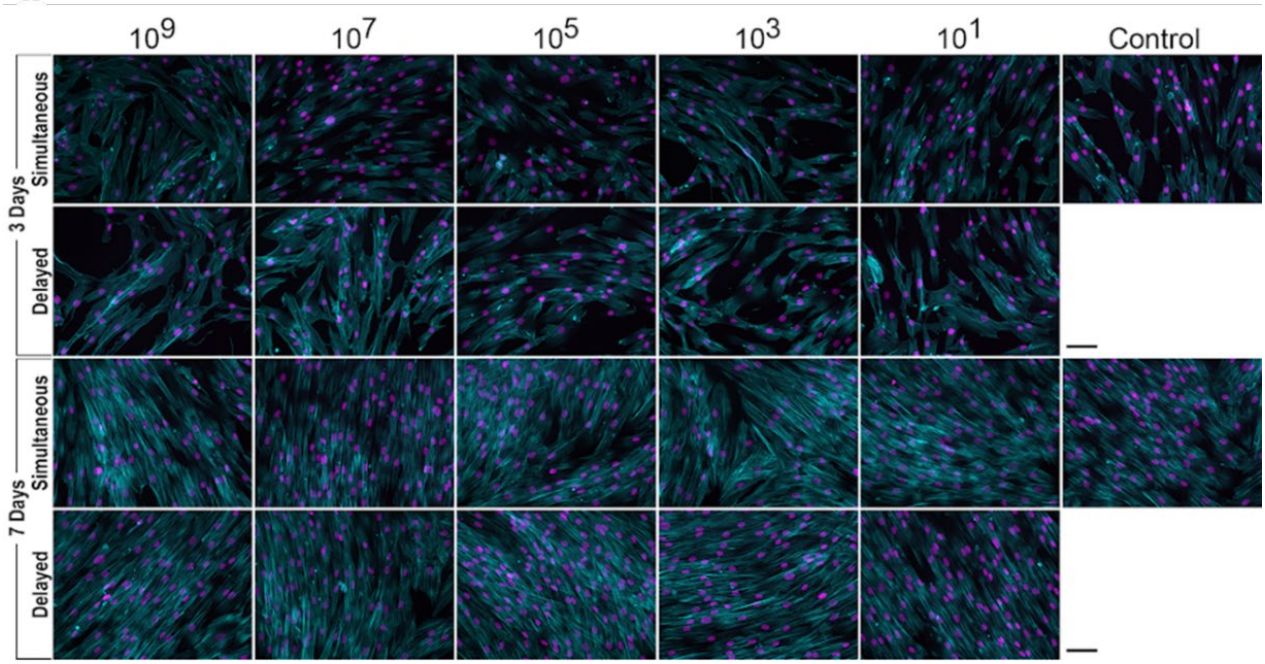

Figure 22. (C) Images of fibroblast actin cytoskeleton (cyan) and nuclei (magenta) after 3- and 7-days exposure to either simultaneous or delayed nanoparticles. Neither nanoparticle type nor concentration had any effect on cell morphology (scale bar = 50 µm).

3.4. Conclusions

We demonstrated a non-invasive, environmentally friendly, cost-effective, and rapid process for the fabrication of plasma polymerized nanoparticles. We have presented evidence that delaying the inflow of the polymerizable gas, acetylene, into the discharge strikingly enhances the collection yield of PPNs in commercial well-plates. The increase in yield is proposed to be due to pressure gradients regulating the net force on the particles and controlling their drift, as supported by *COMSOL MultiPhysics* simulations. Optical emission spectroscopy provided insights on the fragmentation of C_2H_2, and the subsequent PPN growth mechanism was revealed to be comparable to that resulting from a production strategy with simultaneous inflow of all gases. Furthermore, our surface analysis studies showed that the chemical and morphological characteristics of the PPNs were not altered by employing the delayed acetylene inflow strategy. In addition, this plasma polymerization strategy is also capable of creating active binding sites on the PPNs that facilitate single-step, reagent-free conjugation of functional biomolecules. This capability of the PPNs was demonstrated using rGFP as a model fluorescent protein via a single-step and reagent-free immobilization of the functional biomolecules. LDH cytotoxicity assays validated that the PPNs were remarkably well tolerated by cells, which indicates their strong potential for future *in vivo* studies. Our findings indicate that the technology presented here is a leap forward in facile, simple, and solvent-free fabrication of biofunctional polymeric nanoparticles with important implications for large-scale industrial synthesis.

Chapter 4. Direct covalent attachment of fluorescent molecules on plasma polymerized nanoparticles: a simplified approach for biomedical applications.

This chapter aimed to assess the feasibility of directly covalently attaching fluorescent molecules, such as FITC and Nile Blue, to the surfaces of plasma polymerized nanoparticles without additional reagents. Plasma polymerization was used to synthesize and enrich the nanoparticles with functional groups, facilitating the on-contact immobilization process. It highlights the method's efficiency over traditional nanoparticle functionalization techniques, addressing critical biomolecular attachment challenges in nanoparticle application for real-time imaging and drug delivery.

Chapter 4 has been submitted for publication in Nanoscale entitled: 'Direct covalent attachment of fluorescent molecules on plasma polymerized nanoparticles: a simplified approach for biomedical applications.'

4.1. Introduction

Surface-functionalized nanoparticles have become extensively popular over the past few decades as a versatile platform for a variety of applications ranging from environmental remediation[405] and gas sensing [406] to printed electronics [407] and numerous applications in the ever-growing biomedical field [408-410]. Where bioactive molecules and fluorescent molecules are coupled unprecedented functionalities can be achieved, making them attractive for applications in disease treatment [411, 412], diagnostic assays [413], delivery of therapeutic agents [414, 415], or a combination of the above [416, 417]. In particular, their surface modification with fluorescent markers has amplified their functional capabilities for in vivo multi-modal imaging [418-420] and hybrid sensing techniques[421, 422]. The development of fluorescent nanoparticles provides the additional benefit of enabling their real-time tracking with a higher stability and better resistance to photobleaching than that of the common fluorescent dyes[423].

Numerous methods for coupling fluorescent molecules with nanoparticles have been explored. Physical adsorption between fluorescent molecules and polymer matrices is considered a relatively minimally complicated procedure; however, the resultant association force is weak, and the fluorescent molecules tend to leach into the surrounding environment of the particle [424, 425]. Electrostatic capture, involving the attraction between charged fluorescent dyes and oppositely charged nanoparticles, is another commonly applied method for fluorescent molecule attachment onto polymeric nanoparticles. Despite its prevalence in chemical research, it yields pH-dependent bonding, which can readily deteriorate with minor changes in pH [426, 427]. An alternative method for attaching fluorescent molecules onto polymeric nanoparticles involves relying on hydrophobic interactions [158, 243], yet its major downsides arise from the need for numerous wet-chemistry steps and the variable and often weak nature of such interactions [428, 429].

Covalent attachment provides higher robustness and bond stability compared to physical attachment methods, but the process is often tedious and time-consuming [430]. For example, the covalent labelling of FITC onto chitosan-coated nanoparticles required a 3-hour reaction in the dark, precipitation using a high pH solvent, and dissolution in acetic acid before being dialyzed in distilled water for 3 days in darkness [262, 431-433]. The chemicals and reagents utilised in the covalent binding process may also be toxic, posing challenges for regulatory approvals. As such, there is a growing demand for a simple, yet versatile, approach that offers the advantages of covalent attachment but without these limitations.

Plasma polymerization is an emerging technology for the production of nanoparticles that results in highly stable and non-toxic organic materials, ideal for biomedical applications [434]. In this process, a precursor monomer is introduced into the reactor chamber where it is subject to a strong electric field [100]. The resulting energetic electrons drive the activation of the monomer by mutual collisions. This activation leads to the fragmentation of polymer-forming species that triggers the nucleation of clusters or “proto-particles” with sizes of up to around 10 nm [435, 436]. Once formed, these proto-particles grow into larger particles by accretion of radicals and/or ions onto their surfaces. A negative charge then accumulates as they collect electrons in their final phase of coagulation before reaching a critical mass that leads to their expulsion out of the plasma volume via gravitational forces.

Plasma polymerization has gained considerable attention recently due to its potential to create nanoparticles enriched with functional groups which are highly desirable for biomedical applications. Carboxyl-enriched particles produced by radical-induced polymerization reactions of acrylic acid has been previously studied[122, 337]. In our previous work, we demonstrated the synthesis of functional nanoparticles using a low-temperature, low-pressure plasma polymerization of mixtures

of acetylene, argon and nitrogen [123, 124, 363]. The highly radical-activated surfaces of the collected plasma polymerized nanoparticles (PPNs) render them promising candidates for covalent linking of biocompatible and fluorescent molecules, without the need for extra coatings, intermediate layers or any other reagents.

Here, we demonstrate that the synthesis of surface-active polymeric nanoparticles via the plasma polymerization technology facilitates the covalent attachment of fluorescent molecules, while also providing evidence validating the covalent nature of the bonds. As a proof of concept, we use a single incubation step to conjugate each of model fluorescent molecules: Fluorescein isothiocyanate (FITC) and Nile Blue (NB). FITC is a traditional fluorescein molecule widely prevalent for its fluorescent properties [174, 437, 438], while NB is a lipid-targeting fluorescent molecule, most popular in photodynamic tumour therapy [439]. Both fluorescent molecules have relatively large extinction coefficients, high quantum yields, and solvent-dependent optical properties that make them ideal for the development of nanoprobes. We anticipate that this work will broaden the scope of covalently surface-functionalised nanoparticles, paving the way for creating the next generation of robust fluorescently labelled polymeric nanoparticles with modern applications in biomedicine and beyond.

4.2. Materials and Methods

4.2.1. Plasma polymerization of nanoparticles

Nanoparticles were synthesized in a stainless-steel chamber as explained in Section 2.2 and depicted in Figure 11. Briefly, plasma polymerization took place with argon and nitrogen gases initially introduced at a base pressure, followed by a delayed inflow of acetylene to maximize the yield. The process was controlled to maintain a working pressure of $1.5 \times 10^{\wedge-1}$ Torr and a power input of 100 W, with the resultant PPNs collected on a 24-well culture plate on the lower electrode.

4.2.2. pH-Dependent Hydrodynamic Size and ζ Potential measurements

For experiments involving varied pH levels, different pH buffer solutions were prepared while maintaining a consistent ionic strength with 0.001 M NaCl solutions. Six 50 mL 0.001 M NaCl solutions were adjusted to different pH values using titration methods. Specifically, 0.1 mL of 0.05 M HCl solution was added to each NaCl solution, followed by the addition of 0 mL, 0.45 mL, 0.695 mL, 0.8 mL, 0.9 mL, and 1.15 mL of 0.01 M NaOH solution into samples 1 to 6 respectively. The actual pH values of these solutions were measured using a pH meter, resulting in values of 4, 5, 6, 7, 8 and 9 for samples 1 to 6 respectively. Next, 8×10^8 nanoparticles were suspended in 2 mL of each pH-adjusted solution, achieving a concentration of 4×10^8 particles/mL. Absorbance at 405 nm excitation light was measured using an ELx800 Biotek plate reader, yielding a value of 0.44 ± 0.05 with Milli-Q water as the control. The nanoparticles were then transferred to disposable folded capillary cells under sterile conditions using 1 mL syringes. Zeta (ζ) potential measurements were conducted, and the average ζ potential values for specific pH levels, along with standard deviations representing errors, were reported. Hydrodynamic size measurements and the average size were determined based on three measurements obtained from at least three independent runs.

4.2.3. X-ray photoelectron spectroscopy (XPS)

The chemical state and composition of the PPN sample surfaces were investigated using XPS with a Thermo Fisher K-Alpha+ XPS/UPS system (Thermo Fisher Scientific, USA). The XPS system

utilized a monochromated, microfocused Al K-Alpha X-ray source and a 180° double focusing hemispherical analyzer equipped with a 128-channel detector. The PPNs collected in the 24-well plate were suspended post-synthesis in 10 mL milli-Q water and transferred to a 15-mL centrifuge tube, followed by centrifugation using an Eppendorf 5810 centrifuge at 8000 rpm for 10 minutes. The PPNs were freeze-dried using an Alpha 2-4 LSCbasic Freeze Dryer for 24 hours then arranged on an indium foil affixed into a double-sided conductive carbon tape on the XPS sample holder. The survey spectra were collected at a pass energy of 200 eV and a resolution of 1 eV, while the high-resolution C 1s spectra were recorded at a pass energy of 50 eV and a resolution of 0.1 eV. The base pressure was below $5x10^{-8}$ mbar for all the measurements. A total of 10 scans were conducted for each sample. Elemental composition calculations and peak fitting for high-resolution peaks were performed using the Avantage software (Thermo Fisher Scientific, USA).

4.2.4. Time of flight secondary ion mass spectrometry (ToF-SIMS)

ToF-SIMS was performed using a Physical Electronics Inc. PHI TRIFT V nanoTOF® instrument, with a pulsed liquid $^{79+}$Au primary ion gun, operated at 30 kV. Dual charge neutralization was utilized in the form of an electron flood gun and Ar^+ ions (both 10 eV). The collection time per spot was 3 minutes, and the raster size was 10^{-4} cm^2, with 7 spots per sample. All resulting spectra were processed using WincadenceN® software (version 1.8.1.3 Physical Electronics Inc.).

4.2.5. Water contact angle measurements

The hydrophobicity of the nanoparticles was assessed by measuring the contact angle formed by a water droplet on a silicon substrate coated with a dense layer of nanoparticles. The measurements were performed using a Biolin Scientific Theta Tensiometer in the sessile drop configuration. 10 water droplets with volumes of 3 µL were deposited onto the particle-coated substrate. The interaction behavior with water was closely observed and the average minimum contact angle was measured to be (23.8 ± 0.6) °. The reported contact angle value of each sample is the average of at least three measurements.

4.2.6. Scanning Electron Microscopy (SEM)

The surface morphology of plasma polymerized nanoparticles was investigated using a Zeiss Ultra Plus scanning electron microscope (SEM). The experimental setup involved configuring the microscope with an aperture size of 30 µm, operating at a low voltage of 5 kV, and maintaining a working distance of 5 mm, using the In-lens detector. Subsequently, the SEM micrographs were analyzed and processed using the Smart Tiff software. Nanoparticles were stored in a dry state for one week then dispersed in MilliQ® water at a concentration of 4×10^8 particles/mL. They were then dropped onto a clean silicon wafer and left to naturally air dry before capturing Scanning Electron Microscopy (SEM) images.

4.2.7. Electron Paramagnetic Resonance (EPR) spectroscopy

A Bruker EMX X-band EPR spectrometer was utilized to measure spin density in the PPNs two hours after synthesis. The spectrometer operated at room temperature with a microwave frequency of 9.8 GHz, a central magnetic field of 3510 G,sampling time of 90 ms, modulation amplitude of 3 G and a microwave power of 25 mW . The reported EPR spectra represent the average of 10 scans.

4.2.8. Conjugation of FITC to plasma polymerized nanoparticles

FITC (1 μg/mL) was incubated with nanoparticles (5×10^7 nanoparticles/mL) in 100 μL of MilliQ® water at room temperature for 30 minutes. The conjugated particles were extracted by centrifugation at 1×10^5 rpm for 5 minutes. 80 μL of the supernatant was removed and replaced with 80 μL of MilliQ® water. This washing procedure was carried out three times unless otherwise specified, and the fluorescence intensity of supernatant and re-suspended conjugated particles was measured using a CLARIOstar Plus plate reader after each wash. The excitation and emission wavelengths were set to 405 nm and 504 nm, respectively.

4.2.9. Detergent washing of FITC-conjugated PPNs

To confirm that the FITC molecules were covalently immobilized onto the nanoparticle surfaces, washing protocols were enlisted between measurements. Nanoparticles, initially washed with water for three times as described above, were then incubated for 1 hour in 100 μL of 5% sodium dodecyl sulfate (SDS) or 5% Tween20 detergent at room temperature. The solutions were centrifuged at 10000 rpm for 5 minutes, after which the supernatants were decanted and reserved for analysis. The remaining conjugated particles were then washed with water as specified in each section followed by measurements of the immobilized fluorescent molecule.

4.2.10. Flow cytometry of FITC-conjugated PPNs (Flow nanometry)

Nanoparticles (5×10^7 nanoparticles/mL) were incubated in distilled water, DMSO or FITC (1 μg/mL) as described above. Nanoparticles were analysed using a Gallios Flow Cytometer (Beckman Coulter, Brea, CA, USA) located in the Bosch Institute Live Cell Analysis Facility (University of Sydney). The machine parameters were adjusted to reduce the size threshold, enabling the detection of PPNs. FITC fluorescence was assessed using fluorescent channel 1. Flow cytometry data was analysed using Flowjo version 10 and data analysed using Graphpad Prism.

4.2.11. Conjugation of Nile Blue to plasma polymerized nanoparticles

Nile Blue (N0766, Sigma-Aldrich) was dissolved in MilliQ® water to a stock concentration of 0.25 mM. Fresh nanoparticles were suspended in 10 mL MilliQ® water at an initial concentration of 3.76×10^{11} PPN/mL. For NB conjugation, 3.8 mL of the diluted 0.25 mM NB solution were added to 3mL of nanoparticles stock, achieving approximately 30 pg of NB per 10^5 nanoparticles. The mixture was left to incubate on a rocker, covered in foil, at room temperature for 30 minutes. The samples were then centrifuged at 8000 rpm for 10 minutes and washed with 10 mL MilliQ® water. Detergent washing was achieved by mixing with 10 mL of 5% SDS solution for 30 minutes, followed by three water washes. After each step, the samples were centrifuged, and the supernatant was saved for XPS, ATIR-FTIR, or fluorescence measurements Nile Blue (Ex: 624/13nm, Em: 678/17) using fluorescent black plate UV Greiner box with clear-bottom 96 well plates. Finally, for cellular uptake imaging, the above steps were repeated and the pellets were dispersed in 1 ml sterile PBS.

4.2.12. Cell Culture Assay

MCF-7 human breast cancer cells were maintained at 37°C in an atmosphere with 5% CO2 in Minimum essential medium, 10% (v/v) Fetal Bovine Serum (FBS), and 0.01 mg/ml recombinant human insulin. Cell density was determined using a trypan blue dye exclusion assay. For the process of passaging and plating, detachment of the cells was carried out using 0.05% trypsin-EDTA (Invitrogen).

4.2.13. Confocal Laser Scanning Microscopy

The internalization and intracellular behaviour of NB-PPNs were examined using confocal laser scanning microscopy. MCF-7 cells were seeded onto 1.5 cm coverslips in 24-well plates at 250,000 cells per well in 500 µL. Nile Blue conjugated PPNs were produced as mentioned above. After removing the medium, the cells were treated with NB-PPNs at a final concentration of 7,500 PPNs per cell in the culture medium for 4 hours. Untreated cells served as the control. Subsequently, the solution was aspirated, and cells were washed with 200 µL PBS. Nuclei were stained with 200 µL of NucBlue™ Live reagent (Hoechst 33342) (ThermoFisher Scientific, R37609) for 3 minutes, washed, and fixed with 10% Neutral buffered formalin (Sigma-Aldrich) at room temperature. After a 10-minute incubation, cells were washed again and stained with ActinRed™ (ThermoFisher Scientific) followed by a 10-minute incubation protected from light. The solution was removed, cells were washed twice with PBS, stained cultures were stored at 4 degrees Celsius in PBS until being mounted on slides for imaging. Confocal images were captured using a Nikon C2 Confocal microscope (Lasers: 405 nm, 488 nm, 561 nm, 640 nm. Detectors: 3 Standard PMTs using Filter Blocks: DAPI/Cy5, FITC, TRITC). Image analysis was performed using ImageJ (version 1.53c, NIH) Maximum intensity projections were generated, and Mean fluorescence intensity of Nile Blue associated with cells was determined by applying a binary selection mask of the actin cytoskeleton.

4.2.14. Statistical analysis

The data is presented as mean ± standard deviation (SD), unless otherwise stated, and was analyzed using Prism (version 9.5.1, Graphpad) or Excel (Microsoft 365 MSO, Version 2309 Build 16.0.16827.20278). Flow cytometry data was processed using Flowjo (TreeStar, Ashland, OR, USA), with statistical analysis conducted via Prism (version 9.5.1, Graphpad). Data shown is the mean ± standard error of the mean (n=6 from 2 independent experiments) and data points were compared using a one-way ANOVA. Mean fluorescence intensity (MFI) at specific channels was compared using an ordinary one-way ANOVA with a Tukey post hoc test. Significance levels in figures are indicated as ns if $P > 0.05$, *$P \leq 0.05$, **$P \leq 0.01$, ***$P \leq 0.001$, and highly significant if ****$P \leq 0.0001$.

4.3. Results and discussion

4.3.1. Plasma polymerization of nanoparticles

PPNs were generated using a mixture of argon, nitrogen, and acetylene gases as the precursor (Figure 23a). The generated particles were collected in a 24-well cell culture plate positioned on the lower electrically floating electrode (Figure 23b). To provide insights into the molecular species present during the plasma polymerization, optical emission spectroscopy was employed for real-time diagnostics. The observation of transitions in the spectral range of 385–395 nm unveiled molecular species like excited N_2 neutral molecules, N_2^+ molecular ions, and CN radical molecules (Figure 24a). These observations within the nitrogen-based spectrum highlight the role of the gas mixture in shaping the spectral signature and influencing the biocompatibility and formation of nanoparticles [123, 124].

XPS was employed to examine the elemental composition of PPNs post-synthesis, showing strong signals from carbon (C1s) and nitrogen (N1s) (Figure 24b), with atomic concentrations of 64.9%, and 29.9% respectively (Figure 24c). Despite no oxygen in the initial gas mix, around 5.2 atm% was detected, likely due to oxidation after production when exposed to air, a process commonly known as autoxidation. This phenomenon occurs as reactive radicals interact with atmospheric oxygen, and it has been previously observed in plasma polymers deposited from similar gases in the form of

coatings [114, 340, 440, 441] and others generated from other precursor monomers [111, 130, 132, 442].

Functional group analysis through ATR-FTIR was employed to further understand the molecular composition and surface functionalities of the synthesized nanoparticles. The FTIR spectra obtained for PPNs (Figure 24d) revealed distinctive peaks associated with bending and stretching vibrations of C=C, C-O, C-N, and C-H from alkene, primary alcohol, amine, and methyl groups at 980-1630 cm^{-1}, along with C≡N stretching from nitrile functional groups at 2000-2500 cm^{-1}. Additionally, peaks corresponding to stretching vibrations of C-H, N-H, and O-H were observed in the 2800-3600 cm^{-1} spectral region. The presence of these functional groups correlate well with the bonding species determined by peak fitting the C1s XPS high resolution peak (Figure 24e), indicative of the formation oxygen and/or nitrogen-containing species within the samples. Three primary carbon environments were identified with respective binding energies of 284.6 eV for C–C /C–H, 286.5 eV for C–N/C–O, and 288.0 eV for C═O/N–C═O [443], with approximately 68%, 26%, and 6% of the total carbon content, respectively (Figure 24f). The identification of these bonds and functional groups reaffirms our earlier conclusions regarding the role of molecular nitrogen in the synthesis process, influencing both the chemical composition and surface characteristics of PPNs [434, 442]. These results are in good agreement with the FTIR data (Figure 24d), which indicate the presence of alkenes, alcohols, amines, methyl, and nitrile groups.

EPR spectroscopy examines materials with unpaired electrons like free radicals, unveiling details about their structure, bonding, and electronic properties through analysis of electron spin. The EPR spectrum of the PPNs affirms the presence of radicals within the PPNs (Figure 24g). It exhibits a singular symmetric resonance peak positioned at 3510 G, featuring a calculated g-factor of 2.004, indicating unpaired electrons linked with radical compounds. During the plasma polymerization process, the fragmentation of the organic precursor leads to the initial formation of small nanometer-sized clusters through gas-phase chemical reactions [366, 444]. These clusters grow into larger entities by coagulating and adhering together. Within this dynamic environment, radicals generated from the precursor fragmentation that are unable to form bonds with neighbouring species due to steric constraints become entrapped within the growing nanoparticles. This encapsulation of radicals is a key feature of the plasma polymerization process, contributing to the unique properties of the PPNs.

To assess the hydrophobicity of nanoparticles in solution, a tensiometer was employed to measure the water contact angle formed between water droplets and layers of nanoparticles deposited on silicon wafers. The minimal contact angle was measured at (23.8 ± 0.6) ° which indicates low hydrophobicity and reflects the affinity of the nanoparticle surfaces to water. This observation aligns with the FTIR and XPS data, showing the presence of polar groups such as C-O and C-N, rendering the surfaces hydrophilic.

The size and charge of nanoparticles critically impact their function and stability. Smaller particles enhance cellular entry but face instability challenges, prone to aggregation. PPN size distribution shown in Figure 24h indicates a uniform nanoparticle size (~230 nm) with a polydispersity index of 0.094. SEM micrographs, shown in Figure 25, confirmed their spherical shape, revealing smaller particles forming chains. Particle interaction with the environment was explored by varying pH, impacting size and charge. Size increased with pH (~4.5-9.0), showing a slight drop from pH 3.7 to 4.5 (Figure 25b), while the zeta potential gradually decreased from ~47mV to ~35mV (Figure 25c). Due to the dissolution of CO_2 from the surrounding air, the MilliQ® water remains generally acidic. Consequently, the size and zeta potential of nanoparticles in MilliQ® water deviated slightly from the trend observed for nanoparticles in an NaCl solution, exhibiting a size of approximately 220 nm

and a zeta potential of around 50 mV. Agglomeration can be explained by the classical Derjaguin-Landau-Verwey-Overbeak (DLVO) theory, which considers the interplay of van der Waals (vdW) attractive forces and electrostatic double layer (EDL) forces [445]. Agglomeration occurs when EDL forces are diminished relative to vdW forces. The surfaces of most nanoparticles contain titratable surface chemical groups (e.g., N_2, CH, COOH), which can be protonated by H^+ (resulting in a positively charged surface at low pH) or deprotonated by OH^- (yielding a negatively charged surface at high pH). The Isoelectric Point (IEP), where particles become electrically neutral, is expected above pH 7, driving agglomeration at higher pH due to reduced repulsion.

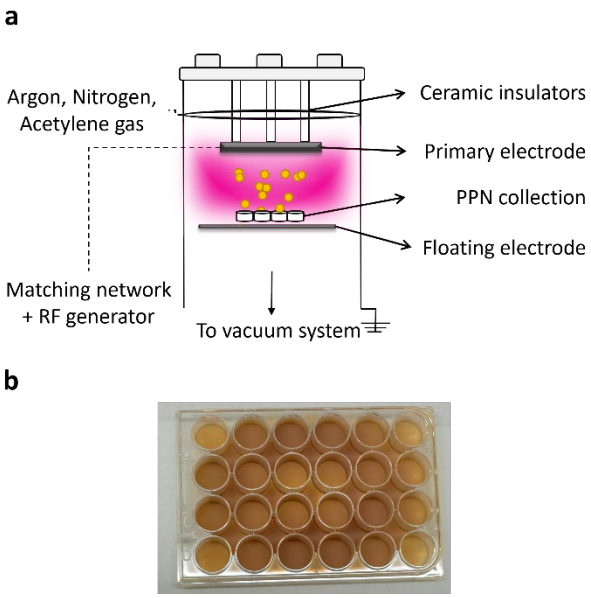

Figure 23. (a) Sketch of the plasma polymerization system depicting the nanoparticle collection process. In the sketch, the primary and floating electrodes can be seen as well as the top gas dispenser tube through which argon, nitrogen, and acetylene gases are let in at 3, 10, and 6 sccm respectively. (b) PPNs collected in a 24-well plate following the plasma polymerization process.

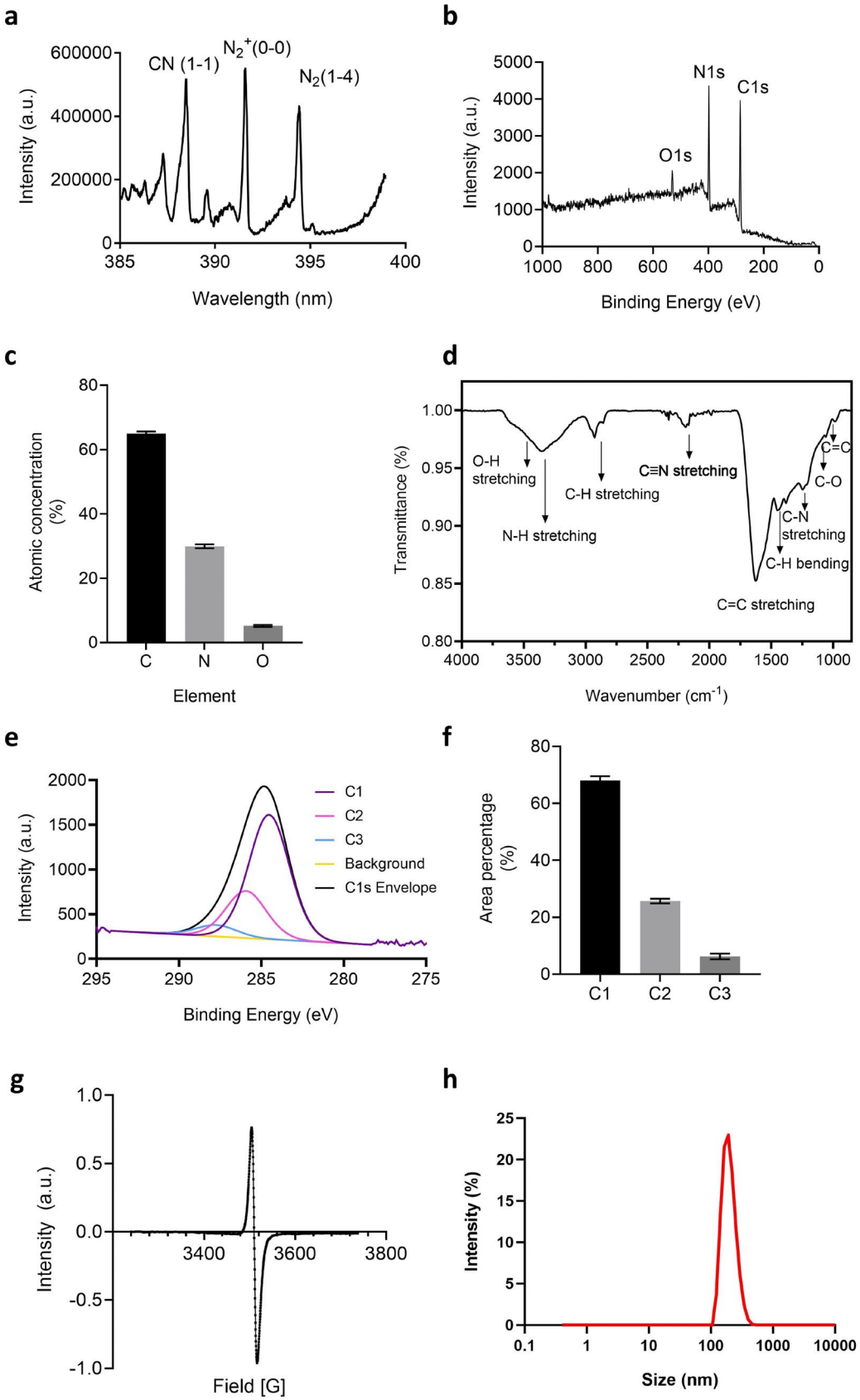

Figure 24. PPN physical and surface chemical characterization panel showing (a) Optical emission spectrum (OES) of the plasma, (b) XPS survey scan, (c) Atomic concentrations of carbon, nitrogen and oxygen, (d)

FTIR, (e) XPS C1s high resolution spectra, (f) XPS area percentage of carbon bonding components, (g) EPR spectrum and (h) particle size distribution of the synthesised nanoparticles.

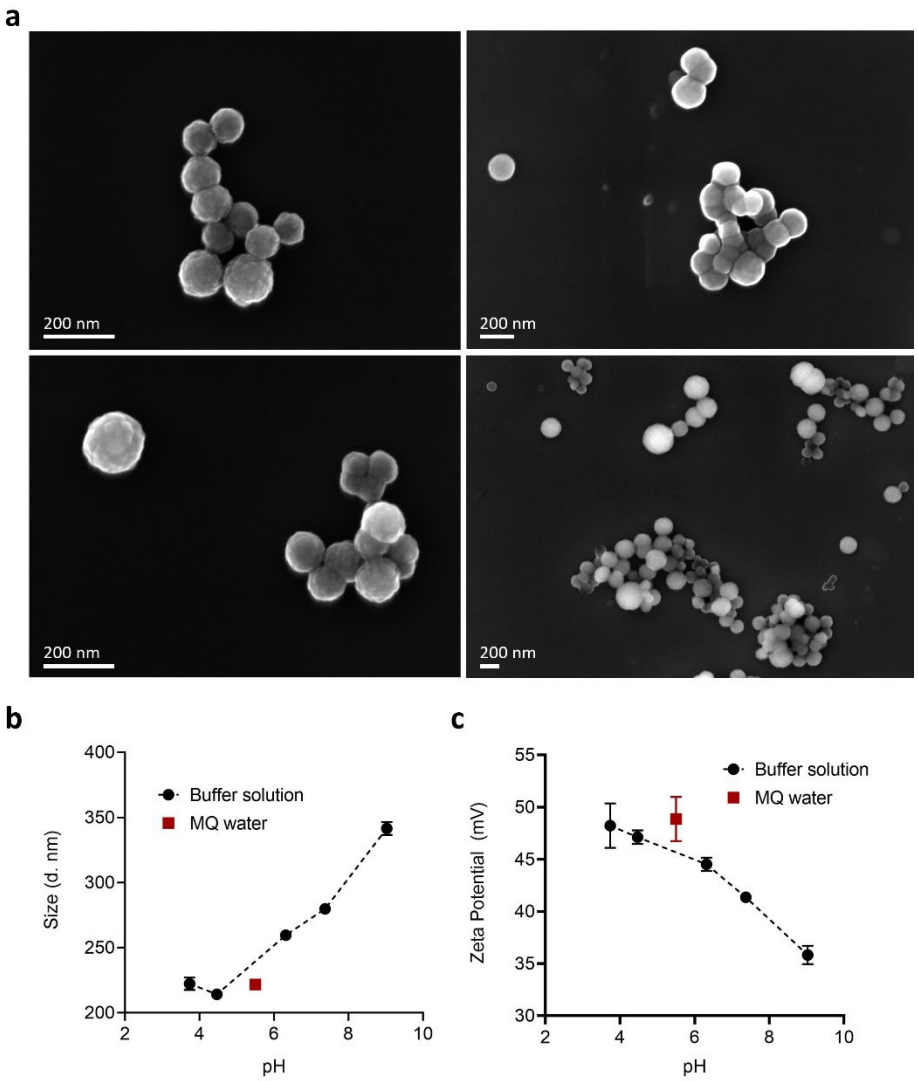

Figure 25. (a) SEM images of PPNs captured at different magnifications showing the various populations of PPNs including singular unit spheres, coagulates of PPNs and long chain-like aggregates. The scale indicated is 200 nm, (b) PPN size variation with pH and (k) PPN zeta potential changes with pH.

4.3.2. Covalent attachment of fluorescent molecules to plasma polymerized particles

In evaluating the capacity of PPNs to covalently bind fluorescent molecules, we used Fluorescein Isothiocyanate (FITC) and Nile Blue (NB), well-established and widely recognized fluorescent compounds. FITC is reporter fluorescent molecule with reactive group (-N=C=S) known for its hydrophilic nature, its bright fluorescence intensity, and its prevalence over the past several decades for labelling proteins, drugs, cells, molecules, and polymers. NB is a targeting fluorescent molecule with high affinity to unsaturated free fatty acids with chain lengths of more than 16-carbon atoms [446], especially in tumour therapy [439]. Their attachment to nanoparticles is of paramount significance as it enhances particle functionality by enabling precise tracking, labelling, and real-time monitoring in various biomedical applications. Here, the radical-containing nanoparticles serve

as a conducive nanocarrier for the direct binding of FITC and NB molecules, enabling their immobilization through a straightforward, one-step incubation process at room temperature.

To verify that FITC was covalently bonded to nanoparticles' surfaces, nanoparticles incubated in FITC solution were rigorously washed with SDS or Tween20 and characterised using XPS and ToF-SIMS before and after the detergent wash. SDS and Tween20 are detergents that have a well-documented ability to remove physisorbed molecules, while retaining those robustly attached to a surface [65, 66, 107]. SDS, in particular, is an ionic detergent that disrupts physical interactions to unfold proteins [447] while leaving covalent bonds unaffected, rendering it suitable for assessing the attachment of macromolecules onto surfaces [448]. SDS disrupts the physical forces that underpin the physisorption of proteins and hence it is used to identify biological molecules that are covalently attached to surfaces [449-451].

XPS aimed to identify and quantify FITC bound to the surface by analyzing its sulfur component (Figure 26a). The absence of sulfur signals in the XPS data (Figure 26b) of plasma polymer nanoparticles before exposure to FITC (Figure 26b(i), <0.15 at. %, the XPS signal sensitivity) served as a robust baseline for comparison. Following incubation in FITC solution and subsequent water washing thrice, a sulfur atomic concentration of 0.56 ± 0.13 at.% was measured (Figure 26b(ii)). After Tween20 washing, a detection of 0.48 ± 0.12 at.% sulfur was observed (Figure 26b(iii)), suggesting covalent attachment of FITC molecules to the surface. SDS washing was excluded from XPS measurements due to its sulfur content, rendering sulfur ineffective for detecting residual FITC.

ToF-SIMS was used to detect molecular signatures unique to FITC, providing strong evidence on their covalent attachment to the nanoparticle surfaces. ToF-SIMS spectra of the PPNs before and after incubation in FITC solution are shown in Figure 26c. The observed peak at m/z 333 corresponds to FITC molecules, while the other peaks originate from the plasma polymer structure. The nanoparticle surfaces retained a dominant m/z 333 peak after the Tween20 wash. Tween-specific cations at m/z 227, 255, and 283 were undetectable, which also supports the removal of any remaining detergent [452]. The presence of fragments associated with FITC molecules on the surface after the Tween wash further validates the XPS results and presents additional evidence of robust immobilization.

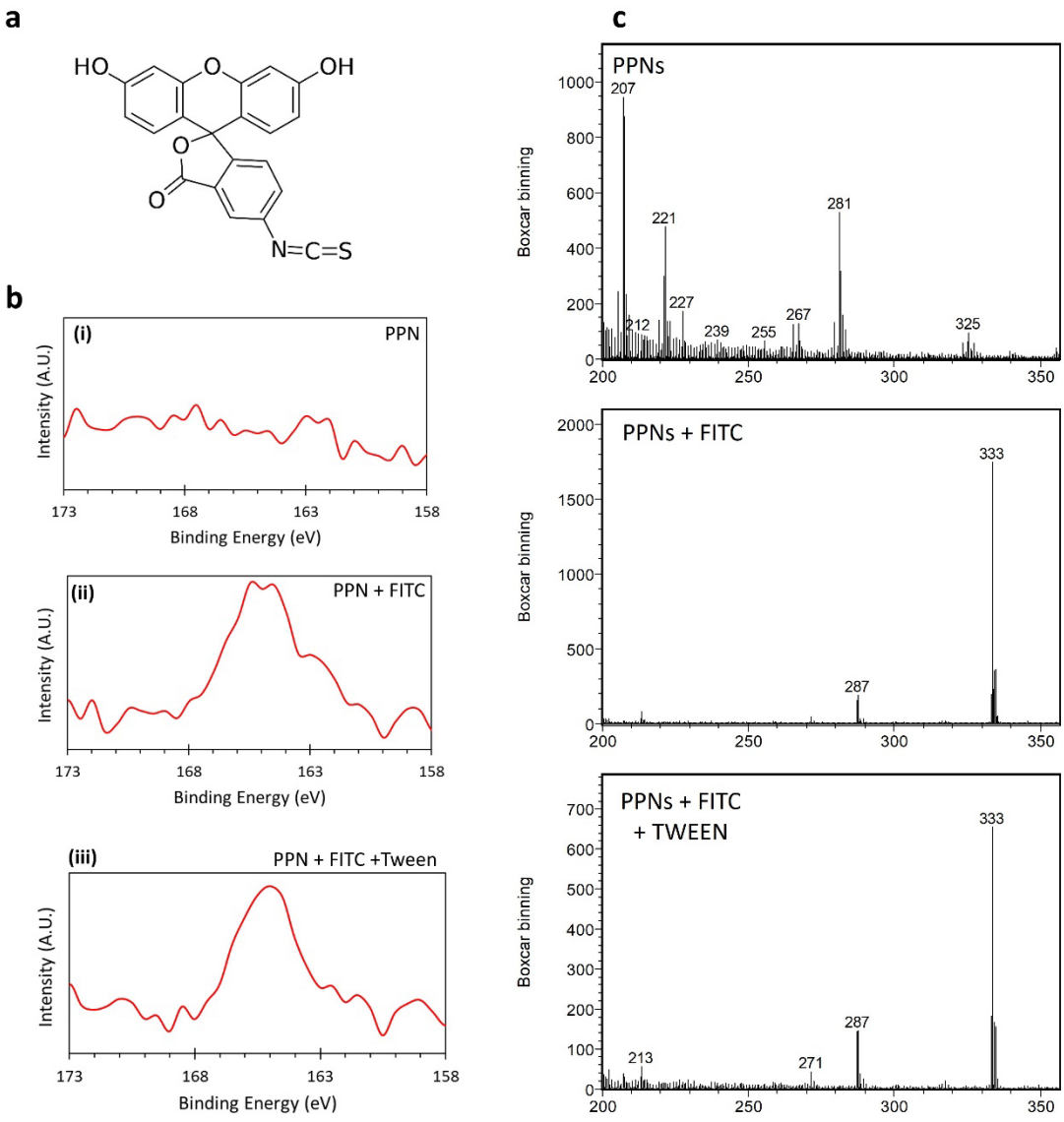
a
HO
O
OH
O
O
N=C=S
b
(i)
PPN
Intensity (A.U.)
173
168
163
158
Binding Energy (eV)
(ii)
PPN + FITC
Intensity (A.U.)
173
168
163
158
Binding Energy (eV)
(iii)
PPN + FITC +Tween
Intensity (A.U.)
173
168
163
158
Binding Energy (eV)
c
PPNs
Boxcar binning
207
221
227
212
239
255
267
281
325
PPNs + FITC
Boxcar binning
287
333
PPNs + FITC
+ TWEEN
Boxcar binning
213
271
287
333

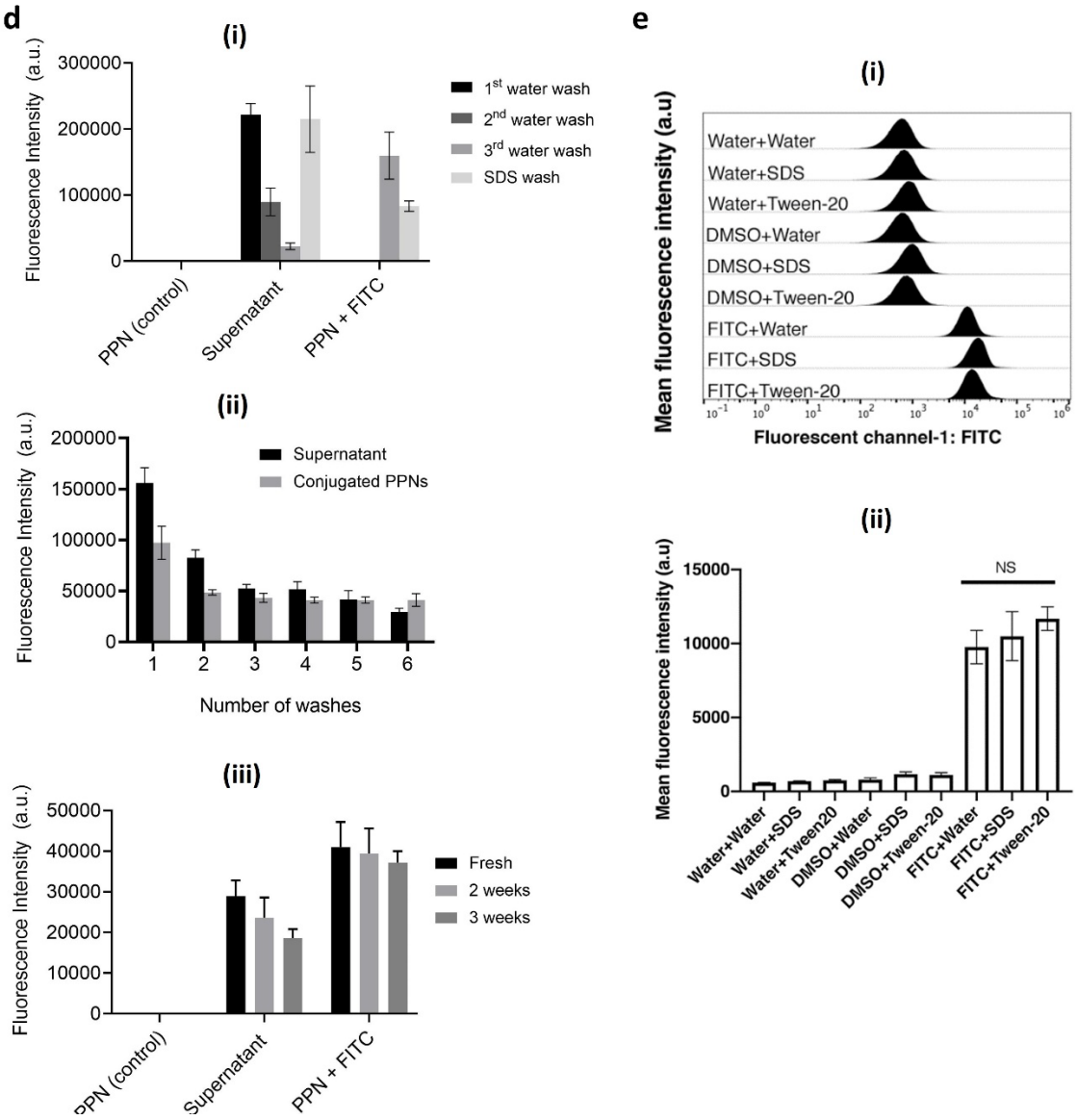

Figure 26. a) Chemical structure of FITC used in these experiments. b) XPS sulphur S2p high resolution spectra obtained from (i) plasma poylmerized nanoparticles and FITC-incubated nanoparticles after washing with (ii) water and (iii) Tween20. c) ToF-SIMS spectra obtained from (a) plasma poylmerized nanoparticles (top) and FITC-incubated nanoparticles after washing with water (middle) and Tween20 (bottom). (d) Fluorescence intensities obtained from FITC-incubated nanoparticles and their corresponding supernatant solutions. (i) Samples were washed with MilliQ water and SDS. The SDS washing was carried out following the third water wash. (ii) Samples were washed for up to 6 times with MilliQ® water. (iii) Samples were washed 6 times with water and stored in MilliQ® water for 2 and 3 weeks before the fluorescence measurements. The measurement of samples stored for 2 and 3 weeks was conducted after they were washed three times with water. (e) Flow cytometric analysis of FITC-conjugated nanoparticles. Nanoparticles were incubated in the presence of distilled water, DMSO or FITC and washed with distilled water, SDS or Tween-20 and analysed using a Gallios flow cytometer. (i) shows representative flow cytometric profiles of FITC fluorescence of nanoparticles from each treatment group. (ii) shows the mean fluorescence intensity (arbitrary units) of nanoparticles from each treatment group. NS: not significant.

To further validate the covalent conjugation of FITC fluorophores to PPNs, a comprehensive suite of fluorescence spectroscopy analyses was conducted. The fluorescence emission from both the

supernatant and the resuspended FITC-conjugated PPNs was quantified in solution (Excitation/Emission: 405 nm/504 nm). PPNs conjugated with FITC (FITC-PPNs) were then subject to a systematic series of water washes followed by SDS detergent treatment (Figure 26d). Following the SDS treatment, there was a decrease in fluorescence intensity observed in the resuspended FITC-conjugated PPNs. However, a signal, significantly higher than the control group remained, affirming the covalent binding of FITC molecules. The decrease in fluorescence intensity post-SDS washing is attributed to the removal of physically attached FITC molecules from the PPN surface, while the discernible signal that remains is attributed to a persistently attached covalent monolayer. Furthermore, Figure 26d(ii) shows the fluorescence intensities of nanoparticles following a succession of water washes. The appearance of fluorescence in the supernatant after each wash indicates the stepwise removal of consecutive layers of physically-adsorbed FITC. Despite this removal, the fluorescence signals from the nanoparticles remained unwavering, substantiating the robustness of the covalently bound FITC molecules to the PPN surfaces. Moreover, Figure 26d(iii) illustrates the stability of FITC-labeled nanoparticle fluorescence during extended storage in water for up to 3 weeks following 6 water washes. This extended stability corroborated the enduring covalent attachment of FITC to the nanoparticle surfaces, underscoring its potential for sustained performance in various applications requiring steadfast and persistent fluorescence properties.

The fluorescence intensity of FITC-conjugated nanoparticles was also assessed by flow cytometry. Adjusted to a detection threshold suitable for PPNs, flow cytometry allows for large-scale analysis of single nanoparticles, referred to as nanometry [124]. FITC is typically dissolved in aqueous buffer solutions or organic solvents, such as dimethyl sulfoxide (DMSO). PPNs were incubated in FITC, distilled water or DMSO to provide a variety of carrier solutions for evaluation. The conjugated particles were then washed in distilled water, SDS or Tween-20 and analysed for fluorescence with 488 nm excitation using a Gallios flow cytometer. Figure 26e(i) shows representative flow cytometry data from this study. Nanoparticles incubated in distilled water or DMSO showed no fluorescent signal above background. Only FITC-conjugated nanoparticles demonstrated significant increase in fluorescence in the FITC detection range. Figure 26e(ii) illustrates that while the FITC-conjugated nanoparticles showed a statistically significantly higher FITC fluorescence than distilled water or DMSO-treated nanoparticles, there was no significant difference in mean fluorescence intensity between FITC-conjugated nanoparticles washed with distilled water, Tween-20 or SDS, which demonstrates the covalent attachment of FITC molecules that are not removed with a simple water wash. The ease of removal of physically adsorbed FITC can be attributed to its small molecular size which limits the combined strength of the physical interactions relative to large physiosorbed molecules such as proteins. These results align with the conclusion of FITC covalent bonding obtained from XPS, ToF-SIMS and fluorescence spectroscopy by demonstrating consistent fluorescence intensity emitted from FITC-conjugated nanoparticles after different detergent washing procedures.

To ensure that the results observed for FITC are not specific to this particular molecule, we also attached Nile Blue, a cationic benzophenoxazine fluorescent molecule with affinity to unsaturated free fatty acids, onto the PPNs. Nile Blue comprises carbon, hydrogen, nitrogen, and oxygen elements intricately arranged within its phenoxazine ring (Figure 27a). The molecule incorporates diverse substituents and functional groups strategically positioned to impart its characteristic blue hue. These structural features, including side chains, contribute to the solubility, reactivity, and suitability of the fluorescent molecule for applications such as fluorescence and biological staining. This sequential approach allowed us to comprehensively understand the covalent binding process, shedding light on the distinct characteristics and applications of each functionalized nanoparticle variant.

The attachment of Nile Blue onto the PPN surface was investigated through XPS and ATR-FTIR. Changes in the elemental composition of PPN-NB were evident following the conjugation and detergent treatment process as observed in Figure 27b. Specifically, the oxygen content increased from 5.4% to 13.4%, whereas nitrogen content decreased from 26.3% to 22.9%. Post-conjugation, XPS analysis shows a decrease in nitrogen levels, likely due to Nile blue's lower nitrogen-to-carbon ratio compared to the as-synthesized nanoparticles. These changes in surface composition can be primarily attributed to the immobilisation of NB and the autoxidation of the PPN surface as discussed in Section 3.1.

The high-resolution C1s peaks of the PPNs before and after conjugation were investigated to provide further evidence of NB attachment. In terms of peak shape, the PPN-NB exhibits broadening at the high binding energy (BE) tailing end compared to the unconjugated PPN (Figure 27c). Three distinct carbon peaks corresponding to C1: C-C/C-H (BE ≅ 285.0 eV), C2: C-O/C-N (BE ≅ 286.5 eV), and C3: C=O/N-C=O (BE ≅ 288.2 eV) were fitted to the C1s spectra with the best fit area percentages shown in Figure 27d. The C2 peak, corresponding to C-O and C-N bonding species, showed an increase in area percentage from 29.2% to 41.0% after NB conjugation (Figure 27d). This increase that accounts for the observed C1s peak broadening is attributed to the presence of primary, secondary, and aromatic amine groups in the NB structure. The rise in C-O species originates from the oxygen atom present in the aromatic structure of NB, as well as the reaction of atmospheric oxygen with carbon-based radical species on the nanoparticle surfaces. Conversely, the predominant C1 peak (C-C/C-H) decreased in

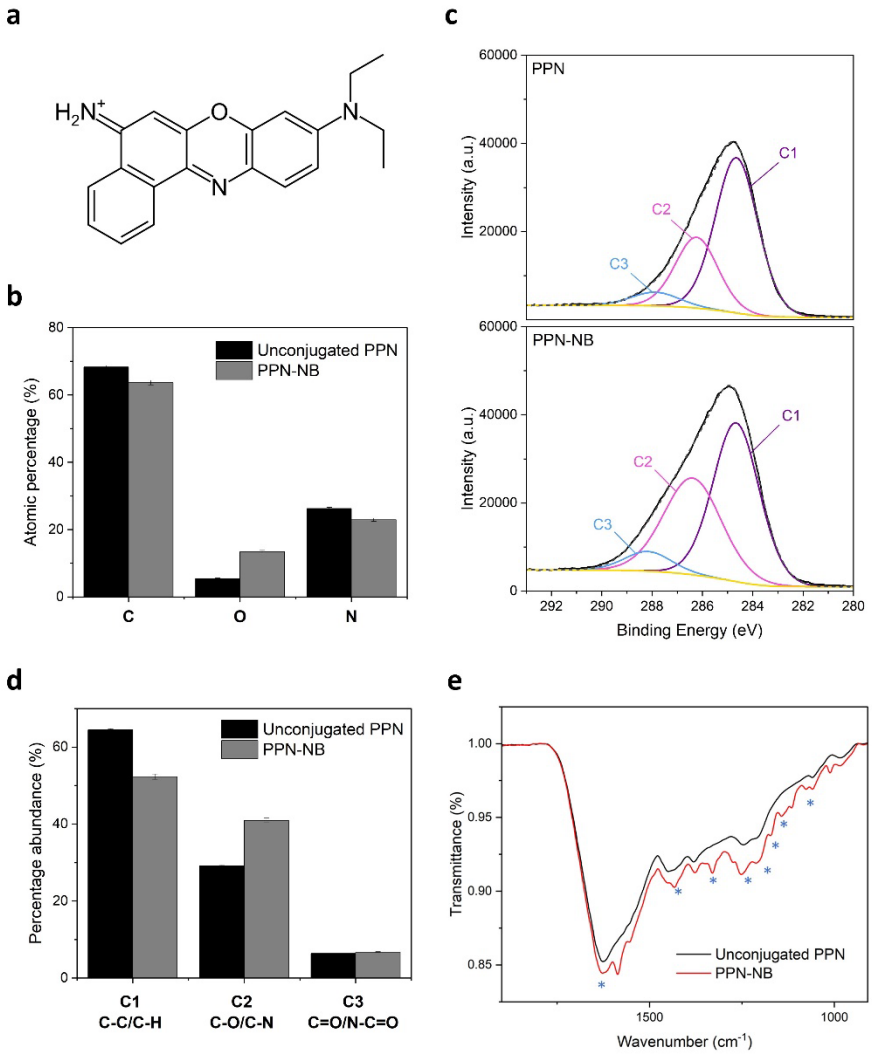

Figure 27. Surface characterization of the PPN and PPN-NB showing successful conjugation of Nile Blue into the PPN. (a) NB chemical structure. (b) Spectral analysis of the XPS survey spectra indicating changes in carbon, nitrogen, and oxygen atomic percentages, (c) peak fitted high-resolution C1s peak of PPN and PPN-NB attributing three bonding components (C-C/C-H, C-O/C-N, and C=O/N-C=O), (d) percentage of each C1s components based on peak area, and (e) Fourier transform infrared (FTIR) spectra highlighting changes in the functional groups present in the PPN surface after conjugation.

abundance from 64.5% to 52.3% which is a direct result of the C2 increase. Lastly, the C3 peak (C=O/N-C=O) exhibited a slight increase from 6.4% to 6.8%. This change may be attributed to the formation of more stable oxidation products such as carbonyl (C=O) and carboxylate (COOH) functionalities due to a chain of auto-oxidation reactions initiated at the carbon-centered radicals at the PPN surface. This is consistent with the oxidative degradation mechanisms previously observed in plasma polymers in the form of coatings of similar composition, where oxygen and water molecules diffusing into the polymer matrix react with metastable species, leading to an increase in oxygen-containing functional groups[443]. The decrease in nitrogen content observed could be explained by the volatilization and leaching of nitrogen-containing compounds from the polymer matrix as well as by the lower nitrogen to carbon ratio of the NB molecules compared to that in the PPNs. The autooxidation is likely accelerated by hydrolysis reactions targeting nitrogen-containing groups within the polymer, further exacerbated by the oxidative environment. The decrease in nitrogen content upon exposure and conjugation with Nile Blue, a benzophenoxazine fluorescent molecule, could also be contributed to by the oxidative degradation of the nitrogen-containing

heterocyclic structures within the fluorescent molecule itself or the plasma polymer matrix. In the presence of oxidative stress, such as exposure to atmospheric oxygen or reactive oxygen species in aqueous environments, the nitrogenous heterocyclic rings can undergo oxidative cleavage, leading to the breakdown of these structures and the consequent release of nitrogen in forms that are more volatile or soluble, thereby reducing the overall nitrogen content measurable on the surface of the plasma polymerized nanoparticles. This degradation process is consistent with the observed increase in oxygen content, suggesting that oxidative reactions are a significant pathway for the alteration of nitrogen-containing components in the polymer-molecule conjugate system.

Functional group analysis of NB conjugation was conducted using ATR-FTIR on both pre- and post-conjugated PPN samples. Distinct amine peaks emerged in the FTIR spectra of PPN-NB (Figure 27e). A secondary shoulder peak at 1587 cm^{-1} is identified and attributed to N-H bending from the primary amine group within the NB. Minor peaks at 1331 and 1271 cm^{-1} are ascribed to C-N stretching originating from the aromatic amine present in the heterocyclic ring of NB. Additionally, multiple C-N stretching peaks at 1211, 1175, 1142, 1118, and 1076 cm^{-1} are also observed, correlating with various amine groups (primary, tertiary, and aromatic) distributed across the NB structure. The other peaks found in the FTIR spectra of PPN-NB overlap with the spectra of the PPN, and all peak assignments are summarized in **Table 5.** Functional group assignment for the ATR-FTIR spectra of the unconjugated PPN and PPN-NB.. Overall, these changes in the FTIR spectra of the PPN post-conjugation indicates the successful covalent attachment of NB onto the PPN surface. The successful covalent binding of NB to PPNs, supported by XPS and ATR-FTIR, aligns with the conclusions drawn from FITC conjugation. Both fluorescent molecules exhibited changes in elemental composition on the PPN surface and robust bonding post-conjugation and detergent washing. The results presented in this section highlight the robustness and versatility of the PPN surface for the covalent attachment of various fluorescent molecules.

***Table 5**. Functional group assignment for the ATR-FTIR spectra of the unconjugated PPN and PPN-NB.*

Frequency range (cm^{-1})	***Type of vibration***	***Functional group***	***Presence in FTIR spectra (Y/N)***	
			Unconjugated PPN	PPN-NB
3490	O-H stretching	alcohol	Yes	Yes
3357	N-H stretching	primary/secondary amine	Yes	Yes
2958	C-H stretching	alkane	Yes	Yes
2934	C-H stretching	alkane	Yes	Yes
2858	C-H stretching	alkane	Yes	Yes
2195	C≡N stretching	nitrile	Yes	Yes
1624	C=C stretching	alkene	Yes	Yes
1587	N-H bending	amine	No	Yes
1448	C-H bending	methyl	Yes	Yes
1376	C-H bending	methyl	Yes	Yes
1330	C-N stretching	aromatic amine	No	Yes
1271	C-N stretching	aromatic amine	No	Yes

1211	C-N stretching	amine	Yes	Yes
1175	C-N stretching	amine	No	Yes
1146	C-N stretching	amine	No	Yes
1118	C-N stretching	amine	No	Yes
1077	C-N stretching	amine	No	Yes
1059	C-O stretching	primary alcohol	Yes	Yes
980	C=C bending	alkene	Yes	Yes

Our XPS results (Figure 24Figure 24) have shown that PPNs are approximately 60% Carbon, 30% Nitrogen, and 10% Oxygen, suggesting a general molecular structure of $C_{6n}H_mO_nN_{3n}$ where n and m are integer numbers. XPS results have also identified bonds: C_1 (C-C/C-H), C_2 (C-O/C-N), and C_3 (C=O), while FTIR (Figure 27 and **Table 5**) revealed functional groups such as CH_3, NH_2, C≡CH, -COOH, and -C≡N. This leads to a general reaction of formation for the PPNs as: $C_2H_2 + N_2 + Ar \rightarrow R\text{-}CH_3 + R\text{-}NH_2 + R\text{-}C{\equiv}CH + R\text{-}COOH + R\text{-}C{\equiv}N$, where R represents carbon chains. Each particle consists of a crosslinked carbon-nitrogen network with surface oxygen groups. The network is amorphous, as shown by the TEM results in Figure 18, and lacks a distinct crystalline structure.

4.3.3. Intracellular cytoplasmic uptake of Nile Blue conjugated nanoparticles

To exemplify one among numerous potential applications of PPNs covalently functionalized with fluorescent molecules, we investigate Nile blue-conjugated nanoparticles for drug delivery. A significant challenge in targeted drug delivery lies in enhancing the cellular uptake of targeting molecules. Current strategies predominantly focus on extracellular delivery through cell surface receptors, where the drug is subsequently released. However, this approach is suboptimal for drugs which exert their effects on intracellular targets. To overcome this limitation, engineering nanoparticles specific to the cell and incorporating elements that promote cytoplasmic uptake becomes crucial. Here, Nile Blue was used as a potent inducer for cellular uptake, with the aim of achieving the direct delivery of therapeutic payloads into the cell's interior.

We investigated the cellular uptake of Nile Blue-conjugated polymeric nanoparticles (NB-PPNs) in MCF7 breast cancer cells. In our control group, untreated cells and those treated with unconjugated PPNs were examined at both low and high magnifications. No observable gross morphological differences were observed, as depicted in Figure 28a and Figure 28b. Unconjugated PPNs displayed no detectable fluorescence signal in the far-red channel. Conversely, NB-PPN treated cells exhibited a robust Nile Blue signal, indicating successful cellular uptake (Figure 28c). We also conducted a detailed qualitative analysis at higher magnification, revealing the observed expression of Nile Blue within the cells. Upon closer examination, Nile Blue stains were visibly present in the cytoplasm of the cells. Notably, the fluorescence signals emanated from both small aggregates and diffusely distributed stain throughout the cells (Figure 28d).

To quantify the cellular uptake of NB-PPNs and evaluate the distribution of Nile Blue within MCF7 cells, we employed a quantitative approach by calculating the Mean Fluorescent Intensity (MFI). The resulting plot in Figure 28e shows individual data points representing MFI in the cells, both with and without NB-PPN treatment. A significant Nile Blue signal was detected following NB-PPNs treatment, contrasting the negligible signal observed in the negative control (Figure 28e).

The confocal images revealed that the PPNs covalently conjugated with NB were successfully internalized by cells into the cytoplasm while maintaining their integrity, avoiding degradation and cellular deformation. They effectively stained the fatty acids, which served as the intracellular target

and achieved intracellular localization of NB-PPNs. This observation can be well explained, given Nile Blue's peak fluorescence in the presence of unsaturated free fatty acids commonly found in the cytosol. The diffuse cellular staining highlights the uptake of nanoparticles into the cytoplasm, distinguishing it from lysosomal entrapment which is typically characterized by compact compartments within the cytoplasm [135]. Moreover, the discrete NB-bright fluorescent aggregates suggest the proximity of NB-conjugated nanoparticles to accumulations of free fatty acids. By covalently conjugating a lipophilic fluorescent dye, we efficiently transported the particles into the cellular cytoplasm, avoiding lysosomal entrapment or peripheral adhesion. This result aligns with our previous findings, where NB-conjugated magnetic microparticles demonstrated comparable effects on cellular uptake and staining [453]. While NB-conjugated microparticles can be utilized for cell filtering or isolating cancer cells in peripheral lymphatic cancers, their potential for therapeutic delivery is hindered by their metallic nature. In contrast, PPNs can not only achieve lipophilic staining though the covalent attachment of NB, but also offer a biocompatible carrier with no cytotoxic effects, as was demonstrated in our previous cytotoxicity studies [124, 454]. Future directions may involve optimizing theranostic capabilities by co-immobilizing a drug and a cellular targeting agent with the lipophilic probe. This strategic approach creates a system where one element guides the particles, while the other enhances their cytoplasmic uptake for efficient drug distribution. The findings presented in this study advance plasma-polymerized nanoparticles as versatile platforms in nanomedicine, enabling direct covalent attachment of fluorescent molecules without the need for additional reagents or steps, thereby broadening their utility across medical and non-medical applications.

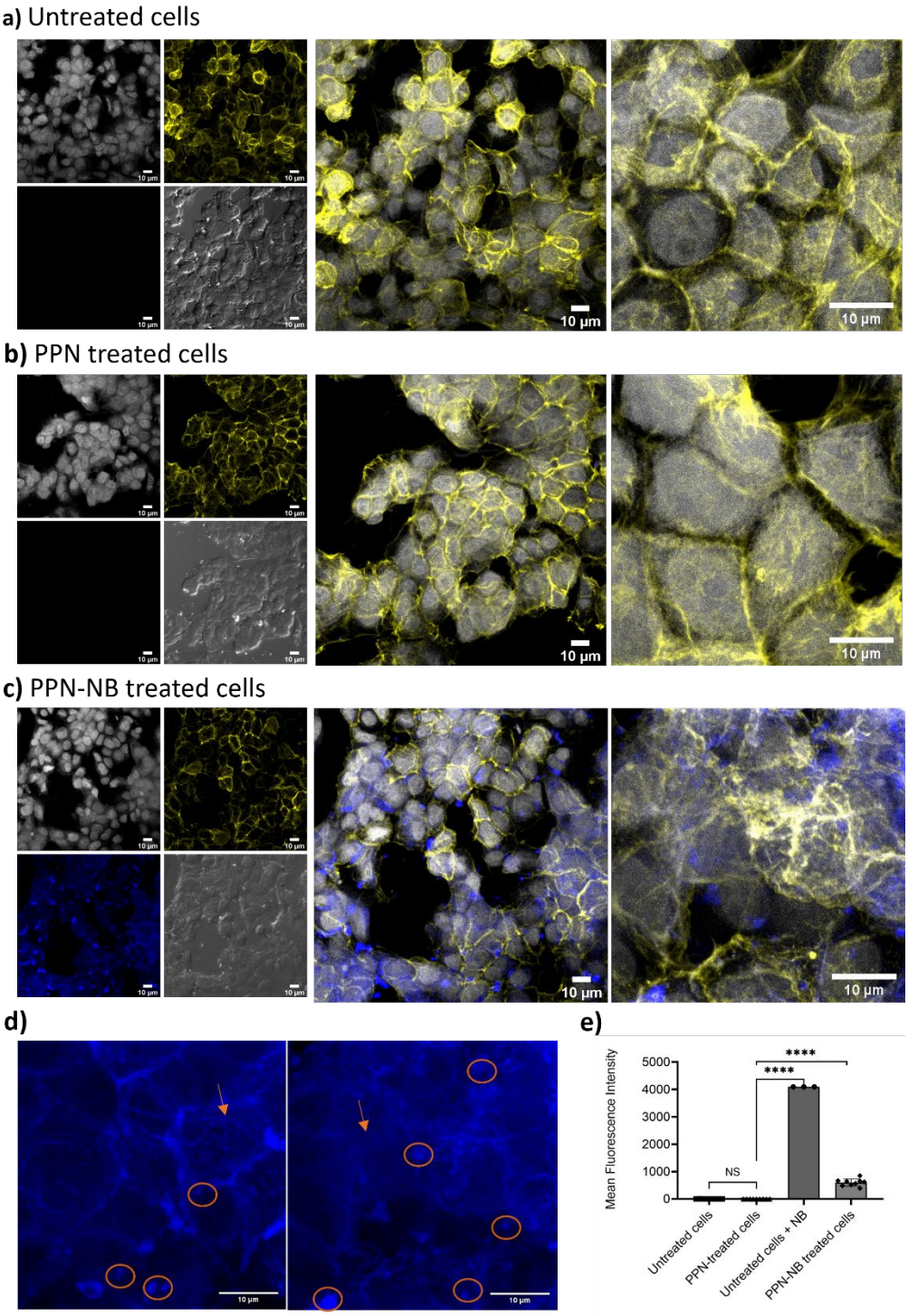

Figure 28. Following incubation, fixation, staining, and imaging with confocal microscopy, MCF-7 cells internalize PPNs conjugated with the lipophilic Nile Blue probe and washed with detergent. Pseudocoloring of the images is performed using ImageJ, with Actin appearing yellow, representing cytoskeletal F-actin; nuclei stained by NucBlue in grayscale; and Nile Blue in blue. Three conditions are compared: (a) untreated cells without PPNs, (b) cells treated with non-conjugated PPNs, and (c) cells treated with Nile Blue-conjugated PPNs. Merged images of all channels under 40× magnification with 2× image zoom and 100× magnification are presented in the large panels on the right. Smaller panels on the left display individual channels for Actin red, NucBlue, and Nile Blue, along with a Transmitted channel. Additionally, (d) exhibits two representative images from PPN-NB treated cells at 100× magnification, focusing on the 660 nm

fluorescent signal for the Nile Blue channel. The images reveal small aggregates (circles) and diffusely distributed stain (arrows) throughout the cells. (e) provides quantification of Mean Fluorescence Intensity (MFI), indicating a significant Nile Blue fluorescence signal in cells treated with PPN-NB. The images were captured using a Nikon C2 Confocal microscope with a 40× dry and a 100× oil immersion objective and analyzed using ImageJ.

4.4. Conclusions

This study investigated plasma polymerized nanoparticles (PPNs) synthesized through radical-induced plasma polymerization, exhibiting well-defined physical and chemical characteristics. The covalent attachment of biofunctional molecules, including Fluorescein Isothiocyanate (FITC) and Nile Blue (NB), was confirmed through its resistance to rigorous washing, validated by XPS, ToF-SIMS, and fluorescence spectroscopy. The successful intracellular uptake of Nile Blue-conjugated PPNs (NB-PPNs) was demonstrated in MCF7 breast cancer cells, showing the potential for PPNs for cell entry, targeted drug delivery and their biocompatibility. The versatility and robust synthesis of plasma polymerized nanoparticles (PPNs) shows that this process not only facilitates surface functionalization but also allows robust covalent conjugations with biofunctional molecules in a single incubation step, minimizing preparation steps and eliminating the need for particle surface modification. This study sets the stage for advancements in employing PPNs as effective carriers in biomedical applications.

Chapter 5. Physicochemical Stability of Plasma Polymerized Nanoparticles

This chapter aimed to address critical gaps in the understanding of long-term stability and surface functionality of plasma polymerized nanoparticles (PPNs) under varied storage conditions. It investigates the effects of polymerization duration, pH levels, and storage temperatures on PPN aggregation, size, and chemical composition, and sheds light on how to preserve PPN integrity and functionality over time. The exploration of ultrasonication as a method to counteract particle aggregation and the examination of molecular conjugation, using Nile Blue as a case study, further bridge the gap in enhancing PPNs for drug delivery and diagnostic purposes. This study contributes to optimizing storage and functionalization strategies, moving one step closer to PPNs' practical utility in healthcare technologies.

5.1. Introduction

Nanoparticles serve as fundamental components across multifaceted industries, leveraging their distinct size-dependent properties and surface functionalities to revolutionize scientific and industrial realms [455-458]. In materials science and electronics, their manipulation at the nanoscale imparts enhanced mechanical properties, conductivity improvements, and novel material engineering capabilities [459, 460]. Polymeric nanoparticles (PPNs), in particular, have transformed drug delivery systems within pharmaceuticals by enabling precise targeting and controlled release of therapeutic agents to specific cellular or tissue targets [286, 346, 461]. Imaging technologies have also been advanced, allowing for highly sensitive diagnostics and intricate cellular studies [462-464]. Owing to their nanoscale precision, nanoparticle offer unparalleled advantages compared to their larger counterparts. Their heightened reactivity [465], customizable surface modifications [466], and superior biocompatibility [467] render them ideal candidates for long-term therapeutic applications.

The physicochemical stability of PPNs is central to nearly every biomedical application and crucial for facilitating their clinical translation. For instance, in drug delivery, where nanoparticles act as carriers for therapeutic agents, the stability of polymeric nanoparticle is critical [468]. Any degradation or instability of the nanoparticle structure compromises the efficacy of the drug, impacting its release profile or its ability to reach specific cellular targets [469]. Moreover, understanding the mechanisms that govern the stability of PPNs is a prerequisite to optimise their durability [470], ensure quality [471], and understand storage impacts for potential large-scale commercialization [472]. This knowledge is key to ensuring the reliability of particle properties, their consistent compliance with requisite standards and performance criteria, and the influence of storage conditions on their characteristics. Changes in stability could affect their interaction with biological systems, by significantly altering particle characteristics, inducing undesirable changes in aggregation, degradation rates, or shifts in size distribution [473].

Particle aggregation is a prevalent phenomenon in particle suspensions which occurs as a consequence of the inherent tendency of suspended nanoparticles to cluster due to mutual attractive forces. As materials shrink from bulk to the nanoscale, their surface area to volume ratio and surface energy increase, placing them in a metastable energetic state compared to bulk materials at standard room-temperature and pressure conditions [474]. These nanomaterial phases exhibit altered electronic, crystal, chemical, and physical properties influenced by their composition, size, and shape [424, 475]. Aggregation in nanoparticle suspensions occurs due to attractive forces between nanoparticles, leading to their adherence and formation of larger agglomerates of varied shapes and sizes [476]. The agglomerate characteristics depend on particle composition and environmental conditions, impacting the stability and sedimentation rate. Techniques like mechanical agitation and electrostatic stabilization aim to reduce the agglomeration rate and enhance stability in nanoparticle suspensions [477, 478]. The propensity for aggregation is closely related to the nanoparticles' degradation rates, as structural changes can further accelerate or instigate the degradation process,

Degradation rates of nanoparticles are another critical factor that can induce undesirable changes, affecting their long-term stability and functionality. The degradation process, influenced by environmental conditions such as pH, temperature, and the presence of reactive species, can lead to the breakdown of nanoparticles, resulting in the loss of structural integrity and functionality [479]. For polymeric nanoparticles, degradation can compromise their ability to encapsulate and release drugs at designed rates, directly impacting therapeutic efficacy [480-482]. Understanding and controlling the degradation kinetics are essential for ensuring the longevity and performance of

nanoparticles, especially in biomedical applications where long-term stability is required [483, 484]. The degradation of nanoparticles not only affects their structural integrity but can also lead to variations in size, which is a significant concern in permeability, nanotoxicity or triggering immunological biological responses [485, 486].

Variations in size due to degradation or swelling can also present significant challenges. Degradation can lead to a reduction in particle size, potentially altering the surface-to-volume ratio and affecting the particles' physical and chemical properties [487]. On the other hand, swelling, influenced by the absorption of surrounding fluids or changes in environmental conditions, can increase particle size and change their mechanical properties and permeability. These size variations can affect the nanoparticles' ability to penetrate biological barriers, target specific sites within the body, and interact with cells and tissues [488-490]. Managing these size changes is crucial for the successful application of nanoparticles in drug delivery and imaging without instigating inflammatory immune responses [491-493]. The interplay between aggregation, degradation, and size variations underscores the complexity of maintaining nanoparticle stability and functionality across diverse storage and application conditions.

Particle stability is significantly influenced by the conditions controlling the particle interaction with their surrounding environments. As suspensions, the pH level profoundly influences particle agglomeration by affecting ionic strength and the potential barrier between suspended particles [494]. This pH-related phenomenon forms a double layer around particles with charged ions, contributing to electrostatic stabilization crucial for preventing particle collisions. Temperature is another key factor that significantly impacts particle agglomeration by altering the kinetic energy of nanoparticles within a suspension [495]. Variations in temperature can influence the Brownian motion of particles, affecting their collision rates and subsequent agglomeration tendencies. However, the synthesis method can also impact the surface energy, morphology, and chemical composition of particles [496, 497]. Subsequently, these properties influence their propensity to agglomerate based on attractive or repulsive forces between particles depending on their formation and growth process [498].

Plasma polymerization has recently emerged as an attracting source of polymeric nanomaterials that have massive potential in the field of biomedical engineering. The intricate process of plasma polymerization involves the controlled fragmentation of organic precursor gases such as acetylene [125] or monomer vapours such as acrylic acid [112, 122] and thiophene [132] in an electric field to initiate a plasma environment [132, 395]. These reactive species like ions, radicals, and electrons interact with the precursor molecules, causing their fragmentation and subsequent recombination into polymerized nanoparticles with reactive surfaces and tailored physicochemical properties [123]. These plasma-synthesized nanoparticles possess a unique surface composition, making them highly adaptable for specific applications across biomedicine [124] and therapeutics [135]. Their significance lies in their potential role as versatile carriers in drug delivery, imaging agents, or components in biosensing systems due to their customizable surface functionalities [100, 106, 337]. Understanding the stability dynamics of these plasma-engineered nanoparticles under diverse storage conditions is critical for unlocking their full potential in biomedical and industrial settings.

This study delves into comprehensively investigating the stability and functionality of plasma polymerized nanoparticles (PPNs) after storage under varied conditions. By examining the influence of polymerization duration, temperature variations, and pH levels on PPN stability in dry and aqueous states, this work aims to explore the impact of storage conditions on particle aggregation, physical composition and surface activity. Additionally, the efficacy of ultrasonication

in mitigating particle aggregation is evaluated and the ability of PPNs to retain functionality post-storage through conjugation experiments is examined with Nile Blue (NB) as a model ligand. The comprehensive analysis seeks to unveil crucial insights into PPN stability and functionality under diverse storage conditions, contributing to the understanding of long-term nanoparticle storage and applications.

5.2. Materials and Methods

5.2.1. Plasma polymerization of nanoparticles

Nanoparticles were produced via a plasma polymerization process in a stainless-steel chamber according to the protocol in [124], explained in Section 2.2 and depicted in Figure 11. PPNs were synthesized in the evacuated chamber, filled with argon, nitrogen, and acetylene using the delayed inflow strategy for acetylene to maximize yield. A 24-well plate placed 79 mm below the RF electrode collected nanoparticles under a $1.5 \times 10^{\wedge -1}$ Torr pressure. The system, powered at 100 W by a 13.56 MHz RF generator, operated for 6.5 minutes before collection for analysis.

5.2.2. pH buffer solution preparation

Different types of nanoparticle suspensions were prepared by dispersing the particles in ultra-pure Milli-Q (Sigma Aldrich, EQ 7000) water (MQ), or buffer solutions at different pH values. The acidic solution involved dissolving 0.3 g of acetic acid in 900 ml water, adding 0.538 g NaCl, and titrating to the target pH 4 at 25°C. The NaH_2PO_4 solution was created by dissolving 0.6 g NaH_2PO_4 in 900 ml water, supplemented with 0.021 g NaCl, and adjusting the pH to 7.4 through titration. Meanwhile, the basic Methylamine Buffer was formed by dissolving 0.311 g Methylamine in 900 ml water, adding 0.4 g NaCl, and titrating to the desired pH 11. In each case, the ionic strength was 0.01 M, and the final volume was adjusted to 1000 ml with water.

5.2.3. Hydrodynamic Size and zeta (ζ) Potential measurements

PPNs were suspended in 2 mL of each pH-adjusted solution, achieving a concentration of 3×10^{10} particles/mL. Absorbance was measured using an ELx800 Biotek plate reader, yielding a value of 0.5. The particle suspensions were vortex mixed for 30 seconds and sonicated using a stainless steel Hwashin PowerSonic405 ultrasonic bath at 350 W 40 kHz for 2 minutes. The nanoparticles were then transferred to disposable folded capillary cells under sterile conditions using 1 mL syringes and sonicated prior to measurements for 2, 5, 10 or 15 minutes, as specified. Zeta (ζ) potential measurements were conducted, and the average ζ- potential values for specific pH levels were reported, along with standard deviations. Hydrodynamic size measurements, the average (effective) size and particle size distribution were also determined based on three measurements obtained from at least three independent runs.

5.2.4. Dry and aqueous storage at different temperatures

For dry storage, collector wells with PPNs were sealed and placed away from the light in an incubator at room temperature (25°C) or in the fridge at 4°C, as specified. On the day of the measurement, the PPNs were dissolved in the specified base solvents prior to size and zeta potential measurements.
For aqueous storage, PPNs from the collector wells were suspended in 10 mL of solvent and

aliquoted to centrifuge tubes for storage. The stock suspensions were stored in an incubator at room temperature (25°C) or in the fridge at 4°C, as specified. On the day of the measurement, PPNs were aliquoted from the stock solutions and diluted to the same concentration as above.

5.2.5. X-ray photoelectron spectroscopy (XPS)

The chemical state and composition of the PPN sample surfaces were investigated using XPS with a Thermo Fisher K-Alpha+ XPS/UPS system (Thermo Fisher Scientific, USA). The XPS system utilized a monochromated, microfocused Al K-Alpha X-ray source and a 180° double focusing hemispherical analyzer equipped with a 128-channel detector. Freeze-dried PPNs were arranged on an indium foil affixed into a double-sided conductive carbon tape within the XPS sample holder. The survey spectra were collected at a pass energy of 200 eV and a resolution of 1 eV, while the high-resolution C 1s spectra were recorded at a pass energy of 50 eV and a resolution of 0.1 eV. The base pressure was below 5x10-8 mbar for all the measurements. A total of 10 scans were conducted for each sample. Elemental composition calculations and peak fitting for high-resolution peaks were performed using the Avantage software (Thermo Fisher Scientific, USA).

5.2.6. Transmitted Electron Microscopy (TEM)

The sample morphology and dimension were investigated by transmission electron microscopy (TEM). Nanoparticles were either collected in a dry state from collector wells or suspended in the base solvent, and then subjected to a 2-day freeze-drying process. For imaging, the nanoparticles were deposited inside the cylindrical containers were scratched off by sharp tweezer and uniformly dispersed on the copper grids with lacy support films. All the samples were observed by transmission electron microscope JEOL-2100 at high tension of 200 kV. The original data was processed by Digital Micrograph Software (Gatan Inc.).

5.2.7. Conjugation of Nile Blue to plasma polymerized nanoparticles

Nile Blue (N0766, Sigma-Aldrich) was dissolved in Milli-Q water to a stock concentration of 0.25 mM. The PPNs were produced at a higher yield following the protocol described in [124]. Fresh nanoparticles were suspended in 10 mL Milli-Q water at an initial concentration of 3.76×10^{11} PPN/mL. For NB conjugation, 3.8 mL of the diluted 0.25 mM NB solution were added to 3 mL of nanoparticles stock, achieving approximately 200 pg of NB per 10^5 nanoparticles. The reaction mixture was covered in foil and incubated under constant shaking at room temperature for 30 minutes. The samples were then centrifuged at 8000 rpm for 10 minutes and washed with 10 mL Milli-Q water three times. The washed samples were centrifuged, and pellets were freeze dried for XPS or ATIR-FTIR using the Freeze Dryer (Alpha 2-4 LSCbasic) for 1 day. For fluorescence measurements, the washed samples were moved to a black plate UV Greiner box with clear-bottom 96 well plates. Fluorescence intensities were measured using a ClarioStar microplate reader (BMG Labtech, Ortenberg, Germany) at excitation and emission wavelengths of 624 nm and 678 nm, respectively.

5.2.8. Statistical analysis

The data in this study is presented as mean ± standard deviation (SD), unless otherwise stated. Analysis was performed using OriginPro (version 9.9.0.220) or Excel (Microsoft 365 MSO, Version 2309 Build 16.0.16827.20278).

5.3. Results and discussions

5.3.1. Plasma polymerization and growth of PPNs

Plasma polymerization involves the generation of precursors in a plasma state, which then fragment and recombine to facilitate the formation of primary nanoparticles. This plasma-based approach is commercially appealing for its rapid processing and scalability, enabling the production of large quantities in a single, environmentally friendly step. However, this process is susceptible to undesired coagulation and coalescence effects where particles join due to collisions and fuse together, respectively [474]. In plasma polymerization, processing parameters such as power input, precursor flow rate and pressure and the polymerization time, play important roles in determining the characteristics of the synthesized nanoparticles. The plasma polymerization time, in particular, directly influences the size, distribution, and aggregation behaviour of the nanoparticles. To shed light on the role of plasma polymerization time in nanoparticles size aggregation, we compared the average (effective) sizes of PPNs synthesized by varied polymerization durations (Figure 29a). The PPNs were collected in cell culture 24-well plate then suspended in Milli-Q water for size measurement via dynamic light scattering.

Figure 29b shows the average hydrodynamic size and polydispersity index (PdI) of the PPNs after 5, 10 and 30 minutes of polymerization. The results signify a positive relationship between the duration of polymerization and the resultant nanoparticle size, showing an increase in size from 190 nm to 440 nm and further to 850 nm as the polymerization time extends. Simultaneously, the PdI showed an upward trend, reflecting the increased variation in particle sizes within the sample as the polymerization duration extends from 5 to 30 minutes. These results indicate that prolonged polymerization periods not only yield larger nanoparticles but also contribute to a broader range of sizes within the nanoparticle population.

The increase in nanoparticle size, observed with prolonged polymerization periods, aligns with the mechanism of PPN formation (Figure 30). Initially, precursors undergo gas-phase generation and decomposition, leading to the creation of supersaturated states contributing to nucleation [366, 474]. This phase triggers the formation of nanometer-sized clusters dominated by negative ions. As coagulation progresses, these clusters collide, resulting in the development of particles approximately 10 nm in diameter. Subsequent growth is primarily governed by the accumulation of positive ions and neutral radicals, ultimately leading to larger particle sizes. Once particles reach a critical size, they either exit the plasma bulk or descend toward a lower electrode due to gravitational forces while a subsequent growth cycle begins [124, 499]. This plasma polymerization of nanoparticles is thus prone to coagulation with polymerization time, where particles collide and agglomerate for longer, as well as coalescence, causing particle fusion, both contributing to the observed increase in particle size. As such, a polymerization time of 5 mins was used in the production of PPNs for the subsequent shelf-life studies.

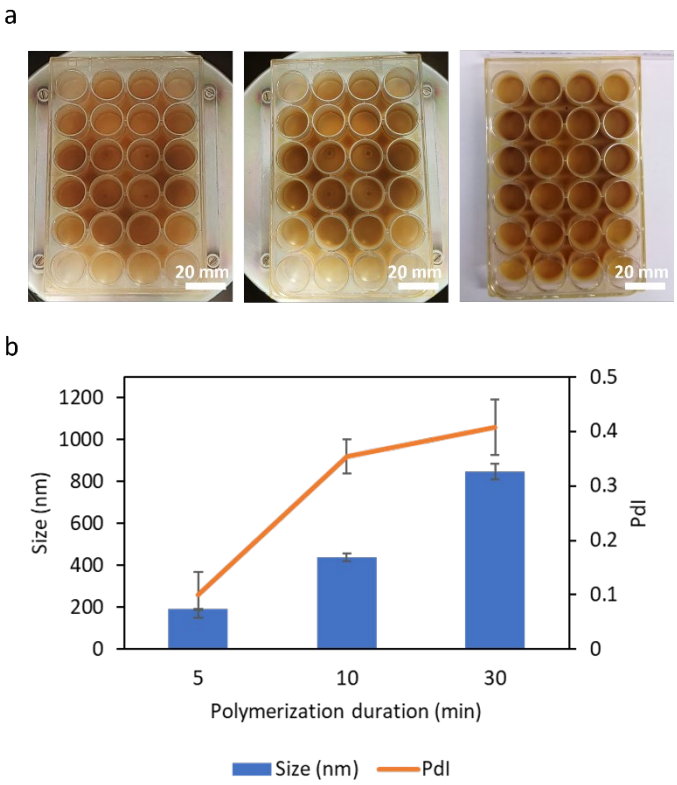

Figure 29. (a) (Left to right) PPNs deposited on collector plates following polymerization durations of 5, 10, and 30 minutes. (b) Average hydrodynamic size and polydispersity index of PPNs collected from different polymerization durations.

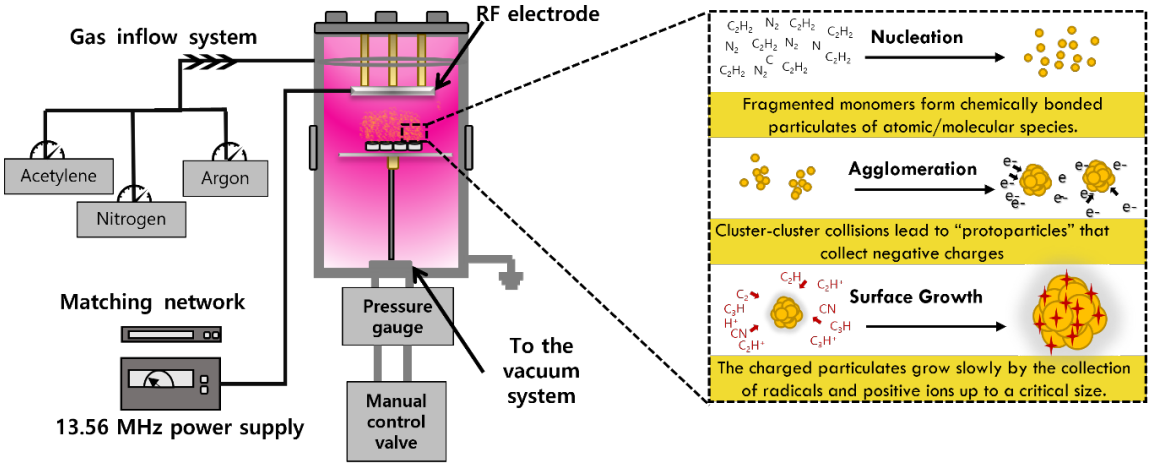

Figure 30. Collection schematic showing the plasma reactor and PPN growth mechanism.

5.3.2. Physical stability

The physical properties of nanoparticles, including their size and morphology are profoundly influenced by their surrounding environment. The pH of a solution significantly impacts the stability of nanoparticles, influencing their agglomeration tendencies and altering degradation rates [494]. To examine pH effects on PPN agglomeration, various water-based PPN suspensions were created

at pH 4, 7.4, and 11. This involved dispersing nanoparticles in ultra-pure Milli-Q water and buffer solutions, enabling analysis under acidic, neutral, and basic conditions.

Figure 31a shows the PPN suspensions in the collector wells imaged upon adding the four base solvents. The particles appeared to be easily dispersible and a homogeneous interface could be observed with signs of sedimentation only in the centre of the well with the pH 4 buffer. When left to sediment overnight, a layer of particles can be seen depositing at the base of the wells with buffer solutions, while the PPN solution in Milli-Q water appears to be less heterogeneous and sedimenting at a slower rate (Figure 31b). Agitating the particles through mechanical stirring and vortex mixing was sufficient to redisperse the particles.

To quantify these observations, the PPN suspensions were characterized by obtaining the average (effective) hydrodynamic particle size upon dispersion immediately after production. In Figure 31c, the effective size of PPNs dispersed in Milli-Q water, pH 7.4 and pH 11 immediately after suspension were around 200, 180 and 270 nm respectively. However, a substantive increase in size to microns was noted at pH 4. The particle size distribution curves of the PPNs in Figure 31d show distinctive characteristics influenced by pH variations. The size distribution curves for pH 7.4 and Milli-Q suspensions demonstrated closely aligned peaks around 200nm, indicating greater stability and homogeneity relative to the other solvents. The similarity in peak values implies minimal aggregation, with the Milli-Q suspension showing slightly superior stability, denoted by its marginally narrower distribution. At pH 4, a narrow peak is observed in the distribution curve, yet with a larger peak value at 2600nm, suggesting considerable aggregation tendencies in this acidic medium. In contrast, at pH 11, a broader size distribution curve is evident, accompanied by a smaller peak value at 300nm, indicating a more dispersed state of the nanoparticles.

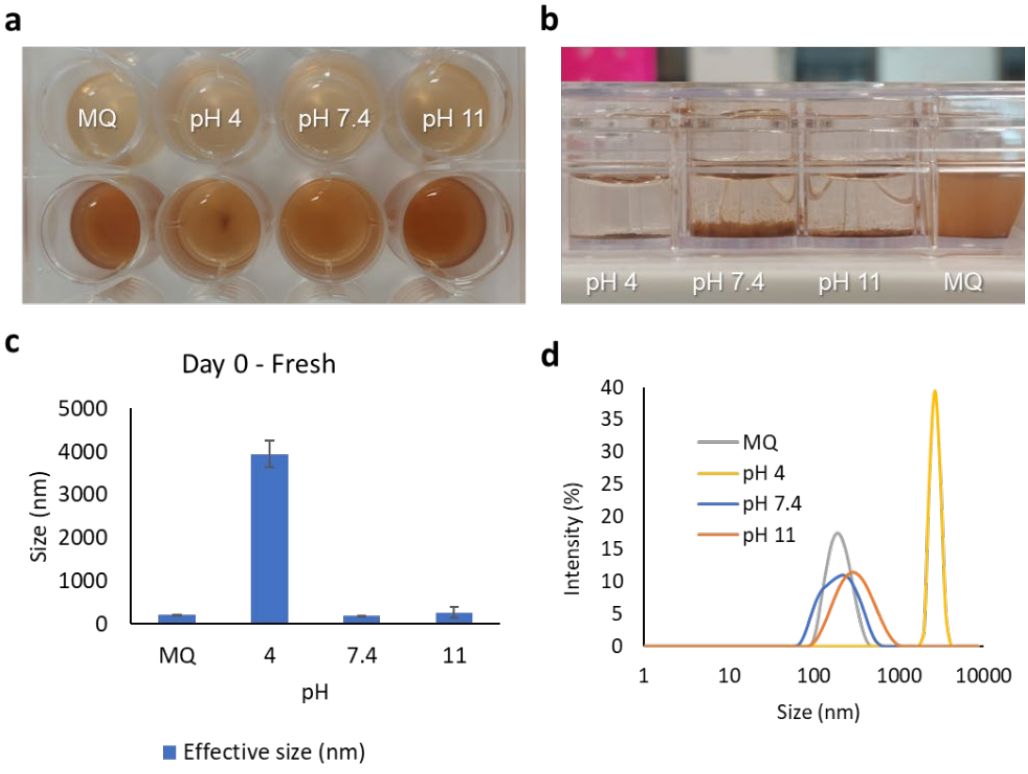

Figure 31. (a) PPN suspensions immediately after dispersion with the different base solvents of Milli-Q (MQ) and buffer solutions at pH 4, 7.4 and 11 and (b) after sedimentation. (c) Effective hydrodynamic size

and (d) the particle size distribution of PPNs in Milli-Q (MQ) and buffer solutions at pH 4, 7.4 and 11 after fresh production of PPNs.

Studying the impact of different storage temperatures determines the stability profile of PPNs, identifying optimal storage conditions that maintain their physical properties. To assess changes in the physical properties of PPNs with temperature, we measured the effective hydrodynamic particle size after 3 months of storage at room temperature and 4°C. This involved evaluating the effective particle sizes post-storage in both dry and aqueous states across the various base solvents. The results in Figure 32 show that particles stored in a dry state had a consistently smaller effective size compared to those stored in an aqueous state, regardless of temperature. Moreover, the largest particle sizes was found at pH 4 and smallest sizes in Milli-Q water across all conditions. Regarding temperature influence, particles stored dry had smaller sizes at room temperature with the largest size near 2 microns occurring in pH 4 (Figure 32a). On the other hand, PPNs stored in aqueous state displayed smaller sizes at 4°C and significant increases in size at room temperature ranging from 2 – 6 µm (Figure 32b). These results indicate that storing particles in dry or aqueous states yields distinct effects on their stability and behaviour. Dry storage tends to preserve particle stability by minimizing inter-particle interactions, reducing the risk of aggregation or agglomeration [500]. Dry particles are less prone to agglomeration as the absence of a solvent medium limits particle movement and collision. This method also extends particle shelf life by preventing potential degradation from reactions with solvents. The presence of a solvent introduced challenges in maintaining stability, potentially leading to aggregation, coalescence, or sedimentation over time. In aqueous environments, particle aggregation is intensified by Brownian motion, with higher temperatures increasing kinetic energy and collision rates, thus fostering aggregation [501, 502]. Conversely, lower temperatures stabilize suspensions by reducing movement and collisions. In dry states, lower thermal energy enhances van der Waals forces among particles, promoting aggregation through closer particle interactions and moisture-mediated bridges, especially in fine powders where surface interactions are significant [503, 504]. This effect is compounded by moisture condensation at lower temperatures, contributing to particle size increase and altered morphology [505].

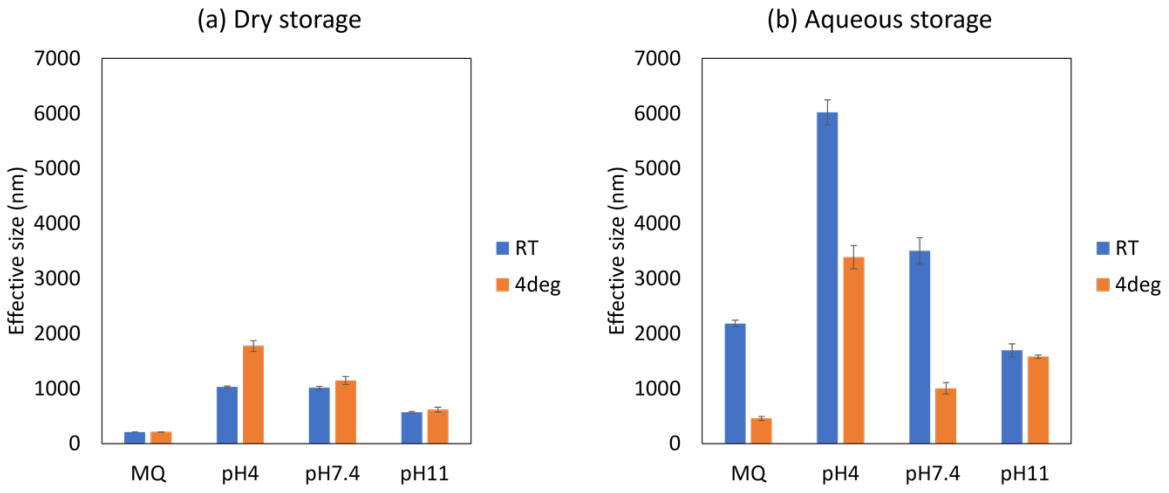

Figure 32. Effective size measurements of PPNs in Milli-Q (MQ) and buffer solutions at pH 4, 7.4 and 11 after (a) dry and (b) aqueous storage for 3 months at room temperature and 4°C after 3 months.

Figure 33 presents TEM images of PPNs that were stored at room temperature or 4°C. The particles were either kept in various base solvents, or in a dry state then resuspended directly before imaging on the same day. The TEM analysis revealed that PPNs exhibit a morphology resembling that of cauliflower in their overall shape and composition. These representative images confirm the anticipated spherical structure and demonstrate smaller particles aligning to form chains. Estimations suggest the individual particles within these chains measure up to 200 nm in diameter, while the chains themselves vary in size, spanning from 300 to 900 nm. The large aggregates at pH 4 can also be seen, consistent with the previous findings on the effective size of freshly suspended PPNs. The smaller (<200 nm) particles visible in these images emphasize the range of particle sizes present and their interactions within the plasma system.

The TEM images indicate a similar morphology across all storage conditions, implying consistency in shape and structure. Displaying a spheroid shape is commonly associated with homogeneous growth in plasma environments. During the sample collection phase, the dominance of grain-molecule collisions likely propelled the particle growth process, as evidenced by the presence of similar grains observed in various dusty plasmas [506, 507]. The uniformity in particle size within the plasma environment is attributed to the charging mechanism at play. Larger particles, owing to electron mobility dominance, typically maintain negative charges, whereas smaller particles (<5 nm) undergo stochastic charging, intermittently acquiring positive charges. This stochastic charging phenomenon significantly influences rapid particle coagulation, ultimately contributing to the consistent and uniform growth of particles. As particles grow larger within the plasma, their negative charge fosters the attraction and absorption of smaller particles—a phenomenon illustrated in TEM images displaying particles as small as 50 nm. This observation highlights how larger particles act as collectors for smaller ones, influencing the dynamics of their growth within the plasma environment [366].

Nevertheless, discernible differences in the particle interactions within the distinct storage conditions emerge when exposed to the two varying temperatures. The images show that PPNs stored dry at 4°C form larger chains compared to those at room temperature, while PPNs stored in solution are slightly larger at room temperature than at 4°C. This trend aligns with the observed details in the effective size measurements above. Particles stored in dry conditions at room temperature exhibit certain characteristics, such as individual particle segregation or minimal agglomeration due to the absence of moisture. Conversely, those stored in aqueous conditions at room temperature displayed signs of clustering or aggregation owing to the presence of a solvent, altering their morphology. For longer durations of storage, PPNs stored in dry state were kept at room temperature while those stored in aqueous states were kept at 4°C.

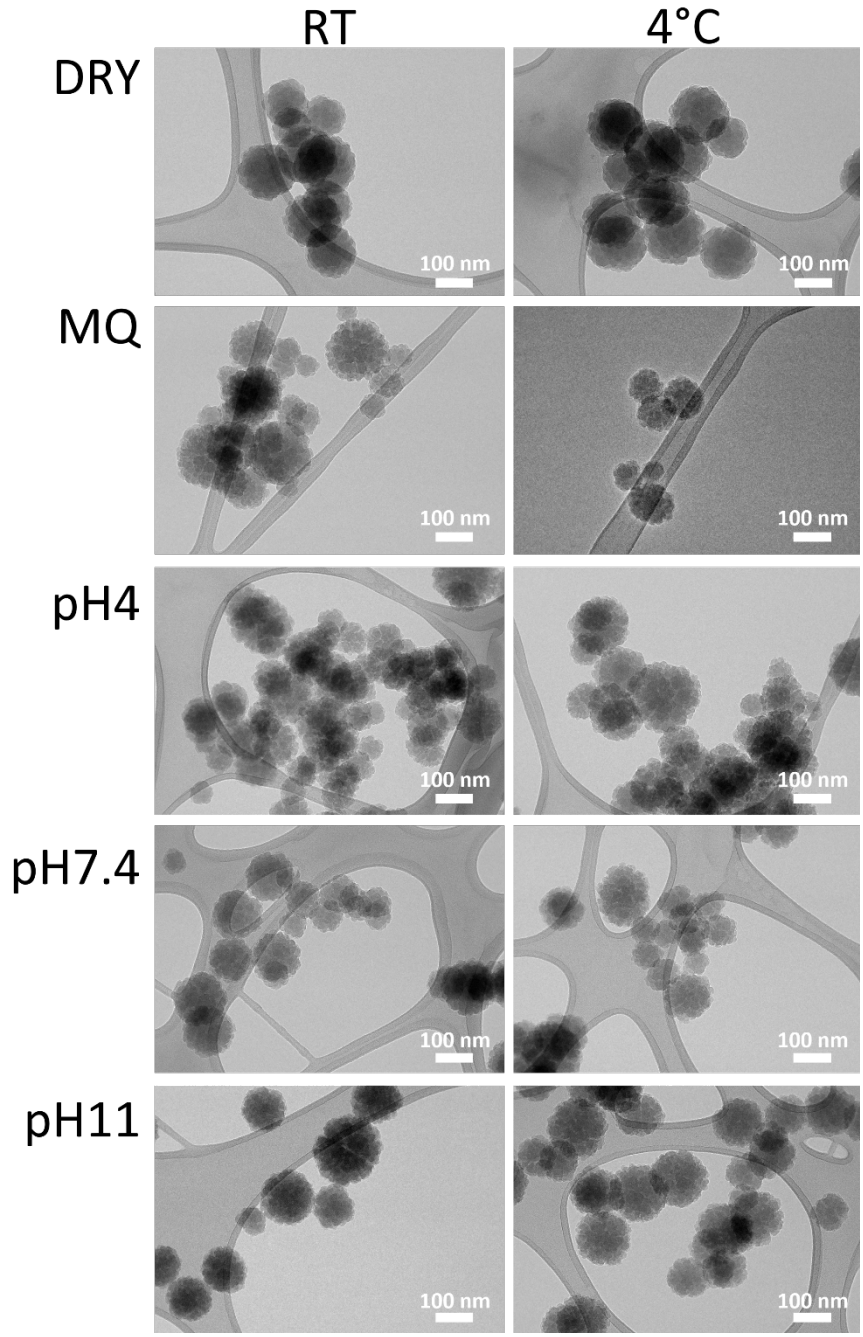

Figure 33. TEM images of PPNs stored under two temperature conditions 4°C and RT in dry and aqueous state across the different solvents (Milli-Q (MQ) and buffer solutions at pH 4, 7.4 and 11).

To assess the impact of storage media on the physical stability of nanoparticle suspensions over time, the PPN effective size was monitored over a duration of 6 months. Figure 34a shows the changes in particle size after they were resuspended in the four different solvents from a dry state. Over the course of the experiment, the particles consistently grew in size and the increase in particle size after resuspension varied with the solution used. The smallest growth was seen in Milli-Q water, with particles reaching 350 nm. As the pH of the solution decreased from 11 to 4, the particle size progressively enlarged to 600 nm, 2600 nm, and finally 4000 nm at pH 4, indicating that lower pH

levels led to greater increases in particle size. This significant size increase at acidic conditions indicates that lower pH levels exacerbate the aggregation process, possibly due to the destabilization of surface charges on the nanoparticles, leading to reduced electrostatic repulsion and enhanced aggregation. This trend was consistent with the fresh measurements obtained from dispersion immediately after production; however, particles resuspended in pH 7.4 and pH 11 gradually surpassed the 500 nm threshold within a month. The smallest size increase in Milli-Q water indicates a relatively stable environment for PPNs due to the absence of ionic strength alterations that can affect the stability of colloidal systems. Notably, while pH 11 suspensions remained within the nanometer range, those in a neutral buffer escalated to the micron size by the three-week mark.

Figure 34b illustrates the size variations of PPN suspensions stored in an aqueous state in the base solvents over the course of 6 months. The aqueous storage of the PPNs in Milli-Q and pH 4 resulted in similar changes in size to dry storage. The effective PPN size in the pH 7.4 buffer increased over 500 nm within 3 weeks, eventually reaching the same micron size as in dry storage. Interestingly, PPNs in pH 11 aggregated to micron size within a week and maintained as such over the 6-month period. Prolonged suspension and redispersion of the plasma polymerized nanoparticles in Milli-Q water seemed to have maintained the most stable effective size, while pH 11 seemed to present a potential candidate for resuspension but not for storage. The rapid increase in size within the first week for PPNs in pH 11 and the subsequent stabilization suggest a swift initial aggregation followed by a plateau, indicating a possible equilibrium state where further aggregation is limited by the formed structure's physical constraints. The results also suggest that pH 7 may be suitable for resuspension of particles stored dry or the resuspension in solution for less than 1 month, while pH 4 caused immediate aggregation and remained as such for the duration of the study.

The observed aggregation patterns of PPNs in acidic conditions (pH 4) over an extended period can be attributed to the intricate interplay between nanoparticle surface chemistry and the surrounding pH environment. In acidic media, the protonation of surface functional groups on PPNs likely leads to a decrease in surface charge density, diminishing electrostatic repulsion between particles and thus facilitating closer particle interactions and aggregation. This effect is compounded in aqueous conditions where the solvent medium enhances particle mobility, allowing for more frequent collisions and potential van der Waals interactions, further driving the aggregation process. On the contrary, in neutral to basic conditions, the deprotonation of surface groups may increase the surface charge, enhancing electrostatic repulsion and stabilizing the colloidal system against aggregation. The minimal aggregation observed in Milli-Q water suggests an optimal balance between electrostatic stabilization and the absence of additional ionic species that could shield surface charges and promote aggregation. The differential aggregation behavior underlines the crucial role of surface charge interactions and solvent-mediated dynamics in governing nanoparticle stability, highlighting the nuanced relationship between nanoparticle surface chemistry, pH, and the mediating role of the solvent in aggregation processes. These insights into the physical behavior of PPNs under various conditions pave the way for a deeper examination of their chemical stability to combine the role of intrinsic material properties and external factors in influencing nanoparticle longevity and functionality.

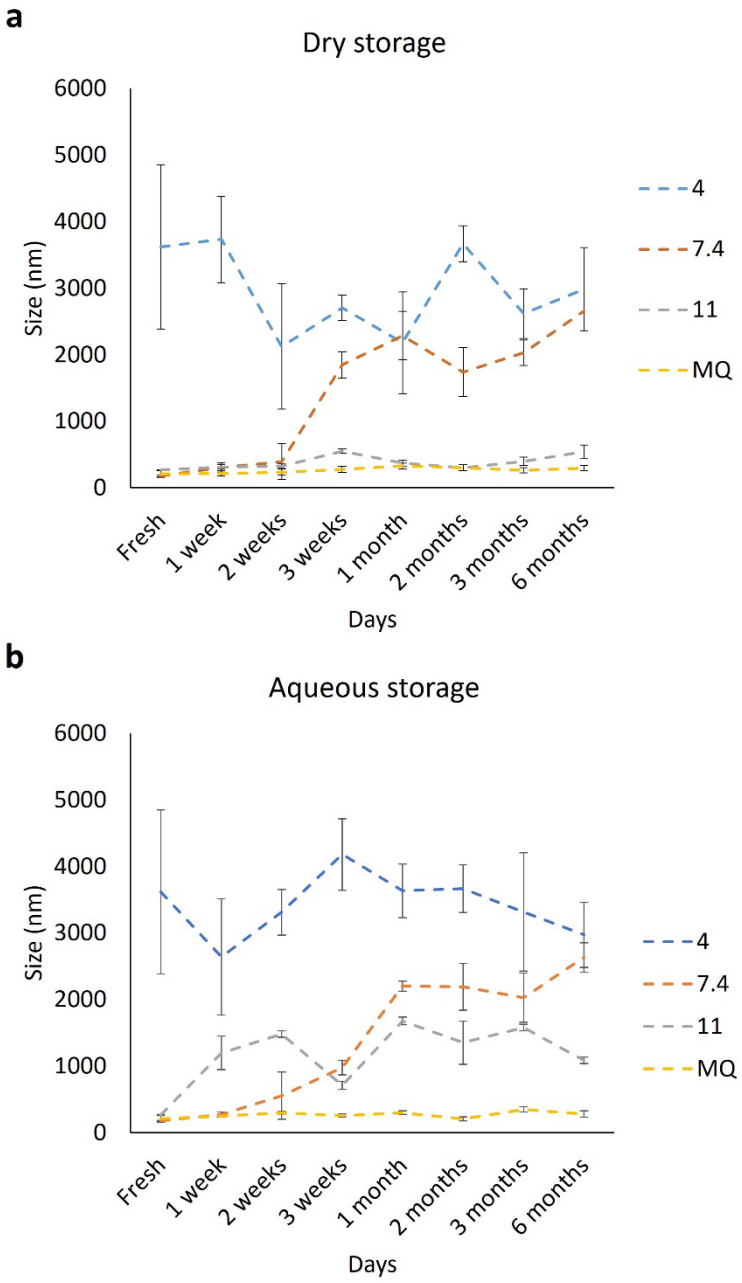

Figure 34. The changes in particle size and zeta potential throughout 6 months (a) after dry storage followed by resuspension in the different base solvents and (b) of PPNs stored aqueously in the base solvents (Milli-Q (MQ) and buffer solutions at pH 4, 7.4 and 11. Particles stored dry were kept at room temperature while those stored in solution were at 4°C.

5.3.3. Chemical stability

To compare the surface chemical characteristics of PPNs stored in dry and aqueous state under two temperature conditions, we explored their surface composition using XPS. The XPS survey spectra analysis indicated the presence of carbon (C1s), nitrogen (N1s), and oxygen (O1s) elements in all the samples, regardless of storage conditions, as has been represented in Figure 35a. The presence of C1s, N1s, and O1s across all samples suggests that the basic elemental composition of the

nanoparticles remains unchanged despite different storage conditions. When comparing the atomic concentrations of the elements between the storage solutions in Figure 35b-f, consistent levels of carbon can be seen across the different storage durations and temperatures, which is expected as carbon is a fundamental element in polymer structures and is less susceptible to significant alterations under typical storage conditions. On the other hand, an increasing trend in oxygen concentration can be observed. The higher concentration of oxygen (O1s) might indicate an autooxidation process occurring with time likely due to exposure to the oxygen in the surrounding environments leading to more oxygen-containing functional groups on the nanoparticle surface [65, 508]. Autooxidation occurs when reactive radicals interact with atmospheric oxygen, a process observed in similar plasma coatings [110, 113, 340] and other polymers derived from different precursor molecules [130, 132]. The increase in O1s could also indicate surface modifications or adsorption of oxygen-containing species from the surrounding environment or buffer solution. This increase is prominent especially at 4°C compared to room temperature, which indicates either a stabilization of oxygen-containing functional groups or a slower rate of degradation at the lower temperature. At 4°C, the surface might interact differently with any residual gases or trace moisture in the environment, leading to increased oxygen incorporation onto the nanoparticle surface.

At pH extremes (pH 4 and pH 11), the O1s atomic concentration exhibits distinct changes whereby its value is the greatest at pH 4 and the lowest at pH 11. One likely explanation is that the protonation of surface functional groups might occur under acidic conditions [509]. This protonation could lead to an increase in oxygen-containing species on the nanoparticle surface, resulting in an elevated O1s signal. Conversely, deprotonation or hydrolysis of various functional groups could occur under basic conditions. This process might result in the breakdown, removal or transformation of oxygen-containing functional groups, potentially reducing their presence on the nanoparticle surface including the O1s signal. Despite these changes, aqueous suspensions find favour in applications such as biomedical uses or drug delivery, where interactions with biological systems or the need for a liquid medium for administration or storage are advantageous.

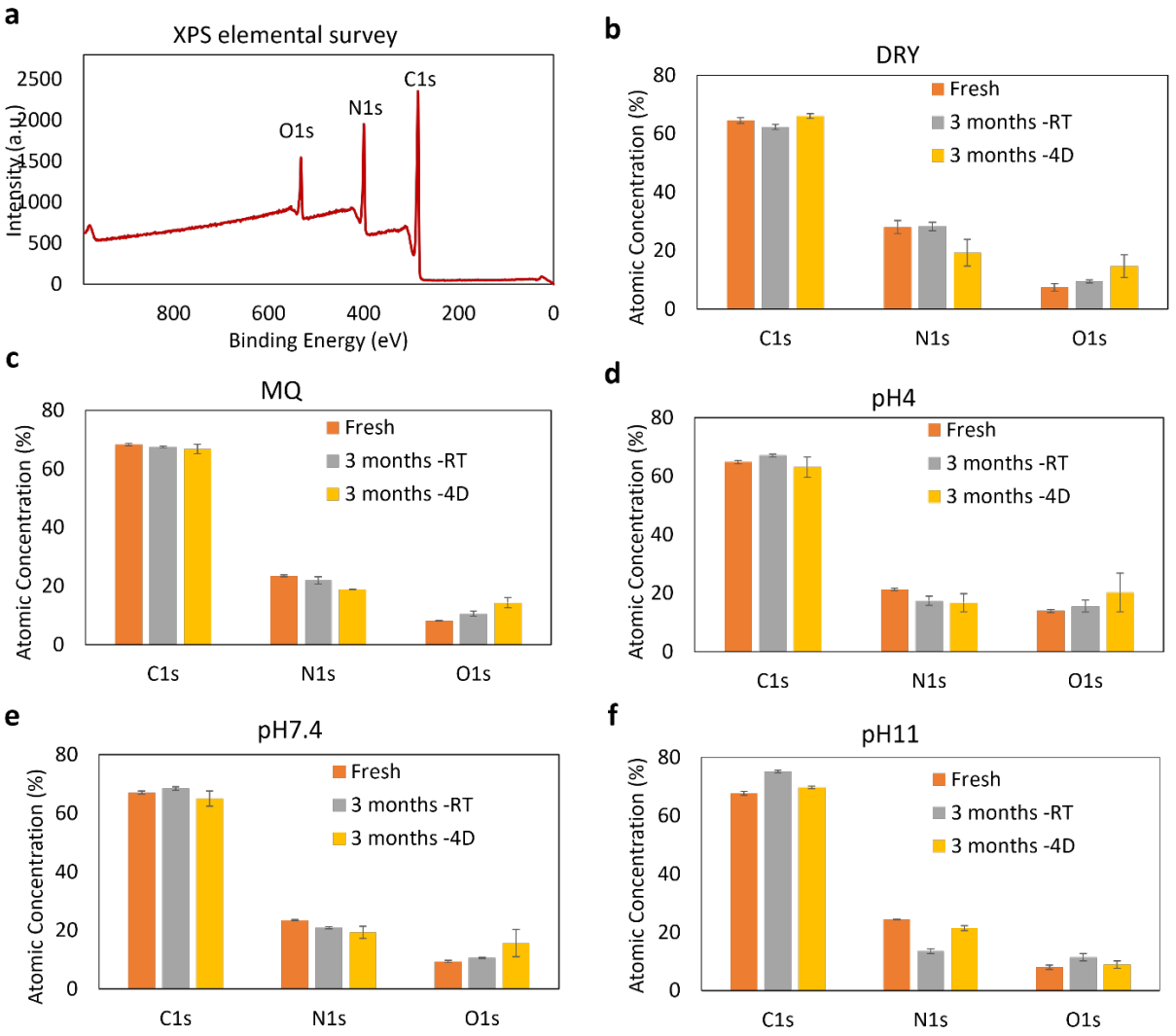

Figure 35. XPS survey and atomic concentrations of C, N and O of PPNs stored dry and aqueous in Milli-Q (MQ) and buffer solutions at pH 4, 7.4 and 11.

Assessing the stability of colloidal systems can be achieved through zeta potential measurements, which serve as a vital indicator of the electrostatic repulsion between particles, thereby aiding in the prevention of agglomeration. As such, the surface charge of the PPN suspensions prepared in the various buffer solutions was estimated by measuring their zeta potential. In Figure 36, the zeta potentials of PPNs dispersed in Milli-Q water, pH 7.4 and pH 11 immediately after suspension were overall decreasing with pH and at magnitudes between 30 and 40 mV, except at pH 4 with zeta potential around 11 mV. Colloidal stability is generally achieved when the zeta potential exceeds ±20 mV, indicating sufficient electrostatic repulsion to prevent particle aggregation [510]. A zeta potential close to zero means there is minimal electrostatic repulsion between particles, making them more prone to agglomerate. This indicates a lower stability of the PPNs at pH 4 compared to other pH conditions, as evidenced by the significantly lower zeta potential value. Higher zeta potentials at pH 7.4 and pH 11 suggest stronger electrostatic repulsion between particles, leading to more stable suspensions that are less prone to agglomeration.

Figure 37a illustrates the changes in zeta potential after dry storage followed by resuspension in the

four different solvents at different time points. The zeta potential gradually declined throughout the six-month storage in all instances except for the pH 11 resuspensions. Specifically, Milli-Q and pH 7.4 resuspensions registered zeta potentials dropping to 27 mV and 0 mV, respectively, while pH 4 resuspensions decreased to 6 mV. In contrast, pH 11 resuspensions fluctuated between -40 and -23 mV. In Figure 37b, the zeta potential of PPN aqueous suspensions in the base solvents were measured throughout the 6 months. The aqueous storage of the PPNs in Milli-Q and pH 4 resulted in similar changes to dry storage, notably with a further decrease in zeta potential in solutions reaching 21 mV and 3mV respectively. This is consistent with the previous effective PPN size measurements.

The comparative analysis of physical and chemical characteristics across these four base solvents and different temperatures underscores the substantive impact of pH on particle agglomeration tendencies. Agglomeration can be explained by the classical Derjaguin-Landau-Verwey-Overbeak (DLVO) theory, which considers the interplay of van der Waals (vdW) attractive forces and electrostatic double layer (EDL) forces [445]. In this framework, agglomeration occurs when EDL forces are diminished relative to vdW forces. The surfaces of most nanoparticles contain titratable surface chemical groups (e.g., N_2, CH, COOH), which can be protonated by H^+ (resulting in a positively charged surface at low pH) or deprotonated by OH^- (yielding a negatively charged surface at high pH). According to the fundamental principles governing particulate systems, colloidal suspensions tend to lose stability when the zeta potential approaches zero with values lower than 20 mV more prone to cause aggregation [511]. This absence of electrical charges within the system diminishes the repulsive forces among suspended particles, leading to increased aggregation. These trends emphasize the intricate interplay between electrostatic repulsion and attractive forces in nanoparticle interactions. At pH 4, the buffer solution introduces a more acidic environment, leading to a rise in proton concentration. In negatively charged particles, this increased proton concentration can neutralize surface charges, reducing the electrostatic repulsion forces between particles. Consequently, with diminished repulsive forces, attractive forces like van der Waals interactions or hydrophobic effects become more dominant, allowing particles to come closer and aggregate. This aggregation tendency at pH 4 is primarily due to the decreased repulsive forces among negatively charged nanoparticles, consistent with the low zeta potential value. This is consistent with the XPS analysis which revealed an increase in oxygen content on the polymer particles' surfaces, indicating the presence of additional oxygen-containing functional groups such as hydroxyl and carboxyl groups. These groups are capable of ionizing in aqueous environments, which can significantly influence the surface charge of the particles. Conversely, in a pH 11 buffer, the environment tends to be more alkaline. This high pH level typically results in an abundance of hydroxide ions (OH-) in the solution. For negatively charged particles, such as many nanoparticles, the alkaline conditions create a scenario where the excess OH- ions can stabilize the negative charge on the particle surfaces. This stabilization prevents repulsion between similarly charged particles, thereby reducing aggregation or clumping over time and promoting stability. In a pH 7.4 buffer, negatively charged particles tend to remain stable over time due to electrostatic repulsion. At this pH, the surface charge of the particles aligns with the surrounding medium's pH, leading to a negative charge on the particle surface. Since particles repel each other due to like charges, this electrostatic repulsion prevents them from aggregating or clumping together, thereby maintaining their stability in the suspension. Overall, these results underscore the critical influence of the pH of the environment on PPN stability and aggregation. pH control significantly impacts nanoparticle size, charge, and stability in different suspensions.

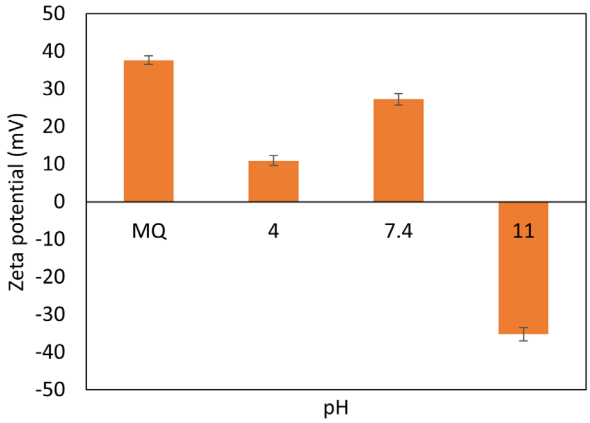

Figure 36. Zeta potential of PPNs in Milli-Q (MQ) and buffer solutions at pH 4, 7.4 and 11 after fresh production.

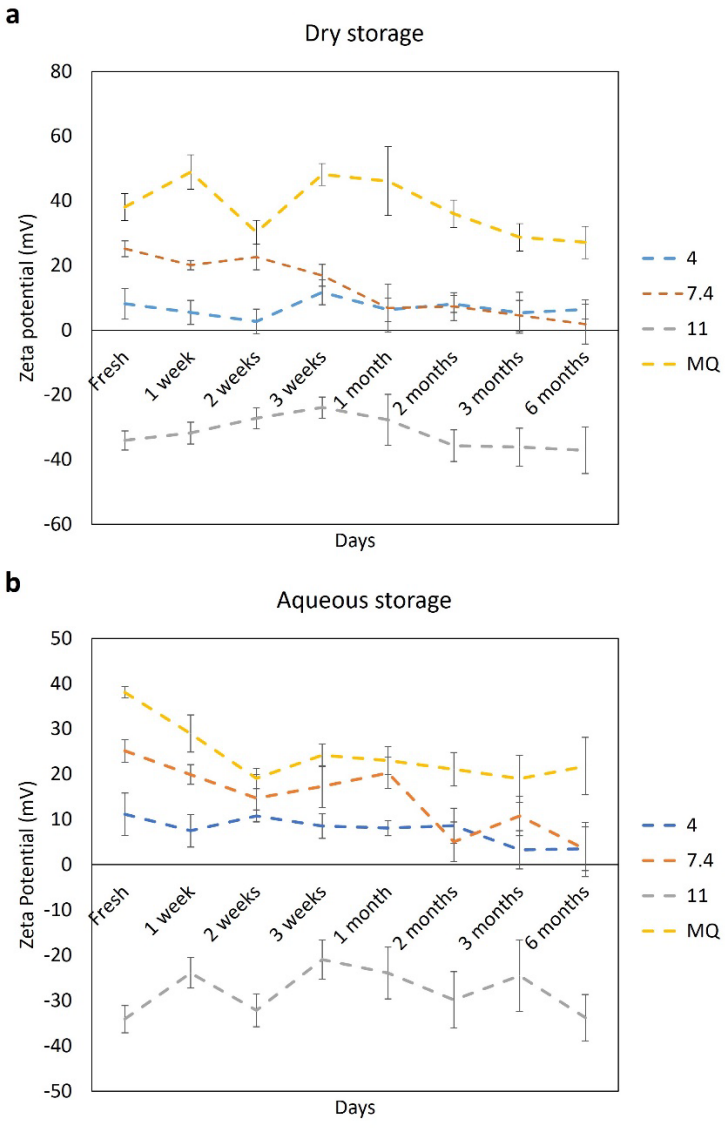

Figure 37. The changes in zeta potential throughout 6 months (a) after dry storage followed by resuspension in the different base solvents and (b) of PPNs stored aqueously in the base solvents Milli-Q (MQ) and buffer solutions at pH 4, 7.4 and 11. Particles stored dry were kept at room temperature while those stored in solution were at 4°C.

5.3.4. Size reduction of PPNs through ultrasonication

Addressing polymer particle aggregation is vital to maintaining the desired properties and performance of materials in various applications, ranging from pharmaceuticals and cosmetics to coatings and industrial processes [512]. Ongoing research aims to develop more effective strategies to prevent or reverse polymer particle aggregation. This includes the exploration of novel additives, surface modifications, and better understanding the fundamental mechanisms underlying aggregation processes [513]. The most common strategy for particle breakdown is mechanical disruption using techniques like ultrasonication which physically break down agglomerates into smaller particles using ultrasound waves [514, 515].

To investigate particle breakdown after long-term storage in different solutions, we sonicated the PPNs and monitored their physical changes. After 3 months of aqueous storage, we measured the PPN effective size in Milli-Q water, pH 4, pH 7.4, and pH 11 solutions over varied sonication durations (0, 2, 5, 10, and 15 minutes), as depicted in Figure 38a. Initially, all curves exhibited a reduction in particle size at 2 minutes, indicating successful breakdown of larger aggregates. However, a subsequent trend emerged across all solvents: a gradual increase in particle size after the initial decrease, resulting in significantly larger sizes by the 15-minute mark compared to the start of sonication. The sonication series suggest a temporary disruption followed by re-agglomeration or further breakdown, possibly due to limited stability, re-agglomeration of smaller particles, insufficient energy input, or solvent-induced influences on particle stability. During the initial 2 minutes of ultrasonication, the energy input from the ultrasound waves effectively disrupts larger aggregates or agglomerates, leading to the release of smaller particles. This stage represents a point where the disruptive forces overcome the intermolecular forces holding the larger particles together, resulting in a reduction in overall particle size. However, prolonged sonication beyond this point may lead to agglomeration due to reduced energy dissipation, allowing smaller particles to re-agglomerate through various attractive forces or lacking stability to resist re-agglomeration [516]. Temperature fluctuations during ultrasonication can also significantly influence particle dynamics within dispersed systems. As ultrasound generates cavitation bubbles and mechanical agitation, it concurrently generates heat due to energy transfer, impacting particle behaviour in multifaceted ways. Elevated temperatures can augment energy input, aiding in initial aggregate breakdown by disrupting intermolecular forces but can exacerbate re-agglomeration tendencies due to changes in particle properties [517].

These size changes after sonication were further confirmed by measuring the effective size and particle distribution of PPNs pre- and post-sonication after 6 months of aqueous storage. In Figure 38b, sonication lead to significant decreases in sizes of the particles from several microns to 1500, 740, and 280 nm in buffers at pH 4, 7.4 and 11. It is worth noting that the particles stored in Milli-Q water had not shown signs of aggregation beyond 300 nm and that sonication at the 3- and 6-month mark for 2 mins was able to reduce the size to around 250 nm. Figure 38c illustrates the particle size distribution in Milli-Q, showing a distinct peak between 200 and 300 nm, alongside a minor peak around 5000 nm. Post-sonication, the disappearance of the smaller peak was observed,

while the major peak remained within the same range, indicating limited breakdown efficacy. At pH 4, a narrow peak in the micron range exhibited a leftward shift, with a small peak emerging near 5000 nm post-sonication. In contrast, pH 7.4 displayed a shift as two smaller peaks, one cantered around 1000 nm and the other at 220 nm. However, sonication in pH 11 intensified the smaller 220 nm peak and reduced the peak cantered around 1500 nm. These results suggest that the particles were destabilized in the acidic, neutral and basic conditions and smaller sized particles were formed due to the particle disintegration with the potential to achieve sizes as small as 220 nm particularly in basic solutions. Sonication shows promise in the reduction of particle size and redispersion.

To visualize the impact of sonication on stored particle morphology in diverse solvents, Transmission Electron Microscopy (TEM) was employed to capture images of the particles before and after the sonication process. In Figure 39, the TEM images are presented in pairs, showing the impact of storage conditions and temperature variations on particle morphology. The images are divided into two main categories: dry storage versus aqueous storage for 6 months (including Milli-Q water, pH 4, pH 7, and pH 11 solutions), and room temperature versus 4 degrees Celsius. Each pair within these categories contrasts original (pre-sonication) images with those obtained after sonication, offering a visual representation of the changes in particle morphology induced by storage conditions and temperature fluctuations. Dry-stored particles exhibit smaller sizes compared to their aqueous counterparts, with those stored in dry conditions at room temperature demonstrating the smallest dimensions, consistent with prior temperature-related findings. Notably, among aqueous storage conditions, evidence of aggregation is prominent, with particles stored at 4 °C exhibiting slightly less aggregation than those at room temperature. Specifically, Milli-Q solution-stored particles display the smallest size aggregates, and as expected, sonication appears to yield minimal alterations in their morphology. In contrast, particles stored in pH 11 solution show elongated chains of smaller particles, albeit exhibiting less clustering compared to pH 7.4 and pH 4 solutions. Sonication interventions in pH 4, 7.4 and 11 solution reveal indications of smaller free particles appearing and reduced clumping, instead favouring a more pronounced length-wise aggregation pattern. Although the morphology of the smaller unit particles seems to remain unchanged, the images indicate a less uniform size distribution with particles of different sizes forming these chains. These observations collectively highlight the influence of storage medium, temperature, and the variable impact of sonication on particle morphology, underscoring the complex interplay of these factors in governing particle aggregation and dispersion dynamics.

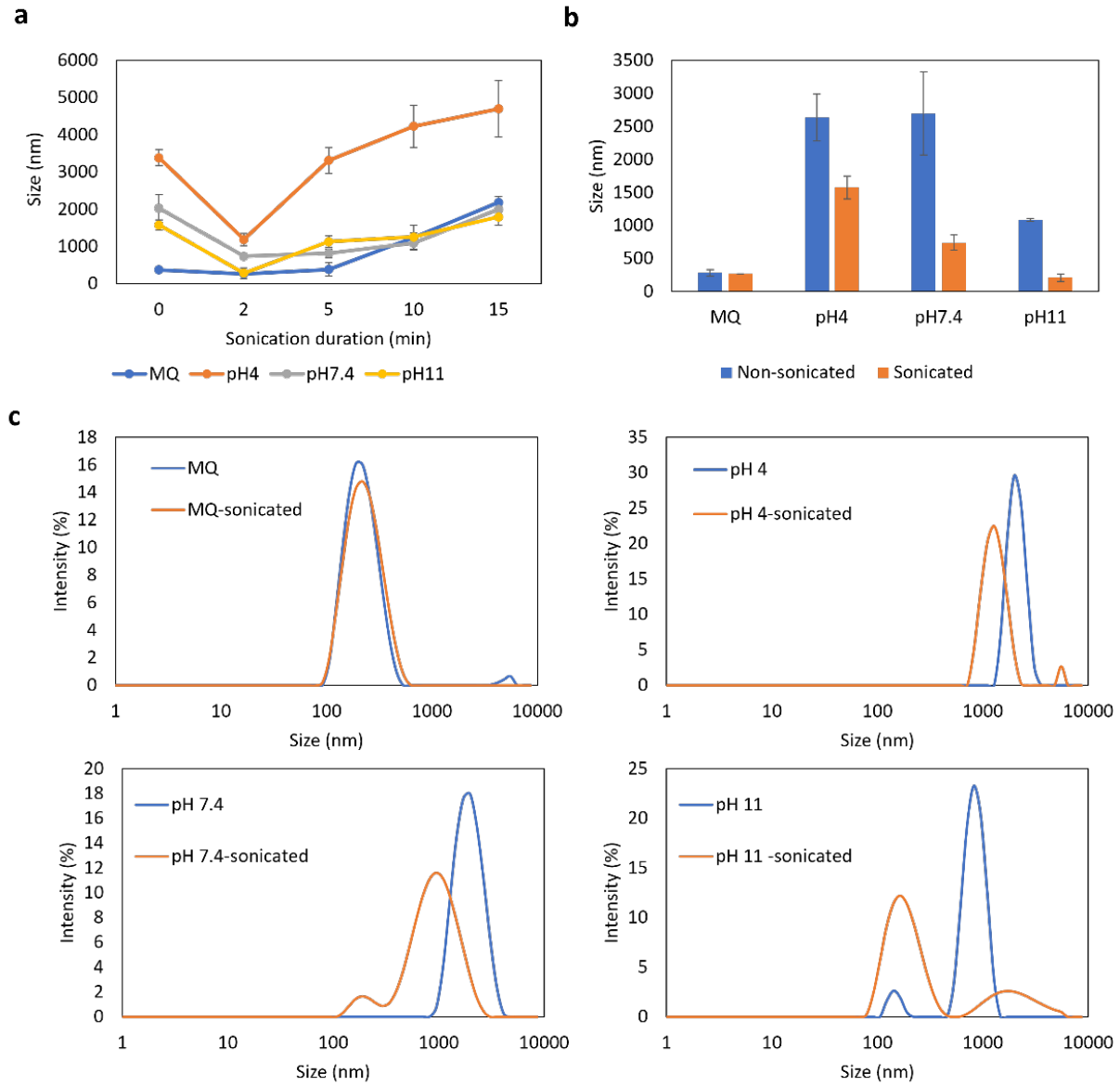

Figure 38. (a) The PPN effective size after 3 months of aqueous storage in Milli-Q water, pH 4, pH 7.4, and pH 11 solutions over varied sonication durations (0, 2, 5, 10, and 15 minutes). (b) The effective size and (c) particle distribution of PPNs pre- and post-sonication after 6 months of aqueous storage. Particles stored in solution were kept at 4°C.

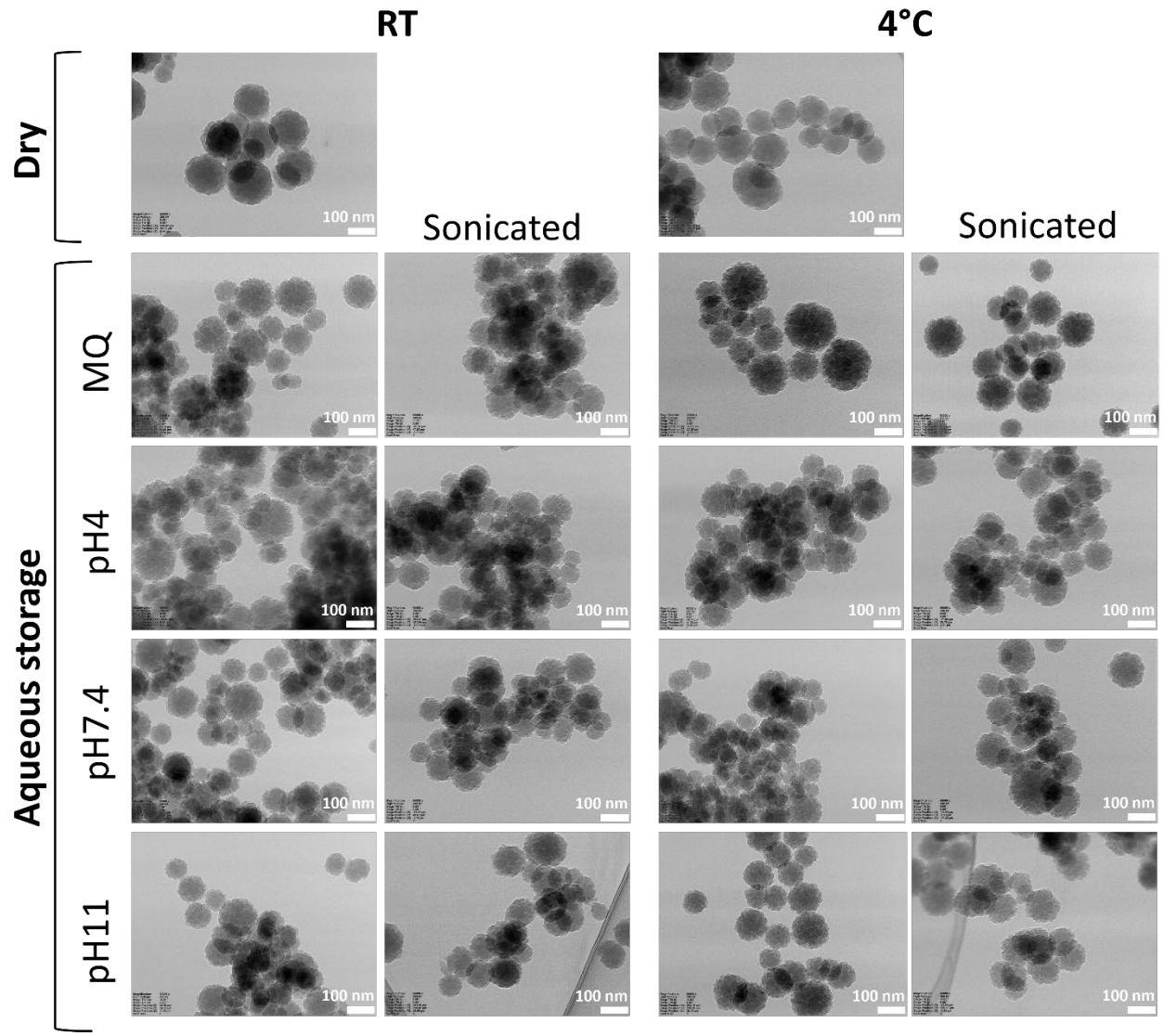

Figure 39. The impact of sonication on particle morphology after 6-month storage in the different base solvents. Transmission Electron Microscopy (TEM) images of the particles before and after the sonication process showing the impact of storage conditions and temperature variations on particle morphology.

5.3.5. Surface activity and functionality post storage

Active particle surfaces enable their customization for targeted drug delivery, biosensing, or imaging purposes. Ensuring that particle surfaces remain active after extended storage periods is essential for maintaining their ability to interact with and bind to specific molecules or cellular targets.

Following the analyses of PPNs physicochemical stability in various solvents, as presented and discussed above, we assessed the capability of these particles to undergo functionalization with fluorescent molecules after long-term storage using Nile Blue as a model ligand. Nile Blue, a popular fluorescent dye extensively used for its distinctive optical properties was chosen to facilitate precise detection. We selected Milli-Q water and pH 11 buffer solutions as media for conjugation experiments after observing the PPN stability and successful size reduction through sonication.

Subsequently, we proceeded with the conjugation of NB with PPNs stored in both Milli-Q and pH 11 buffer solutions, comparing their performance against particles stored under dry conditions for an entire year.

We conducted fluorescence spectroscopy analysis of PPN-Nile Blue conjugates aimed to probe the functionality of the plasma polymerized nanoparticles by evaluating the fluorescence intensity. Figure 40a demonstrates the fluorescence emitted by the NB-conjugated PPNs, indicating distinct observations based on different storage conditions. The fluorescence signals emitted by NB-conjugated PPNs after storage in a pH 11 solution exceeded the background signal of PPNs alone. This finding suggests that the PPN surfaces retained their functionality even after storage in a basic environment, possibly indicating the preservation of binding sites or favourable surface characteristics for NB conjugation at this pH level [518]. Additionally, PPNs stored in Milli-Q water showed notably enhanced signals, indicating a high degree of functionality, while the strongest fluorescence signal originated from PPNs stored under dry conditions. The exceptionally strong signal from dry-stored PPNs implies optimal surface conditions for NB conjugation or maximum accessibility to reactive sites.

Using ATR-FTIR we explored the functional groups involved in the conjugation process of NB onto PPNs sourced from varying storage conditions, including both dry and aqueous environments. The ATR-FTIR spectra presented in Figure 40b showed distinct peaks attributed to amine functionalities within the PPN-NB conjugates from all conditions. Specifically, the discernible peak at 1587 cm^{-1} is associated with the characteristic N-H bending vibrations arising from the primary amine group within NB. Meanwhile, the spectral region between 1200 and 1340 cm^{-1} highlighted the pronounced C-N stretching modes originating from the aromatic amine situated in NB's heterocyclic ring. Additionally, visible peaks spanning the spectral range of 1076 to 1211 cm^{-1} were indicative of C-N stretching from the primary and tertiary amine groups at the opposite ends of the NB's molecular structure. These changes in the FTIR spectra of the PPN post-conjugation indicate the successful attachment of NB onto the various PPN surfaces stored dry and from Milli-Q and pH 11 buffer. The successful binding of NB to PPNs emphasizes the maintenance of surface activity and functionality of the PPN surface for the attachment of various molecules even after one year storage in dry state and in aqueous state. These ATR-FTIR results further corroborated successful NB attachment across all storage conditions, highlighting the robustness of PPN surfaces for molecular attachment, even after extended storage periods in varied environments. The results collectively highlight PPNs' long-term surface activity, critical for biological applications, paving the way for their commercialization.

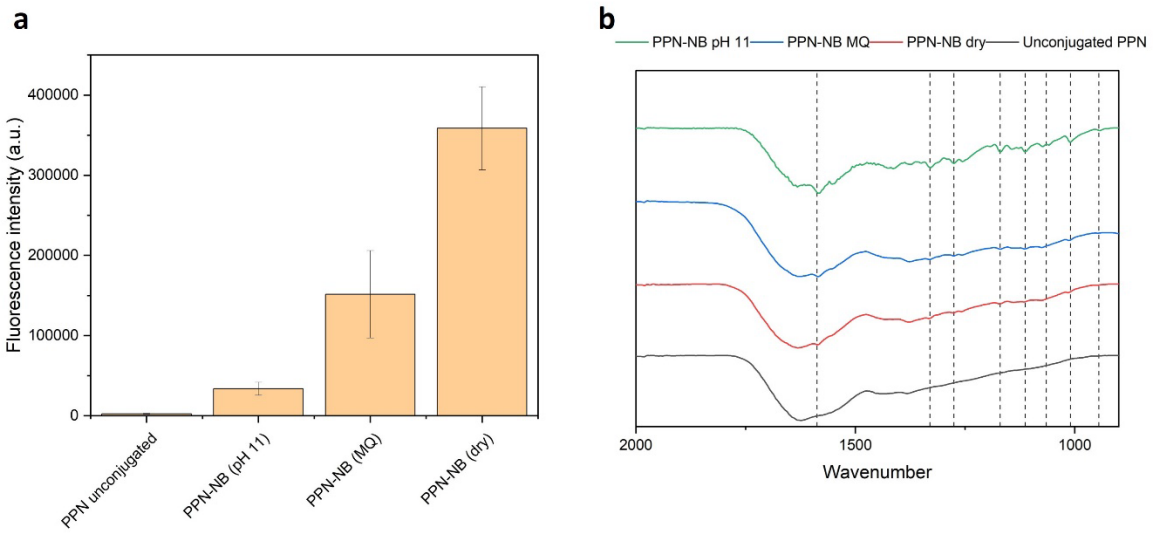

Figure 40. (a) The fluorescence intensity of Nile Bue-conjugated PPNs and (b) ATR FTIR measurements showing the functional groups involved in the conjugation process of Nile Blue onto PPNs sourced from varying storage conditions, including both dry and aqueous environments: Milli-Q (MQ) and buffer solution at pH 11.

5.4. Conclusions

This study investigated the stability and functionality of PPNs when subjected to diverse storage conditions. We systematically adjusted the plasma polymerization time, along with the temperature and pH levels of the aqueous media in which the particles were incubated, to elucidate their role on regulating the physicochemical stability and surface activity of PPNs. Prolonged polymerization durations up to 30 minutes yielded larger nanoparticles and a wider size distribution, indicating a tendency for coagulation and coalescence during gas-phase synthesis in the plasma. Storage temperature variations significantly affected PPN properties, with dry storage consistently resulting in smaller particle sizes compared to aqueous storage. Notably, particles stored in dry conditions at room temperature had the smallest dimensions, whereas PPNs stored in solution had a slightly smaller size at 4°C relative to storage at room temperature. The study also highlighted consistency in chemical elemental composition over time, with a slightly increasing trend in oxygen concentration, likely indicating ongoing autooxidation processes. The influence of pH on particle agglomeration demonstrated diverse size alterations showing the interplay between electrostatic forces and surface charge. Extended storage durations up to 6 months significantly impacted particle size and stability, with sonication demonstrating the ability to disrupt aggregates and reduce particle sizes. After size reduction due to sonication, pH 4 conditions maintained the largest particle sizes and smallest sizes in Milli-Q and pH 11 across all conditions. Extreme pH levels affected particle stability differently, with acidic environments promoting aggregation due to reduced repulsive forces and alkaline conditions relatively stabilizing particles by preventing aggregation through excess ions. Assessment of functionality using Nile Blue as a model ligand indicated that PPN surfaces retained their functionality even after storage in different conditions. Fluorescence spectroscopy and ATR-FTIR analyses confirmed successful attachment of Nile Blue onto PPN surfaces from diverse storage conditions, emphasizing sustained surface activity and functionality for molecular attachment, even after extended storage periods. These insights advance our understanding of how storage conditions impact PPN behaviour, offering valuable guidance for optimizing their stability and functionality for diverse applications, from drug delivery systems to biomedical sensors and beyond.

Chapter 6. Characterization and Model Validation of a CCRF Plasma Discharge with Varying Power and Pressure

This chapter aimed to characterize and model the behavior of our 13.56 MHz capacitively coupled radiofrequency (CCRF) low-pressure plasma reactor for enhanced plasma processing and nanoparticle synthesis, using argon plasma as the preliminary medium. Through a combination of plasma modeling and rigorous experimental validation, it aimed to refine the control over plasma parameters such as plasma potential, electron and ion densities, and electron temperature. The validated model, corroborated by experimental data, advances the understanding of plasma-assisted nanoparticle generation, offering insights into tailoring plasma conditions for precise material properties.

The modeling results and discussions in Chapter 6 are adapted from a manuscript published in Plasma Processes and Polymers as: 'Continuum modelling of an asymmetric CCRF argon plasma reactor: Influence of higher excited states and sensitivity to model parameters.' DOI: https://doi.org/10.1002/ppap.202000243.

6.1. Introduction to the chapter

In the burgeoning field of nanotechnology, the synthesis of nanoparticles with precise control over size and distribution is a cornerstone for advancements in various applications ranging from catalysts to drug delivery systems. Plasma-based particle generation offers a unique and versatile pathway to achieve this control due to the inherent properties of plasmas, which can be finely tuned to affect particle nucleation and growth processes. The control over particle size and distribution is not only pivotal for the optimization of the material properties but also for ensuring consistency and reliability in industrial applications.

Capacitively coupled radiofrequency (CCRF) plasmas, in particular, are extensively used in the generation of nanoparticles due to their ability to provide a uniform and controlled environment for particle synthesis. The critical plasma parameters that influence particle characteristics include electron density (n_e), electron temperature (T_e), ion density (n_i), sheath dynamics, and self-bias voltage (V_{DC}). Precise control over these parameters is essential for manipulating the nucleation and growth kinetics of nanoparticles, ultimately governing their size and distribution.

A combination of plasma modeling and rigorous experimental validation represents a powerful approach towards achieving a detailed understanding and control of these plasma parameters. Plasma models, built upon fundamental principles and validated against experimental data, serve as predictive tools that allow for the optimization of plasma conditions to tailor nanoparticle characteristics to specific needs. The Electron Energy Distribution Function (EEDF) is particularly significant as it dictates the rates of ionization and excitation within the plasma, which are central to the nucleation and growth of particles. Therefore, it becomes imperative to determine the appropriate EEDF—Maxwellian or Druyvesteyn—that accurately represents the plasma under various operational conditions.

While our experimental setup involves a complex plasma composed of argon, nitrogen, and acetylene, the initial phase of our research is anchored in modeling the simpler argon plasma system. The rationale behind this approach lies in the foundational role that argon plays in the plasma dynamics. Argon, being an inert gas, provides a controlled environment to study fundamental plasma processes without the added complexity of reactive species interactions present in nitrogen and acetylene plasmas. By first establishing a robust model for argon plasma, characterized by parameters such as electron density and temperature, we lay the groundwork for understanding more complex plasma systems.

This chapter presents the assessment and validation of a continuum model for a CCRF argon plasma through comprehensive Langmuir probe diagnostics, DC self-bias voltage measurements, and electrical characterization. The model aims to simulate the plasma conditions by assessing the impact of pressure, power and position on plasma parameters and by comparing different EEDFs. Through validation against experimental observations, we seek to refine the model's predictive accuracy and enhance our understanding of plasma-assisted nanoparticle synthesis. The validated model not only stands to propel forward the capabilities of plasma particle generation but also lays the groundwork for future explorations into the synthesis of novel nanomaterials with customized properties.

6.2. Introduction/Literature review

Carbon-based nanostructures like graphene, carbon nanotubes and organic nanospheres are highly versatile materials with exceptional electrical [519], thermal [520], and mechanical properties [521]. They continue to be explored for their potential in a myriad of high-performance applications including advanced electronics [522, 523], energy storage [524], catalysis [525], sensors [526] and nanomedicine [37, 527]. Plasma-based particle generation offers a high purity production pathway that can tailor functional properties through the modification of plasma conditions [370, 528]. For example, capacitively coupled (CC) radio-frequency (RF) plasma techniques have been employed as an economical and efficient approach for the polymerization of nanoparticles, aimed at engineering advanced systems for the precise and safe delivery of therapeutic agents directly to cancerous and cardiac cells [123, 135, 454, 529]. The complexity and effectiveness of these plasma processes hinge on the rich mixture of energetic ions, chemically active species, radicals, and energetic neutral species within the CCRF discharge. The need to precisely engineer interactions between plasma and materials at atomic scales necessitates enhanced accuracy in the control of processing plasma conditions.

For the optimization of plasma processes, a fundamental understanding of plasma physics and chemistry is essential to comprehend how external control parameters impact the process. This includes understanding the interplay of ion and electron fluxes and the resultant electromagnetic and flux pressure forces, which are key to achieving desired material properties [400, 530]. Plasma electron density and energy plays a pivotal role in this context by driving the ionization, excitation, and fragmentation of precursor gases [506, 531, 532]. The electron temperature within the plasma critically influences the dynamics of positive ion flux and the densities of ions in plasma deposition processes [375, 444, 533]. This temperature, or more broadly, the energy distribution of electrons in the plasma, is a key determinant of the plasma chemistry that underpins the stability properties of plasma discharges [534-537]. Another impactful factor in this process is the self-bias voltage that develops on surfaces in contact with the plasma, such as the substrate or reactor walls [538, 539]. The self-bias voltage, a byproduct of differential ion and electron fluxes to these surfaces, plays a pivotal role in modulating the energy with which ions strike substrates, thereby affecting the structure and composition of the modified or synthesized surface [540]. Understanding key plasma parameters such as electron density, electron temperature, and the electron energy distribution function (EEDF) became crucial for optimizing processing conditions and achieving desired material properties. Given the significance of these plasma parameters, a substantial body of research has been dedicated to examining the impact of external factors on each parameter within capacitive RF discharge environments [541-545].

However, to reveal such fundamentals of plasma operation, a synergistic combination of experiments and simulations is typically required, since simulations offer insights into plasma parameters with a level of spatial and temporal resolution that might be unattainable through direct experimentation [546]. When corroborated by experimental data, these simulations become invaluable for plasma source design and optimizing processing methods, offering substantial savings in time and resources by reducing the need for prototype construction and extensive testing. These models then act as predictive tools, enabling the fine-tuning of plasma environments to precisely engineer nanoparticle features for desired applications. Computer based modeling such as particle-in-cell (PIC) and Monte Carlo collision (MCC) simulations have been performed to capture kinetic effects and investigate ion energy distributions at the electrodes, charged particle dynamics, reaction rates, etc. Fatima Jenina Arellano *et al* compared PIC/MMC-computed characteristics in an argon discharge with their experimental counterparts by incorporating phase-resolved optical

emission spectroscopy PROES [547]. Measurements of spectral line intensities showed that the simulation could model the electron density and EEDF well between 2 and 20 Pa. Limitations at higher pressures were attributed to the exclusion of the Ar metastables in the model as identified using tunable diode laser absorption spectroscopy (TDLAS). David A Schulenberg *et al* conducted a comprehensive experimental validation of a PIC/MCC simulation for an argon discharge by evaluating several parameters, including gas temperature, electron density, the spatial and temporal dynamics of electron impact excitation, and the distribution of ion flux-energy at the grounded electrode using five diagnostic methods [548]. The findings indicated that PIC/MCC simulations could accurately replicate experimental outcomes when correct values for gas temperature and surface coefficients were employed; otherwise, significant inaccuracies could arise. With accurately chosen surface coefficients and electron-surface interaction model, Chan-Won Park *et al* were able to demonstrate that their PIC/MCC simulations for a neon CCRF plasma aligned well with their experimental measurements of electron density and electron impact excitation rates under various discharge conditions. Although good agreement was reported across the chosen ranges of the electrode gap, neutral gas pressure and driving voltage, limitations in the 1D simulations were found to reduce the quality of the agreement of the simulation with the experimental results. However, increasing fully kinetic PIC simulations of CCRF plasma discharges to two [549] and three [550] spatial dimensions tend to be extremely computationally expensive. As an alternative, Computational Fluid Dynamics (CFD) simulations offer a fluid model approach, solving fluid-based equations across a structured grid through numerical techniques [551]. A CFD simulation of the Pocket Rocket argon plasma micro-thruster by Amelia Greig *et al* showed good agreement with experiments measuring ion densities, electron densities and temperatures, highlighting the peak plasma density at the tube's center. However, the simulated plasma density resulting in higher values than experimental estimates was believed to be due to an overestimated secondary electron emission coefficient and the neglect of plasma heating effects in the simulation. Integrating electrical measurements and Langmuir probe diagnostics into modeling has proven to further elevate the validation of CCRF discharges across applied RF power levels and pressure ranges [552-556].

In the present study, we present the characterization and modelling of a 13.56 MHz CCRF low-pressure plasma reactor to explore optimum conditions for plasma processing and nanoparticle synthesis. We assess and validate the predictions of a previously published continuum fluid model through comprehensive rf-compensated Langmuir probe diagnostics and electrical discharge measurements. Plasma parameters such as plasma potential, floating potential, the electron and ion densities, electron temperature as well as the DC self-bias voltage and driving voltage amplitudes were experimentally measured. The effect of varying the applied RF power (25 – 100 W) and filling gas pressure (100 – 300 mTorr) on the plasma parameters was explored and compared to the model's predictions. Since Ar is the major constituent in the gas mix used to generate particles, the current work focuses on characterizing and modeling pure Ar plasma as a first step to understanding and controlling the synthesis process. Through validation against experimental observations at a wide range of operational conditions, we seek to refine the model's predictive accuracy and enhance our understanding of the dynamics of the CCP discharge. The validated model not only stands to propel forward the capabilities of plasma modelling but also lays the groundwork for future research of plasma-assisted nanoparticle synthesis.

6.3. Methods

6.3.1. Langmuir probe theory

A single RF compensated Langmuir probe from Impedans Ltd was used to measure the plasma parameters, featuring a tungsten wire with dimensions of 10 mm in length and 0.2 mm in radius. This probe was inserted into the reactor through a top feedthrough to assess the bulk plasma between the top powered electrode and the lower grounded electrode (Figure 41). Plasma parameters were determined by recording the current flowing from the plasma to the probe as a function of the probe's voltage against a reference surface, also known as the IV characteristic curve, and applying Langmuir probe theory. The reference for Langmuir Probe (LP) measurements was established by grounding the lower electrode and the chamber wall. Probe currents were obtained by setting bias voltages ranging from -30 to 50 V, with increments of 0.5 V and an integration period of 100 microseconds, adjusting these settings as necessary to enhance the signal quality. The I-V characteristic curves obtained were analyzed using the Automated Langmuir Probe Software provided by Impedans Ltd, which calculated key plasma parameters such as plasma potential (V_p), floating potential V_f, electron temperature (T_e), electron density (n_e), ion density (n_i) and the Electron Energy Probability Function (EEPF). As can be seen in Figure 42, the IV characteristic is recorded through the probe tip, allowing the software to perform a first and second derivative which can be displayed on the screen. The plasma parameters are also calculated in the right panel with settings for the analysis method to be determined by the user in the bottom right tabs.

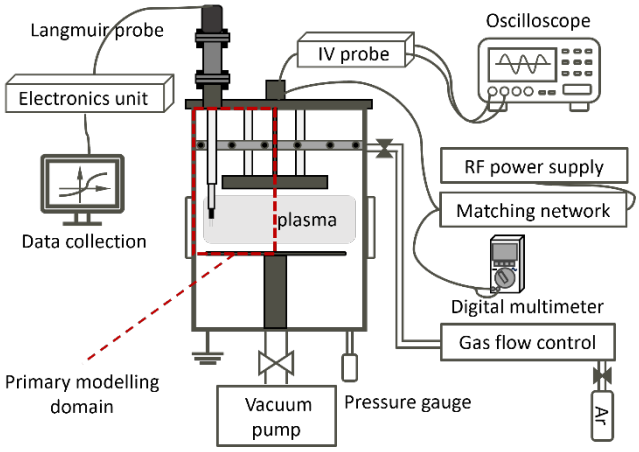

Figure 41. A schematic of the capacitively coupled RF plasma system connected to diagnostic devices and highlighting the primary modelling domain (in red dashes). Figure drawn not to scale.

The space or plasma potential V_p is paramount, representing the electric potential within the plasma bulk relative to a reference point, usually taken at the plasma boundary or far away from it. It is instrumental in determining the energy landscape that electrons and ions navigate, influencing their motion and the overall electric field configuration within the plasma. The plasma potential is defined as the specific voltage point on the I-V characteristic curve where the transition from the electron retarding region to the electron saturation region occurs. This point is characterized by a departure from exponential electron current collection behavior, marking the onset of electron saturation and is determined in the software by the potential at which the maximum in the first derivative occurs or at the zero crossing of the second derivative (Figure 43).

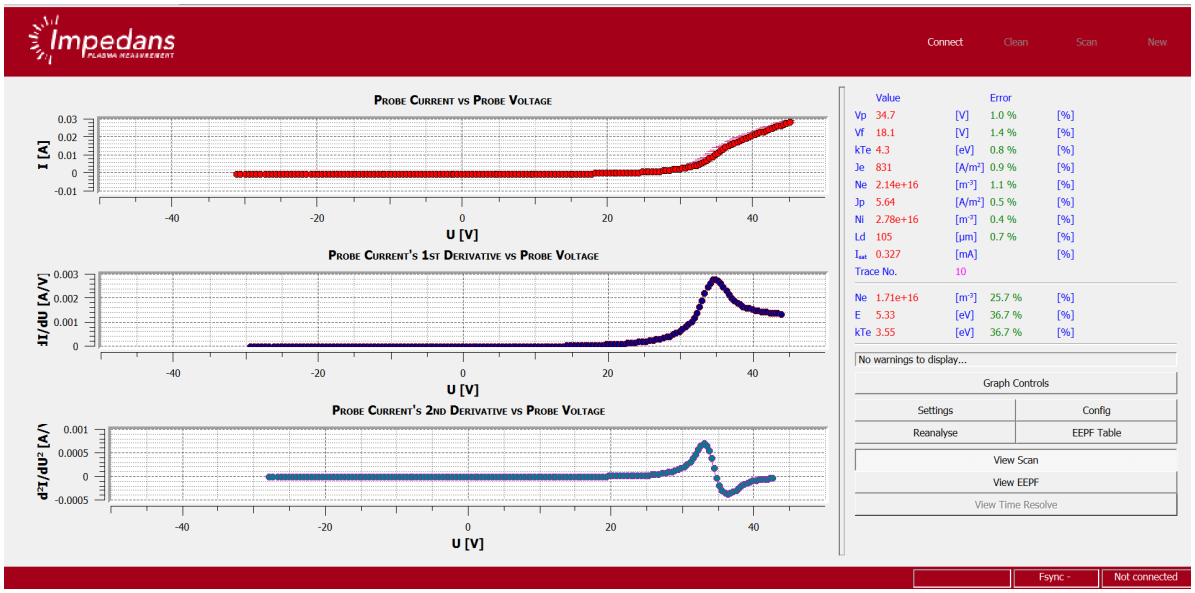

Figure 42. Graphic display of the software showing a representative IV characteristic of an argon plasma (3 sccm) at 100 W applied rf power and 100 mTorr working pressure taken using the Impedans Langmuir probe with the right-angled extension at the central axis of the reactor at 32 mm below the rf electrode (see Section6.4.16.4.1.3below). The IV characteristic is recorded (top), then the user can choose to display the first (middle) and second (bottom) derivatives under Graph Controls. The calculated parameters can be seen on the top right panel and the settings on the bottom right panel.

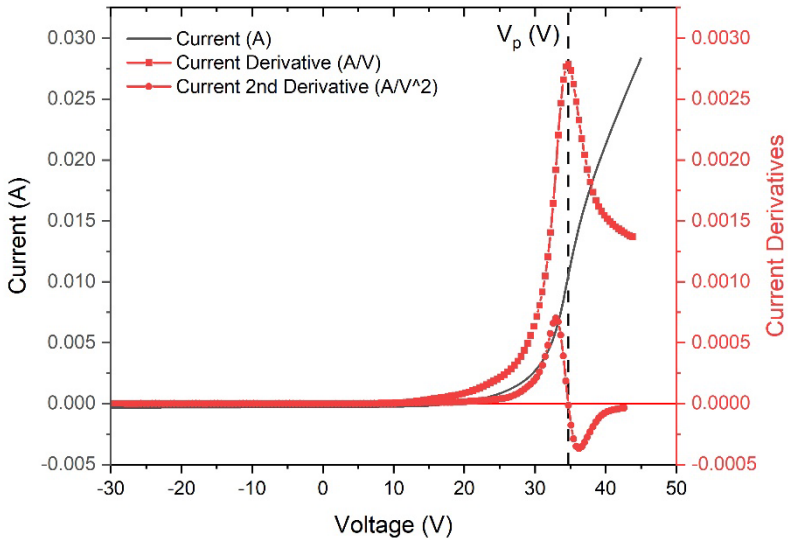

Figure 43. Representative curves showing the representative IV characteristic curve (straight black line) plotted with its first and second derivative (red lines with markers). The plasma potential V_p (dotted vertical line) is calculated in this study using the second derivative method whereby it is the voltage at which the first derivative is at its maximum or the second derivative crosses the zero-line (horizontal axis).

The floating potential V_f, on the other hand, is the potential acquired by an electrically isolated

object immersed in plasma when the net current to its surface is nullified, establishing an equilibrium between the electron and ion currents. It is a critical parameter for understanding how objects interact electrically with the plasma environment such that:

$$I_e = I_i \quad (1)$$

where I_e and I_i are the electron and ion current densities to the surface, respectively. Mathematically, V_f can be approximated from probe measurements, often using the plasma potential as a reference from the Boehm current by [376]:

$$V_p = V_f + \frac{kT_e}{2e} \ln\left(\frac{2m_i}{\pi m_e}\right) \quad (2)$$

Where m_i is the ion mass, T_e is the electron temperature, e is the electron charge, k is Boltzmann's constant and m_e is the electron mass. The plasma floating potential here is found from the IV characteristic obtained by the probe at the potential where the probe collects zero net current (Figure 44).

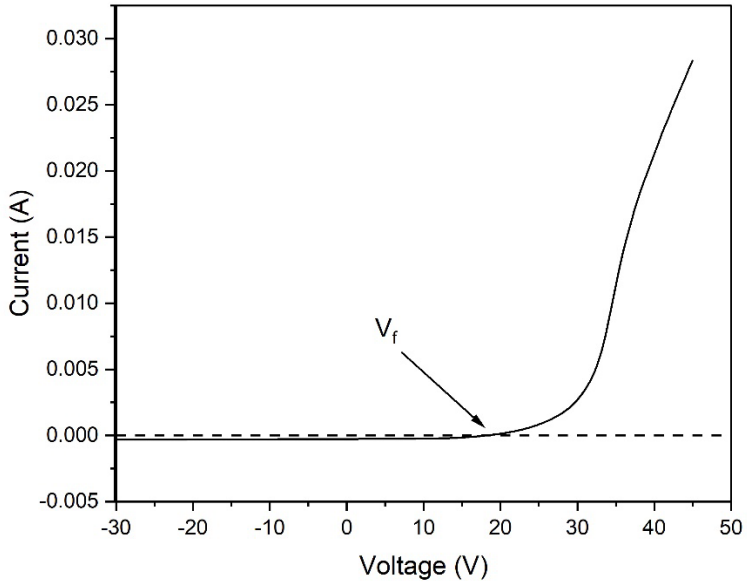

Figure 44. The representative IV characteristic obtained by the probe zoomed in to show the floating potential, the voltage at which the probe current is zero.

The electron temperature kT_e, often expressed in electron volts (eV), reflects the average kinetic energy of the electrons assuming a Maxwellian distribution where k is the Boltzmann constant. It is a key determinant of the plasma's energy distribution and its capability to initiate various physical processes, such as ionization and chemical reactions. It is calculated from the ratio of the current from the IV characteristic at the plasma potential $I(V_p)$ to the integral of the characteristic curve between V_f and V_p as [557]:

$$\frac{1}{kT_e} = \frac{I(V_P)}{\int_{v_f}^{v_P} I_e(v)\, dv} \quad (3)$$

The electron density n_e and ion density n_i, representing the number of electrons and ions per unit volume, respectively, are fundamental for quantifying the plasma's composition and ionization state. These densities are often inferred from probe measurements or optical diagnostics, with the

quasi-neutrality condition in plasmas giving $n_e \approx Z_{avg} n_i$ in the bulk, where Z_{avg} is the average charge state, i.e., the average number of charges per ion in the plasma. The electron and ion densities are calculated from the probe currents as such, respectively [557]:

$$n_e = \frac{I(V_p)}{A_p}\sqrt{\frac{2\pi m_e}{e^2 kT_e}} \quad (4)$$

And

$$n_i = \frac{I_0}{A_p}\sqrt{\frac{2\pi m_i}{e^2 kT_e}} \quad (5)$$

where A_p is the probe area, and I_0 is the ion current at the sheath edge.
The electron saturation current I_{sat} is observed when a Langmuir probe is biased sufficiently positively to collect all electrons reaching it and repel all the positive ions, providing a direct measure of the electron flux and, by extension, the electron density. The current collected by the probe in the electron saturation region can be expressed as [558]:

$$I_{sat} = e\, A_p\, n_e \sqrt{\frac{kT_e}{2\pi m_e}} \quad (6)$$

The EEDF is determined from the second derivative of the IV characteristic, with the ion current subtracted [559], through the Druyvesteyn equation [557]:

$$n(\varepsilon) = n_e f(\varepsilon) = \frac{2I''}{eA_p}\left(\frac{2m\varepsilon}{e}\right)^{\frac{1}{2}} \quad (7)$$

where I'' is the second derivative of the IV curve, and ε is the energy given by (V_p-V) at probe voltage V.

These parameters, including the potentials, electron temperature, electron density, ion density and saturation current were extracted from the software's calculations displayed at the graphical user interface in the top right panel as was shown in Figure 42 .

6.3.2. Discharge current and voltage waveforms

The RF discharge waveforms at the powered electrode were monitored by a high-voltage and current probe and the signals were recorded in a Rigol DS1074 oscilloscope for further analysis. The discharge parameters, such as discharge voltage and current, were measured and the root mean squared values I_{rms} and V_{rms}were calculated from the waveforms. The magnitude of the voltage and the harmonics affecting it were determined using the Fast Fourier Transform FFT function in Excel. The voltage probe has very high impedance (50 MΩ) and therefore should not affect the voltage or current waveforms.

6.3.3. DC self-bias

Sheath dynamics in a plasma are connected to the key plasma parameters and play a crucial role in controlling the interactions between the plasma and the material surfaces. The sheath is a fundamental plasma structure that forms at the interface between a plasma and a material surface,

such as the wall of the plasma container or a probe inserted into the plasma. When a material surface is introduced, the more mobile electrons tend to reach the surface at a faster rate than the heavier and slower ions. This creates a charge imbalance such that the surface acquires a lower potential relative to the plasma, which repels electrons and accelerates ions towards the surface. The potential continues to decrease until it causes an increase in ion current and decrease in electron current such that the ion and electron currents to the surface become equal. The lower potential at the surface is screened by a positive space charge region that builds up adjacent to the surface. This space charge region forms the sheath.

Similarly, a DC self-bias voltage V_{DC} develops across a plasma sheath near the electrode in an asymmetric capacitive RF discharge [533]. This bias is also a result of the differential in electron and ion mobilities and the asymmetric geometric or electrical configurations of the electrodes. The fundamental physics underlying this phenomenon can be traced back to the disparity in mass and mobility between electrons and ions in the plasma. Electrons, being significantly lighter than ions, respond more rapidly to the oscillating electric field of the RF power supply. This rapid response leads to a higher electron flux to the electrode during the negative cycle of the RF waveform, compared to the ion flux during the positive half cycle. This inequality of half-cycle current magnitudes results in a downwaed drift in the electrode potential which ceases when the equilibrium condition that equal ion and electron currents are drawn over each RF cycle (i.e. zero net charge is extracted over each cycle). The self-bias voltage is typically formed on the smaller electrode due to the unequal sheath voltages that develop during the RF cycle and can be qualitatively described by the difference in the time-averaged sheath voltages at each electrode, derived from the Child-Langmuir law in a simplified form, as [560]:

$$V_s = \left(\frac{2e}{m_i}\right)^{\frac{1}{2}} \frac{J_i d^2}{\epsilon_0} \quad (8)$$

where V_s is the sheath voltage, e is the elementary charge, m_i is the ion mass, J_i is the ion current density to the electrode, d is the sheath thickness, and ϵ_0 is the vacuum permittivity.

The self-bias of the RF electrode was measured through a custom-made filter circuit connected to the output of the matching network. The matching network is directly connected to the RF electrode inside the reactor and the DC voltage on the RF at the output of the matching network is captured through this circuit and scaled down using a Tektronix Fluke Digital Multimeter and a 100:1 voltage divider.

6.3.4. The simulation model

A comprehensive numerical study was previously performed on capacitively coupled radiofrequency (CCRF) argon plasma, widely used in surface processing and material synthesis [136]. The goal was to develop a robust continuum model that accurately represents the complex dynamics of large-scale plasma reactors, often simplified in other models. Although the model is consistent with current literature, it requires experimental validation, which is the focus of this study. Key components of the model are briefly described below.

Geometric Considerations and Simulation Domain

A detailed two-dimensional (2D) axisymmetric continuum model of the capacitively coupled RF argon plasma system was constructed using *COMSOL Multiphysics 5.5*. A schematic of the CCRF

plasma system connected to diagnostic devices and highlighting the primary modelling domain (in red dashes) can be seen in Figure 41. The primary modeling domain extends from upper surface of the lower electrode (the substrate holder), up to the top boundary of the reactor chamber. Detailed descriptions of the model's 2D geometry and boundary conditions were further elaborated in our published work [136].

Continuum Framework and Approximations

The continuum model is centered on solving the fluid dynamics equations derived from the moments of the Boltzmann equation. This approach is particularly suited to low-temperature plasmas where the mean free path of electrons is small compared to the system dimensions, justifying the continuum assumption. The drift-diffusion approximation is employed, simplifying the transport of charged species by considering the combined effects of the electric field, particle diffusion, and the influence of collisions. The selection of this modeling approach is justified by the system's parameters: neutral gas pressure (p) was adjusted between 0.1-0.3 Torr over a range of applied RF power (P_{RF}). The momentum transfer collision frequency (ν_m) in an argon discharge at 13.56 MHz with a gas pressure of at least 0.1 Torr is typically significantly below the operational frequency [381, 561]. Moreover, the system's Knudsen number (Kn) at the minimum operational pressure was found to be well within the continuum regime (Kn<0.01) [371], confirming the suitability of employing a drift-diffusion continuum model for this configuration [382, 562]. A time-averaged steady-state approach was used to bypass the computational demand of a full temporal resolution.

Key Equations and Plasma Chemistry

The model is founded by a set of core equations:

1- Electron Continuity Equations: These account for the conservation of electron density n_e, incorporating the effects of electric fields, diffusion, and the rate of energy exchange due to electron collisions [382]:

$$\frac{\partial n_e}{\partial t} + \nabla \cdot \mathbf{\Gamma}_e = R_e \quad (9)$$

where $\mathbf{\Gamma}_e$ is the electron flux representing the net flow of electrons out of a volume and R_e ($m^{-3} \cdot s^{-1}$) is the electron source term, accounting for the net rate of electron production or loss due to various processes like ionization or recombination.

2- Heavy Species Transport: A mixture-averaged diffusion model governs the transport of neutrals and ions, with their motion dictated by electric fields and concentration gradients [563] in Equations (10) and (11):

$$\frac{\partial n_\varepsilon}{\partial t} + \nabla \cdot \mathbf{\Gamma}_\varepsilon + \mathbf{E} \cdot \mathbf{\Gamma}_e = S_{en} \quad (10)$$

where the electron energy density is $n(\varepsilon) = \bar{\varepsilon}\, n_e$, $\bar{\varepsilon}$ is the mean electron energy (eV), $\mathbf{\Gamma}_\varepsilon$ is the electron energy flux, $\mathbf{E}$ is the electric field and S_{en} is the electron energy source term

($V \cdot m^{-3}$).

$$\rho\left(\frac{\partial w_k}{\partial t}\right) = \nabla \cdot \boldsymbol{j}_k + R_k \quad (11)$$

where ρ is the gas density ($kg \cdot m^{-3}$), w_k is the mass fraction of kth species, $\boldsymbol{j}_k$ is the diffusive mass flux and R_k is the species source term for generation or consumption.

3- Poisson's Equation: This self-consistent equation links the electrostatic potential within the plasma to the distribution of charge density, thus defining the electric field [381, 563, 564]:

$$-\nabla \cdot \epsilon \nabla V = q \sum_{k=1}^{N} Z_k n_k - n_e \quad (12)$$

Where ϵ is the electric permittivity ($F \cdot m^{-1}$), q is the unit charge (C), Z_k is the charge number for species k.

Boundary Conditions

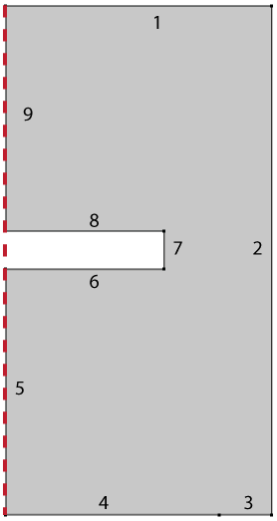

Figure 45. Depiction of the model layout showing defined boundary conditions and the computational zone (highlighted in grey), with the symmetry axis marked by a dashed red line [136].

Figure 45 illustrates the model's geometry, focusing on the domain's boundaries. Boundaries 1, 2, and 4 outline the reactor walls and the substrate holder, all of which are grounded. The RF electrode is defined by boundaries 6 to 8. Boundaries 5 and 9 delineate the axis of symmetry. The gas outlet, situated between the substrate holder and the reactor wall, is represented by boundary 3. Boundary 3 is set with zero electron and electron energy flux, while boundaries 1, 2 and 4 are electrically grounded, maintaining a potential of 0 V. Boundary conditions at boundaries 1, 2, 4, and 6-7 in Figure 45 are governed by the electron flux and electron energy flux (Equations 13 and 14) at the walls:

$$\mathbf{n} \cdot \Gamma_e = \frac{1}{2} \nu_e^{th} n_e - \sum_i \gamma_i (\Gamma_i \cdot \mathbf{n}) \quad (13)$$

$$\mathbf{n} \cdot \Gamma_\varepsilon = \frac{5}{6} v_e^{th} n_\varepsilon - \sum_i \gamma_i \bar{\varepsilon}_i (\Gamma_i \cdot \mathbf{n}) \quad (14)$$

Where γ_i is the ion-induced secondary electron emission coefficient, Γ_i is the ion flux at the wall for the *i*th cation species, $\bar{\varepsilon}_i$ is the mean energy of the secondary electrons and the electron thermal Velocity is defined as (Equation 15) [564, 565]:

$$v_e^{th} = \sqrt{\frac{8 k_B T_e}{\pi m_e}} \quad (15)$$

The RF Electrode between Boundaries 6-8 was characterized by Equations 20-22, with the RF power input (P_{rf}), the DC self-bias (V_{DC} on the RF electrode)[384] and the driving frequency (f_p) set at 13.56 MHz in:

$$P_{RF} = f_p \int_{\partial t} \int_{\partial \Omega} \left(V_s - V_{dc,b}\right)(\mathbf{n} \cdot \mathbf{J}_i + \mathbf{n} \cdot \mathbf{J}_e + \mathbf{n} \cdot \mathbf{J}_d) dS dt \quad (16)$$

$$V_s = V_a \cos\left(2\pi f_p t\right) + V_{DC} \quad (17)$$

$$f_p \int_{\partial t} \int_{\partial \Omega} (\mathbf{n} \cdot \mathbf{J}_i + \mathbf{n} \cdot \mathbf{J}_e + \mathbf{n} \cdot \mathbf{J}_d) dS dt = 0 \quad (18)$$

Where $\mathbf{J}_i$ is the ion current (A), $\mathbf{J}_e$ is the electron current (A), $\mathbf{J}_d$ is the displacement current (A), $\mathbf{V}_i$ is the multicomponent diffusion velocity for species i ($m \cdot s^{-1}$), V_s is the voltage at RF electrode when constant power (P_{RF}) imposed, and V_a is the amplitude of rf voltage.

Reactions And Cross Sections

The selection of cross sections for argon plasma modeling was based on the Plasma Data Exchange Project (LXCat) and literature, aiming to simplify electronic excitation. Cross sections for argon's metastable states, 1s5 and 1s3 (Ar_m), are often merged [566, 567], while higher excited states (2p) are usually omitted or grouped [567, 568], leading to variations in literature on how these processes are aggregated. The choices made for electron impact process classifications and cross-section data are outlined with the aim of constructing a well-defined argon plasma model that can be easily duplicated by other researchers. The model simplifies by excluding ionization from 2p to Ar^+, and categorizes electronic states into Ar_m, resonant Ar_r, and 2p states (Ar_p), focusing on Ar_m for superelastic collisions. Following Bogaerts, the model emphasizes essential reactions at low pressures and assumes all species revert to ground state at chamber walls, excluding total electronic excitation and excited molecular argon species. Key data sources include the IST-Lisbon database for elastic collisions and excitations [569], SIGLO for ionization [570], and Hyman for metastable and 2p state ionizations [571]. **Table 6** enumerates all electron impact processes (reactions) incorporated in the present model.

***Table 6**. Argon reaction set used in the model. DB: detailed balancing, σ (ε) m^{-2}: cross-section data. k: rate expression [136].*

#	Process	Description	Rate Expression	Threshold Energy (eV)
1	$e + Ar \rightarrow e + Ar$	Elastic collision	$\sigma(\varepsilon)$ m^{-2}	1.36×10^{-5}
2	$e + Ar \rightarrow 2e + Ar^+$	Ionisation	$\sigma(\varepsilon)$ m^{-2}	15.76
3	$e + Ar \rightarrow e + Ar_m$	Excitation to metastable states	$\sigma(\varepsilon)$ m^{-2}	11.55

4	$e + Ar_m \rightarrow e + Ar$	Deexcitation of metastables	$\sigma(\varepsilon)$ m^{-2}	-11.55
5	$e + Ar \rightarrow e + Ar_r$	Excitation to resonance states	$\sigma(\varepsilon)$ m^{-2}	11.62
6	$e + Ar_m \rightarrow e + Ar_p$	Excitation from metastable to higher $2p$ states	$\sigma(\varepsilon)$ m^{-2}	3.2
7	$e + Ar \rightarrow e + Ar_p$	Direct excitation to higher $2p$ states	$\sigma(\varepsilon)$ m^{-2}	13
8	$e + Ar_m \rightarrow e + Ar^+$	Ionisation of metastable states	$\sigma(\varepsilon)$ m^{-2}	4.21
9	$Ar_m + e \rightarrow Ar_r + e$	Electron quenching	k=2x10^{-7} cm^3 s^{-1}	-
10	$Ar_m + Ar_m \rightarrow Ar + Ar^+ + e$	Metastable collision	k=6.4x10^{-10} cm^3 s^{-1}	-
11	$Ar_m + Ar \rightarrow 2Ar$	Two-body collision	k=2.3x10^{-15} cm^3 s^{-1}	-
12	$Ar_r \rightarrow Ar$	Radiative emission	k=3x10^7 s^{-1}	-
13	$Ar_p \rightarrow Ar$	Radiative emission	k=3.2x10^7 s^{-1}	-

6.4. Results

6.4.1. Langmuir probe measurements

6.4.1.1. Plasma parameters

In the realm of plasma physics, an understanding of plasma dynamics is facilitated by a set of fundamental parameters, each encapsulating distinct aspects of plasma behavior and properties. Understanding plasma parameters and their interdependencies is crucial for the diagnostic and theoretical exploration of plasma systems. In our investigation of plasma characteristics, we explored the behavior of these parameters across different power settings (25W, 50W, 100W) and pressures (100 mTorr, 200 mTorr, 300 mTorr). Figure 46 shows the trends for each parameter (plasma potential, floating potential, electron temperature, electron density, ion density, electron saturation current) as measured by the Langmuir probe under the various power and pressure conditions.

Monitoring the plasma and floating potentials is crucial for understanding and controlling plasma behaviour. We measured the variation in plasma potential V_p and floating potential (V_f) across the range of power settings and pressures as is illustrated in Figure 46a and Figure 46b, respectively. V_p ranged between 29 and 37 V and an increasing trend was observed as the power input increased from 25W to 100W at all tested pressures. The most pronounced rise occurred at the highest pressure as is expected with higher power as the plasma becomes more energetic. On the other hand, V_f showed an overall minor decrease in magnitude with rising power. A noticeable increase in V_p and V_f with pressure can be observed; however, both parameters tended to converge with pressure at higher powers.

The electron temperature in a plasma is a crucial parameter as it provides insights into the energy obtained by the electrons. In Figure 46c, the electron temperature (T_e) measurements ranged between 1.6 and 3.6 eV and demonstrated a clear trend of increasing electron temperature with increasing powers across all pressures, suggesting that the supplied power significantly bolstered the energy of the electrons. The increase in electron temperature from 25 W to 50 W is noticeable across all pressures. From 50 W to 100 W, the electron temperature increased less drastically at lower pressures and remained relatively stable at 200 mTorr. However, the relationship between pressure and temperature is not linear, as indicated by the decrease in T_e from 200 mTorr to 300 mTorr at all power levels. For example, at 50W, the electron temperature values exhibited an upward trend as pressure increased from 100 mTorr to 200 mTorr, from 2.79 ±0.01 to 3.43 ±0.08 eV. However, at 300 mTorr, a decrease in electron temperature to 2.02 ±0.03 eV was noted. Increasing the power to 100W, the reduction in T_e values between 200 mTorr and 300 mTorr,

although evident, was less pronounced with a decrease from 3.59 ±0.11 to 2.9 ±0.03 eV.

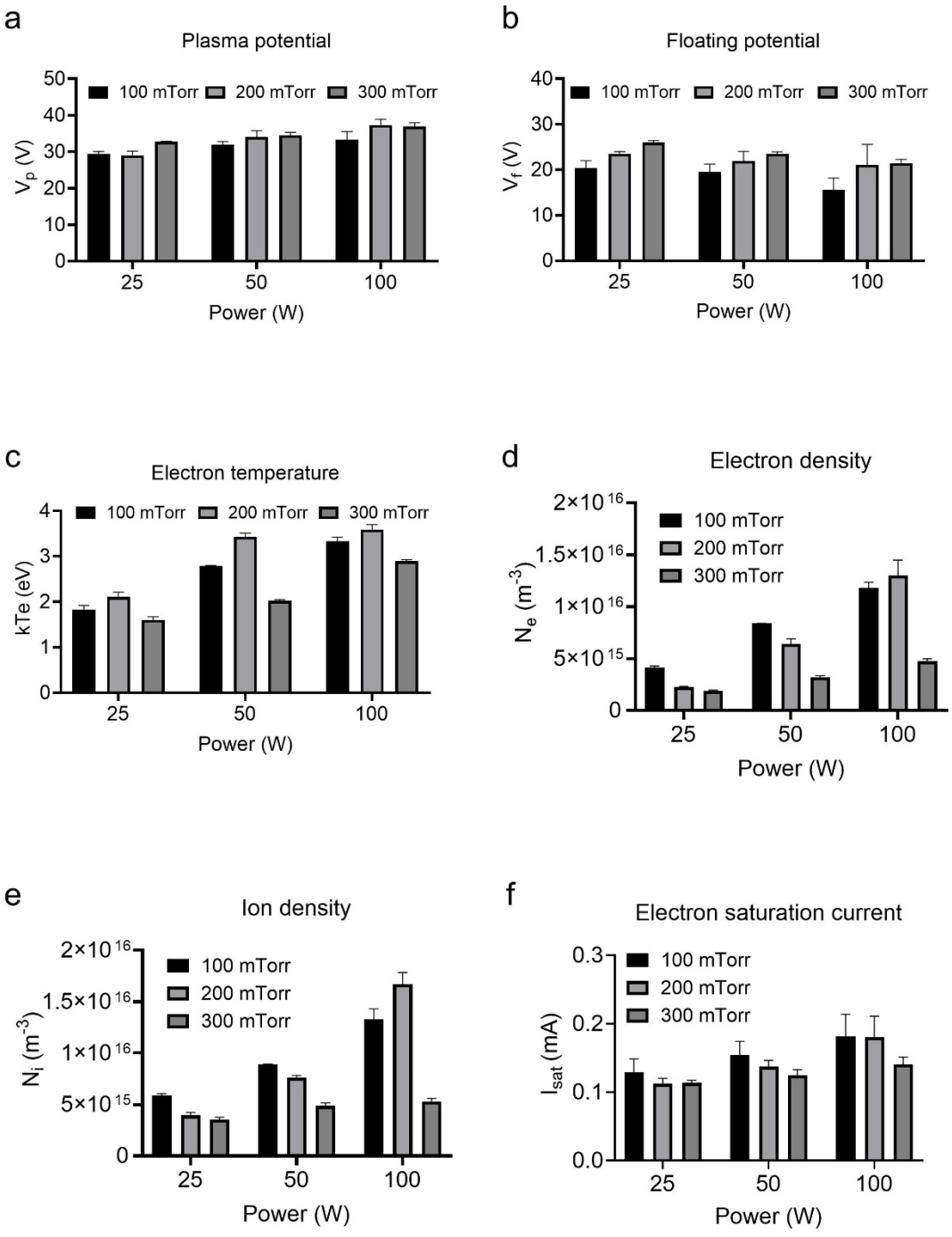

Figure 46. Trends in (a) plasma potential, (b) floating potential, (c) electron temperature, (d) electron density, (e) ion density and (f) electron saturation current as measured by the Langmuir probe across different power settings (25W, 50W, 100W) and pressures (100 mTorr, 200 mTorr, 300 mTorr).

The increase in T_e with power mirrors the rise in V_p, affirming the principle that a higher power input at constant pressure results in increased electron temperature leading to increased electron

losses to the walls and therefore a higher plasma potential is needed to equalize electron and ion losses as required [533]. The observed increase in V_p with power suggests that the potential drop across the sheath increases as the power increases, due to the rising electron temperature. This results in a stronger electric field in the sheath, which accelerates ions more effectively towards the surface to equalize the increased electron losses. The decrease in the magnitude of the floating potential with an increase in power, accompanied by higher electron temperatures, could be attributed to the enhanced electron energy. Higher power input boosts the electron temperature, increasing the kinetic energy of electrons. This change in the electron energy distribution can lead to a situation where more electrons possess sufficient energy to overcome the potential barrier at the sheath edge, resulting in a reduced need for the floating potential to become highly negative to repel excess electrons and maintain current balance. Consequently, the magnitude of V_f decreases as the plasma adapts to the new energy equilibrium [572]. The difference between the plasma potential and the floating potential increasing indicates that the potential drop across the plasma sheath continued to increase. With a larger potential drop across the sheath, ions gain more energy before reaching surfaces or probes. This can lead to more energetic ion bombardment effects, which can be an initiator for plasma etching, sputtering and changes in plasma–sheath boundaries in our system [573]. The impact of pressure on T_e reduced with increased power, particularly at 100W and became less significant when the power was sufficiently high. This suggests that within the 200 - 300 mTorr pressure range, the input power is sufficient to raise the electron energy despite the increased collision rate associated with higher pressures. Beyond this range, the rate of collisional energy loss possibly surpasses the energy input from the power supply, leading to a net cooling effect on the electrons [532].

We also monitored the electron and ion densities in the plasma to better understand its conductivity and electrical properties. The electron density, shown in Figure 46d, exhibited a clear positive correlation with power, rising from 4.15×10^{15} to 1.18×10^{16} m^{-3} at 100W and the lowest pressure of 100 mTorr. The ion density followed a similar trend as the electron density, increasing with power from 5.9×10^{15} to 1.33×10^{16} m^{-3}, as can be seen in Figure 46e. At the intermediate pressure of 200 mTorr, both electron and ion densities again increased with power, reaching notable peaks of 1.3×10^{16} and 1.67×10^{16} m^{-3} at 100 W, respectively. The standard deviations were generally larger at higher powers, indicating more variability in these measurements. Increasing the pressure to 300 mTorr, the densities became comparatively lower across all power settings. In Figure 46f, the electron saturation current increased with power at all pressures, which is consistent with the increase in electron density and temperature. The saturation current was its highest at 100 mTorr, which corresponds with the highest electron densities. At higher pressures, the saturation current was lower, likely due to the combined effect of lower temperatures -compared to 100 mTorr- and the lower electron densities at 300 mTorr.

The rise in electron and ion densities with power input correlates with observed increases in plasma potential and electron temperature. This is attributable to enhanced ionization rates under increased power conditions, leading to a greater concentration of charged particles. Consequently, this results in a heightened plasma potential due to augmented ion-electron collisions and an elevated electron temperature resulting from the additional energy input [573]. The increase in Isat with power implies that the sheath potential barrier is lower, or there are more high-energy electrons available to overcome the barrier due to increased kTe. Isat is related to the number of electrons that have enough energy to overcome the sheath potential barrier and reach the surface. As the plasma becomes more energetic (higher T_e), the electron current increases, and V_f must decrease to maintain the balance of currents since the ion current does not increase as much due to the ions' lower

mobility. As n_e and n_i densities rise with power, the sheath becomes thinner. This could lead to a more responsive sheath that rapidly adjusts to changes in the plasma environment, influencing ion bombardment and plasma-surface interactions [554].

At higher pressures, the electron density decreases gradually as the gas pressure increases from 100 mTorr to 300 mTorr, and has been attributed to electrons not having the sufficient energy for effective ionizations [574]. The electron temperature firstly shows an increase up to 200 mTor and then it increases gradually in the higher-pressure range. The typical expected increase in density due to more frequent collisions is not observed, potentially due to the increased importance of non-ionizing loss mechanisms at higher pressures. Mechanisms such as electron-ion recombination [575], diffusion losses[557], or reduction in plasma confinement [548] can become more influential with increasing pressure. These results could also imply that ions were subject to more recombination or were less effectively produced at higher pressures. Less effective production of ions occurs due to the reduction in mean-free paths between electron creating ionisation collisions or deenergising scattering collisions and the next encouter with a neutral that occurs with the background gas pressure increase. Once the mean free path becomes so small that the energy an electron gains between collisions is no longer enough to ionise the background gas molecules deenergising scattering collisions will dominate over ionisation events, reducing the ion and electron densities in the plasma accordingly. This turning point occurs at lower pressures when the power is lower because the electric fields accelerating electrons between collisions are lower at lower powers.

6.4.1.2. Electron Energy Distribution Function

The Electron Energy Distribution Function (EEDF) is a pivotal property of the plasma, offering profound insights into the energy states of the electron population. It's a fundamental characteristic of plasmas, affecting reaction rates and overall plasma chemistry. On the other hand, the Electron Energy Probability Function (EEPF) offers a probability distribution, showing the probabilities of electrons having different energies across the energy spectrum. It is typically determined from the EEDF and emphasizes features like resonance peaks. The shape and characteristics of the EEDF and EEPF curves are indicative of the underlying electron dynamics and electron energies. For instance, higher magnitudes at higher energies within the EEDF suggest an increased likelihood of encountering electrons with those high energies, hinting at dominant electron energies or significant populations within those ranges. The breadth and definition of any peaks observed in the EEDF can vary; a narrow, pronounced peak typically signifies a dominant electron energy, whereas a broader distribution implies a diversity of electron energies.

The generalised forms of the EEDF and EEPF are given by, respectively:

$$F(\varepsilon) = g\bar{\varepsilon}^{-3/2}\Gamma(5/2g)^{3/2}\Gamma(3/2g)^{-5/2}e^{-\left(\varepsilon\Gamma(5/2g)\Gamma(3/2g)^{-1}/\bar{\varepsilon}\right)^{g}}$$

$$f(\varepsilon) = F(\varepsilon)\varepsilon^{-1/2}$$

where ε is the electron energy, g is the shape parameter, and Γ is the incomplete gamma function.

To discern the nature of the EEPF—whether it resembles a Maxwellian, bi-Maxwellian, or Druyvesteyn distribution—requires an understanding of each type's distinct features. A Maxwellian distribution, representative of a thermal equilibrium state, is characterized by a smooth, bell-shaped

curve that tapers gradually at higher energies. A bi-Maxwellian distribution suggests the coexistence of dual electron populations, distinguished by either dual peaks or a noticeable "shoulder" within the EEPF, indicative of a secondary, high-energy electron group. The Druyvesteyn distribution, often arising in plasmas dominated by inelastic collisions, is marked by a sharper decline at elevated energies compared to its Maxwellian counterpart.

The EEPF's detailed analysis extends beyond identifying the electron energy distribution's form; it involves examining the curve's low-energy region, which typically slopes downward due to elastic and inelastic collisions, and the high-energy tail, which is associated with electron-impact ionization processes. The slope in the low-energy domain can reveal the effective temperature of the bulk electrons, while the tail's presence underscores the role of energetic electrons in ionization and excitation phenomena.

Alterations in experimental conditions or external influences, such as variations in power, pressure, or magnetic fields, can significantly modify the EEPF's shape, thereby affecting the electron energy distribution. Figure 47 shows the EEPFs obtained by differentiating the IV curves from the plasma in the various ranges of pressures and power settings.

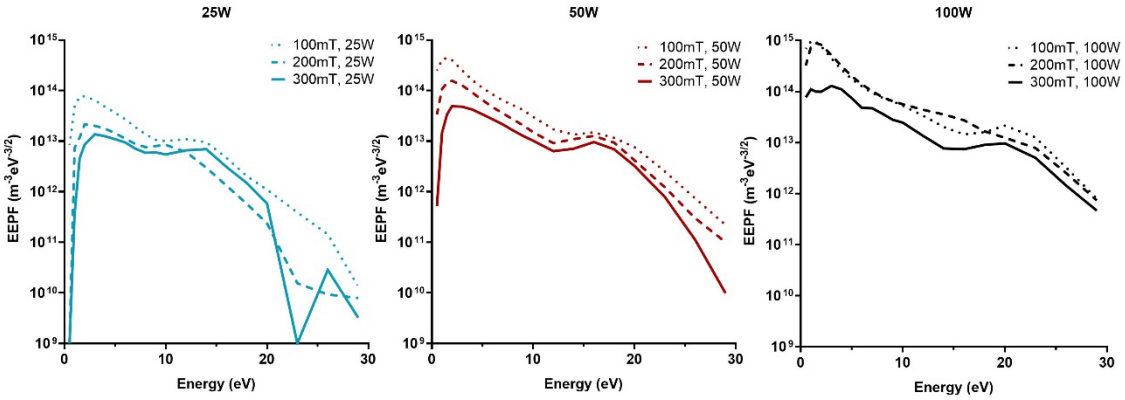

Figure 47. EEPFs obtained by differentiating the IV curves from the plasma under different pressure (100, 200 and 300 mTorr) and power (25, 50 and 100 W) settings.

The variation of the EEPFs at the range of pressures is shown in Figure 47. At 25W, a systematic shift in average energies with increasing pressure is observed: at 100 mTorr, the most probable energy is observed at 1.5 eV, increasing to 2.0 eV at 200 mTorr, and further to 4.0 eV at 300 mTorr. The average electron energies were calculated from the above EEPFs to be 6.5 ± 0.5, 7.1 ± 0.9 and 9.0 ± 0.7 eV at 100, 200 and 300 mTorr respectively. This progression indicates the correlation between increased pressure and the elevation of average electron energies within the plasma. The EEPF at 100 mTorr is particularly noteworthy for its pronounced tail extending beyond 10 eV, suggesting a substantial deviation from a Maxwellian distribution towards a more non-Maxwellian one, characterized by a significant population of high-energy electrons. This feature diminishes progressively with increased pressure, pointing towards a decrease in the relative number of high-energy electrons, likely due to augmented collisionality at higher pressures [557], which acts to thermalize the electron energy distribution more effectively. Upon increasing the power to 50W and 100W, the trend persists with minor variations. At 50W, the EEPF broadens at 100 mTorr, indicating a sizeable high-energy electron population. This broadening is less pronounced at higher

pressures (200 mTorr and 300 mTorr), suggesting a decrease in high-energy electron populations, likely due to enhanced collisional cooling. The trend at 100W mirrors this behavior, albeit less distinctly, with a less distinct shift in average energies at the lower pressures. A gradual narrowing of the EEPF as pressure increases from 100 mTorr to 300 mTorr can still be seen, consistent with the observations at lower power settings.

By observing the effect of power, the EEPF curves at all power settings show a broad distribution of electron energies at 100 mTorr, indicating a substantial population of high-energy electrons. As the power increases, the density of electrons at higher energies also increases, suggesting that more electrons are being accelerated to higher energies, and more atoms are being ionized to create more free electrons as was evident from the increasing electron density measurements. The EEPFs begin to display a shift towards lower electron energies at 200 mTorr. While there is still a significant high-energy electron population at 25W and 50W, it is less pronounced than at 100 mTorr. At 100W, the tail of the EEPF extends less into high energies, indicating that the plasma at this pressure and power setting contains fewer high-energy electrons. At 300 mTorr, the EEPFs across all power settings are considerably steeper after the highest average energy, with a more pronounced decline in electron population at high energies. This steepness is indicative of a lower presence of high-energy electrons. The EEPFs for 25W and 50W show a shift towards even lower energy ranges, while the EEPF for 100W, despite having higher energies, also quickly declines, highlighting a significant cooling effect at this high pressure. A flatter EEPF at higher powers implies a higher electron temperature as it indicates more high-energy electrons, which is consistent with the measurements showing increasing electron temperature with power.

Overall, the EEPF curves rise to a maximum, which is followed by a shoulder and then fall off. The shapes indicate a non-Maxwellian distribution as they shifted to higher energies when subject to higher powers. The lower energy decline seems relatively smooth, which might suggest a Maxwellian-like distribution, but the steepness of the fall-off is consistent with the Druyvesteyn assumption. When the Electron Energy Distribution Function (EEDF) deviates from a Maxwellian distribution, it encompasses both ultrafast and slow electrons. This characteristic arises due to stochastic electron heating at the oscillating boundary between the plasma and sheath [576, 577]. In CCRF discharges, electrons primarily interact with an electric field aligned perpendicular to the electrodes, leading to energy fluctuations. This process, along with collision-induced isotropization, defines electron heating. Historically, two electron heating mechanisms have been identified: "Ohmic heating," a collisional approach, and "stochastic heating," identified for low-pressure conditions where collisions are infrequent. Stochastic heating arises from the electric field's temporal and spatial variations, particularly around the oscillating plasma sheaths in CCRF discharges [532, 574]. The EEDF changes imply that a transition from collisionless stochastic heating to collisional Ohmic heating into the bulk plasma appears at the gas pressure of 300 mTorr. By varying of the gas pressure, a transition appears to take place between different electron heating modes [574].

6.4.1.3. Spatial variations

Langmuir probe diagnostics offer a direct method to gauge critical plasma parameters, including electron temperature and plasma density. The fundamental limitation of single-point Langmuir probe measurements lies in their inability to capture the complex spatial variations characteristic of plasmas. To overcome this, Langmuir probes have been deployed at various positions within the plasma reactor, often closer to the plasma bulk. This approach enables the acquisition of a detailed spatial distribution of plasma parameters, providing a multidimensional perspective of the plasma's

behavior. Such spatially resolved data is indispensable for the rigorous validation of theoretical models, such as the COMSOL Multiphysics simulation model developed in Section 6.7. A right-angled connector was used to extend the Langmuir probe's measurement point further below the powered RF electrode as can be seen in Figure 48. The measurements were taken at the central axis of the reactor at 22, 32 and 42 mm below the RF electrode.

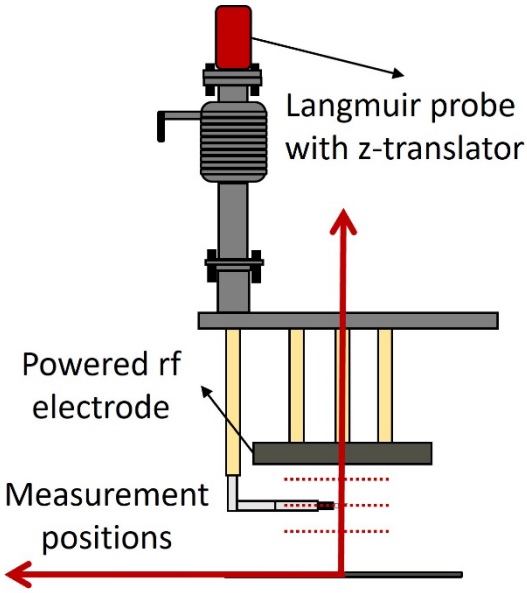

Figure 48. Sketch showing the Langmuir probe setup using the right-angled connection resulting in measurements directly below the RF electrode and further into the plasma bulk. Figure not to scale.

Figure 49a represents a series of plasma potential measurements conducted at varying applied RF powers of 25W, 50W, and 100W under three different pressures (100 mTorr, 200 mTorr, and 300 mTorr), at three distinct probe heights below the RF electrode (42 mm, 32 mm, and 22 mm). A general trend where the plasma potential decreased with distance from the RF electrode and increased with higher pressures across all powers was observed. The lowest potentials were recorded at 42 mm below the electrode, with a gradual increase as the measurement point moves closer, reaching the highest potentials at 22 mm. The plasma potential at 100 mTorr was the lowest at 31 V and at 300 mTorr was the highest at 39 V at 25W. The same trend was noted at 50 W; however, the differences between the potentials with increasing pressures was reduced, especially between 200 and 300 mTorr. The influence of power on the plasma potential was further reduced with pressure, which suggests that higher power input may have led to a more homogeneous plasma. This could indicate a saturation effect where further increases in power had a reduced impact on potential at closer distances.

The electron temperatures recorded at the three positions at various pressures and power settings can be seen in Figure 49b. The overall trend across the heights suggests that as the Langmuir probe moves closer to the RF electrode (from 42mm to 22mm) and with increasing powers, there is a general increase in the electron temperature. Higher electron temperature peaks near the discharge electrode in an unmagnetized CCP discharge are observed and explained through the concept of stochastic electron heating, which occurs due to the dynamic nature of RF sheaths [381, 578]. The temperatures fluctuate slightly with pressure on the other hand. At 25W, electron temperature increases with pressure from 100 mTorr to 200 mTorr but declines at 300 mTorr across all probe positions. This non-linear pattern suggests pressure increases electron temperature up to a point, after which higher pressures reduce it through increased collisional losses. Increasing power to 50W, a similar non-linear trend is observed. Temperatures peak at 200 mTorr at all positions, with

a slight decrease at 300 mTorr, implying optimal conditions for ionization and electron energy absorption at this intermediate pressure. At 100W, a general trend of decreasing electron temperature with increasing pressure is noted. The temperature at 200 mTorr varies, showing an increase at 42mm and a decrease at 22mm compared to 100mTorr. The highest and lowest temperatures of 4.24 eV and 2.63 eV are observed at 22mm and 42mm from the RF electrode at 100mTorr and 300mTorr, respectively, indicating proximity to the electrode and lower pressures favour higher temperatures.

Figure 49c and Figure 49d illustrate the electron and ion densities measured at the three power settings under different pressures and at varying distances from the RF electrode. The increase in both densities with power remained clear. The electron and ion densities increased progressively as the probe moved closer to the RF electrode at all power and pressure combinations. At low powers, the highest density of both electrons and ions was observed at 100 mTorr and decreased with increasing pressure. This decrease became less prominent at intermediate power and a change in trend can be seen at 100W whereby the highest densities were at 200 mTorr. This suggests that only the highest power of 100W produced electric fields strong enough to retain a high level of ionizing collisions at the reduced mean-free-path at 200 mTorr with the drop in ionizing collision frequency occurring at the further reduced mean-free-path at 300 mTorr.

It is apparent that the plasma potential and electron temperature are influenced both by the proximity to the RF electrode and the operating pressure. The trend across the heights suggests that as the Langmuir probe moves closer to the RF electrode (from 42mm to 22mm), there is a general increase in these parameters at any fixed pressure and power combination. This is consistent with expected plasma behavior where higher pressures and closer proximities to the energy source generally result in higher potentials. It could indicate that the electric field strength is greater closer to the RF electrode, as can be seen with the increase in electron and ion densities. At higher powers the increase in densities with position becomes more prominent while the electron temperatures begin to show signs of saturation followed by decline with pressure increase to 300 mTorr. This suggests that pressure plays a dominant role in determining the plasma potential, potentially due to its effect on the density of ionizable species and the frequency of collisions in the plasma.

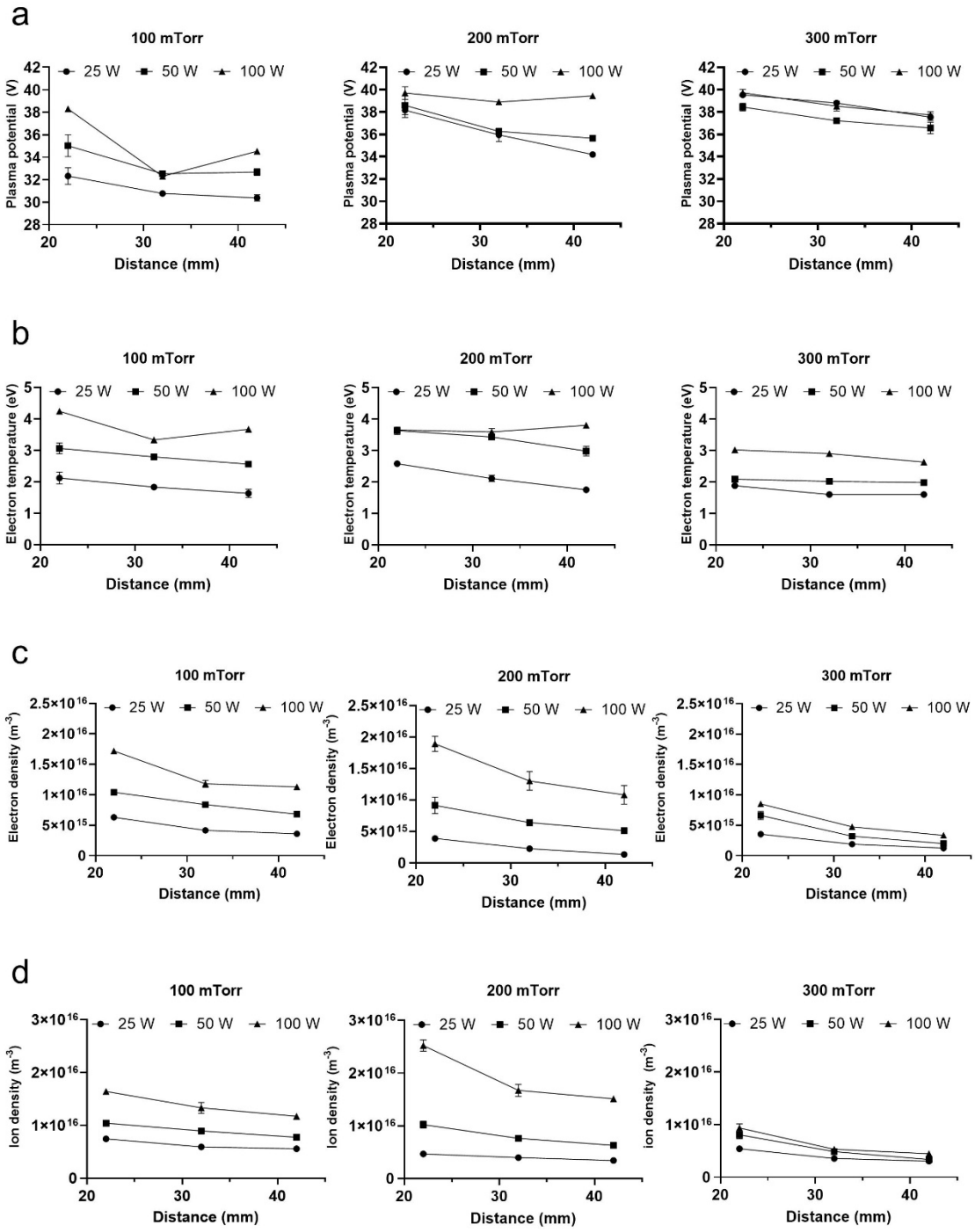

Figure 49. A series of measurements conducted at varying applied RF powers of 25W, 50W, and 100W under three different pressures (100 mTorr, 200 mTorr, and 300 mTorr), at three distinct probe heights below the RF electrode (42 mm, 32 mm, and 22 mm) showing the (a) plasma potential, (b) electron temperature, (c) electron density, and (d) ion density.

6.5. Electrical discharge dynamics

The plasma behaviour with increasing pressure, particularly between 200 and 300 mTorr, may be understood through the lens of the Paschen law. The Paschen law describes the breakdown voltage,

the minimum voltage required to initiate a discharge, as a function of the product of gas pressure and electrode separation distance [579]. This relationship exhibits a minimum value, known as the Paschen minimum, where the breakdown voltage is at its lowest. This relationship has been studied extensively in the literature and can be seen plotted for a variety of gases in Figure 50a. Paschen's Law is given by the formula [580]:

$$V_B = \frac{Bp\,d}{ln(Apd) - ln\left(ln\left(1+\frac{1}{\gamma}\right)\right)}$$

Where V_B is the breakdown voltage, p is the pressure of the gas, d is the distance between the electrodes, A and B are constants that depend on the gas type and γ is the secondary ionization coefficient, which is often considered a constant under certain conditions.

The Paschen minimum occurs at a specific value of the product $p\,d$ (pressure-distance product), which can be found by differentiating the Paschen's Law equation with respect to $p\,d$ and setting the derivative equal to zero to find the critical point. However, in practice, A, B, and γ are experimentally determined constants for each gas, and the exact calculation might require empirical data. In the absence of empirical values for this discussion, the breakdown voltages and the Paschen minimum were inferred from available literature for argon plasmas in CCRF discharges [581-583].

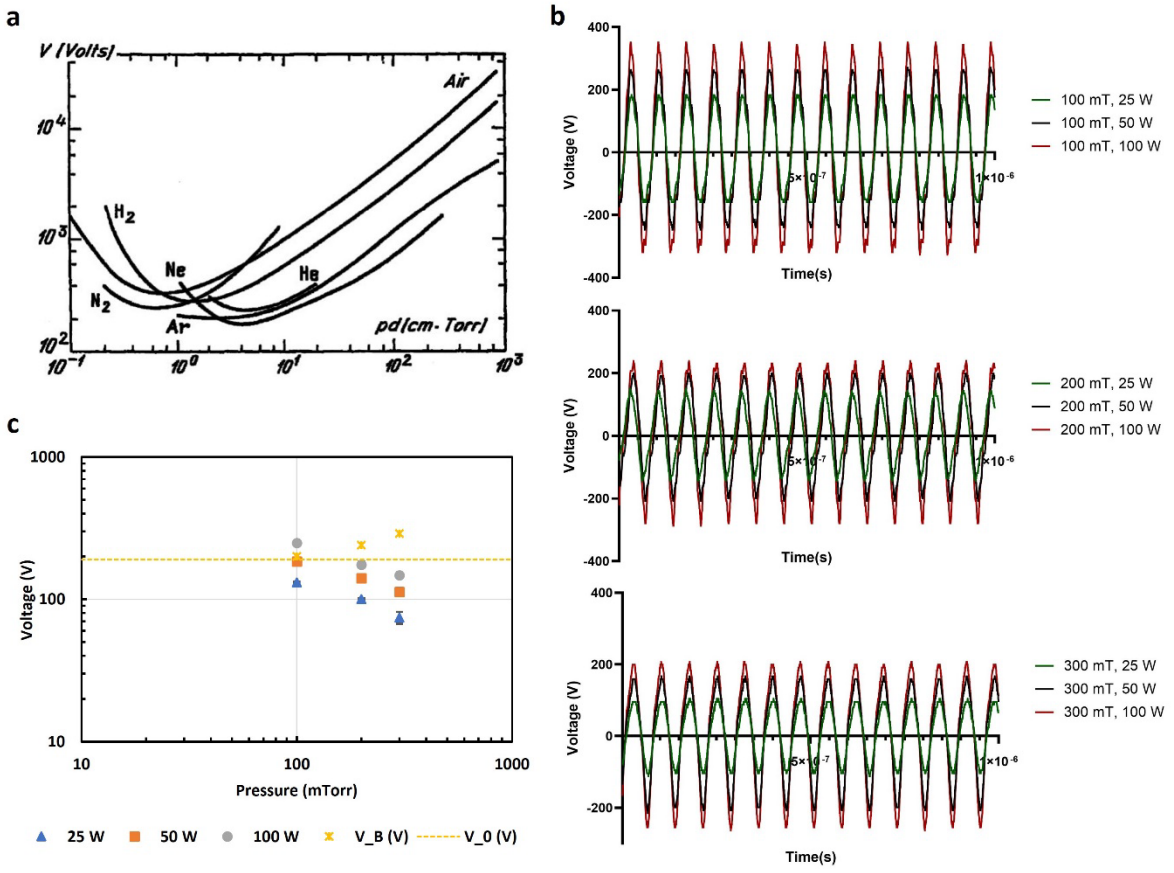

Figure 50. (a) Paschen curves for air, nitrogen, hydrogen, helium and argon [579]. (b) Measured voltage waveforms at 25, 50 and 100W for each pressure of 100 (top), 200 (middle) and 300 (bottom) mTorr. (c) The V_{rms} at each combination of power and pressure, obtained from the waveforms in (b), plotted alongside the

Paschen minimum V_0 and the estimated breakdown voltages V_B for our argon plasma at our fixed electrode gap.

Incorporating input voltage and current waveforms from an RF power generator into plasma research can significantly improve the understanding of plasma characteristics by allowing for precise power dissipation analysis and impedance matching, which are critical for assessing electron density, temperature, and maximizing power transfer. Additionally, these waveforms facilitate the examination of energy distribution, plasma stability, and non-linear behaviors, providing insights into electron heating mechanisms, plasma process fluctuations, and non-linear dynamics such as sheath rectification and mode transitions. The voltage waveforms captured at the powered electrode under various pressure and power inputs are shown in Figure 50b. The voltage amplitude escalated with increasing power across all pressure levels, with a notable surge observed at 100 mTorr. Although this upward trend continued at higher pressures, the rate of increase became less pronounced at 200 and 300 mTorr. This diminishing sensitivity of the voltage amplitude to power increments at elevated pressures suggests that while the plasma's response to power input is initially robust, it becomes more subdued as pressure rises, confirming the likelihood of enhanced collisional damping or a reduced power input into the plasma.

The Root Mean Square Voltage (V_{rms}), or effective voltage (V_{eff}), is often used to express the magnitude of fluctuating voltage in terms of its capacity to deliver power, similar to a constant DC voltage. The significance of V_{rms} is attributed to its direct association with the power dissipation in a resistive element, wherein a sinusoidal AC voltage characterized by a V_{rms} magnitude yields an equivalent average power dissipation in a resistor as would a DC voltage of identical magnitude [552]. V_{rms} is often used when discussing the power delivered to the plasma because it relates directly to the heating and ionization processes that sustain the plasma. In Figure 50c, we plotted the measured V_{rms} alongside the Paschen minimum V_0 and the estimated breakdown voltages for our argon plasma at the various pressure and power combinations and fixed electrode gap. With the Paschen minimum around 200 V, it becomes clear that the observed pressure region of 100 mTorr is notably close to the Paschen minimum for our electrode setup geometry. Around the Paschen minimum, ionization processes tend to be more efficient, leading to increased electron densities [580, 584]. However, when the pressure surpasses this minimum threshold, the ionization process becomes less effective due to a relative increase in non-ionising collisions. At pressures higher than the Paschen minimum, inelastic non-ionising collisions become predominant, causing a reduction in the plasma electron temperatures. This decrease in electron temperatures results in diminished ionization efficiency, as the electrons possess lower energy for gas ionization, consequently causing a reduction in electron density. The effective voltage delivered to the reactor at higher pressures lies below the Paschen minimum and is also a possible indicator that the proper breakdown of the argon gas is not being attained at these conditions.

To investigate non-linear effects in our plasma, we examined the current and voltage waveforms for deviations from a sinusoidal shape at different pressures and powers. Harmonics in CCRF discharges are integer multiples of the fundamental frequency (13.56 MHz) that arise due to nonlinear processes within the plasma or the electrical systems driving the plasma. In Figure 51, the voltage waveforms seem to be a fairly smooth sinusoidal waveform, indicating a primary frequency with potentially some harmonic content. The current waveform, on the other hand, shows more significant distortions, suggesting a higher level of harmonic content. The degree of deviation from a pure sinusoidal waveform can be quantified by measuring the amplitude of each harmonic frequency by a mathematical analysis such as a Fast Fourier Transform (FFT). This analysis can break down the waveform into its constituent frequencies, showing the magnitude of the

fundamental frequency and its harmonics. In Figure 52, considerable distortions in the current waveform are observed and are typically generated due to non-linear elements of the plasma such as its impedance[585]. Several harmonics of the applied frequency are observed in all the current waveforms. The intensities of all the harmonics are seen to increase proportionally with increasing rf power with a relatively significant signal from the second harmonic (27.12 MHz). With increasing pressure, all the harmonics appear to decrease in magnitude while the ones at higher (third and above) frequencies disappear at 300 mTorr. The differences may be due to the change in the bulk plasma resistance with variations of the supplied electric field with pressure and the existence of the plasma series resonance (PSR) effect [586]. This effect occurs when the natural oscillation frequency of electrons in the plasma matches the frequency of an external driving electromagnetic field. At resonance, the plasma exhibits a significant increase in the absorption of electromagnetic energy, leading to enhanced oscillations or waves within the plasma.

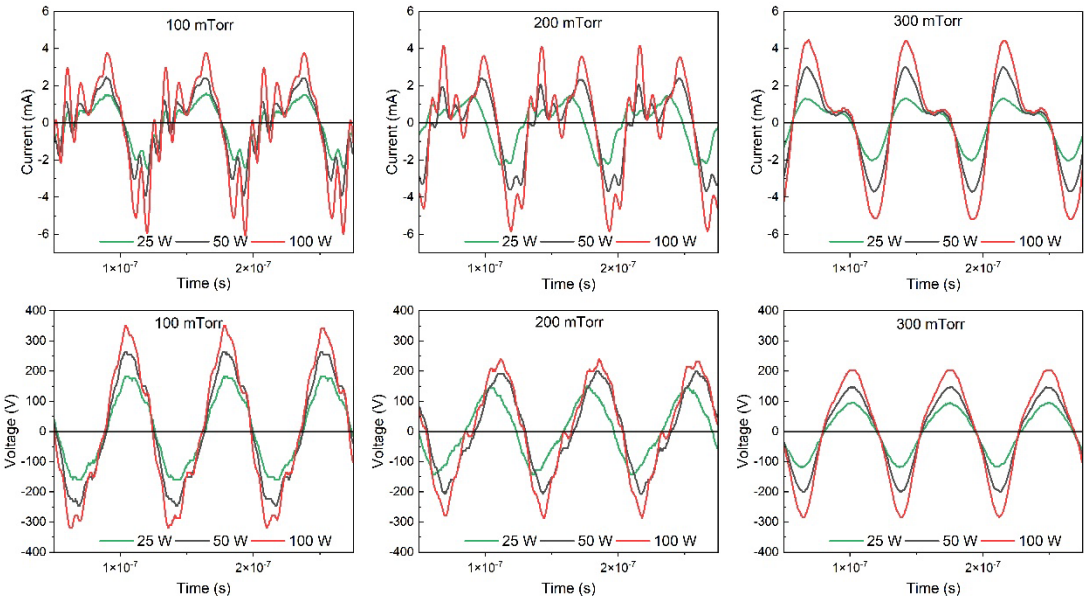

Figure 51. Discharge (top) current and (bottom) voltage waveforms across various pressures and power settings.

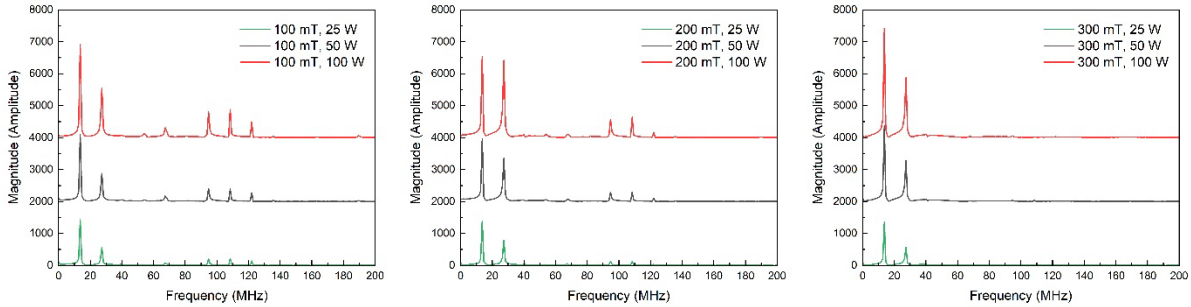

Figure 52. Fast Fourier Transform (FFT) of the current waveform collected at the powered electrode across various pressures and powers showing the harmonics at the signals.

6.6. DC self-bias voltage

The self-bias voltage is particularly important in determining the energy with which ions strike the electrodes or any substrate placed in the plasma. Higher bias voltages typically mean higher ion energies. This energy can significantly affect the quality of thin films, etching profiles, and other

surface modifications in material processing applications. The ability to control and manipulate V_{DC} allows for the optimization of process parameters to achieve desired material properties and device performance.

The DC-self bias in plasma systems arises due to the asymmetric response of electrons and ions to an applied radio frequency electric field. Electrons, being much lighter and more mobile than ions, can respond more quickly to changes in the electric field. As a result, over one RF cycle, electrons tend to accumulate on surfaces (such as electrodes) more readily than ions. This accumulation leads to the development of a self-bias voltage, a negative potential that forms to balance the electron current with the ion current over the RF cycle. The magnitude of this self-bias voltage is directly influenced by the mobility and energy of the electrons; as these increase, the excess electron current becomes more pronounced, necessitating a higher negative bias to suppress this excess and achieve current balance. This bias affects the ion bombardment energy on surfaces and can influence the overall plasma characteristics.

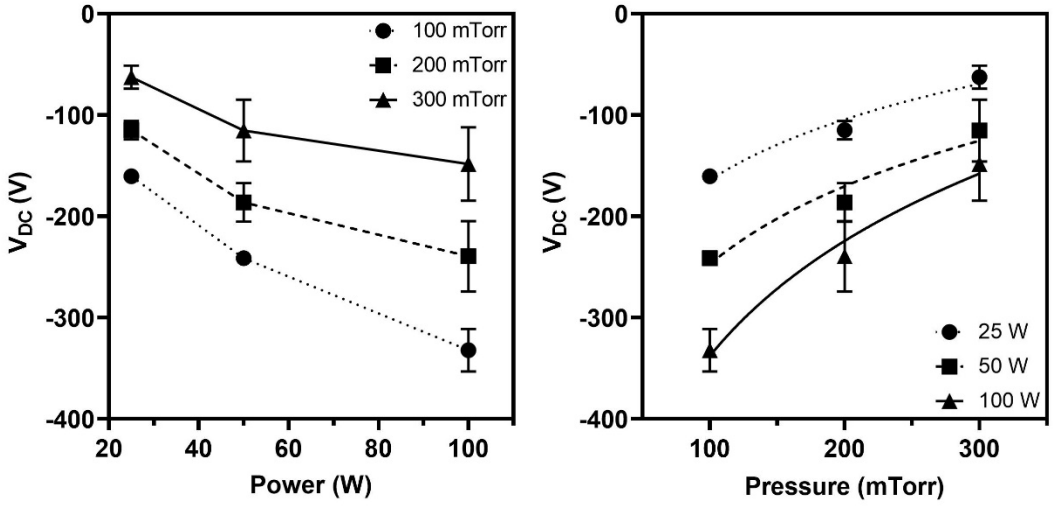

Figure 53. Self-bias voltage recorded at the RF electrode of the plasma reactor. Measurements were taken at pressures of 100, 200 and 300 mTorr and powers of 25, 50 and 100 W.

Figure 53 shows the average and standard deviation of the DC bias voltage measured at the combinations of pressure and power settings. The DC self-bias is always negative due to the higher mobility of electrons compared to ions in RF-driven plasma systems. As the power increases, there is a noticeable increase in the magnitude of the average DC bias voltage across all pressures. This trend is consistent with the increased plasma density and potential that come with higher power inputs. The negative bias becomes more pronounced, which could be indicative of a stronger electric field in the plasma. The magnitude of the average DC bias at 100 W is significantly greater than at 25 W and 50 W, suggesting that the effect of power on the electron density and energy is substantial. This could be a result of a higher electron temperature and density contributing to an increased plasma potential, thus a larger potential drop across the sheath and more negative bias on the probe. Higher power typically leads to a more pronounced DC bias norm due to increased ionization and more energetic plasmas.

The increase in the magnitude of the average DC bias voltage with increasing power aligns with the broader EEPFs observed at higher power settings, indicating a higher population of energetic electrons. A more negative DC bias suggests that the plasma potential is increasing, which is

consistent with the presence of more high-energy electrons that can overcome the potential drop across the sheath. At higher powers, there are more electrons and they have more energy, contributing to the extension of the EEPF tail, as seen in the graphical data. This is consistent with the more negative average DC bias values recorded, which suggest that these energetic electrons contribute to an increase in the electron current to the powered electrode, and hence a greater negative self-bias is required to reduce the excess electron current so as to match the ion current drawn over an rf cycle.

The less negative DC bias at higher pressures also relate to the observed trends in n_e and T_e. The reduced electron temperature and density at higher pressures due to increased collision-related losses, resulting in lower electron currents to the powered electrode and therefore a less negative DC self-bias. The observed decrease in electron density with increasing pressure, despite the increase in plasma potential and power, could be linked to the V_{DC} data. At lower pressures, the higher magnitude V_{DC} might enhance ionization efficiency, contributing to a higher electron density. At higher pressures, the lower V_{DC}, combined with increased collisionality as indicated by lower electron temperatures, might lead to less efficient ionization and increased electron loss mechanisms, resulting in lower electron densities. The variability in the DC bias, indicated by the standard deviation, might also be associated with the variability in floating potential (V_f). The more negative bias and larger standard deviations at higher powers can be a sign of a more dynamic and potentially unstable plasma.

6.7. Simulation model validation and assessment

A 2D axisymmetric continuum model designed for the CCRF reactor using a pure argon 13.56 MHz discharge was developed using COMSOL 5.5. This comprehensive model incorporated critical parameters to consider how plasma behavior responds to operational conditions. Two distinct discharge regions situated above and below the RF powered electrode were identified as a result of the reactor geometry and electrode spacing. The plasma dynamics were systematically analyzed over the various pressures and power input ranges and the model's responses was reflected in the plasma potential, DC self-bias, electron density distribution and electron temperature under different EEDF assumptions.

Figure 54 and Figure 55 illustrate the upper and lower discharge regions and show where relative to the electrode the plasma generation is likely most intense. Figure 54 shows the period-averaged plasma potential at 25 W and different pressures. The plasma potential in the model ranges between 20 and 40V under all pressures and increases with increasing pressure and is more negative closer to the powered electrode and become less negative away from it. The spatial distribution of V_p suggests stronger electric fields near the powered electrode, consistent with the experimental results (Figure 46a). In Figure 55 three contour plots representing model results for period-averaged electron density at a fixed power of 25 W across the various pressures. Increasing the gas pressure led to higher electron density and thinner sheath regions with the higher electron density areas adjacent to the RF electrode.

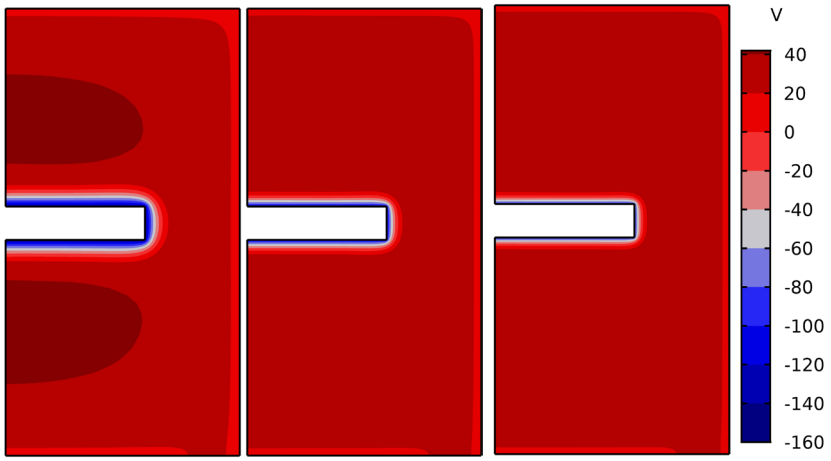

Figure 54. Model results for the period-averaged plasma potential at 25 W for pressures of 100, 200 and 300 mTorr (left to right).

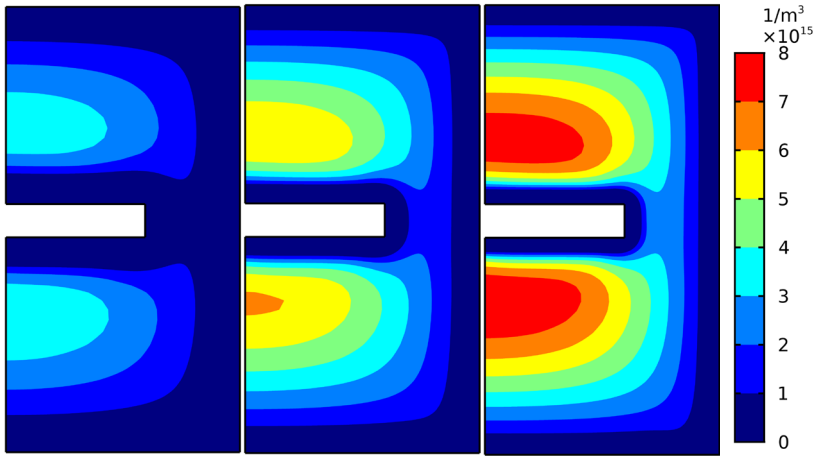

Figure 55. Model results for the period-averaged electron density at 25 W for pressures of 100, 200 and 300 mTorr (left to right).

Figure 56 presents a comparison of simulation outcomes for Electron Energy Distribution Functions (EEDFs) and Electron Energy Probability Functions (EEPFs), obtained by modifying the shape parameter in their equations for the Maxwellian (g=1) and Druyvesteyn (g=2) models. The models emphasize the increased number of electrons at both low (<2 eV) and high (>11 eV) energy extremes in the Maxwellian distribution, in contrast to the significant reduction of high-energy electrons seen in the Druyvesteyn distribution's tail. The Maxwellian EEDF, characterized by a singular temperature parameter, simplified the EEPF to a monotonic decay, indicative of elevated electron temperatures and densities due to its extended high-energy tail. The Druyvesteyn EEDF, distinguished by its relative deficit of high-energy electrons, predicted a more pronounced decline in the EEPF at higher energies, yielding higher electron temperatures but lower densities compared to the Maxwellian model.

EEDF measurements typically deviate from idealized theoretical distributions, influenced by a variety of heating and collisional processes. The experimental increase in electron temperatures (Figure 46c) with power, implied a trend towards a Maxwellian-like EEDF under such conditions, potentially due to diminished collisionality at higher energies. Maxwellian distributions suggest a denser population of high-energy electrons, typically representative of low-pressure plasmas with significant electron-electron collisionality. However, the experimental EEPFs (Figure 47) deviated

from a singular decay curve, indicating a more complex electron energy distribution than a single-temperature Maxwellian model can describe. The anomalies such as the bumps and slope changes in the experimental EEPFs suggest the presence of non-equilibrium effects and that the actual EEDF could be a hybrid of the two models, reflecting the dynamic nature of plasma conditions.

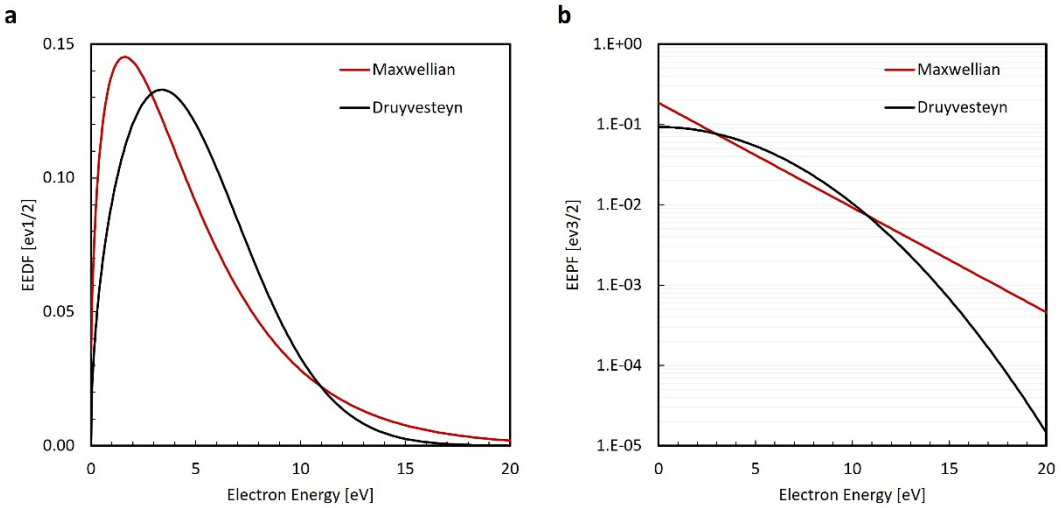

Figure 56. The electron energy distribution function (EEDF) and the electron energy probability function ((EEPF) under a Maxwellian and Druyvesteyn assumption.

The analysis of the model's plasma potential and DC self-bias in relation to applied RF power and varying pressures are depicted in Figure 57a and Figure 57b. In Figure 57a, we observed that the plasma potential for both Maxwellian and Druyvesteyn EEDFs increased with applied RF power, with the Druyvesteyn plasma potential exhibiting a steadier increase compared to the Maxwellian, at a factor of nearly 1.5. Conversely, the DC self-bias for both EEDFs became more negative as the Applied RF power increased, with minimal difference between the two EEDFs assumptions. Figure 57b further elucidated these trends, showing that the DC self-bias voltage consistently became more negative with increased power levels and rising pressure for both EEDFs. The model also showed that DC bias voltage and the electric field magnitude within the sheath region appeared to be minimally impacted by the form of the electron energy distribution function (EEDF). The model's prediction of the increase in plasma potential and DC self-bias becoming more negative with increasing power aligns well with the experimental results. However, the experimental data suggests a more pronounced effect of pressure on DC self-bias than the model predicts, with the experimental self-bias significantly more negative at lower pressures. This implies a more pronounced effect of electron heating than the model captures possibly due to variations in the experimental setup or conditions like electrode surface conditions and secondary electron emission (SEE) effects.

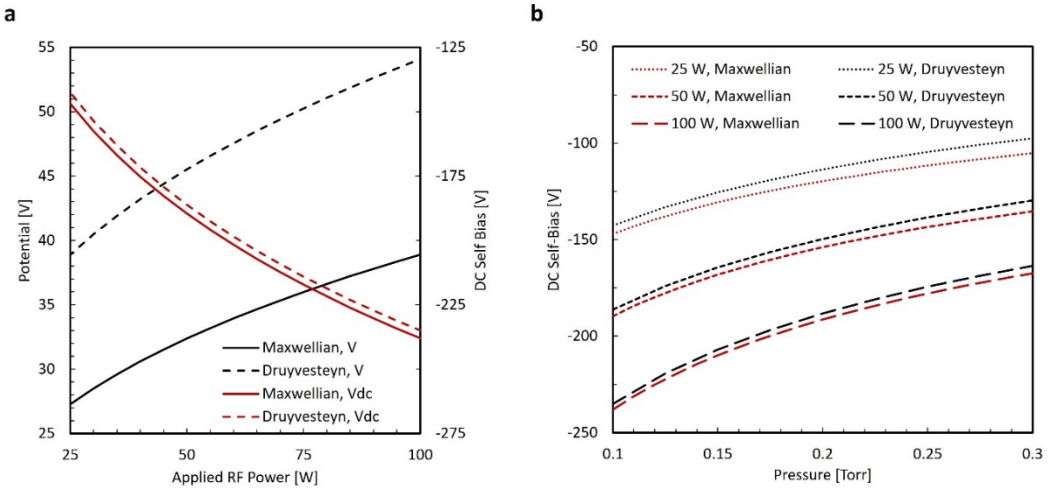

Figure 57. Comparison of EEDF at Langmuir probe point with gas pressure 100 mTorr on (a)period-averaged plasma potential and DC self-bias on RF electrode and (b) Period-averaged DC self-bias on RF electrode for various pressures and applied RF power.

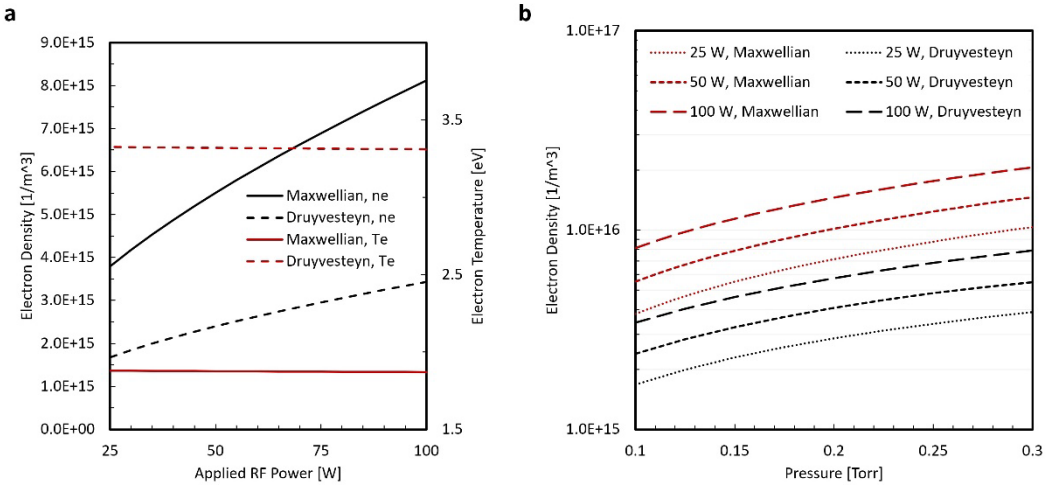

Figure 58. (a) Model predictions for electron density and electron temperatures with a Maxwellian and Druyvesteyn EEDF and various applied RF powers at 100 mTorr. (b) Period-averaged electron density at Langmuir probe position under different EEDFs for various pressures and applied RF power.

In Figure 58a, the electron density and electron temperature are plotted as functions of the input power under the Maxwellian and Druyvesteyn assumptions at 100mTorr. For both EEDF shapes, T_e exhibited minimal variation with respect to applied power, stabilizing at 1.9 eV for Maxwellian and 3.3 eV for Druyvesteyn. The model also showed that electron temperatures for both EEDFs decreased as pressure was raised from 100 to 300 mTorr, with the Druyvesteyn EEDF showing a reduction from 3.3 eV to 2.8 eV, and the Maxwellian EEDF from 1.9 eV to 1.4 eV. The Maxwellian EEDF showed a greater electron density that increased more significantly with applied power from nearly 3.8×10^{15} to 8×10^{15} m^{-3}compared to the Druyvesteyn EEDF increase from 1.6×10^{15} to 3.4×10^{15} m^{-3}. In Figure 58b, the model suggests a consistent increase in electron density with power and pressure, under both EEDFs, which matches the experimental trends. With a Maxwellian EEDF shape, n_e was not only higher but also exhibited a more pronounced increase with pressure compared to Druyvesteyn EEDF models, leading to larger differentials at elevated powers and pressures. The experimental data shown in Figure 46d confirmed the increasing electron density with power ranging between 1.9×10^{15} and 1.3×10^{16} m^{-3}. At 100mTorr, the experimental densities match the Druyvesteyn model predictions well at the lower powers and exceed them at 100 W. The

experimental densities increase with power significantly at 100 and 200 mTorr, but the increase is less pronounced at 300mTorr, treading close to the model's predicted values with the Maxwellian assumption and hinting at a possible intermediate or mixed EEDF in the actual plasma. The experimental electron temperature (Figure 46c) increased with power at all pressures, reaching around double their lowest values ranging from 1.6 eV to 3.6 eV. The trend indicates that for all power levels, the electron temperature initially increases with pressure from 100 to 200 mTorr and then decreases at 300 mTorr. While the model captures an accurate range of electron temperatures, the actual temperatures measured experimentally are affected by the power and do not decrease as uniformly with pressure. These discrepancies could suggest that the experimental conditions may have additional complexities not captured by the model. The lower electron temperatures at 300 mTorr, coupled with a lower electron density and potentials further consolidates that beyond 200mTorr, the plasma reactor could be in a different regime of operation, possibly due to factors such as spatial variation in electron temperature, geometric effects, or differences in actual and assumed electron collision cross-sections.

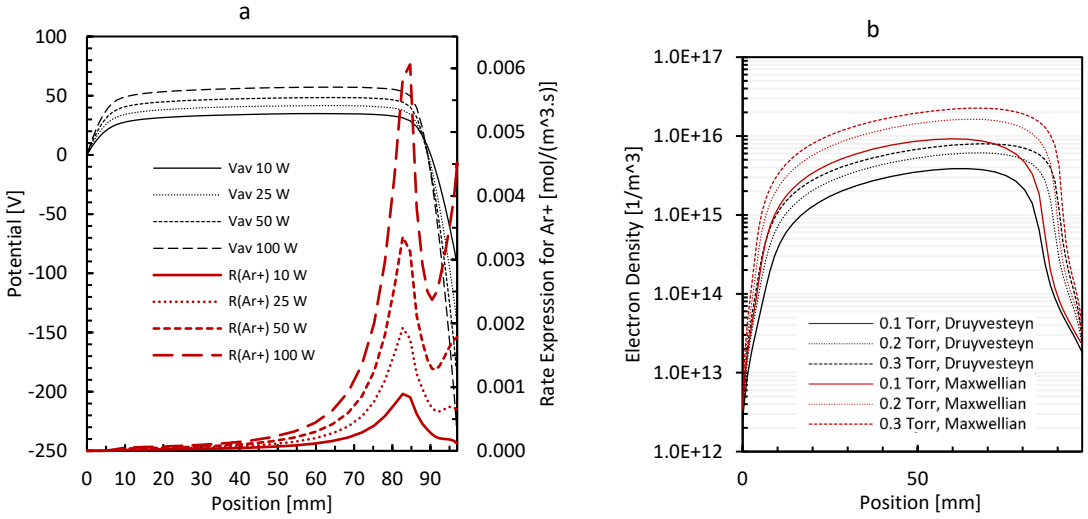

Figure 59. (a) Modelled period-averaged plasma potential and ionization rate along the axis spanning the gap at the lower electrode, measured at a pressure of 0.1 Torr and various powers. (b) Profile of the period-averaged electron density along the central axis of the lower discharge area at different pressures for 25 W of applied RF power are depicted. The powered RF electrode is situated on the right-hand side.

In Figure 59a, the period-averaged plasma potential is modelled along the symmetry axis across the lower electrode gap. An increase in the potential difference is evident across the RF sheath with increasing applied RF power, attributable to rises in both the bulk plasma potential and the DC bias voltage. The plasma potential along the axis of symmetry within the modelled gap area exhibits minimal variation, demonstrating a slight and gradual increase as the measurement point approaches the RF sheath. This figure also shows the rate expression for argon ions (Ar^+), indicating that most ionization occurs at the plasma-sheath interface. This is indicative of a low-power α mode at applied power values up to 100 W [381]. As P_{RF} increases, the ionization contribution from the sheath region intensifies, suggesting a transition to the γ mode. In this mode, the discharge becomes increasingly sustained by secondary electron emission [587]. The spatially-resolved electron density profiles for the central axis in the lower discharge region are shown in Figure 59b. The figure highlights the significantly higher density associated with a Maxwellian EEDF and a stronger sensitivity of n_e to gas pressure. The electrostatic potential was consistently higher in the Druyvesteyn case by around 10-12 V in the bulk plasma region, whilst there was no significant

difference in the sheath regions. The choice of EEDF should ultimately be informed by experimental measurements in the discharge, ideally of the EEDF itself, or by comparison with the plasma parameters.

In comparison with experimental data for spatial variations (Figure 49), the period-averaged plasma potential (V_p) and electron density (n_e) exhibit a slight increment as the proximity to the electrode increases, aligning with the trends observed in Figure 57. This increase is consistent and becomes more pronounced at greater applied RF powers, reinforcing the model's prediction of an intensified potential difference across the RF sheath with elevated power levels. Moreover, experimental results suggest that the plasma density is more closely aligned with the Druyvesteyn EEDF at a power setting of 25W, as opposed to the Maxwellian EEDF which tends to overestimate the density. This discrepancy indicates that the Druyvesteyn EEDF may provide a more accurate representation of the plasma characteristics at lower power regimes.

The model described provides a valuable framework for understanding plasma behavior under various operational conditions, capturing several key aspects of plasma dynamics: The model accurately predicted the increase in plasma potential and DC self-bias with power, aligning with experimental observations. This suggests the model effectively captures the influence of power on these plasma parameters. The predicted increase in electron (n_e) and ion (n_i) densities with power was also consistent with experimental findings, indicating the model's capability in simulating the dependency of ionization rates on power input. Moreover, the electron temperature (T_e) decreased with increased pressure aligned with the general trend observed in experiments at higher pressures, reflecting the model's ability to capture some of the pressure-related dynamics affecting electron energy. By using both Maxwellian and Druyvesteyn EEDFs, the model provided insights into the behavior of high-energy electrons and their impact on plasma characteristics, showing a level of flexibility in representing electron energy distributions. In regard to spatial dynamics, the model was successful in reflecting the increase in plasma potential and density closer to the electrode, consistent with the spatial variations observed in experimental data.

However, there are areas where the model could be improved to provide a more comprehensive and accurate representation of plasma behavior: The primary difference between the experimental observations and the model predictions lies in how they account for the impact of increased pressure on electron densities, particularly at lower powers. Experimentally, an increase in pressure leads to heightened collisional losses, which in turn diminish electron densities. However, the model forecasts a continuous rise in densities with pressure, suggesting that there is sufficient power to sustain ionization of additional gas molecules despite the pressure rise. This divergence could stem from potential inaccuracies in the modeled collision cross sections or the omission of certain collisional loss processes. Additionally, the model might overestimate the energy input into the plasma, possibly through an exaggerated effect of secondary electron emission compared to actual laboratory conditions. Given the challenges in accurately measuring both collisional cross-sections and secondary electron emission coefficients, it's probable that the discrepancies are due to the model's reliance on values that do not precisely match those derived from experiments. Experimental data also suggest a more complex electron energy distribution than what a single-temperature Maxwellian or a Druyvesteyn model can capture, possibly indicating a hybrid or non-equilibrium state. Improving the model to address these aspects would not only enhance its alignment with experimental observations but also expand its utility in predicting plasma behavior under a wider range of conditions, thereby providing a more robust tool for plasma research and applications. The parameters in the model, such as cross sections and rate coefficient, were calculated by using results of experiments or simulations in other literature and may require

improvements to fit our plasma system. The model also assumes uniform electric fields which presents a simplification that may not entirely capture the complex physics of the plasma. Experimental limitations may also present sources of discrepancies such as: The accuracy of the experimental data depends on the calibration and the precision of the measurement tools, such as the Langmuir probe, input IV probe and self-bias voltage meter, all of which can be affected by plasma conditions [552]. Moreover, the Langmuir probe is an intrusive technique and despite its popularity, its error limits can be up to 20% [588, 589]. The frequency and quality level of the cleaning procedure for the probe tip to reduce contaminations between repeated measurements may be another avenue for exploration and error reduction. The input power being dissipated in the reactor at the powered electrode is also a key source of discrepancies as the applied power to the system is often hindered by the losses in the electrical circuit and matching network [542]. Considerations for the combinations of pressure, power and gas flow set for our reactor would be necessary to ensure efficient gas breakdown near the Paschen minimum would occur. Moreover, harmonics arising from nonlinear plasma processes can lead to signal distortion in plasma diagnostic tools, potentially obscuring true plasma parameters and leading to inaccurate measurements. These distortions affect the efficiency and reliability of diagnostics, necessitating careful analysis and filtering to isolate genuine plasma characteristics. Obtaining measurements at more positions and investigating the planar distibution can inform the resolution that the model needs to attain. By comparing our empirical measurements with simulation results, the model's accuracy can be fine-tuned, ensuring it faithfully represents the plasma's spatial dynamics. An iterative process of measurement and validation is pivotal in advancing our understanding of plasma phenomena and enhancing the predictive capability of computational models.

6.8. Conclusions

In this study, we have explored the intricate dynamics of plasma behavior under varying power and pressure conditions through a combination of experimental investigations and computational modeling. Our systematic exploration across different power settings (25 W, 50 W, 100 W) and pressures (100 mTorr, 200 mTorr, 300 mTorr) has provided valuable insights into the fundamental parameters governing plasma systems, including plasma and floating potentials, electron temperature, electron and ion densities, and electron saturation current under varying external conditions. Key findings from our study include the observed increase in plasma potential (V_p) with both power and pressure, indicating more energetic plasma states at higher inputs. The floating potential (V_f), however, displayed a minor decrease with increasing power, suggesting a dynamic balance in the plasma sheath's charge distribution. Notably, the electron temperature (T_e) exhibited a pronounced increase with power across all pressures, highlighting the significant impact of power input on the thermal energy of electrons, which in turn influences the overall plasma energetics. Our investigation into the electron and ion densities revealed a positive correlation with power, underscoring the role of ionization processes in enhancing plasma density under increased power conditions. The electron saturation current (I_{sat}) also increased with power, mirroring the trends in electron density and temperature, and suggesting heightened plasma activity and ionization rates. Spatial variations in plasma parameters, as probed by Langmuir probe diagnostics, further enriched our understanding of plasma behavior. Measurements indicated that plasma potential and electron temperature are influenced by proximity to the RF electrode and operating pressure, with higher values closer to the energy source and at elevated pressures. The Electron Energy Distribution Function (EEDF) and Electron Energy Probability Function (EEPF) analyses offered profound insights into the energy states of the electron population, revealing the presence of high-energy electron populations and the effects of pressure and power on electron energy distributions

transitioning the plasma to a hybrid between Maxwellian and Druyvesteyn distributions. These findings have significant implications for plasma diagnostics, emphasizing the need for detailed EEDF and EEPF analyses to accurately characterize plasma states. Our study also delved into the electrical discharge dynamics, exploring the implications of the Paschen law and the impact of pressure on breakdown voltages. The observed trends in voltage waveforms and the root mean square voltages under different conditions provided valuable information on plasma stability and efficiency, particularly in relation to the Paschen minimum and the operational regime of the plasma. The development and application of a 2D axisymmetric continuum model offered a theoretical perspective on the experimental findings, laying the foundation of a predictive tool to illustrate plasma behavior under various conditions. The model predictions on plasma potential, DC self-bias, electron density, and temperature were generally in good agreement with experimental results, validating the model's utility in understanding plasma dynamics. However, discrepancies between the model and experimental data highlight the complexity of plasma behavior and the need for further refinement of theoretical approaches. In conclusion, our study has significantly advanced the understanding of plasma dynamics under varying power and pressure conditions, providing valuable insights into the behavior of plasma parameters and their interdependencies. The findings not only contribute to the theoretical knowledge of plasma physics but also have practical implications for the optimization of plasma-based processes in various applications. Further research, particularly in refining the model and exploring the complex interplay of plasma parameters, will continue to enhance our understanding and control of plasma systems to develop optimized conditions for plasma treatment and deposition processes. Future work will undoubtedly build upon these findings, exploring further the complex dynamics of plasma systems and their potential for nanoparticle synthesis and plasma process control for industrial scaling.

Chapter 7. Conclusions and Future Directions

7.1. Concluding Remarks

This thesis introduced the critical role of surface-functionalized polymeric nanoparticles (PNPs) in advancing nanotechnology for biomedical purposes. Their capacity to tackle significant health and sustainability challenges by improving diagnostics, drug delivery, and therapeutic measures was extensively evaluated. By exploring both covalent and noncovalent functionalization strategies, insight into the sophisticated interactions between PNPs and biological systems was framed, setting the groundwork for understanding their potential and limitations within biomedicine.

The introduction and literature review in Chapter 1 highlighted the significant challenges hindering the full potential of polymeric nanoparticles in areas of clinical translation, scalability, regulatory concerns, advanced functionalization techniques, and demonstrated the necessity for interdisciplinary collaboration in understanding the immerging field of plasma polymerization for nanomedicine. The transition from laboratory framework to clinical applications remaining in its early stages was attributed largely to biological complexities and the need for a deeper understanding of nano-bio interactions. Moreover, shortcomings in scaling up production while ensuring consistency and functionality of nanoparticles, alongside navigating the regulatory landscape for safety, were identified. The advancement of innovative functionalization strategies was thus established to be crucial for enhancing targeting precision, biocompatibility, and controlled release, which introduced the requirement for novel bioconjugation and surface modification methods. Addressing these challenges called for an integrated approach, bridging gaps between nanotechnology, materials science, biology, and medicine, to develop solutions that can effectively meet clinical needs and navigate the intricacies of nanomedicine.

Following the description of methods used in this study in Chapter 2, Chapter 3 introduced an innovative approach to the fabrication of plasma polymerized nanoparticles (PPNs). This approach, which presents an environmentally friendly and cost-efficient synthesis method relative to conventional techniques, enhanced the particle collection yield through the delayed inflow of the organic gas, acetylene. The delayed inflow resulted in a higher working pressure during nanoparticle synthesis and modified the electrostatic and drag forces such that the net force on the growing plasma polymerized nanoparticles, or PPNs, directed them more effectively towards the collection wells. This technique has implications for the scalability and industrial application of PPN production, underscoring the method's potential to fast-track their synthesis and bulk-production for biomedical application.

Chapter 4 examined the conjugation capability of PPNs as required for biomedical applications through their surface functionalization with imaging and lipid-targeting molecules. The attachment of these molecules on the PPN surfaces was shown to be covalent and robust. The efficacy of plasma polymerization as a simple, dry, low-waste method for the synthesis of PPNs and their surface treatment with functional groups was demonstrated. Their organic cores and radical-infused surfaces facilitated the immobilization of fluorescent molecules while eliminating typical post-synthesis functionalization processes such as purifications and surface coatings for hydrophilicity. The presented cellular biocompatibility and functional versatility of PPNs as platforms for targeting and diagnostics certified their potential for advancing one step closer to *in vivo* intracellular delivery applications.

Chapter 5 examined the impact of polymerization duration and long-term storage conditions on the stability and functionality of PPNs. Polymerization time was optimized at 5 minutes to avoid larger nanoparticles with a tendency towards aggregation. pH levels also influenced nanoparticle agglomeration, with acidic environments promoting aggregation due to decreased electrostatic repulsion, while alkaline conditions stabilized particles by preventing aggregation. Dry storage of PPNs at room temperature was shown to have yielded the smallest nanoparticle sizes over time, which holds significant advantages for industrial and commercial applications. This storage method enhances product consistency, crucial for regulatory approvals and consumer trust, and reduces manufacturing, storage and maintenance costs. Smaller, stable nanoparticles are known to improve the efficacy, safety, and reliability of nanotechnology products, from drug delivery systems to diagnostic tools, making them more competitive in the market. Despite storage-induced variations in aqueous conditions, PPNs were prone to size-reduction under sonication and retained their functionality for biomolecular attachment, evidenced by successful Nile Blue binding across different storage conditions. The adaptability and functional integrity of the PPNs discovered after long-term storage also adds to their commercial appeal. This flexibility allows for tailored nanotechnology solutions, enhancing product consistency and performance across various applications.

Chapter 6 investigated the underlying plasma dynamics and provided a detailed examination of argon plasma behaviour under different operational parameters. Plasma diagnostics and modeling alongside experimental validation were used for understanding key plasma parameters. Electron and ion densities were found to correlate positively with power, highlighting the importance of ionization processes at higher power settings. The electron saturation current also increased with power, reflecting the trends in density and temperature, and indicating increased plasma activity under those conditions. Spatial analysis revealed variations in plasma parameters near the RF electrode and under different pressures, with higher values observed closer to the energy source and at elevated pressures. Electrical discharge dynamics shed light on the effects of pressure on breakdown voltages and plasma stability. The use of a 2D axisymmetric continuum model provided a theoretical framework that largely aligned with experimental findings, offering valuable insights for optimizing plasma-based processes in various applications and setting the stage for future explorations into plasma systems for industrial scaling and nanoparticle synthesis.

This thesis has provided an in-depth analysis of the synthesis of plasma polymerized nanoparticles and their properties making them suitable for the advancement of biomedical nanotechnology. Through detailed studies of plasma polymerization and the functionalization of PPNs, the work has highlighted the potential of these nanoparticles in improving health care through better disease diagnosis, drug delivery systems, and therapeutic approaches. The development of an environmentally friendly and cost-effective method for PPN production at high yields, the successful attachment of molecules to PPN surfaces without the need for post-synthesis modifications, and insights into the stability and functionality of PPNs under various storage conditions have been achieved. Furthermore, the exploration of plasma dynamics through plasma diagnostic experiments and finite element simulations has contributed to a better understanding of the conditions necessary for optimizing the synthesis and functionalization processes. The combined findings from each chapter not only contribute to the scientific community's understanding of PPNs but also suggest a pathway towards their scalable production and practical application in medicine. By focusing on the scientific challenges and potential solutions, this thesis

emphasizes the importance of interdisciplinary research in overcoming the barriers to the clinical adoption of nanotechnology-based solutions.

7.2. Future Directions

Despite the significant progress made in the development of surface biofunctionalized PPNs for diagnostics and therapeutic applications, their clinical translation remains narrow. Future research will focus on overcoming the challenges associated with the in vivo physiological environment, including the precise interactions between nanoparticles and biological media, and immune responses. The biodegradation of PPNs has not been extensively studied, nor has the full potential of our synthesis method for diverse applications. Understanding biodegradation pathways is crucial for clinical translation and in vivo studies, guiding polymerization modifications to explore. Key parameters to adjust include power, pressure, gas ratios, and additional gas mixtures. Our group is actively addressing this gap through various projects, including size variations for transport control and elucidating biodegradation pathways led by Elmer Austria, and investigations into PPN degradation routes like endocytosis, led by Lucy Fraser and colleagues.

Innovations in scaling-up technologies for the fabrication of functionalized PPNs are critical. Emphasis on reproducible manufacturing, progression towards industrial partnerships, and commercialization will be pivotal in bringing these advancements from the laboratory to the clinic.

The potential for creating multi-functional nanostructures that combine diagnostic, therapeutic, and imaging capabilities represents an exciting area for future research. The development of novel biofunctionalization techniques, including covalent attachment of molecules and fluorescent markers, opens new avenues for the creation of targeted therapeutics and advanced imaging systems.

The findings on the stability and functionality of PPNs under varied storage conditions underscore the importance of understanding and controlling the physicochemical properties of nanoparticles. Future studies should aim to extend the investigation to include more diverse environmental conditions and nanoparticle formulations. Exploring innovative methods to mitigate particle aggregation and degradation such as surfactant incorporation and high-sheer mixing, while retaining or enhancing functionality, will be crucial for the successful application of PPNs in drug delivery and biomedical sensors.

The characterization and modeling of argon plasma conditions have laid the groundwork for understanding and achieving control over the physicochemical properties of nanostructures during their synthesis. Future research should aim to refine these models further, incorporating more complex interactions from nitrogen and acetylene gases as well as studies of the effect of variables, including secondary electron emission coefficient and collisional processes to improve predictive accuracy. To support the experimental advancements in plasma polymerization and nanostructure synthesis, there is a need for more sophisticated theoretical and computational models. These models should aim to capture the complex dynamics of plasma-nanostructure interactions, offering insights into the mechanisms at play. Enhancing the accuracy and applicability of these models will be essential for the design and optimization of next-generation nanostructures.

The recent advancements in stem cell research, microfluidics, and organ-on-a-chip technologies offer promising alternatives to traditional animal models. Future work would benefit from delving deeper into these technologies, focusing on their integration with plasma polymerized nanoparticles for enhanced drug delivery systems and diagnostics. The potential for these technologies to accelerate the clinical translation of nanoparticle-based therapeutics presents an exciting frontier for

exploration. Given the exceptional properties of carbon-based nanostructures synthesized through plasma processes, one overlooked direction is to explore their application in emerging fields. The integration of these nanostructures in flexible electronics, wearable sensors, and smart materials holds significant promise. Additionally, the development of environmentally friendly synthesis methods and the study of the lifecycle impact of these materials are crucial for sustainable advancement.

In summary, the evolution of plasma polymerization and nanoparticle synthesis technologies, along with the broadening of their applications, heralds a transformative shift in the biomedical landscape. As these capabilities develop and new functionalities emerge, the importance of surface functionalization of polymeric nanoparticles (PPNs) and the refinement of plasma processing for carbon-based nanostructures is poised to escalate. This progression is anticipated to transition these technologies from research labs to a central role in clinical settings and industrial applications, revolutionizing drug delivery, diagnostics, and therapeutic modalities. Such advancements promise to usher in a new paradigm in healthcare, where treatments are not only more personalized and regenerative but also more accessible across the global healthcare system. The integration of these nano-engineering strategies signifies a move towards a future where healthcare solutions are tailored to individual needs, offering a leap forward in patient care and medical outcomes.

References

1. United Nations. *The Sustainable Development Agenda*. Available from: https://www.un.org/sustainabledevelopment/development-agenda/.
2. Usman, M., M. Farooq, A. Wakeel, A. Nawaz, S.A. Cheema, H.U. Rehman, I. Ashraf, and M. Sanaullah, *Nanotechnology in agriculture: Current status, challenges and future opportunities.* Science of the Total Environment, 2020. **721**: p. 137778.
3. Lowry, G.V., A. Avellan, and L.M. Gilbertson, *Opportunities and challenges for nanotechnology in the agri-tech revolution.* Nature nanotechnology, 2019. **14**(6): p. 517-522.
4. Hofmann, T., G.V. Lowry, S. Ghoshal, N. Tufenkji, D. Brambilla, J.R. Dutcher, L.M. Gilbertson, J.P. Giraldo, J.M. Kinsella, and M.P. Landry, *Technology readiness and overcoming barriers to sustainably implement nanotechnology-enabled plant agriculture.* Nature Food, 2020. **1**(7): p. 416-425.
5. Alvarez, P.J.J., C.K. Chan, M. Elimelech, N.J. Halas, and D. Villagran, *Emerging opportunities for nanotechnology to enhance water security.* Nature nanotechnology, 2018. **13**(8): p. 634-641.
6. Nagar, A. and T. Pradeep, *Clean water through nanotechnology: needs, gaps, and fulfillment.* ACS Nano, 2020. **14**(6): p. 6420-6435.
7. Farooq, U., A. Patil, B. Panjwani, G. Simonsen, and Fuels, *Review on Application of Nanotechnology for Asphaltene Adsorption, Crude Oil Demulsification, and Produced Water Treatment.* Energy and Fuels, 2021. **35**(23): p. 19191-19210.
8. Haidar, E.-A., S.A. Tawfik, and C. Stampfl, *Twist-Dependent Electron Charge Transfer and Transport in Phosphorene–Graphene Heterobilayers.* The Journal of Physical Chemistry C, 2021. **125**(46): p. 25886-25897.
9. Casparis, L., M.R. Connolly, M. Kjaergaard, N.J. Pearson, A. Kringhoj, T.W. Larsen, F. Kuemmeth, T. Wang, C. Thomas, S. Gronin, G.C. Gardner, M.J. Manfra, C.M. Marcus, and K.D. Petersson, *Superconducting gatemon qubit based on a proximitized two-dimensional electron gas.* Nature nanotechnology, 2018. **13**(10): p. 915-919.
10. Liu, Y., M. Pharr, and G.A. Salvatore, *Lab-on-Skin: A Review of Flexible and Stretchable Electronics for Wearable Health Monitoring.* ACS Nano, 2017. **11**(10): p. 9614-9635.
11. Weiss, C., M. Carriere, L. Fusco, I. Capua, J.A. Regla-Nava, M. Pasquali, J.A. Scott, F. Vitale, M.A. Unal, C. Mattevi, D. Bedognetti, A. Merkoci, E. Tasciotti, A. Yilmazer, Y. Gogotsi, F. Stellacci, and L.G. Delogu, *Toward Nanotechnology-Enabled Approaches against the COVID-19 Pandemic.* ACS Nano, 2020. **14**(6): p. 6383-6406.
12. Wibowo, D., S.H.T. Jorritsma, Z.J. Gonzaga, B. Evert, S. Chen, and B.H.A. Rehm, *Polymeric nanoparticle vaccines to combat emerging and pandemic threats.* Biomaterials, 2021. **268**: p. 120597.
13. Khurana, A., P. Allawadhi, I. Khurana, S. Allwadhi, R. Weiskirchen, A.K. Banothu, D. Chhabra, K. Joshi, and K.K. Bharani, *Role of nanotechnology behind the success of mRNA vaccines for COVID-19.* Nano Today, 2021. **38**: p. 101142.
14. Wang, Z., K. Cui, U. Costabel, and X. Zhang. *Nanotechnology-facilitated vaccine development during the coronavirus disease 2019 (COVID-19) pandemic*. in *Exploration*. 2022. Wiley Online Library.
15. Hammad, A.B.A., H.S. Magar, A. Mansour, R.Y. Hassan, and A.M.E. Nahrawy, *Construction and characterization of nano-oval BaTi0. 7Fe0. 3O3@ NiFe2O4 nanocomposites as an effective platform for the determination of H2O2.* Scientific Reports, 2023. **13**(1): p. 9048.
16. Paysen, H., N. Loewa, A. Stach, J. Wells, O. Kosch, S. Twamley, M.R. Makowski, T. Schaeffter, A. Ludwig, and F. Wiekhorst, *Cellular uptake of magnetic nanoparticles imaged and quantified by magnetic particle imaging.* Scientific Reports, 2020. **10**(1): p. 1922.
17. Li, M., X. Jin, T. Liu, F. Fan, F. Gao, S. Chai, and L. Yang, *Nanoparticle elasticity affects systemic circulation lifetime by modulating adsorption of apolipoprotein AI in corona formation.* Nature Communications, 2022. **13**(1): p. 4137.
18. Wei, Y., L. Quan, C. Zhou, and Q. Zhan, *Factors relating to the biodistribution & clearance of nanoparticles & their effects on in vivo application.* Nanomedicine: Nanotechnology, Biology and

Medicine, 2018. **13**(12): p. 1495-1512.
19. Crawley, J.W., I.E. Gow, N. Lawes, I. Kowalec, L. Kabalan, C.R.A. Catlow, A.J. Logsdail, S.H. Taylor, N.F. Dummer, and G.J. Hutchings, *Heterogeneous trimetallic nanoparticles as catalysts.* Chemical Reviews, 2022. **122**(6): p. 6795-6849.
20. Zhang, H.-J., Z. Zhou, L. Jia, Z.-F. Ma, and Y. Xue, *Collaborative Anchoring of Pt Nanoparticles and Metal Oxide Nanoparticles on N-Doped Carbon as Catalysts for Oxygen Reduction.* ACS Applied Nano Materials, 2023.
21. Cormode, D.P., L. Gao, and H. Koo, *Emerging Biomedical Applications of Enzyme-Like Catalytic Nanomaterials.* Trends in biotechnology, 2018. **36**(1): p. 15-29.
22. Wang, D., D. Jana, and Y. Zhao, *Metal–organic framework derived nanozymes in biomedicine.* Accounts of chemical research, 2020. **53**(7): p. 1389-1400.
23. Cheng, L., X. Wang, F. Gong, T. Liu, and Z. Liu, *2D Nanomaterials for Cancer Theranostic Applications.* Advanced Materials, 2020. **32**(13): p. e1902333.
24. Zhao, M., Z. Liang, B. Zhang, Q. Wang, J. Lee, F. Li, Q. Wang, D. Ma, and D. Ling, *Supramolecular Container-Mediated Surface Engineering Approach for Regulating the Biological Targeting Effect of Nanoparticles.* Nano Letters, 2020. **20**(11): p. 7941-7947.
25. Li, X., R. Yue, G. Guan, C. Zhang, Y. Zhou, and G. Song. *Recent development of pH-responsive theranostic nanoplatforms for magnetic resonance imaging-guided cancer therapy*. in *Exploration*. 2023. Wiley Online Library.
26. Kim, D., K. Shin, S.G. Kwon, and T. Hyeon, *Synthesis and biomedical applications of multifunctional nanoparticles.* Advanced Materials, 2018. **30**(49): p. 1802309.
27. Zou, Q., J. Huang, and X. Zhang, *One-Step Synthesis of Iodinated Polypyrrole Nanoparticles for CT Imaging Guided Photothermal Therapy of Tumors.* Small, 2018. **14**(45): p. e1803101.
28. Pitchaimani, A., T.D.T. Nguyen, R. Marasini, A. Eliyapura, T. Azizi, M. Jaberi-Douraki, and S. Aryal, *Biomimetic natural killer membrane camouflaged polymeric nanoparticle for targeted bioimaging.* Advanced Functional Materials, 2019. **29**(4): p. 1806817.
29. Xiong, K., Y. Zhang, Q. Wen, J. Luo, Y. Lu, Z. Wu, B. Wang, Y. Chen, L. Zhao, and S. Fu, *Co-delivery of paclitaxel and curcumin by biodegradable polymeric nanoparticles for breast cancer chemotherapy.* International journal of pharmaceutics, 2020. **589**: p. 119875.
30. Sobska, J., B. Andreiuk, I.O. Aparin, A. Reisch, W. Krezel, and A.S. Klymchenko, *Counterion-insulated near-infrared dyes in biodegradable polymer nanoparticles for in vivo imaging.* Nanoscale Advances, 2022. **4**(1): p. 39-48.
31. Landgraf, L., D. Nordmeyer, P. Schmiel, Q. Gao, S. Ritz, S.G. J, S. Grass, S. Diabate, L. Treuel, C. Graf, E. Ruhl, K. Landfester, V. Mailander, C. Weiss, R. Zellner, and I. Hilger, *Validation of weak biological effects by round robin experiments: cytotoxicity/biocompatibility of SiO(2) and polymer nanoparticles in HepG2 cells.* Scientific Reports, 2017. **7**(1): p. 4341.
32. Moku, G., V.R. Gopalsamuthiram, T.R. Hoye, and J. Panyam, *Surface modification of nanoparticles: methods and applications.* Surface modification of polymers: Methods and applications, 2019: p. 317-346.
33. Lee, H., D.-E. Yoon, S. Koh, M.S. Kang, J. Lim, and D.C. Lee, *Ligands as a universal molecular toolkit in synthesis and assembly of semiconductor nanocrystals.* Chemical Science, 2020. **11**(9): p. 2318-2329.
34. Zhu, X., H. Zhang, and F. Zhang, *Ligand-based surface engineering of lanthanide nanoparticles for bioapplications.* ACS Materials Letters, 2022. **4**(9): p. 1815-1830.
35. Biby, A., H. Crawford, and X. Xia, *Platinum-Group Metal Nanoparticles as Peroxidase Mimics: Implications for Biosensing.* ACS Applied Nano Materials, 2022. **5**(12): p. 17622-17631.
36. Awada, A., M. Potter, D. Wijerathne, J.W. Gauld, B. Mutus, and S. Rondeau-Gagné, *Conjugated Polymer Nanoparticles as a Universal High-Affinity Probe for the Selective Detection of Microplastics.* ACS Applied Materials & Interfaces, 2022. **14**(41): p. 46562-46568.
37. De, K., P. Prasad, S. Sinha, S. Mukhopadhyay, and S.S. Roy, *Synthesis, Characterization, and Biological Evaluation of Radiolabeled Glutamine Conjugated Polymeric Nanoparticles: A Simple Approach for Tumor Imaging.* ACS Applied Bio Materials, 2023.
38. Foster, D. and J. Larsen, *Polymeric Metal Contrast Agents for T1-Weighted Magnetic Resonance*

Imaging of the Brain. ACS Biomaterials Science & Engineering, 2023. **9**(3): p. 1224-1242.
39. Park, Y., A.S. Moses, A.A. Demessie, P. Singh, H. Lee, T. Korzun, O.R. Taratula, A.W. Alani, and O. Taratula, *Poly (aspartic acid)-Based Polymeric Nanoparticle for Local and Systemic mRNA Delivery.* Molecular Pharmaceutics, 2022. **19**(12): p. 4696-4704.
40. Jolugbo, P., T. Willot, W. Hsiang, T. Maisey, D. O'Callaghan, M. Green, D.G. Jayne, and M.I. Khot, *Fluorescent imaging using novel conjugated polymeric nanoparticles-affimer probes in complex in vitro models of colorectal cancer.* Nanoscale, 2023.
41. Melnychuk, N., P. Ashokkumar, I.O. Aparin, and A.S. Klymchenko, *Pre-and postfunctionalization of dye-loaded polymeric nanoparticles for preparation of FRET-based nanoprobes.* ACS Applied Polymer Materials, 2021. **4**(1): p. 44-53.
42. Oh, W.K., Y.S. Jeong, J. Song, and J. Jang, *Fluorescent europium-modified polymer nanoparticles for rapid and sensitive anthrax sensors.* Biosensors and Bioelectronics, 2011. **29**(1): p. 172-7.
43. Pang, L., Y. Pei, G. Uzunalli, H. Hyun, L.T. Lyle, and Y. Yeo, *Surface Modification of Polymeric Nanoparticles with M2pep Peptide for Drug Delivery to Tumor-Associated Macrophages.* Pharmaceutical research, 2019. **36**(4): p. 65.
44. Xie, J., Z. Zhou, S. Ma, X. Luo, J. Liu, S. Wang, Y. Chen, J. Yan, and F. Luo, *Facile Fabrication of BiF(3): Ln (Ln = Gd, Yb, Er)@PVP Nanoparticles for High-Efficiency Computed Tomography Imaging.* Nanoscale research letters, 2021. **16**(1): p. 131.
45. Balegamire, J., M. Vandamme, E. Chereul, S. Si-Mohamed, S.A. Maache, E. Almouazen, L. Ettouati, H. Fessi, L. Boussel, and P. Douek, *Iodinated polymer nanoparticles as contrast agent for spectral photon counting computed tomography.* Biomaterials Science, 2020. **8**(20): p. 5715-5728.
46. Hu, C.-M.J., R.H. Fang, B.T. Luk, and L. Zhang, *Polymeric nanotherapeutics: clinical development and advances in stealth functionalization strategies.* Nanoscale, 2014. **6**(1): p. 65-75.
47. Zhao, Z., A. Ukidve, V. Krishnan, and S. Mitragotri, *Effect of physicochemical and surface properties on in vivo fate of drug nanocarriers.* Advanced drug delivery reviews, 2019. **143**: p. 3-21.
48. Fam, S.Y., C.F. Chee, C.Y. Yong, K.L. Ho, A.R. Mariatulqabtiah, and W.S. Tan, *Stealth Coating of Nanoparticles in Drug-Delivery Systems.* Nanomaterials, 2020. **10**(4): p. 787.
49. Deng, X., J. Zhao, K. Liu, C. Wu, and F. Liang, *Stealth PEGylated chitosan polyelectrolyte complex nanoparticles as drug delivery carrier.* Journal of Biomaterials Science, Polymer Edition, 2021: p. 1-15.
50. Yang, W., L. Wang, M. Fang, V. Sheth, Y. Zhang, A.M. Holden, N.D. Donahue, D.E. Green, A.N. Frickenstein, E.M. Mettenbrink, T.A. Schwemley, E.R. Francek, M. Haddad, M.N. Hossen, S. Mukherjee, S. Wu, P.L. DeAngelis, and S. Wilhelm, *Nanoparticle Surface Engineering with Heparosan Polysaccharide Reduces Serum Protein Adsorption and Enhances Cellular Uptake.* Nano Letters, 2022. **22**(5): p. 2103-2111.
51. Zhong, Y., F. Meng, C. Deng, and Z. Zhong, *Ligand-directed active tumor-targeting polymeric nanoparticles for cancer chemotherapy.* Biomacromolecules, 2014. **15**(6): p. 1955-1969.
52. Saha, K., A. Bajaj, B. Duncan, and V.M. Rotello, *Beauty is Skin Deep: A Surface Monolayer Perspective on Nanoparticle Interactions with Cells and Bio-macromolecules.* Small, 2011. **7**(14): p. 1903-1918.
53. Jiang, Z., J. Guan, J. Qian, and C. Zhan, *Peptide ligand-mediated targeted drug delivery of nanomedicines.* Biomaterials Science, 2019. **7**(2): p. 461-471.
54. Wang, L., P. Quan, S.H. Chen, W. Bu, Y.-F. Li, X. Wu, J. Wu, L. Zhang, Y. Zhao, and X. Jiang, *Stability of ligands on nanoparticles regulating the integrity of biological membranes at the nano–lipid interface.* ACS Nano, 2019. **13**(8): p. 8680-8693.
55. Feng, L., C. Zhu, H. Yuan, L. Liu, F. Lv, and S. Wang, *Conjugated polymer nanoparticles: preparation, properties, functionalization and biological applications.* Chemical Society Reviews, 2013. **42**(16): p. 6620-6633.
56. Kuehne, A.J., *Conjugated polymer nanoparticles toward in vivo theranostics–focus on targeting, imaging, therapy, and the importance of clearance.* Advanced Biosystems, 2017. **1**(11): p. 1700100.
57. Chen, X., S. Hussain, A. Abbas, Y. Hao, A.H. Malik, X. Tian, H. Song, and R. Gao, *Conjugated polymer nanoparticles and their nanohybrids as smart photoluminescent and photoresponsive*

material for biosensing, imaging, and theranostics. Microchimica Acta, 2022. **189**(3): p. 83.
58. Agyare, E. and K. Kandimalla, *Delivery of polymeric nanoparticles to target vascular diseases.* Journal of biomolecular research & therapeutics, 2014. **3**(1).
59. Repenko, T., A. Rix, S. Ludwanowski, D. Go, F. Kiessling, W. Lederle, and A.J. Kuehne, *Biodegradable highly fluorescent conjugated polymer nanoparticles for bio-medical imaging applications.* Nature communications, 2017. **8**(1): p. 1-8.
60. Guo, K., N. Xiao, Y. Liu, Z. Wang, J. Tóth, J. Gyenis, V.K. Thakur, A. Oyane, and Q.T. Shubhra, *Engineering polymer nanoparticles using cell membrane coating technology and their application in cancer treatments: Opportunities and challenges.* Nano Materials Science, 2022. **4**(4): p. 295-321.
61. Capanema, N.S., I.C. Carvalho, A.A. Mansur, S.M. Carvalho, A.P. Lage, and H.S. Mansur, *Hybrid hydrogel composed of carboxymethylcellulose–silver nanoparticles–doxorubicin for anticancer and antibacterial therapies against melanoma skin cancer cells.* ACS Applied Nano Materials, 2019. **2**(11): p. 7393-7408.
62. Zhao, J., S. Wu, J. Qin, D. Shi, and Y. Wang, *Electrical-Charge-Mediated Cancer Cell Targeting via Protein Corona-Decorated Superparamagnetic Nanoparticles in a Simulated Physiological Environment.* ACS Applied Materials & Interfaces, 2018. **10**(49): p. 41986-41998.
63. Cheng, W., J. Nie, L. Xu, C. Liang, Y. Peng, G. Liu, T. Wang, L. Mei, L. Huang, and X. Zeng, *pH-Sensitive Delivery Vehicle Based on Folic Acid-Conjugated Polydopamine-Modified Mesoporous Silica Nanoparticles for Targeted Cancer Therapy.* ACS Applied Materials & Interfaces, 2017. **9**(22): p. 18462-18473.
64. Zhu, J., G. Wang, C.S. Alves, H. Tomas, Z. Xiong, M. Shen, J. Rodrigues, and X. Shi, *Multifunctional Dendrimer-Entrapped Gold Nanoparticles Conjugated with Doxorubicin for pH-Responsive Drug Delivery and Targeted Computed Tomography Imaging.* Langmuir, 2018. **34**(41): p. 12428-12435.
65. Stewart, C., B. Akhavan, S.G. Wise, and M.M. Bilek, *A review of biomimetic surface functionalization for bone-integrating orthopedic implants: Mechanisms, current approaches, and future directions.* Progress in Materials Science, 2019. **106**: p. 100588.
66. Lotz, O., D.R. McKenzie, M.M. Bilek, and B. Akhavan, *Biofunctionalized 3D Printed Structures for Biomedical Applications: A Critical Review of Recent Advances and Future Prospects.* Progress in Materials Science, 2023: p. 101124.
67. Escareño, N., N. Hassan, M.J. Kogan, J. Juárez, A. Topete, and A. Daneri-Navarro, *Microfluidics-assisted conjugation of chitosan-coated polymeric nanoparticles with antibodies: Significance in drug release, uptake, and cytotoxicity in breast cancer cells.* Journal of colloid and interface science, 2021. **591**: p. 440-450.
68. Vroman, L. and A.L. Adams, *Findings with the recording ellipsometer suggesting rapid exchange of specific plasma proteins at liquid/solid interfaces.* Surface Science Reports, 1969. **16**: p. 438-446.
69. Vroman, L., A. Adams, G. Fischer, and P. Munoz, *Interaction of high molecular weight kininogen, factor XII, and fibrinogen in plasma at interfaces.* 1980.
70. Stordy, B., Y. Zhang, Z. Sepahi, M.H. Khatami, P.M. Kim, and W.C. Chan, *Conjugating Ligands to an Equilibrated Nanoparticle Protein Corona Enables Cell Targeting in Serum.* Chemistry of Materials, 2022. **34**(15): p. 6868-6882.
71. Stawicki, C.M., T.E. Rinker, M. Burns, S.S. Tonapi, R.P. Galimidi, D. Anumala, J.K. Robinson, J.S. Klein, and P. Mallick, *Modular fluorescent nanoparticle DNA probes for detection of peptides and proteins.* Scientific Reports, 2021. **11**(1): p. 19921.
72. Sanità, G., B. Carrese, and A. Lamberti, *Nanoparticle surface functionalization: how to improve biocompatibility and cellular internalization.* Frontiers in molecular biosciences, 2020. **7**: p. 587012.
73. Rea, I., N.M. Martucci, L. De Stefano, I. Ruggiero, M. Terracciano, P. Dardano, N. Migliaccio, P. Arcari, R. Taté, and I. Rendina, *Diatomite biosilica nanocarriers for siRNA transport inside cancer cells.* Biochimica et Biophysica Acta (BBA)-General Subjects, 2014. **1840**(12): p. 3393-3403.
74. Banihashem, S., M.N. Nezhati, and H.A. Panahia, *Synthesis of chitosan-grafted-poly (N-vinylcaprolactam) coated on the thiolated gold nanoparticles surface for controlled release of cisplatin.* Carbohydrate polymers, 2020. **227**: p. 115333.

75. Chen, J., Y. Zhang, M. Zhang, B. Yao, Y. Li, L. Huang, C. Li, and G. Shi, *Water-enhanced oxidation of graphite to graphene oxide with controlled species of oxygenated groups.* Chemical Science, 2016. **7**(3): p. 1874-1881.
76. Jiang, L., H. Bai, L. Liu, F. Lv, X. Ren, and S. Wang, *Luminescent, Oxygen-Supplying, Hemoglobin-Linked Conjugated Polymer Nanoparticles for Photodynamic Therapy.* Angewandte Chemie International Edition, 2019. **58**(31): p. 10660-10665.
77. Zhu, S., X. Wang, L. Liu, and L. Li, *Gold nanocluster grafted conjugated polymer nanoparticles for cancer cell imaging and photothermal killing.* Colloids and Surfaces A: Physicochemical and Engineering Aspects, 2020. **597**: p. 124764.
78. Alferiev, I.S., I. Fishbein, R.J. Levy, and M. Chorny, *Robust Chemical Strategy for Stably Labeling Polyester-Based Nanoparticles with BODIPY Fluorophores.* ACS Applied Polymer Materials, 2022.
79. Miranda Calderon, L.G., T. Alejo, S. Santos, G. Mendoza, S. Irusta, and M. Arruebo, *Antibody-functionalized polymer nanoparticles for targeted antibiotic delivery in models of pathogenic bacteria infecting human macrophages.* ACS Applied Materials & Interfaces, 2023. **15**(34): p. 40213-40227.
80. Guyomard-Lack, A., N. Delorme, C. Moreau, J.-F. Bardeau, and B. Cathala, *Site-selective surface modification using enzymatic soft lithography.* Langmuir, 2011. **27**(12): p. 7629-7634.
81. Nogueira, J.C., M.K. Greene, D.A. Richards, A.O. Furby, J. Steven, A. Porter, C. Barelle, C.J. Scott, and V. Chudasama, *Oriented attachment of V NAR proteins, via site-selective modification, on PLGA–PEG nanoparticles enhances nanoconjugate performance.* Chemical Communications, 2019. **55**(53): p. 7671-7674.
82. Shen, M., J.F. Rusling, and C.K. Dixit, *Site-selective orientated immobilization of antibodies and conjugates for immunodiagnostics development.* Methods, 2017. **116**: p. 95-111.
83. Bahou, C., P.A. Szijj, R.J. Spears, A. Wall, F. Javaid, A. Sattikar, E.A. Love, J.R. Baker, and V. Chudasama, *A Plug-and-Play Platform for the Formation of Trifunctional Cysteine Bioconjugates that also Offers Control over Thiol Cleavability.* Bioconjugate chemistry, 2021. **32**(4): p. 672-679.
84. Leach, A., M. Finnegan, M.S. Machado, L. Ferguson, J. Steven, P. Smyth, A. Porter, C. Barelle, E. Themistou, and C.J. Scott, *Functionalization of polymeric nanoparticles with targeting VNAR ligands using vinyl sulfone conjugation.* Journal of Materials Chemistry B, 2023. **11**(19): p. 4181-4190.
85. Leach, A., P. Smyth, L. Ferguson, J. Steven, M.K. Greene, C.M. Branco, A.P. McCann, A. Porter, C.J. Barelle, and C.J. Scott, *Anti-DLL4 VNAR targeted nanoparticles for targeting of both tumour and tumour associated vasculature.* Nanoscale, 2020. **12**(27): p. 14751-14763.
86. Greene, M.K., D.A. Richards, J.C. Nogueira, K. Campbell, P. Smyth, M. Fernández, C.J. Scott, and V. Chudasama, *Forming next-generation antibody–nanoparticle conjugates through the oriented installation of non-engineered antibody fragments.* Chemical Science, 2018. **9**(1): p. 79-87.
87. Dal Poggetto, G., S.S. Troise, C. Conte, R. Marchetti, F. Moret, A. Iadonisi, A. Silipo, R. Lanzetta, M. Malinconico, and F. Quaglia, *Nanoparticles decorated with folate based on a site-selective αCD-rotaxanated PEG-b-PCL copolymer for targeted cancer therapy.* Polymer Chemistry, 2020. **11**(23): p. 3892-3903.
88. Greene, M.K., J.C. Nogueira, S.R. Tracey, D.A. Richards, W.J. McDaid, J.F. Burrows, K. Campbell, D.B. Longley, V. Chudasama, and C.J. Scott, *Refined construction of antibody-targeted nanoparticles leads to superior antigen binding and enhanced delivery of an entrapped payload to pancreatic cancer cells.* Nanoscale, 2020. **12**(21): p. 11647-11658.
89. Badalkhani-Khamseh, F., A. Ebrahim-Habibi, and N.L. Hadipour, *Influence of dendrimer surface chemistry and pH on the binding and release pattern of chalcone studied by molecular dynamics simulations.* Journal of Molecular Recognition, 2019. **32**(1): p. e2757.
90. Guindani, C., M.L. Frey, J. Simon, K. Koynov, J. Schultze, S.R. Ferreira, P.H. Araújo, D. de Oliveira, F.R. Wurm, and V. Mailänder, *Covalently binding of bovine serum albumin to unsaturated poly (globalide-Co-ε-Caprolactone) nanoparticles by thiol-ene reactions.* Macromolecular Bioscience, 2019. **19**(10): p. 1900145.
91. Qie, Y., H. Yuan, C.A. Von Roemeling, Y. Chen, X. Liu, K.D. Shih, J.A. Knight, H.W. Tun, R.E. Wharen, and W. Jiang, *Surface modification of nanoparticles enables selective evasion of phagocytic*

clearance by distinct macrophage phenotypes. Scientific Reports, 2016. **6**(1): p. 26269.
92. Badran, M.M., M.M. Mady, M.M. Ghannam, and F. Shakeel, *Preparation and characterization of polymeric nanoparticles surface modified with chitosan for target treatment of colorectal cancer.* International Journal of Biological Macromolecules, 2017. **95**: p. 643-649.
93. Yildiz, T., R. Gu, S. Zauscher, and T. Betancourt, *Doxorubicin-loaded protease-activated near-infrared fluorescent polymeric nanoparticles for imaging and therapy of cancer.* International journal of nanomedicine, 2018: p. 6961-6986.
94. Crucho, C.I. and M.T. Barros, *Polymeric nanoparticles: A study on the preparation variables and characterization methods.* Materials Science and Engineering: C, 2017. **80**: p. 771-784.
95. Suh, J., K.-L. Choy, S.K. Lai, J.S. Suk, B.C. Tang, S. Prabhu, and J. Hanes, *PEGylation of nanoparticles improves their cytoplasmic transport.* International journal of nanomedicine, 2007. **2**(4): p. 735-741.
96. Zhang, Y., N.V. Hudson-Smith, S.D. Frand, M.S. Cahill, L.S. Davis, Z.V. Feng, C.L. Haynes, and R.J. Hamers, *Influence of the spatial distribution of cationic functional groups at nanoparticle surfaces on bacterial viability and membrane interactions.* Journal of the American chemical society, 2020. **142**(24): p. 10814-10823.
97. Zhao, P., Y. Wu, C. Feng, L. Wang, Y. Ding, and A. Hu, *Conjugated polymer nanoparticles based fluorescent electronic nose for the identification of volatile compounds.* Analytical chemistry, 2018. **90**(7): p. 4815-4822.
98. Vishwanath, R. and B. Negi, *Conventional and green methods of synthesis of silver nanoparticles and their antimicrobial properties.* Current Research in Green and Sustainable Chemistry, 2021. **4**: p. 100205.
99. Alam, A., C. Wan, and T. McNally, *Surface amination of carbon nanoparticles for modification of epoxy resins: plasma-treatment vs. wet-chemistry approach.* European Polymer Journal, 2017. **87**: p. 422-448.
100. Zhianmanesh, M., A. Gilmour, M.M. Bilek, and B. Akhavan, *Plasma surface functionalization: A comprehensive review of advances in the quest for bioinstructive materials and interfaces.* Applied Physics Reviews, 2023. **10**(2).
101. HennikerPlasma. *The cost of cultureware*. 2021 Accessed July 6, 2024]; Available from: https://plasmatreatment.co.uk/knowledge-base/press-releases/249-the-cost-of-cultureware.
102. Oehr, C., D. Hegemann, M. Liehr, and P. Wohlfart, *Cost structure and resource efficiency of plasma processes.* Plasma Processes and Polymers, 2022. **19**(10): p. 2200022.
103. Yasuda, H. and Y. Matsuzawa, *Economical Advantages of Low-Pressure Plasma Polymerization Coating.* Plasma Processes and Polymers, 2005. **2**(6): p. 507-512.
104. Lau, K., B. Akhavan, M.S. Lord, M.M. Bilek, J.J.A.B.S. Rnjak-Kovacina, and Engineering, *Dry surface treatments of silk biomaterials and their utility in biomedical applications.* 2020. **6**(10): p. 5431-5452.
105. Alavi, S.K., O. Lotz, B. Akhavan, G. Yeo, R. Walia, D.R. McKenzie, and M.M. Bilek, *Atmospheric pressure plasma jet treatment of polymers enables reagent-free covalent attachment of biomolecules for bioprinting.* ACS Applied Materials & Interfaces, 2020. **12**(34): p. 38730-38743.
106. Zhang, A., J.K.U. Wong, K. Redzikultsava, M. Baldry, S.K. Alavi, Z. Wang, E. van Koten, A. Weiss, M. Bilek, and G.C. Yeo, *A cost-effective and enhanced mesenchymal stem cell expansion platform with internal plasma-activated biofunctional interfaces.* Materials Today Bio, 2023. **22**: p. 100727.
107. Ainsworth, M.J., O. Lotz, A. Gilmour, A. Zhang, M.J. Chen, D.R. McKenzie, M.M. Bilek, J. Malda, B. Akhavan, and M. Castilho, *Covalent protein immobilization on 3D-printed microfiber meshes for guided cartilage regeneration.* Advanced Functional Materials, 2023. **33**(2): p. 2206583.
108. Redzikultsava, K., M. Baldry, A. Zhang, S.K. Alavi, B. Akhavan, and M.M. Bilek, *Cold plasma treatment of porous scaffolds: Design principles.* Plasma Processes and Polymers, 2022. **19**(7): p. 2200018.
109. Ahmed, H., T.A. Khattab, H. Mashaly, A. El-Halwagy, and M. Rehan, *Plasma activation toward multi-stimuli responsive cotton fabric via in situ development of polyaniline derivatives and silver nanoparticles.* Cellulose, 2020. **27**: p. 2913-2926.
110. Stewart, C.A., B. Akhavan, M. Santos, J. Hung, C.L. Hawkins, S. Bao, S.G. Wise, and M.M. Bilek,

Cellular responses to radical propagation from ion-implanted plasma polymer surfaces. Applied Surface Science, 2018. **456**: p. 701-710.
111. Akhavan, B., K. Jarvis, and P.J.R.A. Majewski, *Development of negatively charged particulate surfaces through a dry plasma-assisted approach.* 2015. **5**(17): p. 12910-12921.
112. Akhavan, B., B. Menges, and R. Förch, *Inhomogeneous growth of micrometer thick plasma polymerized films.* Langmuir, 2016. **32**(19): p. 4792-4799.
113. Stewart, C.A., B. Akhavan, J. Hung, S. Bao, J.-H. Jang, S.G. Wise, and M.M. Bilek, *Multifunctional protein-immobilized plasma polymer films for orthopedic applications.* ACS Biomaterials Science & Engineering, 2018. **4**(12): p. 4084-4094.
114. Dao, A., C. Gaitanos, S. Kamble, O. Sharifahmadian, R. Tan, S.G. Wise, T.L.Y. Cheung, M.M. Bilek, P.B. Savage, and A. Schindeler, *Antibacterial Plasma Polymer Coatings on 3D Materials for Orthopedic Applications.* Advanced Materials Interfaces, 2023: p. 2300063.
115. Ganesan, R., B. Akhavan, M.A. Hiob, D.R. McKenzie, A.S. Weiss, and M.M. Bilek, *HiPIMS carbon coatings show covalent protein binding that imparts enhanced hemocompatibility.* Carbon, 2018. **139**: p. 118-128.
116. Ganesan, R., B. Akhavan, J.G. Partridge, D.G. McCulloch, D.R. McKenzie, and M.M. Bilek, *Evolution of target condition in reactive HiPIMS as a function of duty cycle: An opportunity for refractive index grading.* Journal of Applied Physics, 2017. **121**(17).
117. Huang, B., F. Jing, B. Akhavan, L. Ji, Y. Leng, D. Xie, M. Bilek, and N. Huang, *Multifunctional Ti-xCu coatings for cardiovascular interfaces: Control of microstructure and surface chemistry.* Materials Science and Engineering: C, 2019. **104**: p. 109969.
118. Ren, Q., L. Qin, F. Jing, D. Cheng, Y. Wang, M. Yang, D. Xie, Y. Leng, B. Akhavan, and N. Huang, *Reactive magnetron co-sputtering of Ti-xCuO coatings: Multifunctional interfaces for blood-contacting devices.* Materials Science and Engineering: C, 2020. **116**: p. 111198.
119. Wang, Q., B. Akhavan, F. Jing, D. Cheng, H. Sun, D. Xie, Y. Leng, M.M. Bilek, and N. Huang, *Catalytic formation of nitric oxide mediated by Ti–Cu coatings provides multifunctional interfaces for cardiovascular applications.* Advanced Materials Interfaces, 2018. **5**(6): p. 1701487.
120. Yue, F., Z. Ayaz, Y. Jiang, L. Xiang, N. Huang, Y. Leng, B. Akhavan, and F. Jing, *Dealloyed nano-porous TiCu coatings with controlled copper release for cardiovascular devices.* Biomaterials Advances, 2024. **157**: p. 213728.
121. Liguori, A., E. Traldi, E. Toccaceli, R. Laurita, A. Pollicino, M.L. Focarete, V. Colombo, and M. Gherardi, *Co-Deposition of Plasma-Polymerized Polyacrylic Acid and Silver Nanoparticles for the Production of Nanocomposite Coatings Using a Non-Equilibrium Atmospheric Pressure Plasma Jet.* Plasma Processes and Polymers, 2016. **13**(6): p. 623-632.
122. Pleskunov, P., D. Nikitin, R. Tafiichuk, A. Shelemin, J. Hanus, J. Kousal, Z. Krtouš, I. Khalakhan, P. Kúš, and T. Nasu, *Plasma Polymerization of Acrylic Acid for the Tunable Synthesis of Glassy and Carboxylated Nanoparticles.* The Journal of Physical Chemistry B, 2020.
123. Santos, M., P.L. Michael, E.C. Filipe, A.H. Chan, J. Hung, R.P. Tan, B.S. Lee, M. Huynh, C. Hawkins, and A. Waterhouse, *Plasma synthesis of carbon-based nanocarriers for linker-free immobilization of bioactive cargo.* ACS Applied Nano Materials, 2018. **1**(2): p. 580-594.
124. Haidar, L.L., M. Baldry, S.T. Fraser, B.B. Boumelhem, A.D. Gilmour, Z. Liu, Z. Zheng, M.M. Bilek, and B. Akhavan, *Surface-Active Plasma-Polymerized Nanoparticles for Multifunctional Diagnostic, Targeting, and Therapeutic Probes.* ACS Applied Nano Materials, 2022. **5**(12): p. 17576-17591.
125. Akhavan, B., T.D. Michl, C. Giles, K. Ho, L. Martin, O. Sharifahmadian, S.G. Wise, B.R. Coad, N. Kumar, and H.J. Griesser, *Plasma activated coatings with dual action against fungi and bacteria.* Applied Materials Today, 2018. **12**: p. 72-84.
126. Yang, T., Z. Du, H. Qiu, P. Gao, X. Zhao, H. Wang, Q. Tu, K. Xiong, N. Huang, and Z. Yang, *From surface to bulk modification: Plasma polymerization of amine-bearing coating by synergic strategy of biomolecule grafting and nitric oxide loading.* Bioactive materials, 2020. **5**(1): p. 17-25.
127. Jarvis, K.L. and P. Majewski, *Plasma polymerized allylamine coated quartz particles for humic acid removal.* Journal of colloid and interface science, 2012. **380**(1): p. 150-158.
128. Bachhuka, A., S.N. Christo, A. Cavallaro, K.R. Diener, A. Mierczynska, L.E. Smith, R. Marian, J. Manavis, J.D. Hayball, and K. Vasilev, *Hybrid core/shell microparticles and their use for*

understanding biological processes. Journal of colloid and interface science, 2015. **457**: p. 9-17.
129. Akhavan, B., K. Jarvis, and P. Majewski, *Hydrophobic plasma polymer coated silica particles for petroleum hydrocarbon removal.* ACS APPLIED MATERIALS & INTERFACES, 2013. **5**(17): p. 8563-8571.
130. Akhavan, B., K. Jarvis, and P. Majewski, *Evolution of Hydrophobicity in Plasma Polymerised 1, 7-O ctadiene Films.* Plasma Processes and Polymers, 2013. **10**(11): p. 1018-1029.
131. Akhavan, B., K. Jarvis, and P. Majewski, *Plasma polymer-functionalized silica particles for heavy metals removal.* ACS applied materials & interfaces, 2015. **7**(7): p. 4265-4274.
132. Akhavan, B., K. Jarvis, P.J.S. Majewski, and C. Technology, *Plasma polymerization of sulfur-rich and water-stable coatings on silica particles.* 2015. **264**: p. 72-79.
133. Tu, X. and J.C. Whitehead, *Plasma dry reforming of methane in an atmospheric pressure AC gliding arc discharge: Co-generation of syngas and carbon nanomaterials.* International journal of hydrogen energy, 2014. **39**(18): p. 9658-9669.
134. Merlino, R.L. and J.A. Goree, *Dusty plasmas in the laboratory, industry, and space.* PHYSICS TODAY., 2004. **57**(7): p. 32-39.
135. Michael, P., Y.T. Lam, E.C. Filipe, R.P. Tan, A.H. Chan, B.S. Lee, N. Feng, J. Hung, T.R. Cox, and M. Santos, *Plasma polymerized nanoparticles effectively deliver dual siRNA and drug therapy in vivo.* Scientific Reports, 2020. **10**(1): p. 1-14.
136. Baldry, M., L.L. Haidar, B. Akhavan, and M.M. Bilek, *Continuum modelling of an asymmetric CCRF argon plasma reactor: Influence of higher excited states and sensitivity to model parameters.* Polymers and Polymer Composites, 2021. **18**(6): p. 2000243.
137. Wang, Y. and Y. Xia, *Optical, electrochemical and catalytic methods for in-vitro diagnosis using carbonaceous nanoparticles: a review.* Microchimica Acta, 2019. **186**(1): p. 50.
138. Jiang, S., K.Y. Win, S. Liu, C.P. Teng, Y. Zheng, and M.Y. Han, *Surface-functionalized nanoparticles for biosensing and imaging-guided therapeutics.* Nanoscale, 2013. **5**(8): p. 3127-48.
139. Bao, Y., H. De Keersmaecker, S. Corneillie, F. Yu, H. Mizuno, G. Zhang, J. Hofkens, B. Mendrek, A. Kowalczuk, and M. Smet, *Tunable ratiometric fluorescence sensing of intracellular pH by aggregation-induced emission-active hyperbranched polymer nanoparticles.* Chemistry of Materials, 2015. **27**(9): p. 3450-3455.
140. Chen, J., Y. Tang, H. Wang, P. Zhang, Y. Li, and J. Jiang, *Design and fabrication of fluorescence resonance energy transfer-mediated fluorescent polymer nanoparticles for ratiometric sensing of lysosomal pH.* Journal of colloid and interface science, 2016. **484**: p. 298-307.
141. Benjaminsen, R.V., H. Sun, J.R. Henriksen, N.M. Christensen, K. Almdal, and T.L. Andresen, *Evaluating nanoparticle sensor design for intracellular pH measurements.* ACS Nano, 2011. **5**(7): p. 5864-73.
142. Kumar, E.K., K. Almdal, and T.L. Andresen, *Synthesis and characterization of ratiometric nanosensors for pH quantification: a mixed micelle approach.* Chemical Communications, 2012. **48**(39): p. 4776-8.
143. Song, H., W. Du, C. Liu, Z. Li, H. Zhang, L. Wei, and M. Yu, *Self-Assembled Micellar Nanosensor toward pH with high photo-stability and its application in living cells.* Sensors and Actuators B: Chemical, 2018. **273**: p. 927-934.
144. Sun, H., K. Almdal, and T.L. Andresen, *Expanding the dynamic measurement range for polymeric nanoparticle pH sensors.* Chemical Communications, 2011. **47**(18): p. 5268-70.
145. Carrillo-Carrion, C. and W.J. Parak, *Multiplexed Fluorophore–Nanoparticle Hybrids for Extending the Range of pH Measurements.* Small Methods, 2017. **1**(8): p. 1700153.
146. Wilson, D.R., D. Routkevitch, Y. Rui, A. Mosenia, K.J. Wahlin, A. Quinones-Hinojosa, D.J. Zack, and J.J. Green, *A Triple-Fluorophore-Labeled Nucleic Acid pH Nanosensor to Investigate Non-viral Gene Delivery.* Molecular Therapy, 2017. **25**(7): p. 1697-1709.
147. Yao, Q., S. Lu, F. Lin, T. Zhao, L. Zhao, and X. Chen, *A co-precipitation strategy for making a ratiometric pH nanosensor for intracellular imaging.* Sensors and Actuators B: Chemical, 2017. **250**: p. 484-490.
148. Zhou, K., H. Liu, S. Zhang, X. Huang, Y. Wang, G. Huang, B.D. Sumer, and J. Gao, *Multicolored pH-tunable and activatable fluorescence nanoplatform responsive to physiologic pH stimuli.* Journal

of the American chemical society, 2012. **134**(18): p. 7803-11.
149. Lee, D., S. Khaja, J.C. Velasquez-Castano, M. Dasari, C. Sun, J. Petros, W.R. Taylor, and N. Murthy, *In vivo imaging of hydrogen peroxide with chemiluminescent nanoparticles.* Nature materials, 2007. **6**(10): p. 765-9.
150. Feng, C., F. Wang, Y. Dang, Z. Xu, H. Yu, and W. Zhang, *A Self-Assembled Ratiometric Polymeric Nanoprobe for Highly Selective Fluorescence Detection of Hydrogen Peroxide.* Langmuir, 2017. **33**(13): p. 3287-3295.
151. Oh, W.-K., Y.S. Jeong, S. Kim, and J. Jang, *Fluorescent polymer nanoparticle for selective sensing of intracellular hydrogen peroxide.* ACS Nano, 2012. **6**(10): p. 8516-8524.
152. Qu, S., N. Song, G. Xu, and Q. Jia, *A ratiometric fluorescent probe for sensitive detection of anthrax biomarker based on terbium-covalent organic polymer systems.* Sensors and Actuators B: Chemical, 2019. **290**: p. 9-14.
153. Jain, S., S. Chattopadhyay, R. Jackeray, Z. Abid, and H. Singh, *Detection of Salmonella typhi utilizing bioconjugated fluorescent polymeric nanoparticles.* Journal of Nanoparticle Research, 2016. **18**(5): p. 111.
154. Elgiddawy, N., S. Ren, A. Yassar, A. Louis-Joseph, H. Sauriat-Dorizon, W.M. El Rouby, A.O. El-Gendy, A.A. Farghali, and H. Korri-Youssoufi, *Dispersible conjugated polymer nanoparticles as biointerface materials for label-free bacteria detection.* ACS Applied Materials & Interfaces, 2020. **12**(36): p. 39979-39990.
155. Fratoddi, I., I. Venditti, C. Cametti, C. Palocci, L. Chronopoulou, M. Marino, F. Acconcia, and M.V. Russo, *Functional polymeric nanoparticles for dexamethasone loading and release.* Colloids and Surfaces B: Biointerfaces, 2012. **93**: p. 59-66.
156. Tan, H., C. Ma, Q. Li, L. Wang, F. Xu, S. Chen, and Y. Song, *Functionalized lanthanide coordination polymer nanoparticles for selective sensing of hydrogen peroxide in biological fluids.* Analyst, 2014. **139**(21): p. 5516-22.
157. Kromer, C., K. Schwibbert, A.K. Gadicherla, D. Thiele, N. Nirmalananthan-Budau, P. Laux, U. Resch-Genger, A. Luch, and H.R. Tschiche, *Monitoring and imaging pH in biofilms utilizing a fluorescent polymeric nanosensor.* Scientific Reports, 2022. **12**(1): p. 9823.
158. Jeon, J., D.G. You, A. Dey, B. Yoon, Y. Li, and J.H. Park, *Self-immolative polymer-based chemiluminescent nanoparticles for long-term in vivo imaging of reactive oxygen species.* Chemistry of Materials, 2022. **34**(17): p. 7741-7749.
159. Deswal, R., V. Narwal, P. Kumar, V. Verma, A.S. Dang, and C. Pundir, *An improved amperometric sarcosine biosensor based on graphene nanoribbon/chitosan nanocomposite for detection of prostate cancer.* Sensors International, 2022. **3**: p. 100174.
160. Wang, R., L. Schirmer, T. Wieduwilt, R. Forster, M.A. Schmidt, U. Freudenberg, C. Werner, A. Fery, and C. Rossner, *Colorimetric Biosensors Based on Polymer/Gold Hybrid Nanoparticles: Topological Effects of the Polymer Coating.* Langmuir, 2022. **38**(40): p. 12325-12332.
161. Gigli, V., E. Capecchi, C. Tortolini, A. Isidori, R. Antiochia, and R. Saladino, *Tuning the Effect of Chitosan on the Electrochemical Responsiveness of Lignin Nanoparticles.* ACS Biomaterials Science & Engineering, 2023.
162. Gangopadhyay, B., A. Roy, D. Paul, S. Panda, B. Das, S. Karmakar, K. Dutta, S. Chattopadhyay, and D. Chattopadhyay, *3-Polythiophene Acetic Acid Nanosphere Anchored Few-Layer Graphene Nanocomposites for Label-Free Electrochemical Immunosensing of Liver Cancer Biomarker.* ACS Applied Bio Materials, 2024.
163. Zheng, Z., L. Ma, B. Li, and X. Zhang, *Dual-Modal Biosensor for Staphylococcus aureus Detection Based on a Porphyrin-Based Porous Organic Polymer FePor-TPA with Excellent Peroxidase-like, Catalase-like, and Photoelectrochemical Properties.* Analytical chemistry, 2023. **95**(37): p. 13855-13863.
164. Shirmanova, M.V., I.N. Druzhkova, M.M. Lukina, V.V. Dudenkova, N.I. Ignatova, L.B. Snopova, V.I. Shcheslavskiy, V.V. Belousov, and E.V. Zagaynova, *Chemotherapy with cisplatin: insights into intracellular pH and metabolic landscape of cancer cells in vitro and in vivo.* Scientific Reports, 2017. **7**(1): p. 1-13.
165. Persi, E., M. Duran-Frigola, M. Damaghi, W.R. Roush, P. Aloy, J.L. Cleveland, R.J. Gillies, and E.

Ruppin, *Systems analysis of intracellular pH vulnerabilities for cancer therapy.* Nature Communications, 2018. **9**(1): p. 2997.
166. Dogan, A.E., C. Yuksel, F. Du, V.A. Chouinard, and D. Ongur, *Brain lactate and pH in schizophrenia and bipolar disorder: a systematic review of findings from magnetic resonance studies.* Neuropsychopharmacology, 2018. **43**(8): p. 1681-1690.
167. Juvekar, V., C.S. Lim, D.J. Lee, D.H. Song, C.K. Noh, H. Kang, S.J. Shin, and H.M. Kim, *Near-Infrared Ratiometric Two-Photon Probe for pH Measurement in Human Stomach Cancer Tissue.* ACS Applied Bio Materials, 2021. **4**(3): p. 2135-2141.
168. Liu, M., L. Huang, W. Zhang, X. Wang, Y. Geng, Y. Zhang, L. Wang, W. Zhang, Y.-J. Zhang, and S. Xiao, *A transistor-like pH-sensitive nanodetergent for selective cancer therapy.* Nature nanotechnology, 2022. **17**(5): p. 541-551.
169. Webb, B.A., M. Chimenti, M.P. Jacobson, and D.L. Barber, *Dysregulated pH: a perfect storm for cancer progression.* Nature Reviews Cancer, 2011. **11**(9): p. 671-7.
170. Wang, X.D., J.A. Stolwijk, T. Lang, M. Sperber, R.J. Meier, J. Wegener, and O.S. Wolfbeis, *Ultra-small, highly stable, and sensitive dual nanosensors for imaging intracellular oxygen and pH in cytosol.* Journal of the American chemical society, 2012. **134**(41): p. 17011-4.
171. Chan, K.W., G. Liu, X. Song, H. Kim, T. Yu, D.R. Arifin, A.A. Gilad, J. Hanes, P. Walczak, and P.C. Van Zijl, *MRI-detectable pH nanosensors incorporated into hydrogels for in vivo sensing of transplanted-cell viability.* Nature materials, 2013. **12**(3): p. 268-275.
172. Shrivastav, A.M., S.P. Usha, and B.D. Gupta, *Highly sensitive and selective erythromycin nanosensor employing fiber optic SPR/ERY imprinted nanostructure: Application in milk and honey.* Biosensors and Bioelectronics, 2017. **90**: p. 516-524.
173. Fulaz, S., D. Hiebner, C.H.N. Barros, H. Devlin, S. Vitale, L. Quinn, and E. Casey, *Ratiometric Imaging of the in Situ pH Distribution of Biofilms by Use of Fluorescent Mesoporous Silica Nanosensors.* ACS Applied Materials & Interfaces, 2019. **11**(36): p. 32679-32688.
174. Wang, X., S. Yu, J. Wang, J. Yu, M. Arabi, L. Fu, B. Li, J. Li, and L. Chen, *Fluorescent nanosensor designing via hybrid of carbon dots and post-imprinted polymers for the detection of ovalbumin.* Talanta, 2020. **211**: p. 120727.
175. Li, B., X. Wang, X. Shen, W. Zhu, L. Xu, and X. Zhou, *Aggregation-induced emission from gold nanoclusters for use as a luminescence-enhanced nanosensor to detect trace amounts of silver ions.* Journal of colloid and interface science, 2016. **467**: p. 90-96.
176. Campos, B.B., M.M. Oliva, R. Contreras-Cáceres, E. Rodriguez-Castellón, J. Jiménez-Jiménez, J.C.E. da Silva, and M. Algarra, *Carbon dots on based folic acid coated with PAMAM dendrimer as platform for Pt (IV) detection.* Journal of colloid and interface science, 2016. **465**: p. 165-173.
177. Fan, J., M. Hu, P. Zhan, and X. Peng, *Energy transfer cassettes based on organic fluorophores: construction and applications in ratiometric sensing.* Chemical Society Reviews, 2013. **42**(1): p. 29-43.
178. Wan, Q., S. Chen, W. Shi, L. Li, and H. Ma, *Lysosomal pH rise during heat shock monitored by a lysosome-targeting near-infrared ratiometric fluorescent probe.* Angewandte Chemie International Edition, 2014. **53**(41): p. 10916-20.
179. Lee, M.H., J.H. Han, J.H. Lee, N. Park, R. Kumar, C. Kang, and J.S. Kim, *Two-color probe to monitor a wide range of pH values in cells.* Angewandte Chemie International Edition, 2013. **52**(24): p. 6206-9.
180. Liu, T., J. Hu, Z. Jin, F. Jin, and S. Liu, *Two-photon ratiometric fluorescent mapping of intracellular transport pathways of pH-responsive block copolymer micellar nanocarriers.* Advanced healthcare materials, 2013. **2**(12): p. 1576-81.
181. Sies, H. and D.P. Jones, *Reactive oxygen species (ROS) as pleiotropic physiological signalling agents.* Nature reviews Molecular cell biology, 2020. **21**(7): p. 363-383.
182. Mittler, R., S.I. Zandalinas, Y. Fichman, and F. Van Breusegem, *Reactive oxygen species signalling in plant stress responses.* Nature reviews Molecular cell biology, 2022. **23**(10): p. 663-679.
183. Dickinson, B.C. and C.J. Chang, *Chemistry and biology of reactive oxygen species in signaling or stress responses.* Nature Chemical Biology, 2011. **7**(8): p. 504-11.
184. Van de Bittner, G.C., E.A. Dubikovskaya, C.R. Bertozzi, and C.J. Chang, *In vivo imaging of*

hydrogen peroxide production in a murine tumor model with a chemoselective bioluminescent reporter. Proceedings of the National Academy of Sciences, 2010. **107**(50): p. 21316-21.
185. Kirtonia, A., G. Sethi, and M. Garg, *The multifaceted role of reactive oxygen species in tumorigenesis.* Cellular and Molecular Life Sciences, 2020. **77**(22): p. 4459-4483.
186. Peoples, J.N., A. Saraf, N. Ghazal, T.T. Pham, and J.Q. Kwong, *Mitochondrial dysfunction and oxidative stress in heart disease.* Experimental & Molecular Medicine, 2019. **51**(12): p. 1-13.
187. Watts, L., E.-A. Haidar, and C. Stampfl, *Electron Transport Study of Hydrogen Peroxide Sensing with 2D Phosphorene and Molybdenum Disulfide.* The Journal of Physical Chemistry C, 2022. **126**(36): p. 15397-15404.
188. Bandi, R., M. Alle, C.-W. Park, S.-Y. Han, G.-J. Kwon, N.-H. Kim, J.-C. Kim, and S.-H. Lee, *Cellulose nanofibrils/carbon dots composite nanopapers for the smartphone-based colorimetric detection of hydrogen peroxide and glucose.* Sensors and Actuators B: Chemical, 2021. **330**: p. 129330.
189. Srikhao, N., A. Ounkaew, P. Kasemsiri, S. Theerakulpisut, M. Okhawilai, and S. Hiziroglu, *Green synthesis of silver nanoparticles using the extract of spent coffee used for paper-based hydrogen peroxide sensing device.* Scientific Reports, 2022. **12**(1): p. 20099.
190. Gulaboski, R., V. Mirčeski, R. Kappl, M. Hoth, and M. Bozem, *Quantification of hydrogen peroxide by electrochemical methods and electron spin resonance spectroscopy.* Journal of The Electrochemical Society, 2019. **166**(8): p. G82.
191. Zhang, Y., M. Dai, and Z. Yuan, *Methods for the detection of reactive oxygen species.* Analytical Methods, 2018. **10**(38): p. 4625-4638.
192. Bertrand, N., P. Grenier, M. Mahmoudi, E.M. Lima, E.A. Appel, F. Dormont, J.-M. Lim, R. Karnik, R. Langer, and O.C. Farokhzad, *Mechanistic understanding of in vivo protein corona formation on polymeric nanoparticles and impact on pharmacokinetics.* Nature communications, 2017. **8**(1): p. 1-8.
193. Hao, Y., Y. Chen, X. He, Y. Yu, R. Han, Y. Li, C. Yang, D. Hu, and Z. Qian, *Polymeric Nanoparticles with ROS-Responsive Prodrug and Platinum Nanozyme for Enhanced Chemophotodynamic Therapy of Colon Cancer.* Advanced Science, 2020. **7**(20): p. 2001853.
194. Zhao, Y., R. Xie, N. Yodsanit, M. Ye, Y. Wang, B. Wang, L.W. Guo, K.C. Kent, and S. Gong, *Hydrogen peroxide-responsive platelet membrane-coated nanoparticles for thrombus therapy.* Biomaterials Science, 2021. **9**(7): p. 2696-2708.
195. Albers, A.E., V.S. Okreglak, and C.J. Chang, *A FRET-based approach to ratiometric fluorescence detection of hydrogen peroxide.* Journal of the American chemical society, 2006. **128**(30): p. 9640-1.
196. Zhu, B., H. Jiang, B. Guo, C. Shao, H. Wu, B. Du, and Q. Wei, *A highly selective ratiometric fluorescent probe for hydrogen peroxide displaying a large emission shift.* Sensors and Actuators B: Chemical, 2013. **186**: p. 681-686.
197. Liu, C., C. Shao, H. Wu, B. Guo, B. Zhu, and X. Zhang, *A fast-response, highly sensitive and selective fluorescent probe for the ratiometric imaging of hydrogen peroxide with a 100 nm red-shifted emission.* RSC Advances, 2014. **4**(31): p. 16055-16061.
198. Lampard, E.V., A.C. Sedgwick, X. Sun, K.L. Filer, S.C. Hewins, G. Kim, J. Yoon, S.D. Bull, and T.D. James, *Boronate-Based Fluorescence Probes for the Detection of Hydrogen Peroxide.* ChemistryOpen, 2018. **7**(3): p. 262-265.
199. Bolland, H.R., E.M. Hammond, and A.C. Sedgwick, *A fluorescent probe strategy for the detection and discrimination of hydrogen peroxide and peroxynitrite in cells.* Chemical Communications, 2022. **58**(76): p. 10699-10702.
200. Chen, J., P. Zhang, G. Fang, P. Yi, F. Zeng, and S. Wu, *Design and synthesis of FRET-mediated multicolor and photoswitchable fluorescent polymer nanoparticles with tunable emission properties.* The Journal of Physical Chemistry B, 2012. **116**(14): p. 4354-62.
201. Chen, J., F. Huang, H. Wang, Y. Li, S. Liu, and P. Yi, *One-pot preparation of multicolor polymeric nanoparticles with high brightness by single wavelength excitation.* Journal of Applied Polymer Science, 2015. **132**(8).
202. Pan, W., Y. Li, M. Wang, H. Yang, N. Li, and B. Tang, *FRET-based nanoprobes for simultaneous*

monitoring of multiple mRNAs in living cells using single wavelength excitation. Chemical Communications, 2016. **52**(24): p. 4569-72.
203. Tao, M., X. Liang, J. Guo, S. Zheng, Q. Qi, Z. Cao, Y. Mi, and Z. Zhao, *Dynamic Photochromic Polymer Nanoparticles Based on Matrix-Dependent Forster Resonance Energy Transfer and Aggregation-Induced Emission Properties.* ACS Applied Materials & Interfaces, 2021. **13**(28): p. 33574-33583.
204. Walper, S.A., G. Lasarte Aragones, K.E. Sapsford, C.W. Brown, 3rd, C.E. Rowland, J.C. Breger, and I.L. Medintz, *Detecting Biothreat Agents: From Current Diagnostics to Developing Sensor Technologies.* ACS Sensors, 2018. **3**(10): p. 1894-2024.
205. Gargis, A.S., B. Cherney, A.B. Conley, H.P. McLaughlin, and D. Sue, *Rapid Detection of Genetic Engineering, Structural Variation, and Antimicrobial Resistance Markers in Bacterial Biothreat Pathogens by Nanopore Sequencing.* Scientific Reports, 2019. **9**(1): p. 13501.
206. Roy, C.J., D. Ehrbar, G. Van Slyke, J. Doering, P.J. Didier, L. Doyle-Meyers, O. Donini, E.S. Vitetta, and N.J. Mantis, *Serum antibody profiling identifies vaccine-induced correlates of protection against aerosolized ricin toxin in rhesus macaques.* NPJ Vaccines, 2022. **7**(1): p. 164.
207. Banger, S., V. Pal, N.K. Tripathi, and A.K. Goel, *Development of a PCR Lateral Flow Assay for Rapid Detection of Bacillus anthracis, the Causative Agent of Anthrax.* Molecular Biotechnology, 2021. **63**(8): p. 702-709.
208. Aslantürk, Ö.S., *In vitro cytotoxicity and cell viability assays: principles, advantages, and disadvantages.* Genotoxicity-A predictable risk to our actual world, 2018. **2**: p. 64-80.
209. Dybwad, M., A.L. van der Laaken, J.M. Blatny, and A. Paauw, *Rapid identification of Bacillus anthracis spores in suspicious powder samples by using matrix-assisted laser desorption ionization–time of flight mass spectrometry (MALDI-TOF MS).* Applied Environmental Microbiology, 2013. **79**(17): p. 5372-5383.
210. Zasada, A.A., K. Forminska, K. Zacharczuk, D. Jacob, and R. Grunow, *Comparison of eleven commercially available rapid tests for detection of Bacillus anthracis, Francisella tularensis and Yersinia pestis.* Letters in Applied Microbiology, 2015. **60**(5): p. 409-13.
211. Zhao, Y.W., H.X. Wang, G.C. Jia, and Z. Li, *Application of Aptamer-Based Biosensor for Rapid Detection of Pathogenic Escherichia coli.* Sensors, 2018. **18**(8): p. 2518.
212. Rowland, C.E., C.W. Brown, 3rd, J.B. Delehanty, and I.L. Medintz, *Nanomaterial-based sensors for the detection of biological threat agents.* Materials Today, 2016. **19**(8): p. 464-477.
213. Charelli, L.E., G.C. de Mattos, A. de Jesus Sousa-Batista, J.C. Pinto, and T.A. Balbino, *Polymeric nanoparticles as therapeutic agents against coronavirus disease.* Journal of Nanoparticle Research, 2022. **24**: p. 1-15.
214. Park, C., J.-W. Lim, G. Park, H.-O. Kim, S. Lee, Y.H. Kwon, S.-E. Kim, M. Yeom, W. Na, and D. Song, *Kinetic stability modulation of polymeric nanoparticles for enhanced detection of influenza virus via penetration of viral fusion peptides.* Journal of Materials Chemistry B, 2021. **9**(47): p. 9658-9669.
215. Zhang, Q., A. Honko, J. Zhou, H. Gong, S.N. Downs, J.H. Vasquez, R.H. Fang, W. Gao, A. Griffiths, and L. Zhang, *Cellular nanosponges inhibit SARS-CoV-2 infectivity.* Nano Letters, 2020. **20**(7): p. 5570-5574.
216. Zhang, G., G.R. Campbell, Q. Zhang, E. Maule, J. Hanna, W. Gao, L. Zhang, and S.A. Spector, *CD4+ t cell-mimicking nanoparticles broadly neutralize hiv-1 and suppress viral replication through autophagy.* MBio, 2020. **11**(5): p. 10.1128/mbio. 00903-20.
217. Park, G., J.-W. Lim, C. Park, M. Yeom, S. Lee, K.-S. Lyoo, D. Song, and S. Haam, *Cell-mimetic biosensors to detect avian influenza virus via viral fusion.* Biosensors and Bioelectronics, 2022. **212**: p. 114407.
218. Cho, J., Y. Miyake, A. Honda, K. Kushiro, and M. Takai, *Analysis of the changes in expression levels of sialic acid on influenza-virus-infected cells using lectin-tagged polymeric nanoparticles.* Frontiers in Microbiology, 2016. **7**: p. 1147.
219. Khoris, I.M., A.B. Ganganboina, and E.Y. Park, *Self-assembled chromogenic polymeric nanoparticle-laden nanocarrier as a signal carrier for derivative binary responsive virus detection.* ACS Applied Materials & Interfaces, 2021. **13**(31): p. 36868-36879.

220. Khoris, I.M., A.B. Ganganboina, T. Suzuki, and E.Y. Park, *Self-assembled chromogen-loaded polymeric cocoon for respiratory virus detection.* Nanoscale, 2021. **13**(1): p. 388-396.
221. Park, G., H.-O. Kim, J.-W. Lim, C. Park, M. Yeom, D. Song, and S. Haam, *Rapid detection of influenza A (H1N1) virus by conductive polymer-based nanoparticle via optical response to virus-specific binding.* Nano Research, 2022: p. 1-9.
222. Cai, X., A. Prominski, Y. Lin, N. Ankenbruck, J. Rosenberg, M. Chen, J. Shi, E.B. Chang, P. Penaloza-MacMaster, and B. Tian, *A neutralizing antibody-conjugated photothermal nanoparticle captures and inactivates SARS-CoV-2.* biorxiv, 2020: p. 2020.11. 30.404624.
223. Lauster, D., M. Glanz, M. Bardua, K. Ludwig, M. Hellmund, U. Hoffmann, A. Hamann, C. Böttcher, R. Haag, and C.P. Hackenberger, *Multivalent peptide–nanoparticle conjugates for influenza-virus inhibition.* Angewandte Chemie International Edition, 2017. **56**(21): p. 5931-5936.
224. Donmez, M., M.D. Yilmaz, and B. Kilbas, *Fluorescent detection of dipicolinic acid as a biomarker of bacterial spores using lanthanide-chelated gold nanoparticles.* Journal of hazardous materials, 2017. **324**: p. 593-598.
225. Gao, N., Y. Zhang, P. Huang, Z. Xiang, F.Y. Wu, and L. Mao, *Perturbing Tandem Energy Transfer in Luminescent Heterobinuclear Lanthanide Coordination Polymer Nanoparticles Enables Real-Time Monitoring of Release of the Anthrax Biomarker from Bacterial Spores.* Analytical chemistry, 2018. **90**(11): p. 7004-7011.
226. Celebanska, A., Y. Chiniforooshan, M. Janik, P. Mikulic, B. Sellamuthu, J. Perreault, and W.J. Bock, *Bioinspired carbohydrate-decorated long-period fiber grating for label-free bacteria detection.* IEEE Sensors Journal, 2019. **19**(24): p. 11965-11971.
227. Sauer, M.M., R.P. Jakob, T. Luber, F. Canonica, G. Navarra, B. Ernst, C. Unverzagt, T. Maier, and R. Glockshuber, *Binding of the Bacterial Adhesin FimH to Its Natural, Multivalent High-Mannose Type Glycan Targets.* Journal of the American chemical society, 2019. **141**(2): p. 936-944.
228. Tsakama, M., X. Ma, Y. He, W. Chen, and X. Dai, *A Simple Mannose-Coated Poly (p-Phenylene Ethynylene) for Qualitative Bacterial Capturing.* Molecules, 2018. **23**(8): p. 2056.
229. Zhou, Q., J.C.M. Vega Leonel, M.R. Santoso, C. Wilson, N.S. van den Berg, C.T. Chan, M. Aryal, H. Vogel, R. Cayrol, M.J. Mandella, F. Schonig, G. Lu, S.S. Gambhir, M.E. Moseley, E.L. Rosenthal, and G.A. Grant, *Molecular imaging of a fluorescent antibody against epidermal growth factor receptor detects high-grade glioma.* Scientific Reports, 2021. **11**(1): p. 5710.
230. Salarian, M., R.C. Turaga, S. Xue, M. Nezafati, K. Hekmatyar, J. Qiao, Y. Zhang, S. Tan, O.Y. Ibhagui, Y. Hai, J. Li, R. Mukkavilli, M. Sharma, P. Mittal, X. Min, S. Keilholz, L. Yu, G. Qin, A.B. Farris, Z.R. Liu, and J.J. Yang, *Early detection and staging of chronic liver diseases with a protein MRI contrast agent.* Nature Communications, 2019. **10**(1): p. 4777.
231. Bam, R., M. Laffey, K. Nottberg, P.S. Lown, B.J. Hackel, and K.E. Wilson, *Affibody-indocyanine green based contrast agent for photoacoustic and fluorescence molecular imaging of B7–H3 expression in breast cancer.* Bioconjugate chemistry, 2019. **30**(6): p. 1677-1689.
232. Pan, G.-Y., H.-R. Jia, Y.-X. Zhu, W. Sun, X.-T. Cheng, and F.-G. Wu, *Cyanine-containing polymeric nanoparticles with imaging/therapy-switchable capability for mitochondria-targeted cancer theranostics.* ACS Applied Nano Materials, 2018. **1**(6): p. 2885-2897.
233. Chibhabha, F., Y. Yang, K. Ying, F. Jia, Q. Zhang, S. Ullah, Z. Liang, M. Xie, and F. Li, *Non-invasive optical imaging of retinal Aβ plaques using curcumin loaded polymeric micelles in APP swe/PS1 ΔE9 transgenic mice for the diagnosis of Alzheimer's disease.* Journal of Materials Chemistry B, 2020. **8**(33): p. 7438-7452.
234. Jakhmola, A., N. Anton, H. Anton, N. Messaddeq, F. Hallouard, A. Klymchenko, Y. Mely, and T.F. Vandamme, *Poly-ε-caprolactone tungsten oxide nanoparticles as a contrast agent for X-ray computed tomography.* Biomaterials, 2014. **35**(9): p. 2981-2986.
235. Attia, M.F., N. Anton, M. Chiper, R. Akasov, H. Anton, N. Messaddeq, S. Fournel, A.S. Klymchenko, Y. Mély, and T.F. Vandamme, *Biodistribution of X-ray iodinated contrast agent in nano-emulsions is controlled by the chemical nature of the oily core.* ACS Nano, 2014. **8**(10): p. 10537-10550.
236. Yin, H.Q., P.P. Cao, X.Y. Wang, Y.H. Li, and X.B. Yin, *Computed Tomography Imaging-Guided Tandem Catalysis-Enhanced Photodynamic Therapy with Gold Nanoparticle Functional Covalent*

Organic Polymers. ACS Applied Bio Materials, 2020. **3**(4): p. 2534-2542.
237. Yordanov, A.T., A.L. Lodder, E.K. Woller, M.J. Cloninger, N. Patronas, D. Milenic, and M.W. Brechbiel, *Novel iodinated dendritic nanoparticles for computed tomography (CT) imaging.* Nano Letters, 2002. **2**(6): p. 595-599.
238. Patra, A., J.-M. Koenen, and U. Scherf, *Fluorescent nanoparticles based on a microporous organic polymer network: fabrication and efficient energy transfer to surface-bound dyes.* Chemical Communications, 2011. **47**(34): p. 9612-9614.
239. Srikar, R., A. Upendran, and R. Kannan, *Polymeric nanoparticles for molecular imaging.* Wiley Interdisciplinary Reviews: Nanomedicine and Nanobiotechnology, 2014. **6**(3): p. 245-67.
240. On, K.C., J. Rho, H.Y. Yoon, H. Chang, J.Y. Yhee, J.S. Yoon, S.Y. Jeong, H.K. Kim, and K. Kim, *Tumor-Targeting Glycol Chitosan Nanoparticles for Image-Guided Surgery of Rabbit Orthotopic VX2 Lung Cancer.* Pharmaceutics, 2020. **12**(7): p. 621.
241. He, H., J. Zhou, Y. Liu, S. Liu, Z. Xie, M. Yu, Y. Wang, and X. Shuai, *Near-Infrared-Light-Induced Morphology Transition of Poly(ether amine) Nanoparticles for Supersensitive Drug Release.* ACS Applied Materials & Interfaces, 2018. **10**(8): p. 7413-7421.
242. Nunes, R., F. Araujo, J. Tavares, B. Sarmento, and J. das Neves, *Surface modification with polyethylene glycol enhances colorectal distribution and retention of nanoparticles.* European journal of pharmaceutics and biopharmaceutics, 2018. **130**: p. 200-206.
243. Wang, H., P. Zhang, J. Chen, Y. Li, M. Yu, Y. Long, and P. Yi, *Polymer nanoparticle-based ratiometric fluorescent probe for imaging Hg2+ ions in living cells.* Sensors and Actuators B: Chemical, 2017. **242**: p. 818-824.
244. Hou, S., S. Tong, J. Zhou, and G. Bao, *Block copolymer-based gadolinium nanoparticles as MRI contrast agents with high T1 relaxivity.* Nanomedicine: Nanotechnology, Biology and Medicine, 2012. **7**(2): p. 211-218.
245. Ratzinger, G., P. Agrawal, W. Korner, J. Lonkai, H.M. Sanders, E. Terreno, M. Wirth, G.J. Strijkers, K. Nicolay, and F. Gabor, *Surface modification of PLGA nanospheres with Gd-DTPA and Gd-DOTA for high-relaxivity MRI contrast agents.* Biomaterials, 2010. **31**(33): p. 8716-23.
246. Liao, Z., H. Wang, X. Wang, P. Zhao, S. Wang, W. Su, and J. Chang, *Multifunctional Nanoparticles Composed of A Poly (dl-lactide-coglycolide) Core and A Paramagnetic Liposome Shell for Simultaneous Magnetic Resonance Imaging and Targeted Therapeutics.* Advanced Functional Materials, 2011. **21**(6): p. 1179-1186.
247. Huang, Z., Y. Chen, D. Liu, C. Lu, Z. Shen, S. Zhong, and G. Shi, *Gadolinium-conjugated star-block copolymer polylysine-modified polyethylenimine as high-performance T 1 MR imaging blood pool contrast agents.* RSC Advances, 2018. **8**(9): p. 5005-5012.
248. Shen, C., N. Yu, S. Cai, J. Zhou, J. Sheng, K. Liu, H. Zhou, Y. Guo, and G. Niu, *Quantitative computed tomography analysis for stratifying the severity of Coronavirus Disease 2019.* Journal of Pharmaceutical Analysis, 2020. **10**(2): p. 123-129.
249. Hyeon, C.W., H.K. Yi, E.K. Kim, S.J. Park, S.C. Lee, S.W. Park, J.K. Oh, J.Y. Choi, and S.A. Chang, *The role of (18)F-fluorodeoxyglucose-positron emission tomography/computed tomography in the differential diagnosis of pericardial disease.* Scientific Reports, 2020. **10**(1): p. 21524.
250. Morales-Zavala, F., P. Jara-Guajardo, D. Chamorro, A.L. Riveros, A. Chandia-Cristi, N. Salgado, P. Pismante, E. Giralt, M. Sanchez-Navarro, E. Araya, R. Vasquez, G. Acosta, F. Albericio, R.A. Alvarez, and M.J. Kogan, *In vivo micro computed tomography detection and decrease in amyloid load by using multifunctionalized gold nanorods: a neurotheranostic platform for Alzheimer's disease.* Biomaterials Science, 2021. **9**(11): p. 4178-4190.
251. Lusic, H. and M.W. Grinstaff, *X-ray-computed tomography contrast agents.* Chemical Reviews, 2013. **113**(3): p. 1641-66.
252. Maeda, H., *Toward a full understanding of the EPR effect in primary and metastatic tumors as well as issues related to its heterogeneity.* Advanced drug delivery reviews, 2015. **91**: p. 3-6.
253. Große Hokamp, N., A. Gupta, and R.C. Gilkeson, *Stratification of pulmonary nodules using quantitative iodine maps from dual-energy computed tomography.* American Journal of Respiratory and Critical Care Medicine, 2019. **199**(2): p. e3-e4.
254. Dong, Y.C., M. Hajfathalian, P.S. Maidment, J.C. Hsu, P.C. Naha, S. Si-Mohamed, M. Breuilly, J.

Kim, P. Chhour, and P. Douek, *Effect of gold nanoparticle size on their properties as contrast agents for computed tomography.* Scientific Reports, 2019. **9**(1): p. 1-13.
255. Robison, L., L. Zhang, R.J. Drout, P. Li, C.R. Haney, A. Brikha, H. Noh, B.L. Mehdi, N.D. Browning, and V.P. Dravid, *A bismuth metal–organic framework as a contrast agent for X-ray computed tomography.* ACS Applied Bio Materials, 2019. **2**(3): p. 1197-1203.
256. Liu, J., Z. Xiong, J. Zhang, C. Peng, B. Klajnert-Maculewicz, M. Shen, and X. Shi, *Zwitterionic Gadolinium(III)-Complexed Dendrimer-Entrapped Gold Nanoparticles for Enhanced Computed Tomography/Magnetic Resonance Imaging of Lung Cancer Metastasis.* ACS Applied Materials & Interfaces, 2019. **11**(17): p. 15212-15221.
257. Dunning, C.A., J. O'Connell, S.M. Robinson, K.J. Murphy, A.L. Frencken, F.C. van Veggel, K. Iniewski, and M. Bazalova-Carter, *Photon-counting computed tomography of lanthanide contrast agents with a high-flux 330-μm-pitch cadmium zinc telluride detector in a table-top system.* Journal of Medical Imaging, 2020. **7**(3): p. 033502.
258. Amato, C., L. Klein, E. Wehrse, L.T. Rotkopf, S. Sawall, J. Maier, C.H. Ziener, H.P. Schlemmer, and M. Kachelriess, *Potential of contrast agents based on high-Z elements for contrast-enhanced photon-counting computed tomography.* Medical Physics, 2020. **47**(12): p. 6179-6190.
259. Jeon, J., S. Kim, H. Yoo, K. Kim, Y. Kim, S. Park, H.R. Jang, D.K. Kim, W. Huh, Y.G. Kim, D.J. Kim, H.Y. Oh, and J.E. Lee, *Risk Prediction for Contrast-Induced Nephropathy in Cancer Patients Undergoing Computed Tomography under Preventive Measures.* Journal of Oncology, 2019. **2019**: p. 8736163.
260. Gerk, U., R.P. Franke, A. Kruger-Genge, and F. Jung, *Acute effects of Iodixanol on renal function after intra-arterial administration in patients with end-stage kidney disease.* Clinical Hemorheology and Microcirculation, 2018. **70**(4): p. 391-398.
261. Fu, Y., D.E. Nitecki, D. Maltby, G.H. Simon, K. Berejnoi, H.J. Raatschen, B.M. Yeh, D.M. Shames, and R.C. Brasch, *Dendritic iodinated contrast agents with PEG-cores for CT imaging: synthesis and preliminary characterization.* Bioconjugate chemistry, 2006. **17**(4): p. 1043-56.
262. Ge, Y., Y. Zhang, S. He, F. Nie, G. Teng, and N. Gu, *Fluorescence modified chitosan-coated magnetic nanoparticles for high-efficient cellular imaging.* Nanoscale research letters, 2009. **4**(4): p. 287-295.
263. Cheng, F.-Y., C.-H. Su, P.-C. Wu, and C.-S. Yeh, *Multifunctional polymeric nanoparticles for combined chemotherapeutic and near-infrared photothermal cancer therapy in vitro and in vivo.* Chemical Communications, 2010. **46**(18): p. 3167-3169.
264. Feng, X., F. Lv, L. Liu, H. Tang, C. Xing, Q. Yang, and S. Wang, *Conjugated polymer nanoparticles for drug delivery and imaging.* ACS Applied Materials & Interfaces, 2010. **2**(8): p. 2429-2435.
265. Lee, K.J., W.K. Oh, J. Song, S. Kim, J. Lee, and J. Jang, *Photoluminescent polymer nanoparticles for label-free cellular imaging.* Chemical Communications, 2010. **46**(29): p. 5229-31.
266. Shokeen, M., E.D. Pressly, A. Hagooly, A. Zheleznyak, N. Ramos, A.L. Fiamengo, M.J. Welch, C.J. Hawker, and C.J. Anderson, *Evaluation of multivalent, functional polymeric nanoparticles for imaging applications.* ACS Nano, 2011. **5**(2): p. 738-747.
267. Hu, X., G. Liu, Y. Li, X. Wang, and S. Liu, *Cell-penetrating hyperbranched polyprodrug amphiphiles for synergistic reductive milieu-triggered drug release and enhanced magnetic resonance signals.* Journal of the American Chemical Society, 2015. **137**(1): p. 362-368.
268. Machado, M.G.C., G. Pound-Lana, M.A. de Oliveira, E.G. Lanna, M.C.P. Fialho, A.C.F. de Brito, A.P.M. Barboza, R.D. de Oliveira Aguiar-Soares, and V.C.F. Mosqueira, *Labeling PLA-PEG nanocarriers with IR780: physical entrapment versus covalent attachment to polylactide.* Drug Delivery and Translational Research, 2020. **10**(6): p. 1626-1643.
269. Chen, N., W. Fu, J. Zhou, L. Mei, J. Yang, Y. Tian, Q. Wang, and W. Yin, *Mn2+-doped ZrO2@ PDA nanocomposite for multimodal imaging-guided chemo-photothermal combination therapy.* Chinese Chemical Letters, 2021.
270. Wiwatchaitawee, K., K. Ebeid, J.C. Quarterman, Y. Naguib, M.Y. Ali, C. Oliva, C. Griguer, and A.K. Salem, *Surface Modification of Nanoparticles Enhances Drug Delivery to the Brain and Improves Survival in a Glioblastoma Multiforme Murine Model.* Bioconjugate chemistry, 2022. **33**(11): p. 1957-1972.

271. Chen, J., J. Qi, C. Chen, J. Chen, L. Liu, R. Gao, T. Zhang, L. Song, D. Ding, and P. Zhang, *Tocilizumab–Conjugated Polymer Nanoparticles for NIR-II Photoacoustic-Imaging-Guided Therapy of Rheumatoid Arthritis.* Advanced Materials and Processes, 2020. **32**(37): p. 2003399.
272. Zhao, Z., C. Chen, S. Wei, H. Xiong, F. Hu, Y. Miao, T. Jin, and W. Min, *Ultra-bright Raman dots for multiplexed optical imaging.* Nature Communications, 2021. **12**(1): p. 1-12.
273. Creamer, A., C.S. Wood, P.D. Howes, A. Casey, S. Cong, A.V. Marsh, R. Godin, J. Panidi, T.D. Anthopoulos, C.H. Burgess, T. Wu, Z. Fei, I. Hamilton, M.A. McLachlan, M.M. Stevens, and M. Heeney, *Post-polymerisation functionalisation of conjugated polymer backbones and its application in multi-functional emissive nanoparticles.* Nature Communications, 2018. **9**(1): p. 3237.
274. Yang, Z., A. Sharma, J. Qi, X. Peng, D.Y. Lee, R. Hu, D. Lin, J. Qu, and J.S. Kim, *Super-resolution fluorescent materials: an insight into design and bioimaging applications.* Chemical Society Reviews, 2016. **45**(17): p. 4651-4667.
275. Gao, M., F. Yu, C. Lv, J. Choo, and L. Chen, *Fluorescent chemical probes for accurate tumor diagnosis and targeting therapy.* Chemical Society Reviews, 2017. **46**(8): p. 2237-2271.
276. Shuai, Q., G. Zhao, X. Zhang, B. Yu, R.J. Lee, and W.K. Su, *Selection of fluorescent dye for tracking biodistribution of paclitaxel in live imaging.* Colloids and Surfaces B: Biointerfaces, 2019. **181**: p. 872-878.
277. Panych, L.P. and B. Madore, *The physics of MRI safety.* Journal of Magnetic Resonance Imaging, 2018. **47**(1): p. 28-43.
278. Schmeel, F.C., J.A. Luetkens, P.J. Wagenhauser, M. Meier-Schroers, D.L. Kuetting, A. Feisst, J. Gieseke, L.C. Schmeel, F. Traber, H.H. Schild, and G.M. Kukuk, *Proton density fat fraction (PDFF) MRI for differentiation of benign and malignant vertebral lesions.* European Radiology, 2018. **28**(6): p. 2397-2405.
279. Cabrera-García, A., E. Checa-Chavarria, J. Pacheco-Torres, Á. Bernabeu-Sanz, A. Vidal-Moya, E. Rivero-Buceta, G. Sastre, E. Fernández, and P. Botella, *Engineered contrast agents in a single structure for T 1–T 2 dual magnetic resonance imaging.* Nanoscale Advances, 2018. **10**(14): p. 6349-6360.
280. Jacques, V., S. Dumas, W.-C. Sun, J.S. Troughton, M.T. Greenfield, and P. Caravan, *High relaxivity MRI contrast agents part 2: Optimization of inner-and second-sphere relaxivity.* Investigative radiology, 2010. **45**(10): p. 613.
281. Zhang, S., Y. Zheng, D.Y. Fu, W. Li, Y. Wu, B. Li, and L. Wu, *Biocompatible supramolecular dendrimers bearing a gadolinium-substituted polyanionic core for MRI contrast agents.* Journal of Materials Chemistry B, 2017. **5**(22): p. 4035-4043.
282. Fingerhut, S., A.C. Niehoff, M. Sperling, A. Jeibmann, W. Paulus, T. Niederstadt, T. Allkemper, W. Heindel, M. Holling, and U. Karst, *Spatially resolved quantification of gadolinium deposited in the brain of a patient treated with gadolinium-based contrast agents.* Journal of Trace Elements in Medicine and Biology, 2018. **45**: p. 125-130.
283. Yang, C.T., A. Hattiholi, S.T. Selvan, S.X. Yan, W.W. Fang, P. Chandrasekharan, P. Koteswaraiah, C.J. Herold, B. Gulyas, S.E. Aw, T. He, D.C.E. Ng, and P. Padmanabhan, *Gadolinium-based bimodal probes to enhance T1-Weighted magnetic resonance/optical imaging.* Acta Biomaterialia, 2020. **110**: p. 15-36.
284. Food, U. and D. Administration, *Medical Imaging Drugs Advisory Committee Meeting; gadolinium retention after gadolinium based contrast magnetic resonance imaging in patients with normal renal function*. 2019.
285. Li, D., J. Yang, S. Wen, M. Shen, L. Zheng, G. Zhang, and X. Shi, *Targeted CT/MR dual mode imaging of human hepatocellular carcinoma using lactobionic acid-modified polyethyleneimine-entrapped gold nanoparticles.* Journal of Materials Chemistry B, 2017. **5**(13): p. 2395-2401.
286. Zu, M., Y. Ma, B. Cannup, D. Xie, Y. Jung, J. Zhang, C. Yang, F. Gao, D. Merlin, and B. Xiao, *Oral delivery of natural active small molecules by polymeric nanoparticles for the treatment of inflammatory bowel diseases.* Advanced drug delivery reviews, 2021. **176**: p. 113887.
287. Dancy, J.G., A.S. Wadajkar, N.P. Connolly, R. Galisteo, H.M. Ames, S. Peng, N.L. Tran, O.G. Goloubeva, G.F. Woodworth, J.A. Winkles, and A.J. Kim, *Decreased nonspecific adhesivity, receptor-targeted therapeutic nanoparticles for primary and metastatic breast cancer.* Science

advances, 2020. **6**(3): p. eaax3931.
288. Ding, Y., J. Liu, Y. Zhang, X. Li, H. Ou, T. Cheng, L. Ma, Y. An, J. Liu, and F. Huang, *A novel strategy based on a ligand-switchable nanoparticle delivery system for deep tumor penetration.* Nanoscale Horizons, 2019. **4**(3): p. 658-666.
289. Leitner, N.S., M. Schroffenegger, and E. Reimhult, *Polymer Brush-Grafted Nanoparticles Preferentially Interact with Opsonins and Albumin.* ACS Applied Bio Materials, 2021. **4**(1): p. 795-806.
290. Hayashi, Y., M. Takamiya, P.B. Jensen, I. Ojea-Jimenez, H. Claude, C. Antony, K. Kjaer-Sorensen, C. Grabher, T. Boesen, and D. Gilliland, *Differential nanoparticle sequestration by macrophages and scavenger endothelial cells visualized in vivo in real-time and at ultrastructural resolution.* ACS Nano, 2020. **14**(2): p. 1665-1681.
291. Liu, Y., B. Workalemahu, and X. Jiang, *The effects of physicochemical properties of nanomaterials on their cellular uptake in vitro and in vivo.* Small Fruits Review, 2017. **13**(43): p. 1701815.
292. Yamamoto, Y., Y. Nagasaki, M. Kato, and K. Kataoka, *Surface charge modulation of poly (ethylene glycol)–poly (d, l-lactide) block copolymer micelles: conjugation of charged peptides.* Colloids and Surfaces B: Biointerfaces, 1999. **16**(1-4): p. 135-146.
293. Patil, Y.B., U.S. Toti, A. Khdair, L. Ma, and J. Panyam, *Single-step surface functionalization of polymeric nanoparticles for targeted drug delivery.* Biomaterials, 2009. **30**(5): p. 859-866.
294. Shen, Y., E. Jin, B. Zhang, C.J. Murphy, M. Sui, J. Zhao, J. Wang, J. Tang, M. Fan, and E. Van Kirk, *Prodrugs forming high drug loading multifunctional nanocapsules for intracellular cancer drug delivery.* Journal of the American Chemical Society, 2010. **132**(12): p. 4259-4265.
295. Aryal, S., C.-M.J. Hu, and L. Zhang, *Polymeric nanoparticles with precise ratiometric control over drug loading for combination therapy.* Molecular Pharmaceutics, 2011. **8**(4): p. 1401-1407.
296. Yuan, Y., J. Liu, and B. Liu, *Conjugated-polyelectrolyte-based polyprodrug: targeted and image-guided photodynamic and chemotherapy with on-demand drug release upon irradiation with a single light source.* Angewandte Chemie International Edition, 2014. **53**(28): p. 7163-7168.
297. Hyun, H., J. Park, K. Willis, J.E. Park, L.T. Lyle, W. Lee, and Y. Yeo, *Surface modification of polymer nanoparticles with native albumin for enhancing drug delivery to solid tumors.* Biomaterials, 2018. **180**: p. 206-224.
298. Le Droumaguet, B., J. Nicolas, D. Brambilla, S. Mura, A. Maksimenko, L. De Kimpe, E. Salvati, C. Zona, C. Airoldi, and M. Canovi, *Versatile and efficient targeting using a single nanoparticulate platform: application to cancer and Alzheimer's disease.* ACS Nano, 2012. **6**(7): p. 5866-5879.
299. Carradori, D., C. Balducci, F. Re, D. Brambilla, B. Le Droumaguet, O. Flores, A. Gaudin, S. Mura, G. Forloni, and L. Ordoñez-Gutierrez, *Antibody-functionalized polymer nanoparticle leading to memory recovery in Alzheimer's disease-like transgenic mouse model.* Nanomedicine: Nanotechnology, Biology and Medicine, 2018. **14**(2): p. 609-618.
300. He, Y., S. Guo, L. Wu, P. Chen, L. Wang, Y. Liu, and H. Ju, *Near-infrared boosted ROS responsive siRNA delivery and cancer therapy with sequentially peeled upconversion nano-onions.* Biomaterials, 2019. **225**: p. 119501.
301. Han, R., K. Tang, Y. Hou, J. Yu, C. Wang, and Y. Wang, *Fabrication of core/shell/shell structure nanoparticle with anticancer drug and dual-photosensitizer co-loading for synergistic chemotherapy and photodynamic therapy.* Microporous and Mesoporous Materials, 2020. **297**: p. 110049.
302. Li, N., D. Gao, C. Li, B. Wang, B. Li, B. Bao, M. Wu, M. Li, and C. Xing, *Polymer Nanoparticles Overcome Drug Resistance by a Dual-Targeting Apoptotic Signaling Pathway in Breast Cancer.* ACS Applied Materials & Interfaces, 2022. **14**(20): p. 23117-23128.
303. Kang, M., H.Y. Kim, and S.H. Bhang, *T-cell membrane coating for improving polymeric nanoparticle-based cancer therapy.* Journal of Industrial and Engineering Chemistry, 2023. **119**: p. 252-260.
304. Murar, M., S. Pujals, and L. Albertazzi, *Multivalent effect of peptide functionalized polymeric nanoparticles towards selective prostate cancer targeting.* Nanoscale Advances, 2023. **5**(5): p. 1378-1385.
305. Mixich, L., E. Boonstra, K. Masuda, S.-W. Li, Y. Nakashima, F. Meng, M. Sakata, T. Goda, S.

Uchida, and H. Cabral, *Ionizable Polymeric Micelles with Phenylalanine Moieties Enhance Intracellular Delivery of Self-Replicating RNA for Long-Lasting Protein Expression In Vivo.* Biomacromolecules, 2024.
306. Cheng, W., X. Zeng, H. Chen, Z. Li, W. Zeng, L. Mei, and Y. Zhao, *Versatile Polydopamine Platforms: Synthesis and Promising Applications for Surface Modification and Advanced Nanomedicine.* ACS Nano, 2019. **13**(8): p. 8537-8565.
307. Li, F., J. Meng, J. Ye, B. Yang, Q. Tian, and C.J.D. Deng, *Surface modification of PES ultrafiltration membrane by polydopamine coating and poly (ethylene glycol) grafting: Morphology, stability, and anti-fouling.* 2014. **344**: p. 422-430.
308. Gullotti, E., J. Park, and Y. Yeo, *Polydopamine-based surface modification for the development of peritumorally activatable nanoparticles.* Pharmaceutical research, 2013. **30**(8): p. 1956-67.
309. Park, J., T.F. Brust, H.J. Lee, S.C. Lee, V.J. Watts, and Y. Yeo, *Polydopamine-based simple and versatile surface modification of polymeric nano drug carriers.* ACS Nano, 2014. **8**(4): p. 3347-56.
310. Abouelmagd, S.A., Y.J. Ku, and Y. Yeo, *Low molecular weight chitosan-coated polymeric nanoparticles for sustained and pH-sensitive delivery of paclitaxel.* Journal of Drug Targeting, 2015. **23**(7-8): p. 725-35.
311. Xue, H., J. Zhao, Q. Zhou, D. Pan, Y. Zhang, Y. Zhang, and Y. Shen, *Boosting the sensitivity of a photoelectrochemical immunoassay by using SiO2@ polydopamine core–shell nanoparticles as a highly efficient quencher.* ACS Applied Nano Materials, 2019. **2**(3): p. 1579-1588.
312. Sileika, T.S., D.G. Barrett, R. Zhang, K.H.A. Lau, and P.B. Messersmith, *Colorless multifunctional coatings inspired by polyphenols found in tea, chocolate, and wine.* Angewandte Chemie International Edition, 2013. **125**(41): p. 10966-10970.
313. Cui, X., J. Liu, L. Ma, X. Wang, Y. Zheng, X. Wang, and G. Wu, *Grafting of the hierarchical natural tannic acid and polyethyleneimine onto carbon fiber for significantly improved surface/interface properties.* Polymers for Advanced Technologies, 2020. **31**(12): p. 3126-3133.
314. Abouelmagd, S.A., F. Meng, B.K. Kim, H. Hyun, and Y. Yeo, *Tannic acid-mediated surface functionalization of polymeric nanoparticles.* ACS Biomaterials Science & Engineering, 2016. **2**(12): p. 2294-2303.
315. Zhang, Y., K. Cai, C. Li, Q. Guo, Q. Chen, X. He, L. Liu, Y. Zhang, Y. Lu, X. Chen, T. Sun, Y. Huang, J. Cheng, and C. Jiang, *Macrophage-Membrane-Coated Nanoparticles for Tumor-Targeted Chemotherapy.* Nano Letters, 2018. **18**(3): p. 1908-1915.
316. Simon, J., T. Wolf, K. Klein, K. Landfester, F.R. Wurm, and V. Mailander, *Hydrophilicity Regulates the Stealth Properties of Polyphosphoester-Coated Nanocarriers.* Angewandte Chemie International Edition, 2018. **57**(19): p. 5548-5553.
317. He, X., L. Li, H. Su, D. Zhou, H. Song, L. Wang, and X. Jiang, *Poly (ethylene glycol)-block-poly (ε-caprolactone)–and phospholipid-based stealth nanoparticles with enhanced therapeutic efficacy on murine breast cancer by improved intracellular drug delivery.* International journal of nanomedicine, 2015. **10**: p. 1791.
318. Lück, M., B.R. Paulke, W. Schröder, T. Blunk, and R. Müller, *Analysis of plasma protein adsorption on polymeric nanoparticles with different surface characteristics.* Journal of Biomedical Materials Research, 1998. **39**(3): p. 478-485.
319. Bhattacharya, S., *Fabrication and characterization of chitosan-based polymeric nanoparticles of Imatinib for colorectal cancer targeting application.* International Journal of Biological Macromolecules, 2020. **151**: p. 104-115.
320. Badran, M.M., A.H. Alomrani, G.I. Harisa, A.E. Ashour, A. Kumar, and A.E. Yassin, *Novel docetaxel chitosan-coated PLGA/PCL nanoparticles with magnified cytotoxicity and bioavailability.* Biomedicine & Pharmacotherapy, 2018. **106**: p. 1461-1468.
321. Keyvan Rad, J., A.R. Mahdavian, S. Khoei, and S. Shirvalilou, *Enhanced photogeneration of reactive oxygen species and targeted photothermal therapy of C6 glioma brain cancer cells by folate-conjugated gold–photoactive polymer nanoparticles.* ACS Applied Materials & Interfaces, 2018. **10**(23): p. 19483-19493.
322. Andhariya, J.V., S. Choi, Y. Wang, Y. Zou, D.J. Burgess, and J. Shen, *Accelerated in vitro release testing method for naltrexone loaded PLGA microspheres.* International journal of pharmaceutics,

2017. **520**(1-2): p. 79-85.
323. Yin, J., S.S. Kim, E. Choi, Y.T. Oh, W. Lin, T.H. Kim, J.K. Sa, J.H. Hong, S.H. Park, H.J. Kwon, X. Jin, Y. You, J.H. Kim, H. Kim, J. Son, J. Lee, D.H. Nam, K.S. Choi, B. Shi, H.S. Gwak, H. Yoo, A. Iavarone, J.H. Kim, and J.B. Park, *ARS2/MAGL signaling in glioblastoma stem cells promotes self-renewal and M2-like polarization of tumor-associated macrophages.* Nature Communications, 2020. **11**(1): p. 2978.
324. Merry, T.L., A.E. Brooks, S.W. Masson, S.E. Adams, J.K. Jaiswal, S.M. Jamieson, and P.R. Shepherd, *The CSF1 receptor inhibitor pexidartinib (PLX3397) reduces tissue macrophage levels without affecting glucose homeostasis in mice.* International Journal of Obesity, 2020. **44**(1): p. 245-253.
325. Chen, H., J. Liu, H.U. Kaniskan, W. Wei, and J. Jin, *Folate-Guided Protein Degradation by Immunomodulatory Imide Drug-Based Molecular Glues and Proteolysis Targeting Chimeras.* Journal of medicinal chemistry, 2021. **64**(16): p. 12273-12285.
326. Banga, R.J., S.A. Krovi, S.P. Narayan, A.J. Sprangers, G. Liu, C.A. Mirkin, and S.T. Nguyen, *Drug-loaded polymeric spherical nucleic acids: enhancing colloidal stability and cellular uptake of polymeric nanoparticles through DNA surface-functionalization.* Biomacromolecules, 2017. **18**(2): p. 483-489.
327. Correa, S., N. Boehnke, A.E. Barberio, E. Deiss-Yehiely, A. Shi, B. Oberlton, S.G. Smith, I. Zervantonakis, E.C. Dreaden, and P.T. Hammond, *Tuning nanoparticle interactions with ovarian cancer through layer-by-layer modification of surface chemistry.* ACS Nano, 2020. **14**(2): p. 2224-2237.
328. Meng, Q., A. Wang, H. Hua, Y. Jiang, Y. Wang, H. Mu, Z. Wu, and K. Sun, *Intranasal delivery of Huperzine A to the brain using lactoferrin-conjugated N-trimethylated chitosan surface-modified PLGA nanoparticles for treatment of Alzheimer's disease.* International journal of nanomedicine, 2018. **13**: p. 705.
329. Tallapaka, S.B., B.V.K. Karuturi, P. Yeapuri, S.M. Curran, Y.A. Sonawane, J.A. Phillips, D. David Smith, S.D. Sanderson, and J.A. Vetro, *Surface conjugation of EP67 to biodegradable nanoparticles increases the generation of long-lived mucosal and systemic memory T-cells by encapsulated protein vaccine after respiratory immunization and subsequent T-cell-mediated protection against respiratory infection.* International journal of pharmaceutics, 2019. **565**: p. 242-257.
330. Bukchin, A., M. Sanchez-Navarro, A. Carrera, M. Teixidó, A.M. Carcaboso, E. Giralt, and A. Sosnik, *Amphiphilic polymeric nanoparticles modified with a retro-enantio peptide shuttle target the brain of mice.* Chemistry of Materials, 2020. **32**(18): p. 7679-7693.
331. Del Amo, L., A. Cano, M. Ettcheto, E.B. Souto, M. Espina, A. Camins, M.L. García, and E. Sánchez-López, *Surface Functionalization of PLGA Nanoparticles to Increase Transport across the BBB for Alzheimer's Disease.* Applied Sciences, 2021. **11**(9): p. 4305.
332. Petkau, K., A. Kaeser, I. Fischer, L. Brunsveld, and A.P. Schenning, *Pre- and postfunctionalized self-assembled pi-conjugated fluorescent organic nanoparticles for dual targeting.* Journal of the American chemical society, 2011. **133**(42): p. 17063-71.
333. Feng, G., Y. Fang, J. Liu, J. Geng, D. Ding, and B. Liu, *Multifunctional conjugated polymer nanoparticles for image-guided photodynamic and photothermal therapy.* Small, 2017. **13**(3): p. 1602807.
334. Liu, Y., L. Feng, T. Liu, L. Zhang, Y. Yao, D. Yu, L. Wang, and N. Zhang, *Multifunctional pH-sensitive polymeric nanoparticles for theranostics evaluated experimentally in cancer.* Nanoscale, 2014. **6**(6): p. 3231-42.
335. Shan, X., X. Gong, J. Li, J. Wen, Y. Li, and Z. Zhang, *Current approaches of nanomedicines in the market and various stage of clinical translation.* Acta Pharmaceutica Sinica B, 2022.
336. Choukourov, A., P. Pleskunov, D. Nikitin, V. Titov, A. Shelemin, M. Vaidulych, A. Kuzminova, P. Solař, J. Hanuš, and J. Kousal, *Advances and challenges in the field of plasma polymer nanoparticles.* Beilstein journal of nanotechnology, 2017. **8**(1): p. 2002-2014.
337. Pleskunov, P., D. Nikitin, R. Tafiichuk, A. Shelemin, J. Hanuš, I. Khalakhan, and A. Choukourov, *Carboxyl-Functionalized Nanoparticles Produced by Pulsed Plasma Polymerization of Acrylic Acid.* The Journal of Physical Chemistry B, 2018. **122**(14): p. 4187-4194.

338. Levato, R., T. Jungst, R.G. Scheuring, T. Blunk, J. Groll, and J. Malda, *From shape to function: the next step in bioprinting.* Advanced Materials, 2020. **32**(12): p. 1906423.
339. Martin, L.J., B. Akhavan, and M.M. Bilek, *Electric fields control the orientation of peptides irreversibly immobilized on radical-functionalized surfaces.* Nature communications, 2018. **9**(1): p. 357.
340. Sharifahmadian, O., C. Zhai, J. Hung, G. Shineh, C.A. Stewart, A.A. Fadzil, M. Ionescu, Y. Gan, S.G. Wise, and B.J.M.T.A. Akhavan, *Mechanically robust nitrogen-rich plasma polymers: Biofunctional interfaces for surface engineering of biomedical implants.* 2021. **12**: p. 100188.
341. Stewart, C.A., B. Akhavan, M. Santos, J. Hung, C.L. Hawkins, S. Bao, S.G. Wise, and M.M.J.A.S.S. Bilek, *Cellular responses to radical propagation from ion-implanted plasma polymer surfaces.* 2018. **456**: p. 701-710.
342. Kim, T., H. Kang, S. Jeong, D.J. Kang, C. Lee, C.-H. Lee, M.-K. Seo, J.-Y. Lee, and B.J. Kim, *Au@ polymer core–shell nanoparticles for simultaneously enhancing efficiency and ambient stability of organic optoelectronic devices.* ACS Applied Materials & Interfaces, 2014. **6**(19): p. 16956-16965.
343. Jiang, Y., P.K. Upputuri, C. Xie, Y. Lyu, L. Zhang, Q. Xiong, M. Pramanik, and K. Pu, *Broadband absorbing semiconducting polymer nanoparticles for photoacoustic imaging in second near-infrared window.* Nano Letters, 2017. **17**(8): p. 4964-4969.
344. Motaharian, A., F. Motaharian, K. Abnous, M.R.M. Hosseini, and M. Hassanzadeh-Khayyat, *Molecularly imprinted polymer nanoparticles-based electrochemical sensor for determination of diazinon pesticide in well water and apple fruit samples.* Analytical and bioanalytical chemistry, 2016. **408**(24): p. 6769-6779.
345. Liu, S.G., D. Luo, N. Li, W. Zhang, J.L. Lei, N.B. Li, and H.Q. Luo, *Water-soluble nonconjugated polymer nanoparticles with strong fluorescence emission for selective and sensitive detection of nitro-explosive picric acid in aqueous medium.* ACS Applied Materials & Interfaces, 2016. **8**(33): p. 21700-21709.
346. Palanikumar, L., S. Al-Hosani, M. Kalmouni, V.P. Nguyen, L. Ali, R. Pasricha, F.N. Barrera, and M.J.C.b. Magzoub, *pH-responsive high stability polymeric nanoparticles for targeted delivery of anticancer therapeutics.* 2020. **3**(1): p. 1-17.
347. Bojdi, M.K., M.H. Mashhadizadeh, M. Behbahani, A. Farahani, S.S.H. Davarani, and A. Bagheri, *Synthesis, characterization and application of novel lead imprinted polymer nanoparticles as a high selective electrochemical sensor for ultra-trace determination of lead ions in complex matrixes.* Electrochimica Acta, 2014. **136**: p. 59-65.
348. Esser, L., N.A. Lengkeek, B.A. Moffat, M.N. Vu, I. Greguric, J.F. Quinn, T.P. Davis, and M.R. Whittaker, *A tunable one-pot three-component synthesis of an 125 I and Gd-labelled star polymer nanoparticle for hybrid imaging with MRI and nuclear medicine.* Polymer Chemistry, 2018. **9**(25): p. 3528-3535.
349. Guo, L., G. Niu, X. Zheng, J. Ge, W. Liu, Q. Jia, P. Zhang, H. Zhang, and P. Wang, *Single near-infrared emissive polymer nanoparticles as versatile phototheranostics.* Advanced Science, 2017. **4**(10): p. 1700085.
350. Lyu, Y. and K. Pu, *Recent advances of activatable molecular probes based on semiconducting polymer nanoparticles in sensing and imaging.* Advanced Science, 2017. **4**(6): p. 1600481.
351. Maya-Vetencourt, J.F., G. Manfredi, M. Mete, E. Colombo, M. Bramini, S. Di Marco, D. Shmal, G. Mantero, M. Dipalo, and A. Rocchi, *Subretinally injected semiconducting polymer nanoparticles rescue vision in a rat model of retinal dystrophy.* Nature nanotechnology, 2020. **15**(8): p. 698-708.
352. Kröger, A.P.P., N.M. Hamelmann, A. Juan, S. Lindhoud, and J.M. Paulusse, *Biocompatible Single-Chain Polymer Nanoparticles for Drug Delivery—A Dual Approach.* ACS Applied Materials & Interfaces, 2018. **10**(37): p. 30946-30951.
353. Prabhu, R.H., V.B. Patravale, and M.D. Joshi, *Polymeric nanoparticles for targeted treatment in oncology: current insights.* International journal of nanomedicine, 2015. **10**: p. 1001.
354. Piazzini, V., E. Landucci, M. D'Ambrosio, L.T. Fasiolo, L. Cinci, G. Colombo, D.E. Pellegrini-Giampietro, A.R. Bilia, C. Luceri, and M.C.J.I.j.o.b.m. Bergonzi, *Chitosan coated human serum albumin nanoparticles: A promising strategy for nose-to-brain drug delivery.* 2019. **129**: p. 267-280.
355. Harguindey, A., D.W. Domaille, B.D. Fairbanks, J. Wagner, C.N. Bowman, and J.N. Cha, *Synthesis*

and Assembly of Click-Nucleic-Acid-Containing PEG–PLGA Nanoparticles for DNA Delivery. Advanced Materials, 2017. **29**(24): p. 1700743.
356. Liu, Y., G. Yang, D. Zou, Y. Hui, K. Nigam, A.P. Middelberg, C.-X.J.I. Zhao, and E.C. Research, *Formulation of nanoparticles using mixing-induced nanoprecipitation for drug delivery.* 2019. **59**(9): p. 4134-4149.
357. Piñón-Segundo, E., V.G. Llera-Rojas, G. Leyva-Gómez, Z. Urbán-Morlán, N. Mendoza-Muñoz, and D. Quintanar-Guerrero, *The emulsification-diffusion method to obtain polymeric nanoparticles: Two decades of research*, in *Nanoscale Fabrication, Optimization, Scale-Up and Biological Aspects of Pharmaceutical Nanotechnology*. 2018, Elsevier. p. 51-83.
358. Vauthier, C., *Methods for the Preparation of Nanoparticles by Polymerization*, in *Polymer Nanoparticles for Nanomedicines*. 2016, Springer. p. 123-157.
359. Akhavan, B., K. Jarvis, and P. Majewski. *Development of hydrophobic silica powders using plasma polymerization technology*. in *2012 Abstracts IEEE International Conference on Plasma Science*. 2012. IEEE.
360. Akhavan, B., S. Bakhshandeh, H. Najafi-Ashtiani, A.C. Fluit, E. Boel, C. Vogely, B.C. Van Der Wal, A.A. Zadpoor, H. Weinans, and W.E. Hennink, *Direct covalent attachment of silver nanoparticles on radical-rich plasma polymer films for antibacterial applications.* Journal of Materials Chemistry B, 2018. **6**(37): p. 5845-5853.
361. Yasuda, H., *Glow discharge polymerization.* Journal of Polymer Science: Macromolecular Reviews, 1981. **16**(1): p. 199-293.
362. Kobayashi, H., A.T. Bell, and M. Shen, *Formation of an amorphous powder during the polymerization of ethylene in a radio-frequency discharge.* Journal of Applied Polymer Science, 1973. **17**(3): p. 885-892.
363. Santos, M., B. Reeves, P. Michael, R. Tan, S.G. Wise, and M.M. Bilek, *Substrate geometry modulates self-assembly and collection of plasma polymerized nanoparticles.* Communications Physics, 2019. **2**(1): p. 1-11.
364. Kylián, O., A. Choukourov, and H. Biederman, *Nanostructured plasma polymers.* Thin Solid Films, 2013. **548**: p. 1-17.
365. Hinz, A., E. von Wahl, F. Faupel, T. Strunskus, and H. Kersten, *Nanoparticle forming reactive plasmas: a multidiagnostic approach.* The European Physical Journal D, 2018. **72**(5): p. 91.
366. Kovacevic, E., J. Berndt, T. Strunskus, and L. Boufendi, *Size dependent characteristics of plasma synthesized carbonaceous nanoparticles.* Journal of Applied Physics, 2012. **112**(1): p. 013303.
367. Winter, J., V. Fortov, and A. Nefedov, *Radioactive dust levitation and its consequences for fusion devices.* Journal of nuclear materials, 2001. **290**: p. 509-512.
368. Batryshev, D., Y. Yerlanuly, M. Gabdullin, and T.J.I.T.o.P.S. Ramazanov, *Study of a Transportation Process of Dust Particles in the Plasma of Radio Frequency Discharge.* 2019. **47**(8): p. 4209-4212.
369. Schlebrowski, T., H. Bahre, M. Böke, and J. Winter, *Monitoring particle growth in deposition plasmas.* Plasma Sources Science and Technology, 2013. **22**(6): p. 065014.
370. Hinz, A., E. von Wahl, F. Faupel, T. Strunskus, and H. Kersten, *Versatile particle collection concept for correlation of particle growth and discharge parameters in dusty plasmas.* Journal of Physics D: Applied Physics, 2015. **48**(5): p. 055203.
371. Karniadakis, G., A. Beskok, and N. Aluru, *Microflows and nanoflows: fundamentals and simulation*. Vol. 29. 2006: Springer Science & Business Media.
372. Baker, R.W., *Membrane technology and applications*. 2012: John Wiley & Sons.
373. Baldry, M., *Advanced Thermal Control for Cryotherapy using Thermoelectric Cooling*. 2019, University of New South Wales.
374. Shukla, P.K. and B. Eliasson, *Colloquium: Fundamentals of dust-plasma interactions.* Reviews of Modern Physics, 2009. **81**(1): p. 25.
375. Shukla, P.K. and A. Mamun, *Introduction to dusty plasma physics*. 2015: CRC Press.
376. Chen, F.F., *Introduction to plasma physics and controlled fusion*. Vol. 1. 1984: Springer.
377. Couedel, L.G.H.F., *Nanoparticle formation and dynamics in a complex (dusty) plasma: from the plasma ignition to the afterglow.* 2009.
378. Nosenko, V., R. Fisher, R. Merlino, S. Khrapak, G. Morfill, and K. Avinash, *Measurement of the*

ion drag force in a collisionless plasma with strong ion-grain coupling. Physics of Plasmas, 2007. **14**(10): p. 103702.
379. Becker, M. and D. Loffhagen, *Enhanced reliability of drift-diffusion approximation for electrons in fluid models for nonthermal plasmas.* AIP Advances, 2013. **3**(1): p. 012108.
380. Gogolides, E. and H.H. Sawin, *Continuum modeling of radio-frequency glow discharges. I. Theory and results for electropositive and electronegative gases.* Journal of Applied Physics, 1992. **72**(9): p. 3971-3987.
381. Liu, Q., Y. Liu, T. Samir, and Z. Ma, *Numerical study of effect of secondary electron emission on discharge characteristics in low pressure capacitive RF argon discharge.* Physics of Plasmas, 2014. **21**(8): p. 083511.
382. Passchier, J. and W. Goedheer, *A two-dimensional fluid model for an argon rf discharge.* Journal of Applied Physics, 1993. **74**(6): p. 3744-3751.
383. Hagelaar, G. and L. Pitchford, *Solving the Boltzmann equation to obtain electron transport coefficients and rate coefficients for fluid models.* Plasma Sources Science and Technology, 2005. **14**(4): p. 722.
384. Lymberopoulos, D.P. and D.J. Economou, *Two-dimensional self-consistent radio frequency plasma simulations relevant to the gaseous electronics conference RF reference cell.* Journal of research of the National Institute of Standards and Technology, 1995. **100**(4): p. 473.
385. Zafiu, C., A. Melzer, and A. Piel, *Ion drag and thermophoretic forces acting on free falling charged particles in an rf-driven complex plasma.* Physics of Plasmas, 2002. **9**(11): p. 4794-4803.
386. Marvi, Z., E. von Wahl, T. Trottenberg, and H.J.J.o.A.P. Kersten, *Spatiotemporal sampling of growing nanoparticles in an acetylene plasma.* 2020. **127**(17): p. 173301.
387. Mikikian, M., L. Couëdel, M. Cavarroc, Y. Tessier, and L.J.E.P.J.A.P. Boufendi, *Dusty plasmas: synthesis, structure and dynamics of a dust cloud in a plasma.* 2010. **49**: p. 13106.
388. Santos, M., *Synthesis of bio-functional nanomaterials in reactive plasma discharges.* 2017.
389. Denysenko, I., E. von Wahl, M. Mikikian, J. Berndt, S. Ivko, H. Kersten, E. Kovacevic, and N.J.J.o.P.D.A.P. Azarenkov, *Plasma properties as function of time in Ar/C2H2 dust-forming plasma.* 2020. **53**(13): p. 135203.
390. Fatima, H., M.U. Ullah, S. Ahmad, M. Imran, S. Sajjad, S. Hussain, and A.J.S.A.S. Qayyum, *Spectroscopic evaluation of vibrational temperature and electron density in reduced pressure radio frequency nitrogen plasma.* 2021. **3**(6): p. 1-11.
391. Sewraj, N., N. Merbahi, J. Gardou, P.R. Akerreta, and F.J.J.o.P.D.A.P. Marchal, *Electric and spectroscopic analysis of a pure nitrogen mono-filamentary dielectric barrier discharge (MF-DBD) at 760 Torr.* 2011. **44**(14): p. 145201.
392. Lock, E., R. Fernsler, S. Slinker, and S. Walton, *Experimental and Theoretical Estimation of Excited Species Generation in Pulsed Electron Beam-Generated Plasmas Produced in Pure Argon, Nitrogen, Oxygen, and Their Mixtures*. 2011, NAVAL RESEARCH LAB WASHINGTON DC PLASMA PHYSICS DIV.
393. Benedikt, J., *Plasma-chemical reactions: low pressure acetylene plasmas.* Journal of Physics D: Applied Physics, 2010. **43**(4): p. 043001.
394. Le Dû, G., N. Celini, F. Bergaya, F.J.S. Poncin-Epaillard, and C. Technology, *RF plasma-polymerization of acetylene: Correlation between plasma diagnostics and deposit characteristics.* 2007. **201**(12): p. 5815-5821.
395. Akhavan, B., K. Jarvis, and P.J.L. Majewski, *Development of oxidized sulfur polymer films through a combination of plasma polymerization and oxidative plasma treatment.* 2014. **30**(5): p. 1444-1454.
396. Akhavan, B., M. Croes, S.G. Wise, C. Zhai, J. Hung, C. Stewart, M. Ionescu, H. Weinans, Y. Gan, and S.A. Yavari, *Radical-functionalized plasma polymers: Stable biomimetic interfaces for bone implant applications.* Applied Materials Today, 2019. **16**: p. 456-473.
397. Guerrini, L., R.A. Alvarez-Puebla, and N.J.M. Pazos-Perez, *Surface modifications of nanoparticles for stability in biological fluids.* 2018. **11**(7): p. 1154.
398. Ferrari, R., M. Lupi, C. Colombo, M. Morbidelli, M. D'Incalci, and D. Moscatelli, *Investigation of size, surface charge, PEGylation degree and concentration on the cellular uptake of polymer nanoparticles.* Colloids and Surfaces B: Biointerfaces, 2014. **123**: p. 639-647.

399. Foroozandeh, P. and A.A.J.N.r.l. Aziz, *Insight into cellular uptake and intracellular trafficking of nanoparticles.* 2018. **13**(1): p. 1-12.
400. Mikikian, M., S. Labidi, E. Von Wahl, J.-F. Lagrange, T. Lecas, V. Massereau-Guilbaud, I. Géraud-Grenier, E. Kovacevic, J. Berndt, and H. Kersten, *Optical diagnostics of dusty plasmas during nanoparticle growth.* Plasma Physics and Controlled Fusion, 2016. **59**(1): p. 014034.
401. Cavarroc, M., M. Mikikian, Y. Tessier, and L. Boufendi, *Successive generations of dust in complex plasmas: A cyclic phenomenon in the void region.* Physical review letters, 2008. **100**(4): p. 045001.
402. Liu, R., W. Xiao, C. Hu, R. Xie, and H.J.J.o.c.r. Gao, *Theranostic size-reducible and no donor conjugated gold nanocluster fabricated hyaluronic acid nanoparticle with optimal size for combinational treatment of breast cancer and lung metastasis.* 2018. **278**: p. 127-139.
403. Hong, Y., S. Che, B. Hui, Y. Yang, X. Wang, X. Zhang, Y. Qiang, H.J.B. Ma, and Pharmacotherapy, *Lung cancer therapy using doxorubicin and curcumin combination: targeted prodrug based, pH sensitive nanomedicine.* 2019. **112**: p. 108614.
404. Wacker, M.G., *Nanomedicines—A Scientific Toy or an Emerging Market?*, in *Polymer Nanoparticles for Nanomedicines*. 2016, Springer. p. 591-614.
405. Wang, B., Y. Liu, Y. Zhang, Z. Guo, H. Zhang, J.H. Xin, and L. Zhang, *Bioinspired superhydrophobic Fe3O4@ polydopamine@ Ag hybrid nanoparticles for liquid marble and oil spill.* Advanced Materials Interfaces, 2015. **2**(13): p. 1500234.
406. Malik, R., V.K. Tomer, Y.K. Mishra, and L. Lin, *Functional gas sensing nanomaterials: A panoramic view.* Applied Physics Reviews, 2020. **7**(2): p. 021301.
407. Tomotoshi, D. and H. Kawasaki, *Surface and Interface Designs in Copper-Based Conductive Inks for Printed/Flexible Electronics.* Nanomaterials, 2020. **10**(9): p. 1689.
408. Jeong, H.-H., E. Choi, E. Ellis, and T.-C. Lee, *Recent advances in gold nanoparticles for biomedical applications: from hybrid structures to multi-functionality.* Journal of Materials Chemistry B, 2019. **7**(22): p. 3480-3496.
409. Ma, J., S.M.-Y. Lee, C. Yi, and C.-W. Li, *Controllable synthesis of functional nanoparticles by microfluidic platforms for biomedical applications–a review.* Lab on a Chip, 2017. **17**(2): p. 209-226.
410. Sotiriou, G.A., *Biomedical applications of multifunctional plasmonic nanoparticles.* Wiley Interdisciplinary Reviews: Nanomedicine and Nanobiotechnology, 2013. **5**(1): p. 19-30.
411. Xu, M., H. Zhou, Y. Liu, J. Sun, W. Xie, P. Zhao, and J. Liu, *Ultrasound-excited protoporphyrin IX-modified multifunctional nanoparticles as a strong inhibitor of tau phosphorylation and β-amyloid aggregation.* ACS Applied Materials & Interfaces, 2018. **10**(39): p. 32965-32980.
412. Lee, S.-M., H.J. Kim, Y.-J. Ha, Y.N. Park, S.-K. Lee, Y.-B. Park, and K.-H. Yoo, *Targeted chemo-photothermal treatments of rheumatoid arthritis using gold half-shell multifunctional nanoparticles.* ACS Nano, 2013. **7**(1): p. 50-57.
413. Joo, J., D. Kwon, C. Yim, and S. Jeon, *Highly sensitive diagnostic assay for the detection of protein biomarkers using microresonators and multifunctional nanoparticles.* ACS Nano, 2012. **6**(5): p. 4375-4381.
414. Shu, D., Y. Shu, F. Haque, S. Abdelmawla, and P. Guo, *Thermodynamically stable RNA three-way junction for constructing multifunctional nanoparticles for delivery of therapeutics.* Nature nanotechnology, 2011. **6**(10): p. 658-667.
415. Lee, D.-E., H. Koo, I.-C. Sun, J.H. Ryu, K. Kim, and I.C. Kwon, *Multifunctional nanoparticles for multimodal imaging and theragnosis.* Chemical Society Reviews, 2012. **41**(7): p. 2656-2672.
416. Huynh, E. and G. Zheng, *Engineering multifunctional nanoparticles: all-in-one versus one-for-all.* Wiley Interdisciplinary Reviews: Nanomedicine and Nanobiotechnology, 2013. **5**(3): p. 250-265.
417. Cho, N.-H., T.-C. Cheong, J.H. Min, J.H. Wu, S.J. Lee, D. Kim, J.-S. Yang, S. Kim, Y.K. Kim, and S.-Y. Seong, *A multifunctional core–shell nanoparticle for dendritic cell-based cancer immunotherapy.* Nature nanotechnology, 2011. **6**(10): p. 675-682.
418. Zhao, Y., F. Ye, T.B. Brismar, X. Li, R. He, R. Heuchel, R. El-Sayed, N. Feliu, W. Zheng, and S. Oerther, *Multimodal Imaging of Pancreatic Ductal Adenocarcinoma Using Multifunctional Nanoparticles as Contrast Agents.* ACS Applied Materials & Interfaces, 2020.
419. Shin, K., J.W. Choi, G. Ko, S. Baik, D. Kim, O.K. Park, K. Lee, H.R. Cho, S.I. Han, and S.H. Lee,

Multifunctional nanoparticles as a tissue adhesive and an injectable marker for image-guided procedures. Nature Communications, 2017. **8**(1): p. 1-12.
420. Carrasco, E., B. del Rosal, F. Sanz-Rodríguez, Á.J. de la Fuente, P.H. Gonzalez, U. Rocha, K.U. Kumar, C. Jacinto, J.G. Solé, and D. Jaque, *Intratumoral thermal reading during photo-thermal therapy by multifunctional fluorescent nanoparticles.* Advanced Functional Materials, 2015. **25**(4): p. 615-626.
421. Chatterjee, S., X.S. Li, F. Liang, and Y.W. Yang, *Design of Multifunctional Fluorescent Hybrid Materials Based on SiO2 Materials and Core–Shell Fe3O4@ SiO2 Nanoparticles for Metal Ion Sensing.* Small, 2019. **15**(44): p. 1904569.
422. Upadhyayula, V.K., *Functionalized gold nanoparticle supported sensory mechanisms applied in detection of chemical and biological threat agents: a review.* Analytica chimica acta, 2012. **715**: p. 1-18.
423. Ruedas-Rama, M.J., J.D. Walters, A. Orte, and E.A. Hall, *Fluorescent nanoparticles for intracellular sensing: a review.* Analytica chimica acta, 2012. **751**: p. 1-23.
424. Mao, L., M. Liu, D. Xu, Q. Wan, Q. Huang, R. Jiang, Y. Shi, F. Deng, X. Zhang, and Y. Wei, *Synthesis, surface modification and biological imaging of aggregation-induced emission (AIE) dye doped silica nanoparticles.* Applied Surface Science, 2017. **403**: p. 396-402.
425. Chen, J., Y. Jin, N. Fahruddin, and J.X. Zhao, *Development of gold nanoparticle-enhanced fluorescent nanocomposites.* Langmuir, 2013. **29**(5): p. 1584-1591.
426. Zhao, X., L.R. Hilliard, S.J. Mechery, Y. Wang, R.P. Bagwe, S. Jin, and W. Tan, *A rapid bioassay for single bacterial cell quantitation using bioconjugated nanoparticles.* Proceedings of the National Academy of Sciences of the United States of America, 2004. **101**(42): p. 15027-15032.
427. Zhao, X., R. Tapec-Dytioco, and W. Tan, *Ultrasensitive DNA detection using highly fluorescent bioconjugated nanoparticles.* Journal of the American chemical society, 2003. **125**(38): p. 11474-11475.
428. Behnke, T., C. Würth, K. Hoffmann, M. Hübner, U. Panne, and U.J.J.o.F. Resch-Genger, *Encapsulation of Hydrophobic Dyes in Polystyrene Micro- and Nanoparticles via Swelling Procedures.* 2011. **21**(3): p. 937-944.
429. Santra, S., C. Kaittanis, J. Grimm, and J.M. Perez, *Drug/Dye-Loaded, Multifunctional Iron Oxide Nanoparticles for Combined Targeted Cancer Therapy and Dual Optical/Magnetic Resonance Imaging.* 2009. **5**(16): p. 1862-1868.
430. Robin, M.P. and R.K. O'Reilly, *Strategies for preparing fluorescently labelled polymer nanoparticles.* Polymer International, 2015. **64**(2): p. 174-182.
431. Wang, Z., X. Hong, S. Zong, C. Tang, Y. Cui, and Q. Zheng, *BODIPY-doped silica nanoparticles with reduced dye leakage and enhanced singlet oxygen generation.* Scientific reports, 2015. **5**: p. 12602-12602.
432. Tauk, L., A.P. Schröder, G. Decher, and N. Giuseppone, *Hierarchical functional gradients of pH-responsive self-assembled monolayers using dynamic covalent chemistry on surfaces.* Nature chemistry, 2009. **1**(8): p. 649.
433. Kotsuchibashi, Y., Y. Zhang, M. Ahmed, M. Ebara, T. Aoyagi, and R. Narain, *Fabrication of FITC-doped silica nanoparticles and study of their cellular uptake in the presence of lectins.* 2013. **101A**(7): p. 2090-2096.
434. Santos, M., P.L. Michael, E.C. Filipe, A.H.P. Chan, J. Hung, R.P. Tan, B.S.L. Lee, M. Huynh, C. Hawkins, A. Waterhouse, M.M.M. Bilek, and S.G. Wise, *Plasma Synthesis of Carbon-Based Nanocarriers for Linker-Free Immobilization of Bioactive Cargo.* ACS Applied Nano Materials, 2018. **1**(2): p. 580-594.
435. Winter, J., J. Berndt, S.H. Hong, E. Kovačević, I. Stefanović, and O. Stepanović, *Dust formation in Ar/CH4and Ar/C2H2plasmas.* Plasma Sources Science and Technology, 2009. **18**(3): p. 034010.
436. Mao, M., J. Benedikt, A. Consoli, and A. Bogaerts, *New pathways for nanoparticle formation in acetylene dusty plasmas: a modelling investigation and comparison with experiments.* Journal of Physics D: Applied Physics, 2008. **41**(22): p. 225201.
437. Kiss, É., G. Gyulai, E. Pári, K. Horváti, and S. Bősze, *Membrane affinity and fluorescent labelling: Comparative study of monolayer interaction, cellular uptake and cytotoxicity profile of*

carboxyfluorescein-conjugated cationic peptides. Amino acids, 2018. **50**(11): p. 1557-1571.
438. Chaganti, L.K., N. Venkatakrishnan, and K. Bose, *An efficient method for FITC labelling of proteins using tandem affinity purification.* Bioscience reports, 2018. **38**(6).
439. Martinez, V. and M.J.C.A.E.J. Henary, *Nile red and nile blue: applications and syntheses of structural analogues.* 2016. **22**(39): p. 13764-13782.
440. Stewart, C.A.C., B. Akhavan, M. Santos, J. Hung, C.L. Hawkins, S. Bao, S.G. Wise, and M.M.M. Bilek, *Cellular responses to radical propagation from ion-implanted plasma polymer surfaces.* Applied Surface Science, 2018. **456**: p. 701-710.
441. Stewart, C.A.C., B. Akhavan, J. Hung, S. Bao, J.-H. Jang, S.G. Wise, and M.M.M. Bilek, *Multifunctional Protein-Immobilized Plasma Polymer Films for Orthopedic Applications.* ACS Biomaterials Science & Engineering, 2018. **4**(12): p. 4084-4094.
442. Sharifahmadian, O., C. Zhai, J. Hung, G. Shineh, C.A.C. Stewart, A.A. Fadzil, M. Ionescu, Y. Gan, S.G. Wise, and B. Akhavan, *Mechanically robust nitrogen-rich plasma polymers: Biofunctional interfaces for surface engineering of biomedical implants.* Materials Today Advances, 2021. **12**: p. 100188.
443. Akhavan, B., M. Croes, S.G. Wise, C. Zhai, J. Hung, C. Stewart, M. Ionescu, H. Weinans, Y. Gan, S.A. Yavari, and M.M.M. Bilek, *Radical-functionalized plasma polymers: Stable biomimetic interfaces for bone implant applications.* Applied Materials Today, 2019. **16**: p. 456-473.
444. Boufendi, L., M.C. Jouanny, E. Kovacevic, J. Berndt, and M. Mikikian, *Dusty plasma for nanotechnology.* Journal of Physics D: Applied Physics, 2011. **44**(17): p. 174035.
445. Derjaguin, B., N. Churaev, V. Muller, B. Derjaguin, N. Churaev, and V. Muller, *The Derjaguin—Landau—Verwey—Overbeek (DLVO) theory of stability of lyophobic colloids.* Surface forces, 1987: p. 293-310.
446. Boumelhem, B.B., C. Pilgrim, V.E. Zwicker, J.L. Kolanowski, J.H. Yeo, K.A. Jolliffe, E.J. New, M.L. Day, S.J. Assinder, and S.T. Fraser, *Intracellular flow cytometric lipid analysis–a multiparametric system to assess distinct lipid classes in live cells.* Journal of cell science, 2022. **135**(5): p. jcs258322.
447. Laemmli, U.K., *Cleavage of structural proteins during the assembly of the head of bacteriophage T4.* Nature, 1970. **227**(5259): p. 680-685.
448. Bilek, M.M., D.V. Bax, A. Kondyurin, Y. Yin, N.J. Nosworthy, K. Fisher, A. Waterhouse, A.S. Weiss, C.G. dos Remedios, and D.R. McKenzie, *Free radical functionalization of surfaces to prevent adverse responses to biomedical devices.* Proceedings of the National Academy of Sciences, 2011. **108**(35): p. 14405-14410.
449. Shlyakhtenko, L.S., A.A. Gall, J.J. Weimer, D.D. Hawn, and Y.L. Lyubchenko, *Atomic force microscopy imaging of DNA covalently immobilized on a functionalized mica substrate.* Biophysical journal, 1999. **77**(1): p. 568-576.
450. Vandenberg, E., H. Elwing, A. Askendal, and I. Lundström, *Protein immobilization of 3-aminopropyl triethoxy silaneglutaraldehyde surfaces: Characterization by detergent washing.* Journal of colloid and interface science, 1991. **143**(2): p. 327-335.
451. Hodneland, C.D., Y.-S. Lee, D.-H. Min, and M. Mrksich, *Selective immobilization of proteins to self-assembled monolayers presenting active site-directed capture ligands.* Proceedings of the National Academy of Sciences, 2002. **99**(8): p. 5048-5052.
452. Yang, Z., A.M. Belu, A. Liebmann-Vinson, H. Sugg, and A. Chilkoti, *Molecular imaging of a micropatterned biological ligand on an activated polymer surface.* Langmuir, 2000. **16**(19): p. 7482-7492.
453. Feng, X., B.B. Boumelhem, C.T. Tran, M.M. Bilek, and S.T. Fraser, *Histochemical targeting: Combining plasma immersion ion implantation and histochemical probes to target magnetic particles to intracellular cytological features.* Materials Today Advances, 2022. **16**: p. 100304.
454. Michael, P.L., Y.T. Lam, J. Hung, R.P. Tan, M. Santos, and S.G. Wise, *Comprehensive Evaluation of the Toxicity and Biosafety of Plasma Polymerized Nanoparticles.* Nanomaterials, 2021. **11**(5): p. 1176.
455. Li, P., X. Zou, X. Wang, M. Su, C. Chen, X. Sun, and H. Zhang, *A preliminary study of the interactions between microplastics and citrate-coated silver nanoparticles in aquatic environments.*

Journal of hazardous materials, 2020. **385**: p. 121601.
456. Sun, L., H. Liu, Y. Ye, Y. Lei, R. Islam, S. Tan, R. Tong, Y.-B. Miao, and L. Cai, *Smart nanoparticles for cancer therapy.* Signal Transduction and Targeted Therapy, 2023. **8**(1): p. 418.
457. Ali, M.A., M.S. Irfan, T. Khan, M.Y. Khalid, and R. Umer, *Graphene nanoparticles as data generating digital materials in industry 4.0.* Scientific Reports, 2023. **13**(1): p. 4945.
458. Gigault, J., H. El Hadri, B. Nguyen, B. Grassl, L. Rowenczyk, N. Tufenkji, S. Feng, and M. Wiesner, *Nanoplastics are neither microplastics nor engineered nanoparticles.* Nature nanotechnology, 2021. **16**(5): p. 501-507.
459. Fernandes, I.J., A.F. Aroche, A. Schuck, P. Lamberty, C.R. Peter, W. Hasenkamp, and T.L. Rocha, *Silver nanoparticle conductive inks: Synthesis, characterization, and fabrication of inkjet-printed flexible electrodes.* Scientific Reports, 2020. **10**(1): p. 8878.
460. Yang, Y., J. Han, J. Huang, J. Sun, Z.L. Wang, S. Seo, and Q. Sun, *Stretchable energy-harvesting tactile interactive interface with liquid-metal-nanoparticle-based electrodes.* Advanced Functional Materials, 2020. **30**(29): p. 1909652.
461. Grosskopf, A.K., G.A. Roth, A.A. Smith, E.C. Gale, H.L. Hernandez, and E.A. Appel, *Injectable supramolecular polymer–nanoparticle hydrogels enhance human mesenchymal stem cell delivery.* Bioengineering & translational medicine, 2020. **5**(1): p. e10147.
462. Zhen, X., K. Pu, and X. Jiang, *Photoacoustic imaging and photothermal therapy of semiconducting polymer nanoparticles: signal amplification and second near-infrared construction.* Small, 2021. **17**(6): p. 2004723.
463. Long, X., H. Wang, J. Yan, Y. Li, X. Dong, S. Tian, Y. Sun, K. Luo, B. He, and Y. Liang, *Tailor-Made Autophagy Cascade Amplification Polymeric Nanoparticles for Enhanced Tumor Immunotherapy.* Small, 2023: p. 2207898.
464. Ben-Akiva, E., R.A. Meyer, H. Yu, J.T. Smith, D.M. Pardoll, and J.J. Green, *Biomimetic anisotropic polymeric nanoparticles coated with red blood cell membranes for enhanced circulation and toxin removal.* Science advances, 2020. **6**(16): p. eaay9035.
465. Seo, B.-B., Y. Kwon, J. Kim, K.H. Hong, S.-E. Kim, H.-R. Song, Y.-M. Kim, and S.-C. Song, *Injectable polymeric nanoparticle hydrogel system for long-term anti-inflammatory effect to treat osteoarthritis.* Bioactive materials, 2022. **7**: p. 14-25.
466. Yurtdaş-Kırımlıoğlu, G. and Ş. Görgülü, *Surface modification of PLGA nanoparticles with chitosan or Eudragit® RS 100: Characterization, prolonged release, cytotoxicity, and enhanced antimicrobial activity.* Journal of Drug Delivery Science and Technology, 2021. **61**: p. 102145.
467. Yazdani-Ahmadabadi, H., K. Yu, S. Khoddami, D. F. Felix, H.H. Yeh, H.D. Luo, I. Moskalev, Q. Wang, R. Wang, and D. Grecov, *Robust Nanoparticle-Derived Lubricious Antibiofilm Coating for Difficult-to-Coat Medical Devices with Intricate Geometry.* ACS Nanoscience Au, 2022. **3**(1): p. 67-83.
468. Gonsalves, A., P. Sorkhdini, J. Bazinet, M. Ghumman, D. Dhamecha, Y. Zhou, and J.U. Menon, *Development and characterization of lung surfactant-coated polymer nanoparticles for pulmonary drug delivery.* Biomaterials Advances, 2023. **150**: p. 213430.
469. Kang, H., S. Rho, W.R. Stiles, S. Hu, Y. Baek, D.W. Hwang, S. Kashiwagi, M.S. Kim, and H.S. Choi, *Size-dependent EPR effect of polymeric nanoparticles on tumor targeting.* Advanced healthcare materials, 2020. **9**(1): p. 1901223.
470. Omerović, N., M. Djisalov, K. Živojević, M. Mladenović, J. Vunduk, I. Milenković, N.Ž. Knežević, I. Gadjanski, and J. Vidić, *Antimicrobial nanoparticles and biodegradable polymer composites for active food packaging applications.* Comprehensive Reviews in Food Science and Food Safety, 2021. **20**(3): p. 2428-2454.
471. Guenday, C., S. Anand, H.B. Gencer, S. Munafo, L. Moroni, A. Fusco, G. Donnarumma, C. Ricci, P.C. Hatir, and N.G. Tuereli, *Ciprofloxacin-loaded polymeric nanoparticles incorporated electrospun fibers for drug delivery in tissue engineering applications.* Drug Delivery and Translational Research, 2020. **10**: p. 706-720.
472. Trenkenschuh, E. and W. Friess, *Freeze-drying of nanoparticles: How to overcome colloidal instability by formulation and process optimization.* European journal of pharmaceutics and biopharmaceutics, 2021. **165**: p. 345-360.

473. Kenry, T. Yeo, P.N. Manghnani, E. Middha, Y. Pan, H. Chen, C.T. Lim, and B. Liu, *Mechanistic understanding of the biological responses to polymeric nanoparticles.* ACS Nano, 2020. **14**(4): p. 4509-4522.
474. Shrestha, S., B. Wang, and P. Dutta, *Nanoparticle processing: Understanding and controlling aggregation.* Advances in colloid and interface science, 2020. **279**: p. 102162.
475. Gutiérrez, L., L. De la Cueva, M. Moros, E. Mazarío, S. De Bernardo, J.M. De la Fuente, M.P. Morales, and G. Salas, *Aggregation effects on the magnetic properties of iron oxide colloids.* Nanotechnology, 2019. **30**(11): p. 112001.
476. Jeldres, R.I., P.D. Fawell, and B.J. Florio, *Population balance modelling to describe the particle aggregation process: A review.* Powder technology, 2018. **326**: p. 190-207.
477. Liu, L., M. Borghei, Z. Wang, J. Xu, Y. Fan, and O.J. Rojas, *Salt-induced colloidal destabilization, separation, drying, and redispersion in aqueous phase of cationic and anionic nanochitins.* Journal of agricultural and food chemistry, 2018. **66**(35): p. 9189-9198.
478. Ansar, S.M., B. Fellows, P. Mispireta, O.T. Mefford, and C.L. Kitchens, *pH triggered recovery and reuse of thiolated poly (acrylic acid) functionalized gold nanoparticles with applications in colloidal catalysis.* Langmuir, 2017. **33**(31): p. 7642-7648.
479. Xu, L., H.-W. Liang, Y. Yang, and S.-H. Yu, *Stability and reactivity: positive and negative aspects for nanoparticle processing.* Chemical Reviews, 2018. **118**(7): p. 3209-3250.
480. de Gracia Lux, C., S. Joshi-Barr, T. Nguyen, E. Mahmoud, E. Schopf, N. Fomina, and A. Almutairi, *Biocompatible polymeric nanoparticles degrade and release cargo in response to biologically relevant levels of hydrogen peroxide.* Journal of the American chemical society, 2012. **134**(38): p. 15758-15764.
481. Meder, F., S.S. Thomas, L.W. Fitzpatrick, A. Alahmari, S. Wang, J.G. Beirne, G. Vaz, G. Redmond, and K.A. Dawson, *Labeling the structural integrity of nanoparticles for advanced in situ tracking in bionanotechnology.* ACS Nano, 2016. **10**(4): p. 4660-4671.
482. Panyam, J., M.M. Dali, S.K. Sahoo, W. Ma, S.S. Chakravarthi, G.L. Amidon, R.J. Levy, and V. Labhasetwar, *Polymer degradation and in vitro release of a model protein from poly (D, L-lactide-co-glycolide) nano-and microparticles.* Journal of Controlled Release, 2003. **92**(1-2): p. 173-187.
483. Gupta, N.K., Y. Ghaffari, S. Kim, J. Bae, K.S. Kim, and M. Saifuddin, *Photocatalytic degradation of organic pollutants over MFe2O4 (M= Co, Ni, Cu, Zn) nanoparticles at neutral pH.* Scientific Reports, 2020. **10**(1): p. 4942.
484. Muramatsu, H., K. Lam, C. Bajusz, D. Laczkó, K. Karikó, P. Schreiner, A. Martin, P. Lutwyche, J. Heyes, and N. Pardi, *Lyophilization provides long-term stability for a lipid nanoparticle-formulated, nucleoside-modified mRNA vaccine.* Molecular Therapy, 2022. **30**(5): p. 1941-1951.
485. Gustafson, H.H., D. Holt-Casper, D.W. Grainger, and H. Ghandehari, *Nanoparticle uptake: the phagocyte problem.* Nano Today, 2015. **10**(4): p. 487-510.
486. Sukhanova, A., S. Bozrova, P. Sokolov, M. Berestovoy, A. Karaulov, and I. Nabiev, *Dependence of nanoparticle toxicity on their physical and chemical properties.* Nanoscale research letters, 2018. **13**: p. 1-21.
487. Pandit, A., A. Indurkar, C. Deshpande, R. Jain, and P. Dandekar, *A systematic review of physical techniques for chitosan degradation.* Carbohydrate Polymer Technologies and Applications, 2021. **2**: p. 100033.
488. Brown, T.D., N. Habibi, D. Wu, J. Lahann, and S. Mitragotri, *Effect of nanoparticle composition, size, shape, and stiffness on penetration across the blood–brain barrier.* ACS Biomaterials Science & Engineering, 2020. **6**(9): p. 4916-4928.
489. Bandi, S.P., Y.S. Kumbhar, and V.V.K. Venuganti, *Effect of particle size and surface charge of nanoparticles in penetration through intestinal mucus barrier.* Journal of Nanoparticle Research, 2020. **22**: p. 1-11.
490. Lang, T., R. Zhu, X. Zhu, W. Yan, Y. Li, Y. Zhai, T. Wu, X. Huang, Q. Yin, and Y. Li, *Combining gut microbiota modulation and chemotherapy by capecitabine-loaded prebiotic nanoparticle improves colorectal cancer therapy.* Nature Communications, 2023. **14**(1): p. 4746.
491. Yi, Q., Z. Xu, A. Thakur, K. Zhang, Q. Liang, Y. Liu, and Y. Yan, *Current understanding of plant-derived exosome-like nanoparticles in regulating the inflammatory response and immune system*

microenvironment. Pharmacological Research, 2023. **190**: p. 106733.
492. Baranov, M.V., M. Kumar, S. Sacanna, S. Thutupalli, and G. Van den Bogaart, *Modulation of immune responses by particle size and shape.* Frontiers in immunology, 2021. **11**: p. 607945.
493. Nakamura, T., M. Kawai, Y. Sato, M. Maeki, M. Tokeshi, and H. Harashima, *The effect of size and charge of lipid nanoparticles prepared by microfluidic mixing on their lymph node transitivity and distribution.* Molecular Pharmaceutics, 2020. **17**(3): p. 944-953.
494. Rao, A., S. Roy, and P.P. Pillai, *Temporal Changes in Interparticle Interactions Drive the Formation of Transiently Stable Nanoparticle Precipitates.* Langmuir, 2021. **37**(5): p. 1843-1849.
495. Xie, H., M. Hong, E.M. Hitz, X. Wang, M. Cui, D.J. Kline, M.R. Zachariah, and L. Hu, *High-temperature pulse method for nanoparticle redispersion.* Journal of the American chemical society, 2020. **142**(41): p. 17364-17371.
496. Ohtake, T., H. Ito, K. Horiba, and N. Toyoda, *Synthesis of Water-Soluble Polymeric Surfactants Bearing Sulfonic Acid Groups and the Effects of Hydrophilic Components on the Rheology and Dispersive Properties of Dye Dispersions.* ACS Applied Polymer Materials, 2022. **4**(11): p. 8556-8563.
497. Kignelman, G., S. Eyley, C. Zhou, B. Tunca, M. Gonon, D. Lahem, J.W. Seo, and W. Thielemans, *Colloidal Stability and Aggregation Mechanism in Aqueous Suspensions of TiO2 Nanoparticles Prepared by Sol–Gel Synthesis.* Langmuir, 2021. **37**(51): p. 14846-14855.
498. Abiev, R.S., O. Almjasheva, V. Popkov, and O. Proskurina, *Microreactor synthesis of nanosized particles: The role of micromixing, aggregation, and separation processes in heterogeneous nucleation.* Chemical Engineering Research and Design, 2022. **178**: p. 73-94.
499. Kovačević, E., I. Stefanović, J. Berndt, and J. Winter, *Infrared fingerprints and periodic formation of nanoparticles in Ar/C 2 H 2 plasmas.* Journal of Applied Physics, 2003. **93**(5): p. 2924-2930.
500. Pedersen, G., P. Fäldt, B. Bergenståhl, and H. Kristensen, *Solid state characterisation of a dry emulsion: a potential drug delivery system.* International journal of pharmaceutics, 1998. **171**(2): p. 257-270.
501. Ruphuy, G., T. Weide, J. Lopes, M.M. Dias, and M. Barreiro, *Preparation of nano-hydroxyapatite/chitosan aqueous dispersions: From lab scale to continuous production using an innovative static mixer.* Carbohydrate polymers, 2018. **202**: p. 20-28.
502. Velgosova, O., E. Čižmárová, J. Málek, and J. Kavuličova, *Effect of storage conditions on long-term stability of Ag nanoparticles formed via green synthesis.* International Journal of Minerals, Metallurgy, and Materials, 2017. **24**: p. 1177-1182.
503. Kakavandi, A. and M. Akbari, *Experimental investigation of thermal conductivity of nanofluids containing of hybrid nanoparticles suspended in binary base fluids and propose a new correlation.* International Journal of Heat and Mass Transfer, 2018. **124**: p. 742-751.
504. He, Y., A. Hassanpour, and A.E. Bayly, *Combined effect of particle size and surface cohesiveness on powder spreadability for additive manufacturing.* Powder technology, 2021. **392**: p. 191-203.
505. Ojwang, D.O., M. Svensson, C. Njel, R. Mogensen, A.S. Menon, T. Ericsson, L. Häggström, J. Maibach, and W.R. Brant, *Moisture-driven degradation pathways in prussian white cathode material for sodium-ion batteries.* ACS Applied Materials & Interfaces, 2021. **13**(8): p. 10054-10063.
506. El-Taibany, W. and R. Taha, *Variable-size dust grains with generalized (r, q) electrons in a dusty plasma.* Contributions to Plasma Physics, 2019. **59**(7): p. e201800072.
507. Deka, T., A. Boruah, S. Sharma, and H. Bailung, *Observation of self-excited dust acoustic wave in dusty plasma with nanometer size dust grains.* Physics of Plasmas, 2017. **24**(9).
508. Khan, N.A., B. Akhavan, H. Zhou, L. Chang, Y. Wang, L. Sun, M.M. Bilek, and Z. Liu, *High entropy alloy thin films of AlCoCrCu0. 5FeNi with controlled microstructure.* Applied Surface Science, 2019. **495**: p. 143560.
509. Lin, J., E. Pozharski, and M.A. Wilson, *Short carboxylic acid–carboxylate hydrogen bonds can have fully localized protons.* Biochemistry, 2017. **56**(2): p. 391-402.
510. Henry, D., *The cataphoresis of suspended particles. Part I.—The equation of cataphoresis.* Proceedings of the Royal Society of London. Series A, Containing Papers of a Mathematical and Physical Character, 1931. **133**(821): p. 106-129.

511. Kamiya, H., K. Gotoh, M. Shimada, T. Uchikoshi, Y. Otani, M. Fuji, S. Matsusaka, T. Matsuyama, J. Tatami, and K. Higashitani, *Characteristics and behavior of nanoparticles and its dispersion systems*, in *Nanoparticle Technology Handbook*. 2008, Elsevier. p. 113-176.
512. Ashraf, M.A., W. Peng, Y. Zare, and K.Y. Rhee, *Effects of size and aggregation/agglomeration of nanoparticles on the interfacial/interphase properties and tensile strength of polymer nanocomposites.* Nanoscale research letters, 2018. **13**: p. 1-7.
513. Xu, H., H. Tian, J. Deng, Q. Zhuo, J. Cui, J. Wang, Y. Yin, and P. Yu, *Review of influence of steric effect on aggregation behavior of fine particles.* Minerals Engineering, 2023. **203**: p. 108304.
514. Song, L., S. Patil, Y. Song, L. Chen, F. Tian, L. Chen, X. Li, L. Li, and S. Cheng, *Nanoparticle Clustering and Viscoelastic Properties of Polymer Nanocomposites with Non-Attractive Polymer–Nanoparticle Interactions.* Macromolecules, 2022. **55**(17): p. 7626-7636.
515. Ruiz, E., V.H. Orozco, L.M. Hoyos, and L.F. Giraldo, *Study of sonication parameters on PLA nanoparticles preparation by simple emulsion-evaporation solvent technique.* European Polymer Journal, 2022. **173**: p. 111307.
516. Afzal, A., I. Nawfal, I. Mahbubul, and S.S. Kumbar, *An overview on the effect of ultrasonication duration on different properties of nanofluids.* Journal of Thermal Analysis and Calorimetry, 2019. **135**(1): p. 393-418.
517. Ali, F., L. Reinert, J.-M. Lévêque, L. Duclaux, F. Muller, S. Saeed, and S.S. Shah, *Effect of sonication conditions: solvent, time, temperature and reactor type on the preparation of micron sized vermiculite particles.* Ultrasonics sonochemistry, 2014. **21**(3): p. 1002-1009.
518. Lee, J., Z.-L. Zhou, and S.H. Behrens, *Charging mechanism for polymer particles in nonpolar surfactant solutions: influence of polymer type and surface functionality.* Langmuir, 2016. **32**(19): p. 4827-4836.
519. Arooj, N., T.M. Khan, M. Mumtaz, A. Rehman, I. Ahmad, A. Shah, M.u. Hassan, and M. Raffi, *Polymeric Fe3O4 Nanoparticle/Carbon Nanofiber Hybrid Nanocomposite Coatings for Improved Terahertz Shielding.* ACS Applied Nano Materials, 2023. **6**(7): p. 5264-5273.
520. Ren, Y., D. Zhu, T. Shi, B. Song, J. Qi, L. Zhang, and Y. Yu, *Composite Foams of the Graphitic Carbon Nitride@ Carbon Nanofibrils Conferred a Superamphiphilic Property and Reinforced Thermal Stability.* Langmuir, 2023. **39**(42): p. 15122-15130.
521. Zhang, R., X. Zhang, H. Xie, S. Liu, Q. Ye, and F. Zhou, *Fabrication of Zwitterionic Polymer-Functionalized Onion-like Carbon Nanoparticles as Aqueous Lubricant Additives.* Langmuir, 2023. **39**(43): p. 15391-15400.
522. Ahmed, A., S. Verma, P. Mahajan, A.K. Sundramoorthy, and S. Arya, *Upcycling of surgical facemasks into carbon based thin film electrode for supercapacitor technology.* Scientific Reports, 2023. **13**(1): p. 12146.
523. Liu, J., R. Li, and B. Yang, *Carbon dots: A new type of carbon-based nanomaterial with wide applications.* ACS Central Science, 2020. **6**(12): p. 2179-2195.
524. Shao, W., R. Yan, M. Zhou, L. Ma, C. Roth, T. Ma, S. Cao, C. Cheng, B. Yin, and S. Li, *Carbon-Based Electrodes for Advanced Zinc-Air Batteries: Oxygen-Catalytic Site Regulation and Nanostructure Design.* Electrochemical Energy Reviews, 2023. **6**(1): p. 11.
525. Zhang, L.-H., F. Yu, and N.R. Shiju, *Carbon-based catalysts for selective electrochemical nitrogen-to-ammonia conversion.* ACS Sustainable Chemistry & Engineering, 2021. **9**(23): p. 7687-7703.
526. Nath, N., A. Kumar, S. Chakroborty, S. Soren, A. Barik, K. Pal, and F.G. de Souza Jr, *Carbon nanostructure embedded novel sensor implementation for detection of aromatic volatile organic compounds: an organized review.* ACS omega, 2023. **8**(5): p. 4436-4452.
527. Khalin, I., D. Heimburger, N. Melnychuk, M. Collot, B. Groschup, F. Hellal, A. Reisch, N. Plesnila, and A.S. Klymchenko, *Ultrabright fluorescent polymeric nanoparticles with a stealth pluronic shell for live tracking in the mouse brain.* ACS Nano, 2020. **14**(8): p. 9755-9770.
528. Boufendi, L. and A. Bouchoule, *Industrial developments of scientific insights in dusty plasmas.* Plasma Sources Science and Technology, 2002. **11**(3A): p. A211.
529. Clayton, Z.E., M. Santos, H. Shah, J. Lu, S. Chen, H. Shi, S. Kanagalingam, P.L. Michael, S.G. Wise, and J.J. Chong, *Plasma polymerized nanoparticles are a safe platform for direct delivery of growth factor therapy to the injured heart.* Frontiers in Bioengineering and Biotechnology, 2023.

11: p. 1127996.
530. Couëdel, L. and V. Nosenko, *Stability of two-dimensional complex plasma monolayers in asymmetric capacitively coupled radio-frequency discharges.* Physical Review E, 2022. **105**(1): p. 015210.
531. Salpeter, E.E., *Electron density fluctuations in a plasma.* Physical Review, 1960. **120**(5): p. 1528.
532. Wilczek, S., J. Schulze, R.P. Brinkmann, Z. Donkó, J. Trieschmann, and T. Mussenbrock, *Electron dynamics in low pressure capacitively coupled radio frequency discharges.* Journal of Applied Physics, 2020. **127**(18).
533. Lieberman, M.A. and A.J. Lichtenberg, *Principles of plasma discharges and materials processing*. 2005: John Wiley & Sons.
534. Hollenstein, C., *The physics and chemistry of dusty plasmas.* Plasma Physics and Controlled Fusion, 2000. **42**(10): p. R93.
535. Kim, K.-Y., J.H. Kim, C.-W. Chung, and H.-C. Lee, *Effect of electron energy distributions on the electron density in nitrogen inductively coupled plasmas.* Plasma Sources Science and Technology, 2022. **31**(10): p. 105007.
536. France, R.M. and R.D. Short, *Plasma treatment of polymers: the effects of energy transfer from an argon plasma on the surface chemistry of polystyrene, and polypropylene. A high-energy resolution X-ray photoelectron spectroscopy study.* Langmuir, 1998. **14**(17): p. 4827-4835.
537. Andreev, S., A. Bernatskiy, N. Dyatko, I. Kochetov, and V. Ochkin, *Study of the Effect of the Anode on EEDF and the Spatial Profile of the Electron Density in a Discharge with a Hollow Cathode in Helium.* Plasma Physics Reports, 2023. **49**(8): p. 1031-1037.
538. Yin, Y., M. Bilek, and D. McKenzie, *The origins of self-bias on dielectric substrates in RF plasma processing.* Surface and coatings Technology, 2006. **200**(12-13): p. 3670-3674.
539. Masheyeva, R.U., K.N. Dzhumagulova, M. Myrzaly, J. Schulze, and Z. Donko, *Self-bias voltage formation and charged particle dynamics in multi-frequency capacitively coupled plasmas.* AIP Advances, 2021. **11**(7).
540. Karar, P., G. Kumar, R. Kar, D. Patil, and R.O. Dusane, *Diagnostics of Inductively Coupled Plasma Under the Influence of Immersed RF Self-Biased Substrate Electrode.* IEEE transactions on plasma science, 2023.
541. Liu, Y., J. Trieschmann, B. Berger, J. Schulze, and T. Mussenbrock, *Non-linear effects and electron heating dynamics in radio-frequency capacitively coupled plasmas with a non-uniform transverse magnetic field.* Physics of Plasmas, 2021. **28**(5).
542. Wu, H., Z. Chen, S. Yu, Q. Wang, X. Li, W. Jiang, and Y. Zhang, *The effects of match circuit on the breakdown process of capacitively coupled plasma driven by radio frequency.* Journal of Applied Physics, 2022. **131**(15).
543. Wang, X.-K., Y.-X. Liu, X.-Y. Wang, Q.-Z. Zhang, K. Zhao, and Y.-N. Wang, *The effect of a negative direct-current voltage on striated structures and electrical parameters in a capacitively coupled rf discharge in CF4.* Plasma Sources Science and Technology, 2021. **30**(5): p. 055019.
544. Fu, Y.-Y., X.-K. Wang, Y.-X. Liu, J. Schulze, Z. Donkó, and Y.-N. Wang, *Effects of 'step-like'amplitude-modulation on a pulsed capacitively coupled RF discharge: an experimental investigation.* Plasma Sources Science and Technology, 2022. **31**(8): p. 085005.
545. Wang, X.-Y., J.-R. Liu, Y.-X. Liu, Z. Donkó, Q.-Z. Zhang, K. Zhao, J. Schulze, and Y.-N. Wang, *Comprehensive understanding of the ignition process of a pulsed capacitively coupled radio frequency discharge: The effect of power-off duration.* Plasma Sources Science and Technology, 2021. **30**(7): p. 075011.
546. Saikia, P., H. Bhuyan, M. Favre, E. Wyndham, and F. Veloso, *An analytical model of multi-component radio frequency capacitively coupled plasma and experimental validation.* Physics of Plasmas, 2017. **24**(1).
547. Arellano, F.J., M. Gyulai, Z. Donkó, P. Hartmann, T.V. Tsankov, U. Czarnetzki, and S. Hamaguchi, *First-principles simulation of optical emission spectra for low-pressure argon plasmas and its experimental validation.* Plasma Sources Science and Technology, 2023. **32**(12): p. 125007.
548. Schulenberg, D.A., I. Korolov, Z. Donkó, A. Derzsi, and J. Schulze, *Multi-diagnostic experimental validation of 1d3v PIC/MCC simulations of low pressure capacitive RF plasmas operated in argon.*

Plasma Sources Science and Technology, 2021. **30**(10): p. 105003.
549. Quraishi, A., O. Hamo, and I. Kronhaus, *Plasma simulation benchmark for CCRF discharge with secondary electron emission.* IEEE transactions on plasma science, 2019. **48**(1): p. 109-118.
550. Matyash, K., R. Schneider, F. Taccogna, A. Hatayama, S. Longo, M. Capitelli, D. Tskhakaya, and F. Bronold, *Particle in cell simulation of low temperature laboratory plasmas.* Contributions to Plasma Physics, 2007. **47**(8-9): p. 595-634.
551. Becker, M.M., H. Kählert, A. Sun, M. Bonitz, and D. Loffhagen, *Advanced fluid modeling and PIC/MCC simulations of low-pressure ccrf discharges.* Plasma Sources Science and Technology, 2017. **26**(4): p. 044001.
552. Tanışlı, M., N. Şahin, S. Demir, and S. Mertadam, *Electrical Characteristics of Capacitive Coupled Radio Frequency Discharges in Argon and Hydrogen.* Plasma Physics Reports, 2019. **45**: p. 376-386.
553. Xiang, H., L. Chong, Y. Zhang, C. Jianping, C. Yudong, Z. Xiaojun, C. Bingyan, P. Jiaxin, and W. Yibing, *Diagnostic of capacitively coupled radio frequency plasma from electrical discharge characteristics: comparison with optical emission spectroscopy and fluid model simulation.* Plasma Science and Technology, 2017. **20**(2): p. 024005.
554. Saikia, P., H. Bhuyan, M. Escalona, M. Favre, R.S. Rawat, and E. Wyndham, *A nonlinear global model of single frequency capacitively coupled plasma and its experimental validation.* AIP Advances, 2018. **8**(4).
555. Su, Z.-X., D.-H. Shi, Y.-X. Liu, K. Zhao, F. Gao, and Y.-N. Wang, *Radially-dependent ignition process of a pulsed capacitively coupled RF argon plasma over 300 mm-diameter electrodes: multi-fold experimental diagnostics.* Plasma Sources Science and Technology, 2021. **30**(12): p. 125013.
556. Singh, P. and S.K. Karkari, *Equilibrium properties of inhomogeneous partially-magnetized plasma containing negative ions.* Journal of Physics D: Applied Physics, 2022. **55**(23): p. 235201.
557. Anjum, Z., M. Younus, and N. Rehman, *Evolution of plasma parameters in capacitively coupled He–O2/Ar mixture plasma generated at low pressure using 13.56 MHz generator.* Physica Scripta, 2020. **95**(4): p. 045403.
558. Jin, C., C.-S. Yip, Y.-c. Ghim, W. Zhang, D. Jiang, and G.S. Xu, *Parametrization of electron sheath expansion for Langmuir probe IV traces.* Journal of Instrumentation, 2023. **18**(07): p. P07009.
559. Chen, F.F., *Introduction to plasma physics*. 2012: Springer Science & Business Media.
560. Chabert, P. and N. Braithwaite, *Physics of radio-frequency plasmas*. 2011: Cambridge University Press.
561. Derzsi, A., B. Horváth, Z. Donkó, and J. Schulze, *Surface processes in low-pressure capacitive radio frequency discharges driven by tailored voltage waveforms.* Plasma Sources Science and Technology, 2020. **29**(7): p. 074001.
562. Smith, H., C. Charles, and R. Boswell, *Breakdown behavior in radio-frequency argon discharges.* Physics of Plasmas, 2003. **10**(3): p. 875-881.
563. Lymberopoulos, D.P. and D.J. Economou, *Fluid simulations of glow discharges: Effect of metastable atoms in argon.* Journal of Applied Physics, 1993. **73**(8): p. 3668-3679.
564. Yang, B., N. Zhou, and Q. Sun, *Numerical analysis of the non-equilibrium plasma flow in the gaseous electronics conference reference reactor.* Journal of Semiconductors, 2016. **37**(1): p. 016001.
565. Gnybida, M., D. Loffhagen, and D. Uhrlandt, *Fluid modeling and analysis of the constriction of the DC positive column in argon.* IEEE transactions on plasma science, 2009. **37**(7): p. 1208-1218.
566. Proshina, O., T. Rakhimova, A. Kovalev, A. Vasilieva, A. Zotovich, S. Zyryanov, and A. Rakhimov, *Experimental and PIC MCC study of electron cooling—re-heating and plasma density decay in low pressure rf ccp argon afterglow.* Plasma Sources Science and Technology, 2020. **29**(1): p. 015015.
567. Liang, Y., C. Yuan, H. Li, R. Tian, J. Wu, A. Kudryavtsev, Z. Zhou, and H. Tian, *Influence of dust particles on DC glow discharge plasma.* Physics of Plasmas, 2018. **25**(2).
568. Schleede, J., L. Lewerentz, F. Bronold, R. Schneider, and H. Fehske, *Plasma flow around and charge distribution of a dust cluster in a rf discharge.* Physics of Plasmas, 2018. **25**(4).
569. *IST-Lisbon database.* https://fr.lxcat.net/home/. *(accessed: April 2020).*
570. Pitchford, L. and J. Boeuf, *SIGLO Database.* https://fr.lxcat.net/home/ *(accessed: June 2020).*

571. Hyman, H., *Electron-impact ionization cross sections for excited states of the rare gases (Ne, Ar, Kr, Xe), cadmium, and mercury.* Physical Review A, 1979. **20**(3): p. 855.
572. Donkó, Z., J. Schulze, U. Czarnetzki, A. Derzsi, P. Hartmann, I. Korolov, and E. Schüngel, *Fundamental investigations of capacitive radio frequency plasmas: simulations and experiments.* Plasma Physics and Controlled Fusion, 2012. **54**(12): p. 124003.
573. Tanışlı, M., N.h. Şahin, and S. Demir, *Comments on the Langmuir probe measurements of radio-frequency capacitive argon–hydrogen mixture discharge at low pressure.* Canadian Journal of Physics, 2018. **96**(5): p. 494-500.
574. Mansuroglu, D., *Capacitively coupled radio frequency nitrogen plasma generated at two different exciting frequencies of 13.56 MHz and 40 MHz analyzed using Langmuir probe along with optical emission spectroscopy.* AIP Advances, 2019. **9**(5).
575. Baeva, M., D. Loffhagen, M. Becker, and D. Uhrlandt, *Fluid modelling of DC argon microplasmas: effects of the electron transport description.* Plasma chemistry and plasma processing, 2019. **39**(4): p. 949-968.
576. Godyak, V., R. Piejak, and B. Alexandrovich, *Measurement of electron energy distribution in low-pressure RF discharges.* Plasma Sources Science and Technology, 1992. **1**(1): p. 36.
577. Godyak, V. and R. Piejak, *Abnormally low electron energy and heating-mode transition in a low-pressure argon rf discharge at 13.56 MHz.* Physical review letters, 1990. **65**(8): p. 996.
578. You, S. and H.-Y. Chang, *Nonlocal to local transition of electron kinetic property in magnetized plasma.* Physics of Plasmas, 2006. **13**(4).
579. Raizer, Y.P., *Gas discharge physics*. 1991, Springer google schola.
580. Mathew, P., J. George, S. Mathews T, and P. Kurian, *Experimental verification of modified Paschen's law in DC glow discharge argon plasma.* AIP Advances, 2019. **9**(2).
581. Ledernez, L., F. Olcaytug, and G. Urban, *Independent influence of the inter-electrode distance in Paschen curves.* 20th ESCAMPIG, 2010.
582. Staack, D.A., *Characterization and Stabilization of Atmospheric Pressure DC Microplasmas and their Application to Thin Film Deposition Volume*. 2008, Drexel University.
583. Fu, Y., H. Wang, and X. Wang, *Similarity theory and scaling laws for low-temperature plasma discharges: a comprehensive review.* Reviews of Modern Plasma Physics, 2023. **7**(1): p. 10.
584. Shivkumar, G., M. Alrefae, S. Tholeti, S. Macheret, T. Fisher, and A. Alexeenko, *Discharge regimes and emission characteristics of capacitively coupled radio frequency argon plasma with a square wave input.* Journal of Applied Physics, 2019. **125**(22).
585. Bora, B., H. Bhuyan, M. Favre, E. Wyndham, H. Chuaqui, and C. Wong, *Measurements of plasma parameters in capacitively coupled radio frequency plasma from discharge characteristics: correlation with optical emission spectroscopy.* Current Applied Physics, 2013. **13**(7): p. 1448-1453.
586. Liu, Z., Q. Yuan, and G. Yin, *The PSR effect of matching network in 8/100 MHz geometrically symmetrical capacitively coupled Ar plasma.* Physics of Plasmas, 2022. **29**(10).
587. Wen, Y.-Y., Y.-R. Zhang, G. Jiang, Y.-H. Song, and Y.-N. Wang, *Secondary electron effect on sustaining capacitively coupled discharges: A hybrid modeling investigation of the ionization rate.* AIP Advances, 2019. **9**(5).
588. Wu, J., H. Zheng, Y. Wang, Q. Cao, F. Zhou, J. Zhang, and X. Huang, *Experimental diagnosis of electron density and temperature in capacitively coupled argon plasmas: Triple-frequency discharges and two-dimensional spatial distributions.* Physics of Plasmas, 2021. **28**(9).
589. Kudrna, P. and E. Passoth, *Langmuir Probe Diagnostics of a Low Temperature Non-Isothermal Plasma in a Weak Magnetic Field.* Contributions to Plasma Physics, 1997. **37**(5): p. 417-429.